**UNIVERSITY OF SOUTHAMPTON**

FACULTY OF ENGINEERING, SCIENCE AND MATHEMATICS

Institute of Sound and Vibration Research

# Automated Segmentation and Tracking of Lumbar Spine Motion in Low-Dosage Digital Videofluoroscopic Images

by

**Yuxin Zheng**

Thesis submitted for the degree of Doctor of Philosophy

March 2008

UNIVERSITY OF SOUTHAMPTON

ABSTRACT

FACULTY OF ENGINEERING, SCIENCE AND MATHEMATICS

INSTITUTE OF SOUND AND VIBRATION RESEARCH

Doctor of Philosophy

# AUTOMATED SEGMENTATION AND TRACKING OF LUMBAR SPINE MOTION IN LOW-DOSAGE DIGITAL VIDEOFLUOROSCOPIC IMAGES

by Yuxin Zheng

Low back pain is one of the most frequent medical problems in the western world and its consequent cost is enormous. However, despite the high occurrence of low back pain, diagnosis of the causes is still a major problem. Research has indicated that low back pain is often related to mechanical disorders of the spinal or holding elements. Therefore, it could be very helpful for clinical diagnosis to study the motion of lumbar spine in order to determine where abnormal motion exists and hence any sources of mechanical instability. Digital videofluoroscopy (DVF) is currently the only practical medical imaging technique to obtain real-time, continuous motion sequences of the lumbar spine. However, DVF images suffer from the presence of noise, poor contrast and adjacent structures near the vertebrae due to the low radiation dosage.

Recently, wavelet-based approaches have been applied in edge detection to acquire multi-scale gradient images. In multi-scale detection, the edges are more accurately located with low scales but some false edges are produced; with large scales, fewer false edges are identified but traded against a reduced accuracy in the edge location. This project presents a scale multiplication in the identification of spinal vertebrae as a basis for

quantifying kinematics. The scale multiplication is defined as the product of the response of the detection filter at different scales so that it combines the advantages of the low and large scales. Once edges are determined as the local maxima in scale multiplication, more robust detection results are obtained after thresholding. The threshold values are decided by the standard deviation of the noise in the images. With the edge information of the lumbar spine vertebrae, biomechanical parameters, such as rotation and intervertebral angles can be measured via manual landmarking.

Another development of this project is the automated tracking technique by using the Generalized Hough transform algorithm. With the mathematical description of the vertebral edges detected by the wavelet scale multiplication method, the vertebral movements in spine motion are tracked. This approach is applied to the DVF image sequences from a calibration model and from ten human subjects to demonstrate its reliability and robustness.

This research would benefit the diagnosis of low back pain and provide a platform for the further development of other clinical analysis, such as the cervical spine study.

# List of Contents

# List of Figures

# List of Tables

# Symbols and Abbreviations

| | |
|---|---|
| $\psi(x)$ | wavelet function |
| $\phi(t)$ | scaling function |
| $\nabla F$ | 2-D gradient of an image $f(x,y)$ |
| $f(x,y)$ | 2-D image function in a $xy$ coordinates system |
| $s$ | scale of the wavelet transform |
| $W_j$ | Detail signal in the wavelet decomposition |
| $V_j$ | Approximation signal in the wavelet decomposition |

| | |
|---|---|
| A/P | Anterior/Posterior |
| CMT | Centre point of the Template Model |
| CR | Centre of Reaction |
| CT | Computerized axial Tomography |
| CV | Centre point of the Vertebra |
| DSS | Department of Social Security |
| DVF | Digital Videofluoroscopy |
| FDoG | First Derivative of Gaussian |
| FT | Fourier transform |
| GHT | Generalized Hough transform |
| GP | General practitioner |
| HT | Hough transform |
| IAR | Instantaneous Axis of Rotation |
| ICR | Instantaneous Centre of Rotation |
| IVA | Intervertebral angle |
| LoG | Laplacian of Gaussian |
| MME | Mean value of the mean of the error |
| MRA | Multiresolution Analysis |
| MRI | Magnetic resonance imaging |
| MSDE | Mean value of the standard deviation of the error |
| MSE | Mean value of the standard error |
| NHS | National Health Service |
| pdf | Probability density function |
| PMT | Passive Motion Table |
| PSD | Power Spectrum Density |
| R-Table | Reference Table |
| RHT | Randomized Hough transform |

| | |
|---|---|
| ROM | Range of Motion |
| RoS | Region of Support |
| SE | Standard Error |
| SNR | Signal-to-Noise Ratio |
| std | Standard deviation |
| WT | Wavelet transform |

# Acknowledgements

My thanks go to my supervisor Prof Robert Allen for his patience and especially his continual encouragement, guidance throughout my studies during the past three years.

I would also to acknowledge members of ISVR at University of Southampton, especially Prof Paul White, Dr David Simpson, Dr Olie Baumann, Mrs Joyce Shotter and Mrs Maureen Mew for their invaluable suggestions and inspiring discussions. Many thanks also due to the ISVR Workshop staffs, who are always there to give me the help in the equipment problems. It has been a pleasant research process and I enjoyed this three-period in ISVR. I also gratefully acknowledge the Rayleigh Scholarship offered by the ISVR to support my PhD study.

Special thanks also goes to Dr. Michael Kondracki for providing me with the digital fluoroscopic image sequences and for his manual marking data. I would also like to appreciate Ruian People's Hospital for supporting me with the X-ray, CT and MRI images.

I thank my good friends, Muxi Zhu, Liancheng He and Yifeng Zhao, for their advices and supports in my entire PhD study. I would also like to thank many friends that I met here, to name a few, Xiaoli Li, Letu Yang, Benny Lam, Yan Hou, Suogang Wang and Ian Black for their fine encouragement.

Above all, I would like to thank everyone in my family, in particular my parents, not only for their financial support, but also for their undoubted trust, support and cheer throughout my life.

*To My Parents*

# Chapter 1 Introduction

## 1.1 Background and Motivation

Low back pain is defined as pain in the spine or muscle of the low back. Low back pain is one of the most frequent problems treated by chiropractors, osteopathic physicians, physical therapists (physiotherapists), anesthesiologists/pain medicine physicians, and orthopaedic surgeons or neurosurgeons. In the U.S., acute low back pain is the fifth most common reason for all physician visits. The research found that about 80-90% adults experience back pain at some point in their life, and 20-50% working adults have back pain every year (Patel,A.T. et al. 2000; Phillips,D.L. 2004). The evidence from Britain and elsewhere also shows that back pain is an increasing problem – not that there is any evidence of changing pathology, but rather due to changed attitudes and expectations. This trend has been particularly noticeable since the mid '80s. Moreover, the cost of low back pain is enormous. The estimated cost to the National Health Service (NHS) in the U.K. is £481 million a year (min-max range £356-649 million), with non-NHS costs, such as private consultations and prescriptions, being an additional £197 million per year. Costs of the Department of Social Security (DSS) benefit is estimated at about £1.4 billion with lost production estimated at £3.8 billion. This situation breaks down to an annual NHS cost to a purchasing authority with 250,000 people of £2.2 million (range £1.6-2.9 million) (Oxford Radfliffe Hospital 1995). A typical general practitioner (GP) practice with five GPs and 10,000 patients would bear costs of about £88,000 (range £65,000-118,000) (Oxford Radfliffe Hospital 1995). Similarly, the cost of back pain in the U.S. is conservatively estimated to be upwards of 90 billion dollars (Phillips,D.L. 2004).

However, despite the high occurrence of low back pain, diagnosis of the underlying causes is still a major problem. A possible reason is that low back pain is a symptom and it could be caused by different sources, such as muscle strain, arthritis, trauma, and osteoporosis. The other reason could be the complicated structure of spine and the difficulty of undertaking in *vivo* diagnosis and analysis. However, low back pain is often related to the mechanics of the spine and can often be described as due to mechanical disorders. Therefore, it could be very helpful to study the motion of spine.

Currently, digital videofluoroscopy (DVF) is the only practical medical imaging technology available with which to acquire spine motion sequences. However, digital videofluoroscopic images have poor quality and, in addition, quality varies across the image. Images are normally analyzed manually, which is very time consuming, and inter- and intra-observations should be carried out repeatedly to improve the accuracy. These fundamental problems inspire this project of the development of spine motion analysis with DVF image sequences. In summary, spine motion analysis with DVF images currently suffers from the following problems:

1. Poor quality of DVF images due to the low dosage radiation in image acquisition. In order avoid the potential health risks of radiation exposure, the dosage rate is set as low as possible. Furthermore, the skilled radiographer is required to follow the subject's motion. This can cause the loss of the anatomical details and then reduce the confidence and accuracy of both manual and computer-aid landmarking.

2. Lack of a suitable edge detection method for the segmentation of the lumbar vertebrae in DVF images. The development of an appropriate edge detector will benefit the motion tracking and the spinal biomechanics studies. However, poor quality of DVF images makes the edge detection very difficult. Moreover, too many unwanted fake edges are generated or too many edge details are lost when a uniform threshold value is applied.

3. Although the segmentation of the lumbar vertebrae and the tracking of the spine motion can be carried out by manual landmarking. The experience and sufficient *prior* knowledge on radiographic anatomy are needed. Furthermore, the landmarking procedure is time-consuming and labour-intensive, which could cause errors.

4. Knowledge of biomechanical parameters such as rotation angle, intervertebral angle, and translation in the spine motion, is not enough to model normal or abnormal spinal movement. There is a lack of comprehensive quantitative modeling tools for the diagnosis of low back pain.

## 1.2 Objectives

This study attempts to bridge the spine kinematics and computer vision fields and it is expected that this multidisciplinary effort can benefit the diagnosis of low back pain. This research aims to develop a method of automated segmentation and tracking of lumbar spine motion for low back pain diagnosis. Patients suffering from low back pain could display irregular movement at one or more intervertebral levels during movements of the lumbar spine. Hence, it is expected that the source of the damage could be located by identifying the abnormal motion at the vertebral level. Characterization of the normal motion of the lumbar spine could therefore be very valuable as a basis for diagnosing low back pain. The main objective of this research is to develop an automated segmentation and tracking algorithm for the analysis of spine motion. Biomechanical parameters describing the spine motion can be obtained by using this method and they should be close to 'gold standard' values generated by a experienced clinician of the method is to become accepted in clinical practice.

## 1.3 Overview of the Thesis

In Chapter 2, the anatomy and function of the human spine is briefly introduced and the main components of human spine are discussed in detail. The emphasis is then on the lumbar spine and its motion. Several concepts in spine biomechanics, such as rotation angle, intervertebral angle, instantaneous centre of rotation, instantaneous axis of rotation, and range of motion are introduced. Finally, low back pain, the common causes and the problems created are discussed. This chapter will be helpful for understanding the motivation and the clinical background of the research.

Several popular medical imaging technologies are introduced in Chapter 3. The analysis of their suitability for the study of spine motion is also given. The reason that the digital videofluoroscopy (DVF) method is chosen is then discussed. The DVF system, the radiation dosage and the image acquisition procedure are then presented in detail. Finally the advantages and disadvantages of DVF images are discussed.

Chapter 4 deals with the edge detection problem. Edge information is of great interest in many computer vision applications and how to obtain edges efficiently and effectively has been a main concern in image processing. In this study, vertebral edges become an crucial part of the processing because it affects the tracking results of spine motion. The conventional edge detection methods are introduced briefly and then a literature review of the application of the edge detection to vertebral identification is presented. Finally, some current results are given and discussed.

Since the conventional edge operators are not able to yield the vertebral edges sufficiently well for subsequent processing, we propose a better edge detection method in Chapter 5. We first introduce the wavelet transform (WT) theory and multiresolution

analysis (MRA) in brief. Moreover, their application in image processing and edge detection is discussed to show the potential of the wavelet-based method in our project. Our edge detection approach using scale multiplication method in both one-dimensional and two-dimensional analysis is then presented. Some examples of edge detection results on DVF images are then shown to indicate the performance of the multi-scale product method in detecting the vertebral contours from DVF images. Finally, spine biomechanical parameters, such as the rotation angle and intervertebral angle, are studied based upon the manual landmarking of our edge detection results on DVF images.

Chapter 6 represents the Generalized Hough transform technique developed for automated tracking of the vertebrae from the edge detection results of DVF images. After a brief introduction to the Hough transform, its development and application, our Generalized Hough transform (GHT) algorithm is described, including the selection of the template model, the building of a table to describe arbitrary shapes (the Reference Table) and the tracking procedure. The description of shape is essential in arbitrary shape tracking. The Reference Table is introduced to represent the shape of target object. To evaluate the performance, the GHT algorithm is applied to DVF image sequences from a calibration model. Moreover, the comparison with the pre-set values of the calibration model is conducted and the tracking error is measured. Finally, the approach is applied to human subject DVF sequences and tracking results are presented.

In Chapter 7, our automated segmentation and tracking method is further tested using real DVF image sequences from 10 healthy subjects. The biomechanical parameters, such as rotation and intervertebral angles are measured and compared with the 'gold standard' results obtained from an experienced clinician. Statistical analysis shows that they are very close but, importantly, our automated method avoids many problems inherent with manual landmarking. The track of the translation of the vertebra in the spine motion sequence is also shown in this chapter. The study is based on both flexion/extension and lateral bending of the lumbar spine.

Chapter 8 summarizes the work of this thesis, draws the conclusions and points out some likely directions for future development of the spine motion analysis and other applications of our method.

## 1.4 Contributions of the Research

The main contributions of the research developed in this thesis are:

1. First application of a wavelet scale multiplication edge detection method for digital videofluoroscopy (DVF) image processing. The good performance of this wavelet-based operator overcomes the need for manual landmarking of the vertebral contour which had to be conducted in previous researches. The vertebral shapes obtained by this method can be used directly to describe the target shapes for the spine motion tracking.

2. Development of an automated tracking approach to locate lumbar vertebrae for DVF spine motion analysis. The Generalized Hough transform is employed in our spine motion study due to its good performance in handing noise and describing shapes. The automated tracking method alleviates substantially the laborious and time-consuming manual landmarking procedure.

3. The ability of study the continuous motion of the lumbar spine. First, DVF technique has enabled the possibility of obtaining the continuous motion information of the lumbar spine with low radiation dosage. Second, the proposed wavelet scale multiplication is designed to be suitable for the segmentation of the vertebrae in poor quality DVF images. Finally, the Generalized Hough transform is applied to the edge detections to conduct the spine motion tracking. This automated segmentation and tracking algorithm has been

tested using DVF image sequences from a calibration model and from healthy human subjects. The experimental results are close to the pre-set values and the 'gold standard' values obtained from the experienced clinician.

# Chapter 2

# Human Spine and Low Back Pain

## 2.1 The Anatomy and Functions of the Spine

### 2.1.1 Introduction

The spine is one of the most important structural parts of the human body. Without it, humans could not keep themselves in an upright posture or even stand erect. It allows people to move about freely and to bend with flexibility. The spine is also designed to protect the spinal cord, which transmits neural signals between the periphery and the brain.

The spine is composed of thirty-four small bones called vertebrae that are stacked on top of each other via intervertebral discs to create the spinal column. From the top and downwards, these vertebrae can be described as five components: the cervical spine consisting of seven vertebral bodies; the thoracic spine consisting of twelve thoracic vertebral bodies; the lumbar spine consisting of five lumbar vertebral bodies; the sacrum; and the coccyx (Dykes,M.I. 2002; Oliver,J. et al. 1995). The vertebral column is shown in Figure 2-1. In anatomy, lateral view means away from the midline and toward the body side, shown in the middle column of Figure 2-1 and anterior means toward the front of the body while posterior means toward the rear of the body. Moreover, the terms of anterior and posterior (A/P) are almost always used in pairs in this thesis.

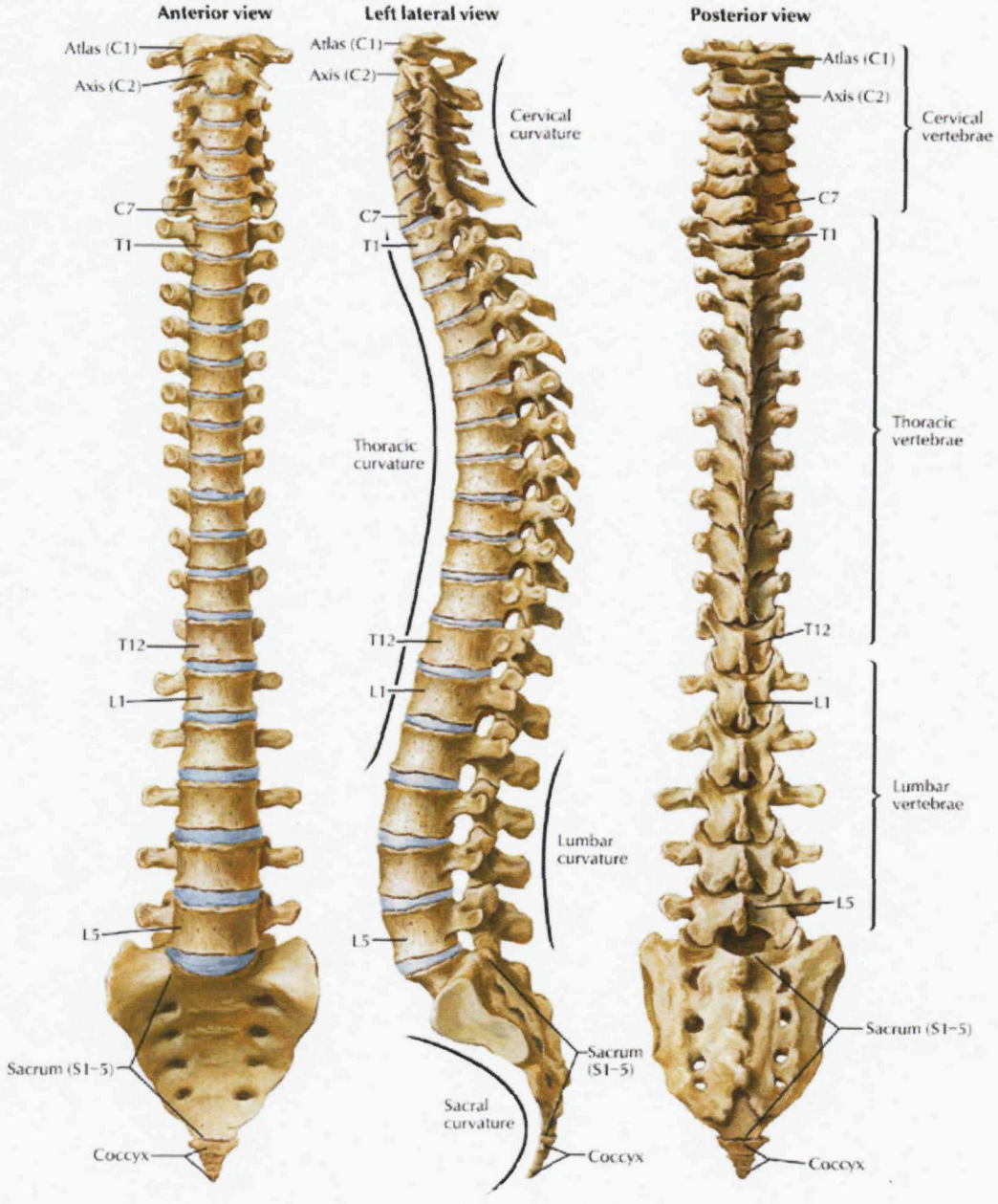


**Figure 2-1** Spine column (adapted from Hosmat Institute for Spine Problem (HISP) with kind permission).

Between each vertebra, there is a soft, gel-like cushion called the intervertebral disc. It helps absorb pressure and keeps the bones from rubbing against each other. Moreover, the discs allow flexibility in the spine and assist the muscles as shock absorbers.

Each vertebra is linked to others by groups of ligaments, called articular ligaments. An articular ligament is a short band of tough fibrous dense regular connective tissue composed mainly of long, stringy collagen fibers. Ligaments connect bones to other bones to form a joint. They are elastic and lengthen under tension. There are also tendons that fasten muscles to vertebrae. Tendons are similar to ligaments except that ligaments join bone to bone and tendons are inelastic. Furthermore, each vertebral motion segment (a term for the functional spinal unit, which is the smallest physiological motion unit of the spine.) has two facet joints, also known as zygapophysial joints. They are located on the posterior of the spine on each side of the vertebrae where they overlap the neighbouring vertebrae. The biomechanical function of each pair of facet joints is to allow a small amount of lateral bending, flexion and extension of the spine and prevent excessive twisting.

The spinal column also holds and protects the entire spinal cord and its thirty-one pairs of spinal nerve roots. Each root consists of the union of a sensory dorsal root and a motor ventral root (Bergman,R.A. et al. 1989). The roots exit the spine on both sides through spaces (intervertebral foramina) between each vertebra and transmit sensory and motor impulses to and from different parts of the body.

The normal spine has an S-shape when looking at it from the lateral surface. The cervical spine curves slightly inward, the thoracic curves outward, and the lumbar curves slightly inward. The S-shape of the healthy spine allows for an even distribution of weight and other stress applied on the spine. In particular, the lower potions of the spine hold most of

the body's weight, so the segments in this part of spine have stronger structures, which will be discussed later.

## 2.1.2 Basic Spine Anatomy

### 2.1.2.1 Spinal Vertebrae

The vertebrae, as shown in Figure 2-2, are the building blocks of the spinal column. The body of each vertebra is the large, round portion of bone that is attached to a bony ring. When the vertebrae are stacked one on top of the other, the ring creates a hollow tube where spinal cord passes through.

The bony ring attached to the vertebral body consists of several parts. First, the laminae, which are two broad plates directed backward and medially from the pedicles, extend from the body to transmit the forces from the spinous and inferior articular processes. Secondly, the spinous process is directed backward and downward from the junction of the laminae and serves for the attachment of muscles and ligaments. Then there are two transverse processes projecting one at either side from the point where the lamina joins the pedicle, between the superior and inferior articular processes. The transverse processes function as the attachment of muscles and ligaments. Finally, the pedicles are two short, thick processes that connect to both sides of the laminae (Bogduk,N. 2005; White,A.A. et al. 1990).

The vertebra, like all bones, has an outer shell called cortical bone. It is extremely hard and composed of multiple stacked layers with few gaps. Cortical bone forms the surface of bones and contributes about 80% of the weight of a human skeleton (Hubal,M.J. et al. 2005). The main function of cortical bone is to support the body, protect organs, provide

levers for movement and store minerals. The inside is made of a soft, spongy type of bone, called cancellous bone, which has a honeycomb structure. The cancellous bone fills the inner cavity of bones with the low density and strength of osseous tissue.

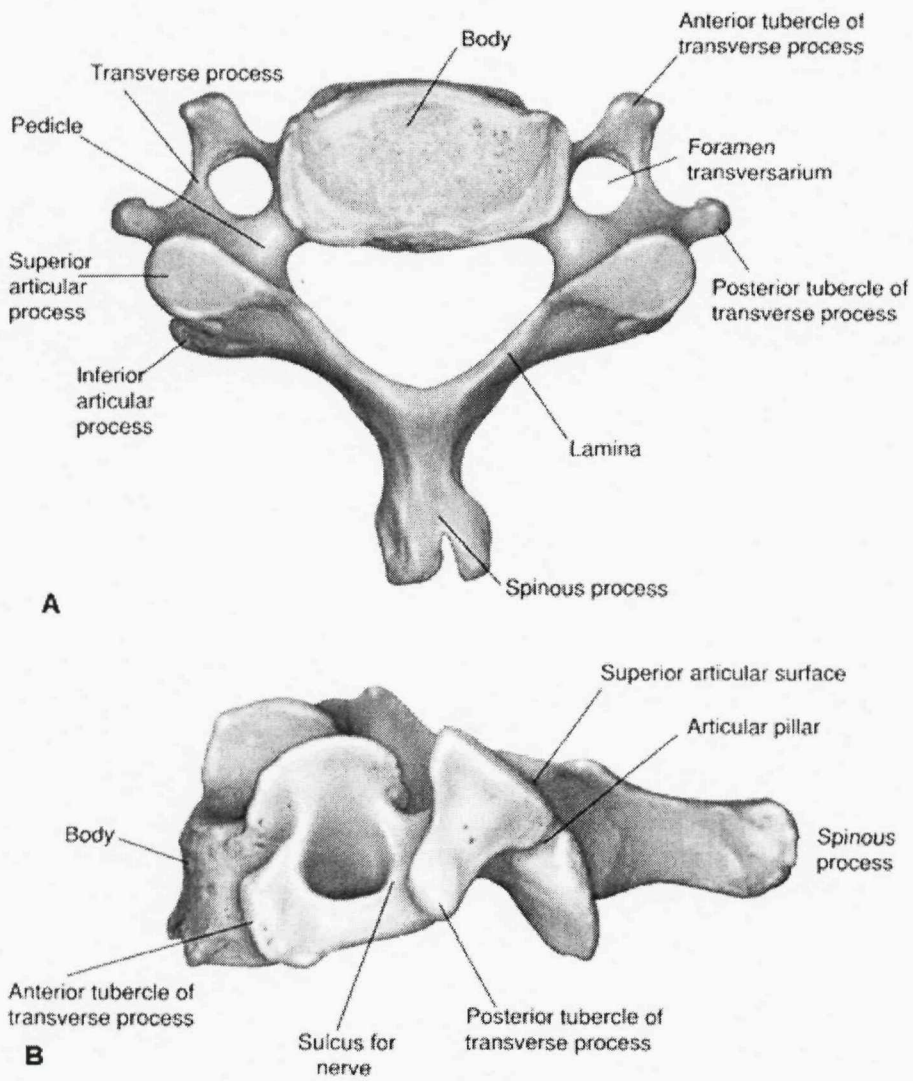


**Figure 2-2** Spinal vertebrae (Hochamn,M. et al. 2005).

### 2.1.2.2 Intervertebral Disc

The intervertebral discs are flat, round "cushions" that act as shock absorbers between each vertebra in the spine, as shown in Figure 2-3. There is one disc between each pair of adjacent vertebrae. Each disc has a strong outer ring of fibres called the annulus fibrosus, and a soft, jelly-like centre called the nucleus pulposus (Bogduk,N. 2005; Giles,L.G.F. et al. 2003; Oliver,J. et al. 1995; White,A.A. et al. 1990).

The annulus fibrosus consists of several layers of fibrocartilage, with the fibres of each layer running perpendicular its neighbours. So the annulus fibrosus is designed to be the strongest area of the disc and it also helps keep the disc's center intact. The strong annular fibers contain the nucleus pulposus and distribute pressure evenly across the disc.

The nucleus pulposus is viscous and fluid, like jelly. The nucleus pulposus is made up of tissue that is very moist because it has high water content. The water content helps the disc to act like a shock absorber – if subjected to pressure from any direction, the nucleus pulposus will attempt to deform and will thereby transmit the applied pressure in all directions.

### 2.1.2.3 Spinal Cord and Nerve Roots

The spinal cord is a column of millions of nerve fibers that run through the spinal canal, as shown in Figure 2-4. The main function of the spinal cord is transmission of neural inputs between the periphery and the brain. It extends from the brain to the area between the end of the first lumbar vertebra and top of the second lumbar vertebra. At the second lumbar vertebra, the spinal cord divides into several different groups of fibers that form the nerves that will go to the lower half of the body. For a small distance, the nerves

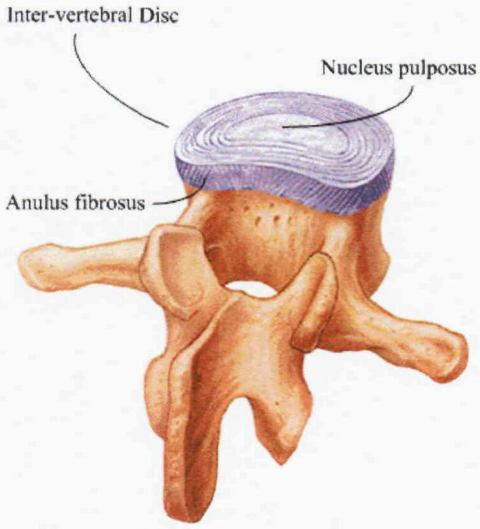


**Figure 2-3** Intervertebral Disc.

actually travel through the spinal canal before exiting the neural foramen. This collection of nerves is called the cauda equine while it is still inside the spinal canal (Oliver,J. et al. 1995; Phillips,D.L. 2004).

The spinal cord is covered by three meninges – the outer dura mater, the arachnoid mater, and the innermost pia mater. The dura mater forms a watertight sack around the spinal cord and the spinal nerves. Inside this sack, the spinal cord is surrounded by cerebrospinal fluid. The arachnoid mater, attached to the inside of the dura, surrounds the spinal cord. Cerebrospinal fluid flows under this layer in the subarachnoid space, which is full of the delicate fibers of the arachnoid extending down to attach to the pia mater. Finally the pia mater attaches to the dura mater by the denticular ligaments through the arachnoid mater in the spinal cord.

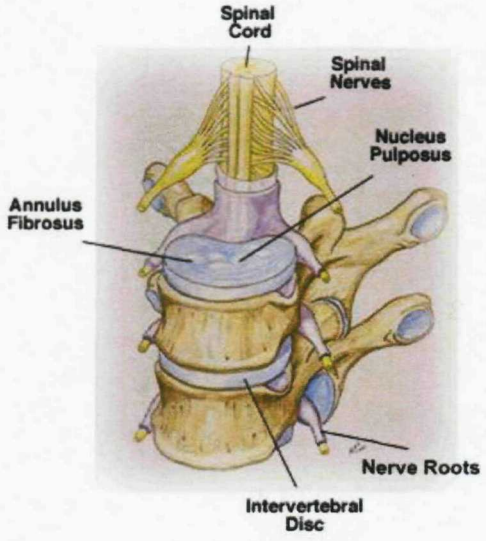


**Figure 2-4** Spinal cord and nerve roots.

The nerve fibers in the spinal cord branch off to form pairs of nerve roots that travel through the small openings (foramina) between the vertebrae. The nerves in each area of the spinal cord connect to specific parts of the body. This is why damage to the spinal cord can cause paralysis in certain areas and not others – it depends on which spinal nerves are affected (White,A.A. et al. 1990). The nerves also carry electrical signals back to the brain that allow sensations to be felt and so damage to the nerve roots can cause pain, tingling, or numbness.

## 2.2 Lumbar Spine and Low Back Pain

### 2.2.1 Lumbar Spine

The lumbar spine, as shown in Figure 2-5, consists of five lumbar vertebral bodies, which are named according to their locations in the intact spinal column. The lumbar spine's shape has what it called a lordotic curve (Bogduk,N. 2005). The lordotic shape is like

backwards "C". If the spine is considerd to have an "S"-like shape, the lumbar region would be the bottom of the "S".

Each lumbar vertebra consists of a vertebral body and a vertebral arch (also called as bony ring). The lumbar spine supports most of weight of the body, therefore the lumbar vertebral bodies are the largest of the spine. They are wider from side to side than from front to back, and a little thicker at the front than at the back. It is flattened or slightly concave above and below, concave behind, and deeply constricted in front and at the sides. The vertebral arch, consisting of a pair of pedicles and a pair of laminae, encloses the vertebral opening (foramen) and supports seven processes. The pedicles are very strong, directed backward from the upper part of the vertebral body. Consequently, the inferior vertebral notches are of considerable depth. The vertebral notches are the concavities above and below the pedicles. When the vertebrae are articulated, the notches of each contiguous pair of bones form the intervertebral foramina. In general, the pedicle width increases gradually from the upper lumbar to the lower lumbar. The laminae are broad, short, and strong. They form the posterior portion of the vertebral arch. In the upper lumbar region the lamina are taller than they are wide but in the lower lumbar vertebra the lamina are wider than they are tall. The lamina connect the spinous process to the pedicles (Ebraheim,N.A. et al. 2005).

Low back pain is very common complaint for a simple reason. Since the lumbar spine is connected to the pelvis, this is where most of the body weight is concentrated and most of the movements take place. Typically, this is where people tend to place too much pressure, such as carrying a heavy object or twisting to move a heavy load. The repetition of these tasks can lead to damage to the parts of the lumbar spine.

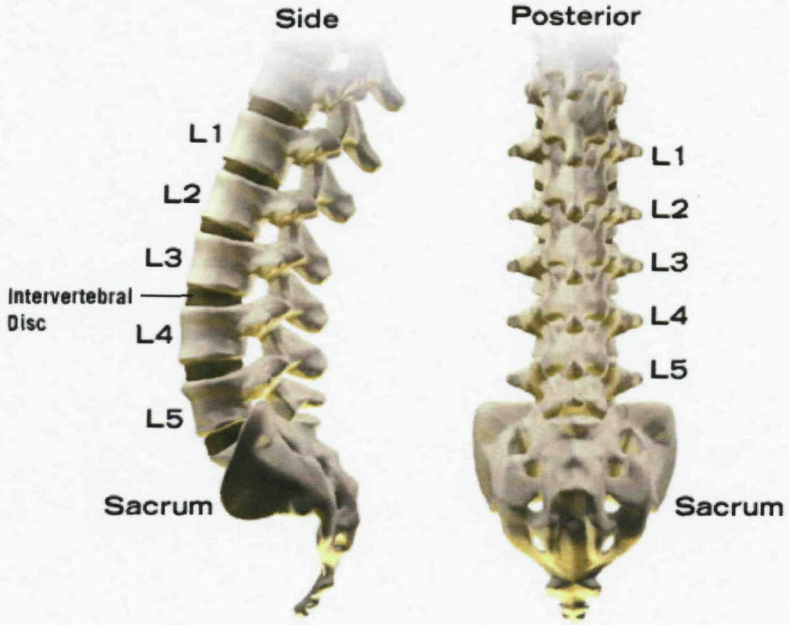


**Figure 2-5** Lumbar spine.

## 2.2.2 Movements of the Lumbar Spine

As we discussed above, the human lumbar spine is a complex structure consisting of five vertebrae, associated with intervertebral discs and many attached ligaments and muscles. Each of these components is fundamental for stability and movement. However, little is known about the inter-connection between components. Images obtained from videofluoroscopy (see Section 3.2) offer an opportunity to discuss the actual movement of the lumbar spine between the extremes of motion. In the following, the two principal spinal movements, flexion/extension and lateral flexion, which are involved in this project, are briefly introduced.

### 2.2.2.1 Flexion/Extension

Flexion is defined as forward bending projected onto the sagittal plane, i.e. the plane which divides the body right and left halves; and extension is defined as backward bending in the same plane.

During the process of flexion, the entire lumbar spine leans forwards. This is achieved basically by the straightening of the lumbar lordosis. At the full range of forward flexion, the lumbar spine assumes a straight alignment or is curved slightly forward, tending to reverse the curvature of the original lordosis. The reversal occurs principally at the upper lumbar levels. Forward flexion is therefore achieved for the most part by each of the lumbar vertebrae rotating from their backward titled position in the upright lordosis to a position in which the upper and lower surface of adjacent vertebral bodies are parallel to one another. This relieves the posterior compression of the intervertebral discs and facet joints, present in the upright lordotic lumbar spine. Some additional range of movement is achieved by the upper lumbar vertebrae rotating further forwards and compressing their intervertebral discs anteriorly (Bogduk,N. 2005; Dvorak,J. et al. 1991; Harvey,S.B. et al. 1998).

In general, extension movement of the lumbar spine is the converse of those that occur in flexion. Basically, the vertebral bodies undergo posterior sagittal rotation and a small posterior translation. However, certain differences are involved because of the structure of the lumbar vertebrae. During flexion, the inferior articular processes are free to move upwards until their movement is resisted by ligamentous and capsular tension. On the other hand, extension involves downward movement of the inferior articular processes and the spinous process, and this movement is limited not by ligamentous tension but by bony impaction.

### 2.2.2.2 Lateral Flexion

Lateral flexion, also known as lateral bending, of the lumbar spine involves a complex and variable combination of lateral bending and rotatory movements of the inter-vertebral joints and diverse movements of the facet joints. As a result, lateral flexion of the lumbar spine has not been subjected to detailed biomechanical analysis, probably because of its complexity and the greater clinical relevance of sagittal plane movements and axial rotation. However, some parameters of the biomechanics of lateral flexion can be studied and will be discussed below.

Lateral flexion studies are commonly used to evaluate spine mobility, which is considered an important parameter in the analysis of scoliosis (Novosad,J. et al. 2004; Takahashi,S. et al. 1997; Vaughan,J.J. et al. 1996).

## 2.3.3 Biomechanical Parameters

After lumbar spine motion images are obtained, several biomechanical parameters, which are available in the DVF image data sets (see Section 3.2), have been developed to qualify the spine motion (Allen,R. et al. 1992; Muggleton,J.M. et al. 1998). The range of parameters includes angles of rotation, intervertebral angles, instantaneous centre of rotation (ICR), instantaneous axis of rotation (IAR), and range of movement (ROM). This section will discuss the definition and measurement of these parameters in brief.

### 2.3.3.1 Rotation Angle

In a flexion/extension or lateral bending motion sequence, each lumbar vertebra begins from the initial neutral position to the extreme positions, and rotation angles measure the changes of the vertebral angle during the movement process. To calculate the vertebral angle, the four corners of the lumbar vertebra are located first and then the midplane of the vertebral body can be obtained. The angle of the midplane and the horizontal reference line is defined as the vertebral angle (Figure 2-6). Finally the change in vertebral angle of each lumbar vertebra is computed frame by frame during the whole motion sequence to obtain a series of rotation angles. The rotation angle should have approximately sinusoidal distribution since the lumbar spine moves from the neutral position to the extreme position and then back to the neutral position during flexion/extension and lateral bending motion.

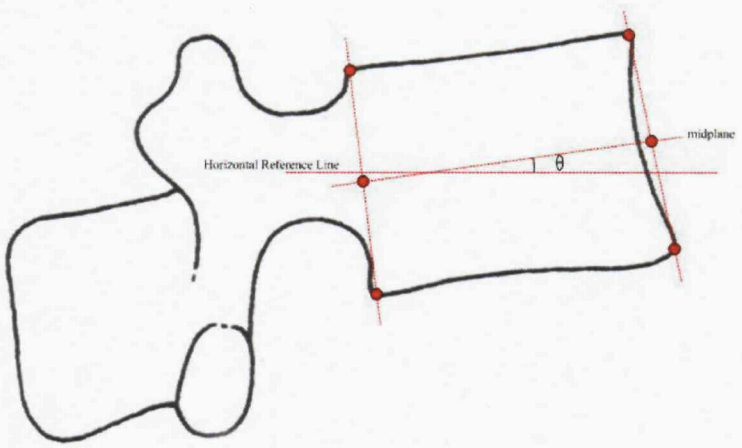


**Figure 2-6** The definition of vertebral angle.

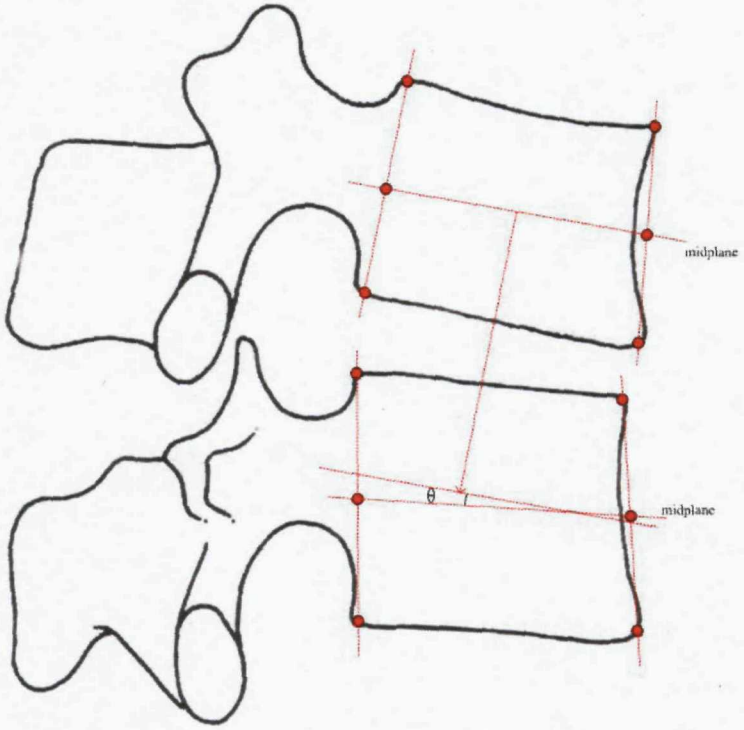


**Figure 2-7** The definition of intervertebral angle.

### 2.3.3.2 Intervertebral Angle (IVA)

The angle between two adjacent vertebrae is defined as intervertebral angle. In computation of the intervertebral angle, midplanes of the two adjacent vertebrae are obtained first and then the angle between the two midplanes is measured to get the inter-vertebral angle (Figure 2-7). Recent research has indicated that a linear model can be built to describe to relationship between the IVA and the range of motion (ROM) in normal lumbar spine motion (Kondracki,M. 2001).

### 2.3.3.3 Instantaneous Centre of Rotation (ICR)

For any body moving in the two-dimensioanl space, the motion can be defined from the position, velocity and acceleration for any point on the body. There is a point for this body for which the instantaneous rotational velocity is zero, which means that the body rotates about this point. This point is called the instantaneous centre of rotation (or ICR). Its location relative to the body is dependent on the relative values of the linear and angular velocities. For near-zero angular velocities, such as pure translation motion, the location of ICR approaches infinity.

The position of the ICR can be defined in several ways. For example, if the direction of the velocities of two points $A$ and $B$ are known and they are different, as shown in Figure 2-8(a), the ICR is obtained by drawing the perpendicular to $v_A$ through $A$ and the perpendicular to $v_B$ through $B$. The point in which these two lines intersect is the ICR. If the velocities of $v_A$ and $v_B$ are perpendicular to the line $AB$ and the magnitude of the velocities are known, the ICR can be found by intersecting $AB$ with the line joining the extremities of the vectors, as shown in Figure 2-8(b).

In Figure 2-9, suppose the vertebra rotates from position 1 to position 2 without any translation, then the intersection of the two perpendicular bisectors of $AA'$ and $BB'$ is the ICR around which the vertebra rotates.

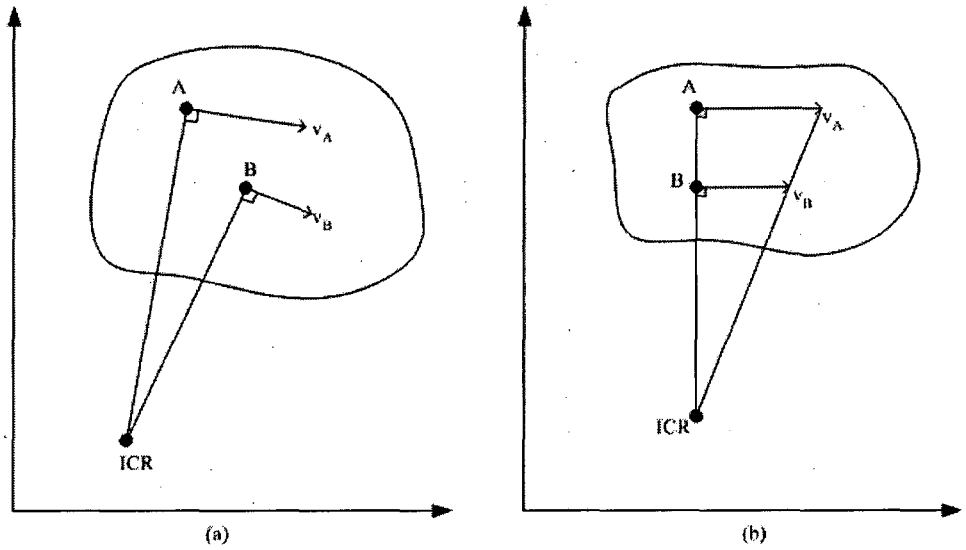


**Figure 2-8** Instantaneous Centre of Rotation (ICR).

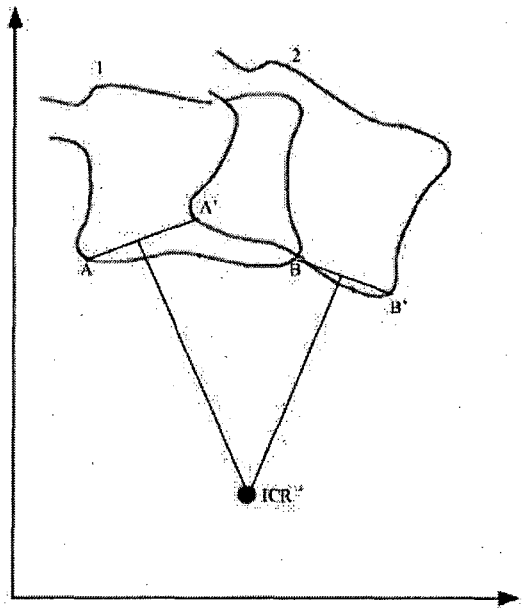


**Figure 2-9** Measurement of ICR in vertebral rotation.

### 2.3.3.4 Instantaneous Axis of Rotation (IAR)

When the combination of sagittal rotation and sagittal translation of each lumbar vertebra occurs during flexion/extension, the instantaneous centre of rotation (ICR) is not suitable for describing such a complicated lumbar spine movement since the ICR considers only rotation motion. Therefore, the biomechanical parameter known as the instantaneous axis of rotation (IAR), is introduced here. The exact location of the IAR is a function of the amount of sagittal rotation and the amount of simultaneous sagittal translation that occurs during the phase of motion defined by the start and end positions selected. During the flexion/extension, each lumbar vertebra exhibits an accurate motion in relation to the vertebra below. The centre of the arc lies below the moving vertebra and is known as the IAR, shown in Figure 2-10.

When IARs are located for each phase of movement and then plotted in sequence, they depict a locus known as centrode of motion (Figure 2-11). The centrode is actually a map of the path taken by the moving axis during the full range of motion of the joints. In Figure 2-11, the flexion/extension of the vertebra can be reduced to small sequential increments. For example, five such phases are illustrated in the figure. Each phase of motion has a unique IAR. In moving from position 0 to position 1, the vertebra moved around IAR 1. In moving from position 1 to position 2, it moved around IAR 2, and so on. Finally, the IARs are connected in sequence and they describe the centrode.

Research shows that in normal lumbar spine motion, the centrode is short and is located in a restricted area in the vicinity of the upper endplate of the adjacent lower vertebra. However, in the abnormal lumbar spine motion, such as degenerative lumbar spine movement, the centrode differs from the normal in length, shape and average location (Gertzbein,S.D. et al. 1986). It can be seen that the centrode of normal vertebra motion is short and tightly clustered (Figure 2-12(a)) and the abnormal vertebra motion may exhibit

a longer, displaced and erratic centrode (Figure 2-12(b)). So the study of the IAR and the centrode generated by the IARs could be very helpful in the diagnosis of low back pain.

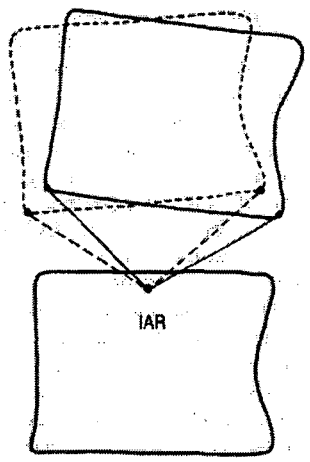


**Figure 2-10** Instantaneous Axis of Rotation during flexion/extension.

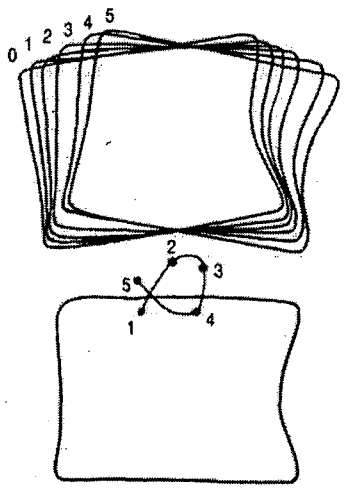


**Figure 2-11** Centrode of flexion/extension.

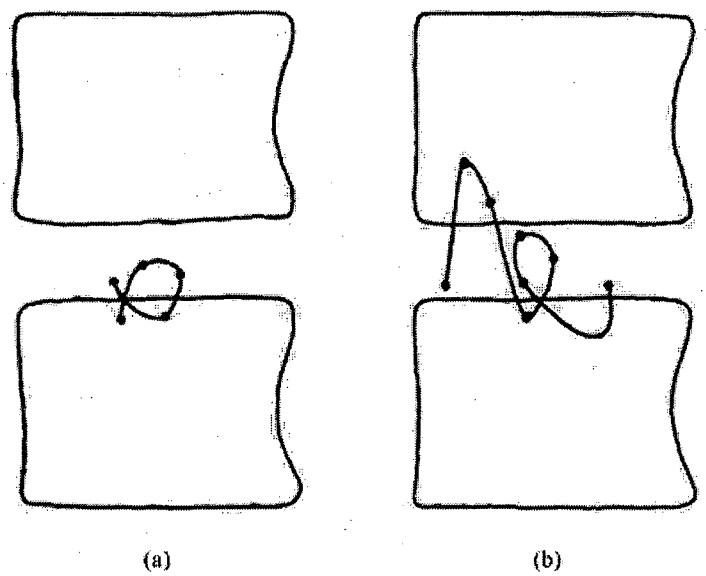


**Figure 2-12** The centrode of normal (a) and abnormal (b) motion.

Mathematically, the location of an IAR can be expressed as:

$$\begin{cases} x_{IAR} = x_{CR} + T/2 \\ y_{IAR} = y_{CR} + \dfrac{T\sin\theta}{2(1-\cos\theta)} = y_{CR} + \dfrac{T}{2\tan(\theta/2)} \end{cases},$$

where $(x_{IAR}, y_{IAR})$ is the coordinate of the IAR, $(x_{CR}, y_{CR})$ is the coordinate of the centre of reaction, $T$ is the translation exhibited by the moving vertebra and $\theta$ is the angular displacement of the vertebra (Bogduk,N. 2005), shown in Figure 2-13. The centre of reaction (CR) is the point on the inferior endplate of the moving vertebra through which the compression forces are transmitted to the underlying inter-vertebral disc. So the CR is the mathematical average of all the forces distributed across the endplate.

However, with the above definition of the CR, it is difficult to locate its coordinate in a DVF image. An important feature of the CR is that it is a point that undergoes no rotation, which is the same as the feature of ICR. So (Kondracki,M. 1991) indicated that

if a motion is divided into a pure rotation and then a pure translation, then the position of the ICR in the pure rotation motion is exactly the position of the CR. Consider three vertebral positions, 1, 2 and 3, as shown in Figure 2-14. In moving from position 1 to position 2, the vertebra undergoes pure rotation around the ICR, by an angle of $\theta$. In moving from position to position 3, the vertebra translates a distance $T$ in a particular direction without further rotation. Hence the coordinate function of the IAR can be rewritten as:

$$\begin{cases} x_{IAR} = x_{ICR} + T/2 \\ y_{IAR} = y_{ICR} + \dfrac{T\sin\theta}{2(1-\cos\theta)} = y_{ICR} + \dfrac{T}{2\tan(\theta/2)} \end{cases},$$

where $(x_{IAR}, y_{IAR})$ are the coordinates of the IAR, $(x_{ICR}, y_{ICR})$ are the coordinates of the ICR, $T$ is the pure translation exhibited by the moving vertebra and $\theta$ is the angle of pure rotation of the vertebra.

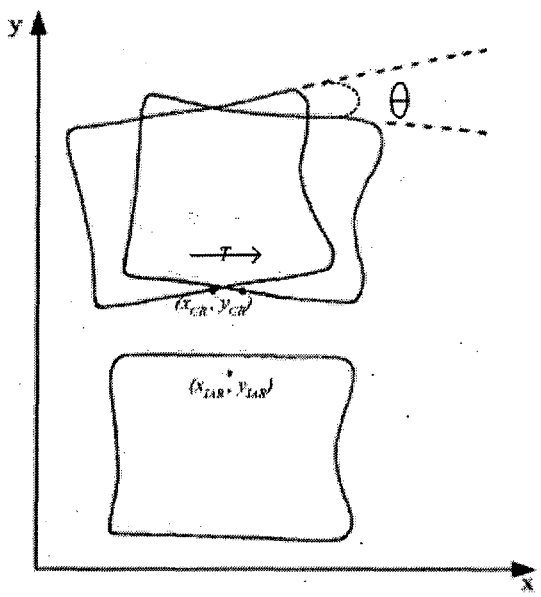


**Figure 2-13** Method I to calculate the IAR.

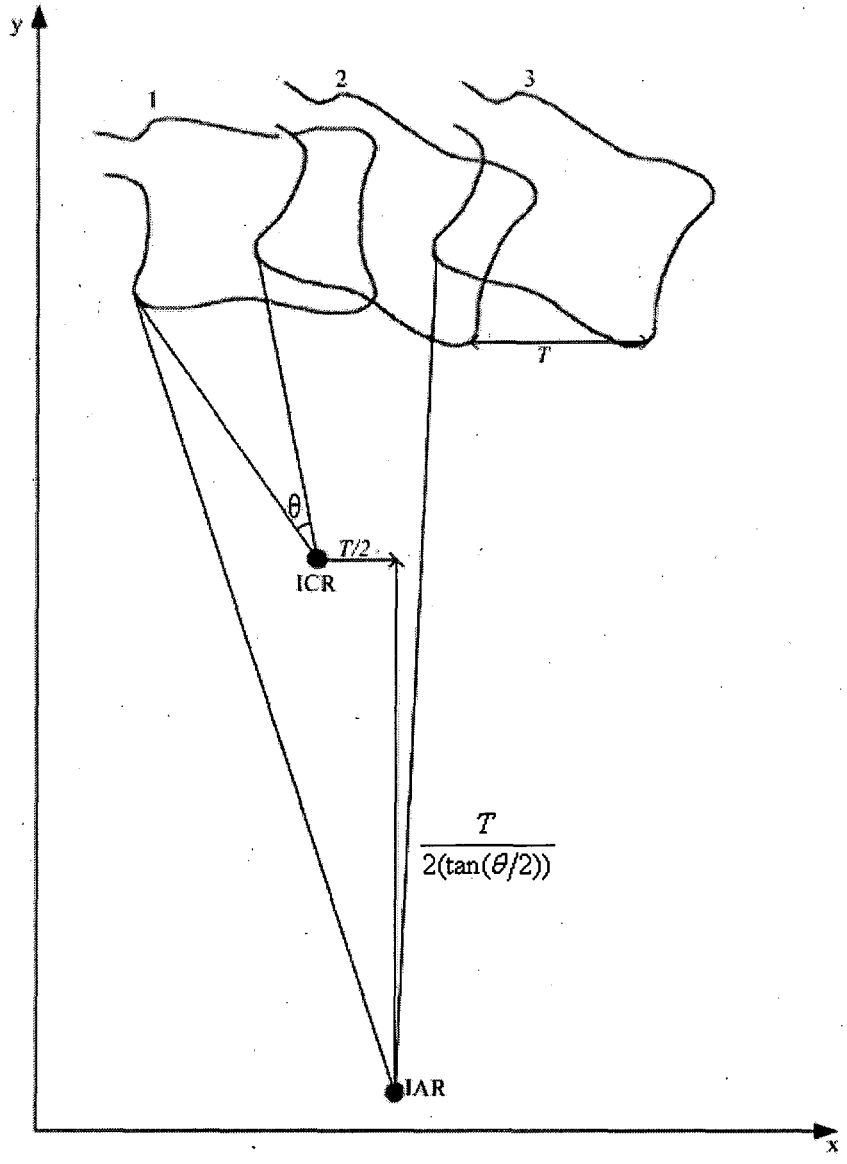


**Figure 2-14** Method II to calculate the IAR.

### 2.3.3.5 Range of Motion (ROM)

Range of motion (ROM) is the measurement of the achievable distance or rotation angle between the fully flexed and extended positions of an observed subject during motion. Radiographic studies provide the most accurate measurements of ROM (Littlewood,C. et al. 2007). The technique of radiography helps to analyze the movement in the sagittal plane for flexion/extension, horizontal plane for axial rotation and coronal plane for lateral bending. For example, the range of motion of flexion/extension can be measured by subtracting the maximum values from the minimum values of the angles of rotation in the flexion/extension motion sequence (Van Herp,G. et al. 2000).

### 2.3.3.6 Summary

In this section, the biomechanical parameters related to spinal flexion/extension and lateral bending are introduced briefly. If the image sequences of these spine motions are available, some biomechanical parameters, such as rotation angle, intervertebral angle and ROM, can be calculated simply by directly manual landmarking or some computer-aided methods. Moreover, with the investigation of the translation of the lumbar spine, the IAR can be obtained and then the distribution of IARs forms the centrode. All these biomechanical parameters will help in the study of spine motion by quantitative analysis or modelling tools using these parameters.

### 2.3.4 Low Back Pain

Low back pain is one of the most frequent clinical problems presented in the western world. It affects most people at some stage in their life and accounts for more sick leave from work than any other single reason. Moreover, the cost of lower back pain is enormous. The statistics have been presented in Chapter 1.

Low back pain is defined as pain perceived as arising from either the lumbar spinal region or the sacral region or from a combination of both (Bogduk,N. 2005). Low back pain can be either an acute or a chronic disabling condition. An acute lower back injury may be caused by a traumatic event, like a car accident or a fall. It occurs suddenly and victims will usually be able to pinpoint exactly when it happened. In acute cases, the structural damage is likely to happen in the soft tissues like muscles, ligaments and tendons. With a serious accident, fractures in the lumbar spine vertebrae may also occur. Chronic lower back pain usually has a more insidious onset, occurring over a long period of time. Causes include osteoarthritis, rheumatoid arthritis, degeneration of the discs between the vertebrae, or tumours.

Psychological factors play a significant role in the onset of low back pain and the transition from acute to chronic pain and disability. Depression, anxiety, distress and cognitive factors have been linked to pain and disability (Linton,S.J. 2000). However, recent research shows that psychological factors influence low back pain but are not the most important causes of pain itself. Severe low back pain often arises from biomechanical factors, such as inter-vertebral discs, apophyseal joints and sacroiliac joints. These structures and their physical disruptions are strongly linked to low back pain (Adams,M.A. et al. 2005). The cardinal movements of the lumbar spine include flexion, extension, side flexion and rotation. Flexion and extension occur predominantly at the lower two lumbar segments. Rotation at each lumbar segment is limited to only a few degrees due to the vertical orientation of the lumbar facets. Combined movements like

flexion and rotation, carry the highest injury potential. Repetitive movements, common in sport, could fatigue the supporting structures of the lumbar spine and overwhelm the protective mechanisms of the lumbar segments (Hainline,B. 1995).

However, diagnosis of low back pain is still a problem because it could be caused by different sources and it is difficult to undertake in *vivo* diagnosis and analysis. Better diagnosis of low back pain probably relies, to some extent, on improving the understanding of spine biomechanics. Many researchers have focused on spinal motion since disorders of spine could be revealed in abnormal spinal motion. Moreover spine kinematics is able to investigate the spine movement without considering the forces acting on the structures involved since the forces are difficult to measure *in vivo*. Therefore spine kinematics could be very useful for better understanding of low back pain and its diagnosis, treatment and rehabilitation.

Nowadays, several main medical imaging techniques have been explored to capture spine images. However, not all of them are suitable in spinal motion studies. These techniques will be discussed in the next chapter.

# Chapter 3

# Digital Videofluoroscopy

## 3.1 Medical Imaging Techniques

Medical imaging techniques began with the discovery of X-rays in 1895 (Bushberg,J.T. 2002; Cho,Z.H. 1993). Since then medical imaging has developed rapidly and has proved to be invaluable in diagnositic medicine. The popular medical imaging techniques will be discussed in the following sections.

- ***X-rays.***

An X-ray is a form of electromagnetic radiation with a wavelength in the range of 10 nanometers to 100 picometers (corresponding to frequencies in the range 30 [+]PHz to 3 [*]EHz) (Bushberg,J.T. 2002). X-rays are primarily used for diagnostic medical imaging and crystallography. Radiology is a specialised field of medicine that applies x-ray and other techniques for diagnostic imaging. X-rays are especially useful in the detection of pathology of the skeletal system, but also useful for detecting some disease in soft tissue. However, traditional X-rays are seldom applied to some soft tissue problems, such as the brain or muscle. In these cases, computerized axial tomography (CT), magnetic resonance imaging (MRI) or ultrasound is used. X-rays images are usually of good quality, but the radiation dosage is relative high. The scientific unit of measurement for

[+] *P is the symbol of SI prefix* peta, *which means* $10^{15}$. *A PHz is* $10^{15}$ *Hz.*

[*] *E is the symbol of SI prefix* exa, *which means* $10^{18}$. *A EHz is* $10^{18}$ *Hz.*

radiation dosage is the [+]millisievert (mSv). Because different tissues and organs have varying sensitivity to radiation exposure, the actual dosage to different parts of the body from an X-ray procedure varies. The term effective dosage is used when referring to the dosage averaged over the entire body. For example, a typical chest X-ray results in an exposure of about 0.1mSv (RadiologyInfo 2007; Shrimpton,P.C. et al. 2003). Compared with an effective dosage of about 3mSv per year of average person from natural background (RadiologyInfo 2007), it is high radiation dosage and only a limited number of static images can be obtained. For spine investigations that would usually be in the neutral position and at the extreme positions of mobility and so it is impossible to analyze spinal motion as the spine moves. An X-ray image of the lumbar spine is shown in Figure 3-1. The vertebral shapes are clear in the image, in particular, the L5 and sacrum can be recognized even though they are covered by the pelvis. However, this image technique is not adapted in our research because of the limitations of high radiation exposure and still images.

- ***Computerized axial tomography (CT)***

CT is a medical imaging method where digital processing is used to generate a 3-D image from a large series of 2-D X-ray images taken around a single axis of rotation (Popov,T.V. 2006). Many data scans are progressively taken as the subject is gradually passed through a gantry containing the X-ray source and detector. They are combined together by the mathematical procedure known as tomographic reconstruction. Since its introduction in 1972 (Cho,Z.H. 1993), CT has become in medical imaging to be a supplement to X-rays and medical ultrasonography and nowadays it is the "gold standard" in the diagnosis of a large of number of different disease entities due to its excellent

[+] *The Sievert (Sv) is the international system unit of equivalent dosage. It attempts to reflect the biological effects of radiation as opposed to the physical aspects, which are characterized by the absorbed dosage, measured in Grays (Gy), which will be discussed in the later part of this section.*

**Figure 3-1** An X-ray image of the lumbar spine (adapted from Ruian People's Hospital for kind permission).

image quality. However, CT is regarded as a high radiation diagnostic technique. For example, compared with a typical chest X-ray exposure of about 0.1mSv, a typical chest CT has an effective dosage of 5.8mSv (Shrimpton,P.C. et al. 2003) or even 8mSv (RadiologyInfo 2007). This amount of exposure is 2-3 times of the average person per year from natural background. Furthermore, in a recent comprehensive survey in the UK (Hart,D. et al. 2004), CT constituted about 7% of all radiologic examinations, but contributed about 47% of the total collective dosage. This means that any increase in CT examinations would lead to an overall increase in the total amount of medical radiation used, despite the reductions of radiation dosage in other techniques. The other

disadvantage of CT is that it cannot yield motion images because patients normally lay on their back and should keep as stationary as possible during image acquisition. A CT image of lumbar spine is shown in Figure 3-2. The vertebral shapes are clear in the image. Moreover, the image is actually a 3-D image so the anatomical information can be analyzed by investigating the horizontal layer in the image.

- ***Magnetic resonance imaging (MRI)***

MRI is a method of creating images of internal organs and is primarily used to demonstrate pathological or other physiological alterations of living tissues. This imaging technique is based on the fact that body tissues act differently in strong magnetic fields. In clinical practice, MRI is used to distinguish pathological tissue from normal tissue. One of the advantages of an MRI scan is that, according to current medical knowledge, it is harmless to the patient. It utilizes strong magnetic fields and non-ionizing radiation in the radio frequency range. Since MRI makes use of radio waves very close in frequency

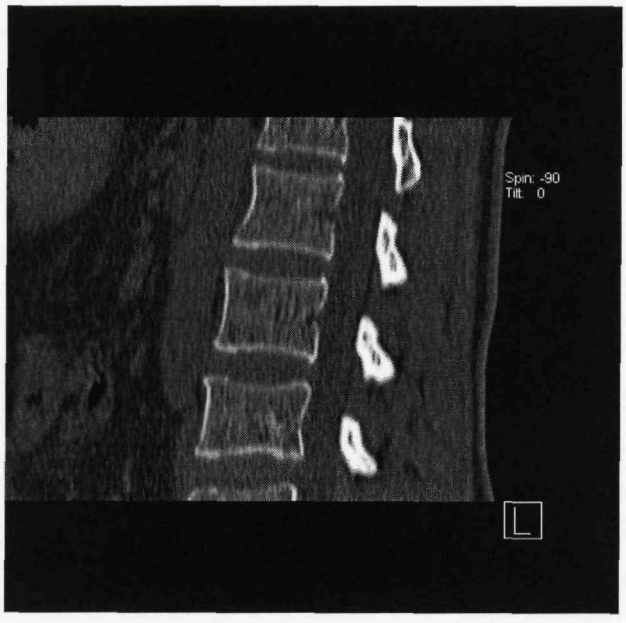


**Figure 3-2** A CT image of the lumbar spine (adapted from Ruian People's Hospital for kind permission).

to those of ordinary FM radio stations, the scanner must be located within a specially shielded room to avoid outside interference. Compare this to CT scans and traditional X-rays which involve doses of ionizing radiation which may increase the chance of malignancy, especially in children receiving multiple examinations. Furthermore, MRI provides far better contrast resolution while CT provides superior spatial resolution. An MRI image of spine is shown in Figure 3-3. The image offers anatomical information in very good quality. The vertebrae bodies, the intervertebral discs and the soft tissues are clear for clinical analysis and diagnosis. For a long time, MRI has been regarded as not fast enough for motion analysis (Cho,Z.H. 1993) and it increases the cost of diagnosis. Again, similar to CT, patients have to keep stationary in the process of image acquisition. Therefore, MRI cannot yield dynamic images although this may change in future.

**Figure 3-3** A MRI image of the lumbar spine (adapted from Ruian People's Hospital for kind permission).

From what has been discussed above, these medical imaging techniques are not suitable for dynamic spine motion studies. They are limited by either radiation safety or by providing static images only.

## 3.2 Digital Videofluoroscopy

Videofluoroscopy is an imaging technique to obtain real-time images by using a fluoroscope which consists of an X-ray source and fluorescent screen. Therefore it allows evaluation of regional spinal movement and specific intervertebral motion. Due to the use of X-rays, patients suffer the potential health risks of radiation during acquisition the procedure. Though physicians usually try to use low dosage rates, the length of a typical procedure often results in a relatively high absorbed dosage. For example, the absorbed dosage rate in the skin from the direct beam of a fluoroscopic X-ray system is typically 20-50 [+]mGy/min (FDA Public Health Advisory 1994). A dosage study was undertaken in order to investigate this problem (Breen,A.C. 1991). The absorbed dosage values proposed in this research was compared with the typical values. The comparison result is shown in Table 3-1. It is clear that there is a great reduction in radiation exposure.

The digital videofluoroscopic system used in this project is composed of a portable passive motion table (PMT) and an X-ray videofluoroscopic system (Kondracki,M. 2001). The passive motion table (PMT) has an upper section fixed and a lower section that can

*[+]mGy is the symbol of milligray. Gray is the international system unit of absorbed dosage. Sv (sievert) is the unit of equivalent dosage. To convert Gy to Sv, the radiation weighting factor $\omega_R$ and tissue weighting factor $\omega_T$ need to be considered. The conversion equation is $H_{T,R}= \omega_R \cdot \omega_T \cdot D_{T,,R}$, where $H_{T,R}$ is equivalent dosage in Sv and $D_{T,R}$ is absorbed dosage in Gy. For X-rays, $\omega_R=1$. For bone surface tissue, $\omega_T=0.01$. So 1Gy=0.01Sv is assumed in this thesis.*

execute a smooth arc from the neutral position to 40° left, or to 40° right, and then back to neutral. The PMT is motor driven and under the image intensifier tube so that the spine movement controlled by the PMT can be recorded. The X-Ray videofluoroscopic system consists of an X-ray generator, an X-ray tube assembly, an image intensifier tube, a television camera, a VCR, and a monitor. The heart of the system is the image intensifier tube. This tube permits diagnostic quality images to be produced at very low radiation levels. It is used instead of intensifying screens and film as the image receptor. The digital videofluoroscopy system (DVF) is shown in Figure 3-4. During spine movement, the system records 5 frames per second. Furthermore, the analogue images are transferred into digital format and then stored in a PC connected to the system.

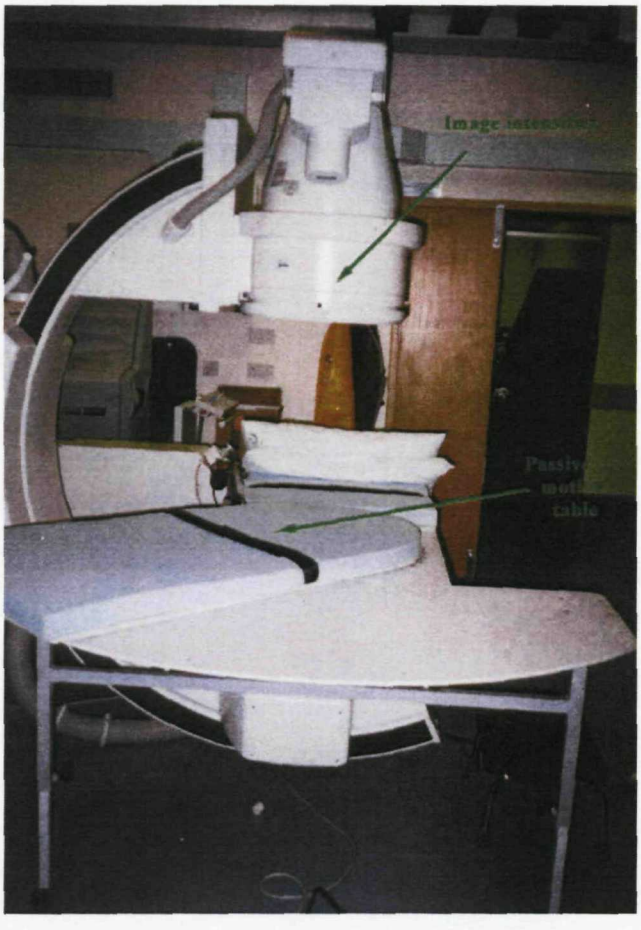

**Figure 3-4** The DVF system used in this project (Kondracki,M. 2001).

**Table 3-1** Absorbed radiation dosage (Breen,A.C. 1991).

| Breen's DVF system | | Typical fluoroscopic X-ray system | |
|---|---|---|---|
| View | Absorbed dosage (mGy) | View | Absorbed dosage (mGy) |
| Lumbar A/P | 2.9 | Lumbar A/P | 20 |
| Lumbar lateral | 12.6 | Lumbar lateral | 50 |

**Table 3-2** Radiation dosage and screening times for ten subjects which will be analyzed in this project (Kondracki,M. 2001).

| Subject Index | Total time (min) | Total dosage-area product (Gy $cm^2$) | Effective dosage equivalent (mSv) |
|---|---|---|---|
| BM | 1.7 | 6.82 | 0.99 |
| CR | 1.9 | 3.43 | 0.46 |
| DE | 1.6 | 5.87 | 0.68 |
| DO | 1.7 | 4.88 | 0.61 |
| GD | 1.7 | 3.85 | 0.44 |
| GP | 1.8 | 5.34 | 0.65 |
| JM | 1.8 | 4.05 | 0.50 |
| JW | 1.9 | 5.98 | 0.70 |
| NW | 1.9 | 4.77 | 0.57 |
| RM | 2.3 | 6.01 | 0.62 |
| Mean value | 1.83 | 5.1 | 0.62 |
| Average value | 0.915 | 2.55 | 0.31 |

In the DVF system, the total radiation dosage of different subjects have been analyzed (Kondracki,M. 2001) and are shown in Table 3-2. The average dosage-area product (DAP) across all ten subjects for one screening is about 2.55 Gy $cm^2$. There is a significant reduction over the recommended maximum value of 15 Gy $cm^2$ by the National Radiation Protection Board (NRPB) of the United Kingdom.

Digital Videofluoroscopy (DVF) was first introduced to study spine motion by Breen and Allen in 1987 and subsequently developed further (Breen,A. et al. 1988; Breen,A.C. et al. 1987; Breen,A.C. et al. 1989a; Breen,A.C. et al. 1989b; Breen,A.C. et al. 1991; Breen,A.C. et al. 1993). Since then DVF has been developed and widely applied in the studies of low back pain (Allen,R. et al. 1992; Cholewicki,J. et al. 1991; Cholewicki,J. et al. 1992; De Stefano,A. et al. 2004; Muggleton,J.M. et al. 1997; Muggleton,J.M. et al. 1998; Simonis,C. et al. 1992; Zheng,Y. et al. 2001; Zheng,Y. et al. 2003; Zheng,Y.L. et al. 2004).

## 3.3 Conclusion

From the discussion in this chapter, digital videofluoroscopy is the only practical medical imaging technique to safety obtain real-time, continuous motion sequences of the lumbar spine. Using DVF images, the whole motion pattern of the lumbar spine could be investigated rather than only at the neutral and extreme positions as in plain X-ray.

However, DVF images suffer from relatively poor quality due to the low radiation dosage. This causes problems in identifying features in DVF images automatically, which is much easier in X-ray, CT and MRI images. Furthermore, similar to plain X-ray images, the quality of DVF images varies across the image. The images are brighter in the middle area while the intensity and contrast are poorer in the other areas, as shown in Figure 3-5. This causes problems in which the L1 vertebra has low contrast against its neighbouring area due to the effect of soft tissues and the L4-L5 area is often difficult to detecte due to occlusion by the pelvis.

In conclusion, digital videofluoroscopy provides the possibility to investigate the spine motion with a very low radiation dosage. However, the quality of DVF images is

relatively poor. This leads to problems with the image processing which will be discussed in the later chapters and forms the focus of the work undertaken in this project.

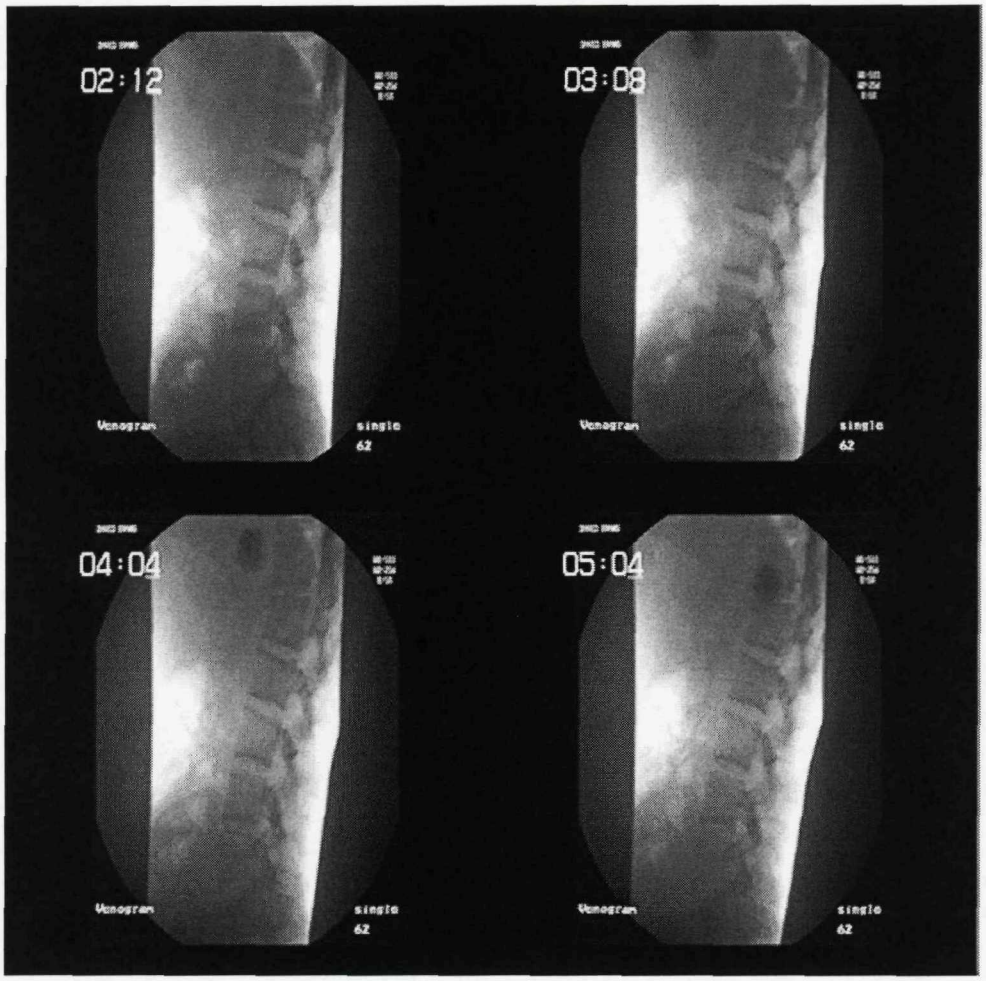


**Figure 3-5** Typical DVF images from a motion sequence of the lumbar spine.

# Chapter 4

# Conventional Edge Detection for Lumbar Spine Vertebrae

## 4.1 Background

Edges characterize boundaries and therefore then detection is a problem of fundamental importance in image processing. Edges in images are areas with strong intensity contrasts – a jump in intensity from one pixel to the next. Edge detecting an image significantly reduces the amount of data and filters out redundant information, while preserving the important structural properties in an image.

This research project aims to develop a method of automated identification and tracking of lumbar spine motion for low back pain diagnosis. Characterization of the normal motion of the lumbar spine would form the basis for locating a source of damage by identifying any abnormal motion at the vertebral level. Therefore development of a suitable edge detector is the first step of this project. With the edge information, the movement of lumbar spine can be tracked and the biomechanical factors can be studied.

Edge detection methods applied in this project are aimed at reducing significantly the amount of data in images and filter out information that could be regarded as preserving

the important structural properties and features of images. There are many conventional approaches to edge detection, but most of them are divided into two approaches, known as gradient-based and phase-based operators, in terms of the information used in these methods.

## 4.2 Introduction to Edge Detection

Intuitively, an ideal edge has the properties of the model shown in Figure 4-1(a). In gray level, an ideal edge of this model is a set of connected pixels, each of which is located at a step transition in intensity as shown by the horizontal profile in Figure 4-1(a).

In practice, optics, sampling and image acquisition imperfections make edges more closely modeled as having a "ramp-like" profile, which is shown in Figure 4-1(b). In this model, a "thin" edge disappears and instead, the edge point now is any point contained along the ramp and would then be a set of such points that are connected. The "thick" edge is determined by the length of ramp, as it makes the transition from an initial to a final gray level.

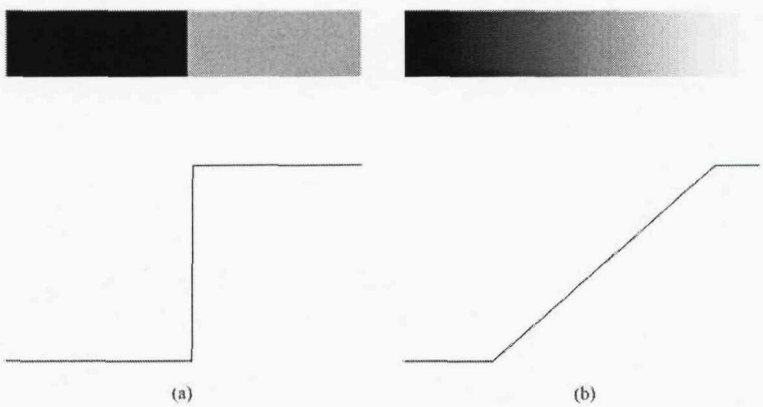


**Figure 4-1** Model of an ideal edge (a) and a ramp edge (b).

Gradient-based edge detectors are most generally applied for edge detecting. They locate the edge by detecting the changes in brightness of images. The gradient-based edge methods are divided into three categories (Nixon,M.S. et al. 2002; Sonka,M. et al. 1993):

1. Operators that calculate the gradient of the image from the first derivate, such as Canny, Sobel, Prewitt and Roberts;
2. Operators that find the zero crossing of the second derivate of the image, such as Laplace and Marr-Hildreth;
3. Operators that attempt to match the image function to a parametric model of the edge, such as the Active Contour (Snake) method.

Figure 4-2 shows a horizontal gray-level profile of a ramp edge, as well as the first and second derivative of the gray-level profile. The first derivative is constant for the points in the ramp and is zero in the areas of constant gray level. The edges are detected by looking for maxima in the first derivative of the images and a threshold can be applied to distinguish the real edges from noise. The second derivative is positive at the transition associated with the low gray-level side, negative at the transition associated with the high gray-level side and zero along the ramp and in areas of constant gray level. An edge could then be detected by finding the zero-crossing of the second derivative. However, the zero-crossing method is more sensitive to noise because zero crossings are difficult to detect in a noisy background (Gonzalez,R.C. 1992), especially in cases of low signal-to-noise ratio.

The 2-D gradient of an image $f(x,y)$ at location $(x,y)$ is defined as the *vector*

$$\nabla F = \begin{bmatrix} G_x \\ G_y \end{bmatrix} = \begin{bmatrix} \frac{\partial f}{\partial x} \\ \frac{\partial f}{\partial y} \end{bmatrix}$$, where $G_i, i \in (x, y)$ are the gradient operators in the $x$ and $y$ direction. There are two important quantities in edge detection, the magnitude and direction of the gradient vector. The magnitude quantity is usually denoted $\nabla f$, where

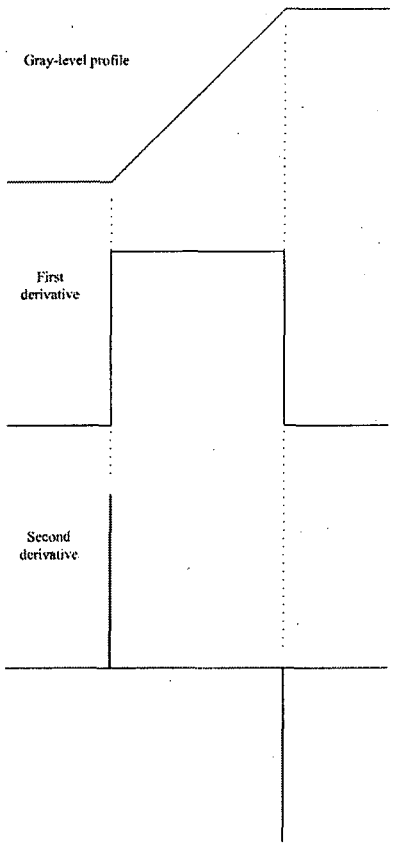


**Figure 4-2** The profiles of gray-level, first derivative and second derivative

$\nabla f = \left[G_x^2 + G_y^2\right]^{1/2}$, while the direction is $\alpha(x,y) = \tan^{-1}\left(\frac{G_y}{G_x}\right)$. However, in practice, absolute values are used to approximate the magnitude instead of squares and square roots: $\nabla f = |G_x| + |G_y|$. This method is much more attractive computationally and still preserves relative changes in gray level.

In order to be useful in digital image processing, these equations have to be expressed in discrete form. A basic discrete definition of the first derivative $f(x,y)$ is the difference

$\frac{\partial f}{\partial x} = f(x+1,y) - f(x,y)$, $\frac{\partial f}{\partial y} = f(x,y+1) - f(x,y)$. Similarly, a second derivative is defined as the difference

$$\frac{\partial^2 f}{\partial x^2} = f(x+1,y) + f(x-1,y) - 2f(x,y) \quad , \quad \frac{\partial^2 f}{\partial y^2} = f(x,y+1) + f(x,y-1) - 2f(x,y) \quad .$$

Therefore, the gradient of each pixel of an image can be calculated from their neighbouring pixels. In image processing, a concept of "subimage" is used so that the neighbouring operation can be performed directly on the pixels of an image. The subimage is also called a mask, which is the most prevalent terminology. In order to obtain the gradient, each component of the mask has its own coefficient. A model of the mask is shown in Figure 4-3. In this way, each gradient-based edge detector detects an edge with its own mask. In Figure 4-4, the masks of several edge operators most widely used in practice are presented. They aim to obtain the gradient at point $z_5$. For the Prewitt operator the mask with size of 3×3 is given by

$$G_x = (z_7 + z_8 + z_9) - (z_1 + z_2 + z_3),\ G_y = (z_3 + z_6 + z_9) - (z_1 + z_4 + z_7).$$

Similarly, the Sobel operator is given by

$$G_x = (z_7 + 2z_8 + z_9) - (z_1 + 2z_2 + z_3),\ G_y = (z_3 + 2z_6 + z_9) - (z_1 + 2z_4 + z_7).$$

The Laplacian masks represent two forms encountered most frequently in practice, in which the right one also considers the diagonal neighbours. For the Method I (left mask), the function is given by $\nabla^2 f = 4z_5 - (z_2 + z_4 + z_6 + z_8)$ while

$\nabla^2 f = 8z_5 - (z_1 + z_2 + z_3 + z_4 + z_6 + z_7 + z_8 + z_9)$ for the Method II (right mask).

In edge detection, the mask is firstly started at the top-left area of an image and is then slid from the left to the right, from the top to the bottom. Finally, it stops at the bottom-right area of the image. This process is similar to the frequency domain concept of convolution. For this reason, the mask is often referred to as a convolution mask. And

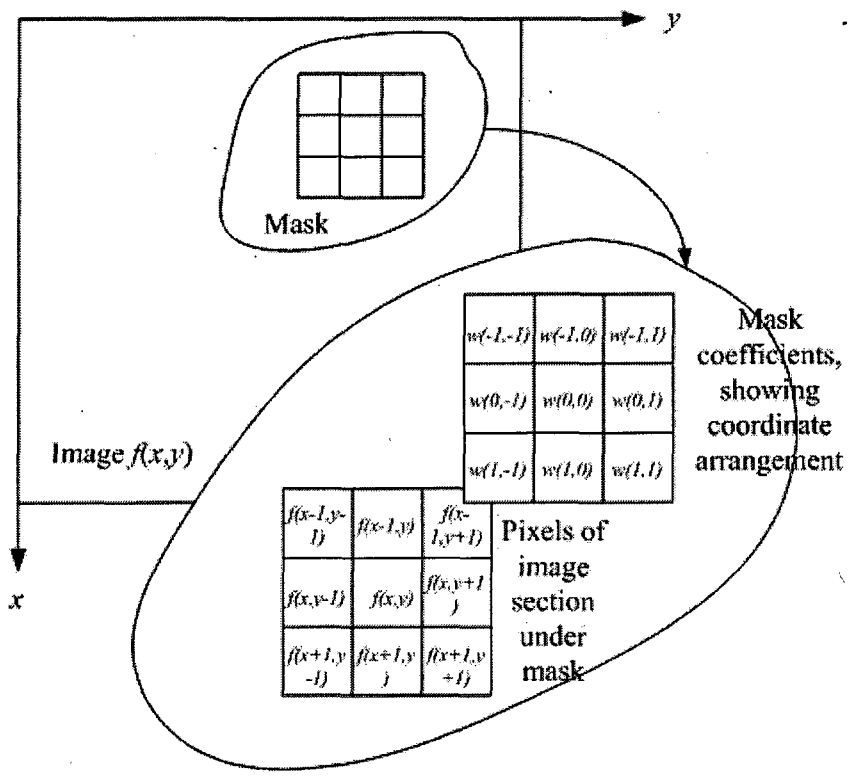


**Figure 4-3** A 3×3 mask for easy of readability

similar to convolution, loss of the edge information in the corners of images happens since the centre of mask cannot cover the corner positions. Gradient-based methods are widely applied for edge detection. However, they suffer from some problems, such as the estimation of the threshold value (Gonzalez,R.C. 1992). This problem is common to all gradient-based edge detection schemes. Although the adaptive algorithm (Jin,J.S. et al. 2000) and statistical method (Rakesh,R.R. et al. 2004) have been applied in some researches, the thresholding values are basically determined by experience. Another problem is the missing of corners, which causes considerable difficulties for line labeling because it relies on the correct identification of corners and junctions.

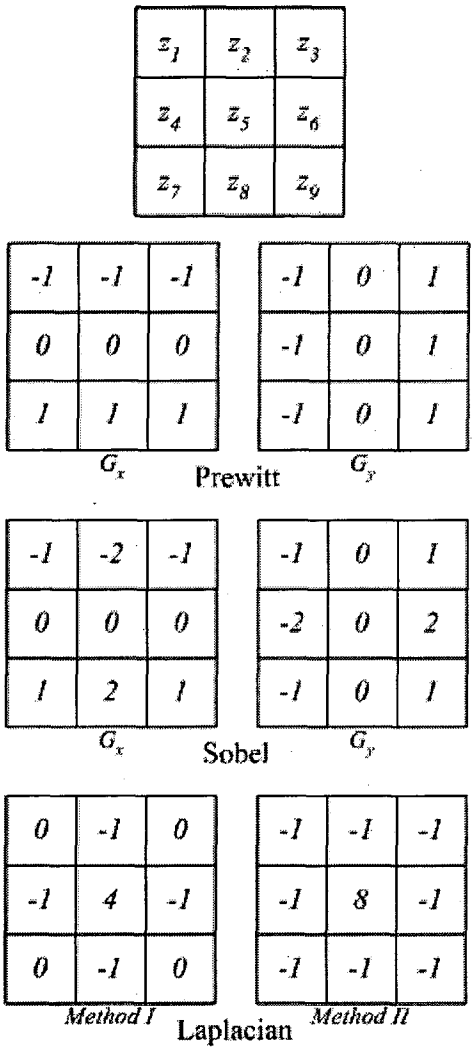


**Figure 4-4** Prewitt, Sobel and Laplacian masks

A phase-based edge detection operator, which is called phase congruency, is also used in edge detection (Cao,G.T. et al. 2006; Kyan,M.J. et al. 2001; Liu,Z. et al. 2006; Wong,A. et al. 2007). Phase congruency is a dimensionless quantity and provides information that is invariant to changes in brightness or contrast of image. It could have good performance in DVF images due to its robustness against low contrast. Phase congruency reflects the behavior of the image in the frequency domain based on the concept that the edge-like features have many of their frequency components in phase. Therefore, it provides an

absolute measure of the significance of feature points, and thus allows a universal threshold value. In the 1980's, a model named *Local Energy Model* was developed (Morrone,M.C. et al. 1987). This model assumes that features are perceived at points in an image where the Fourier components are maximally in phase rather than at points of maximal intensity gradient. Then Morrone and Owens defined the phase congruency function in terms of the Fourier series expansion of a signal at some location $x$ as

$$PC(x) = \max_{\bar{\phi}(x)\in[0,2\pi]} \frac{\sum A_n \cos(\phi_n(x) - \bar{\phi}(x))}{\sum A_n},$$

where $A_n$ is the amplitude of $n^{th}$ Fourier component, $\phi_n(x)$ is the local phase of the Fourier component at position $x$, and $\bar{\phi}(x)$ is the amplitude weighted mean local phase angle of all the Fourier terms at position $x$. Later, a new measure of phase congruency was introduced by (Kovesi,P. 1999) and defined as

$$PC(x) = \frac{\sum W(x)\lfloor A_n(x)(\cos(\phi_n(x) - \bar{\phi}(x)) - |\sin(\phi_n(x) - \bar{\phi}(x))|) - T\rfloor}{\sum A_n(x) + \varepsilon},$$

where $W(x)$ is a weighed factor for frequency spread, $\varepsilon$ is a small constant to avoid division by zero, $T$ is the estimated noise influence, and the others are same as before. Here, the symbol $\lfloor\ \rfloor$ denotes that the enclosed quantity is equal to itself when its value is positive and zero otherwise. The phase congruency does not have a good performance with DVF images, which will be discussed in the next section and the edge detection results of the phase congruency with different threshold values can be found in the Appendix A.

An edge detection technique called the Active Contour (the Snake) is also used in feature extraction. In this method, some initial points are defined around the feature to be extracted. Then, these points are moved through an iterative process and an Energy Function for each point in the neighbourhood image is calculated. Finally, the points are moved to the position where the Energy Function is lowest. Here, the Energy Function is

a function with the variables of continuity, curvature and image energy. The active contour was successfully used in edge detection and segmentation in MRI and CT images (Yezzi,A. et al. 1997). It was also introduced to segment the 3-D MRI images in computer-aided spinal surgery (Booth,S. et al. 2001). However, the snake algorithm is not commonly used in X-ray or DVF images since it is sensitive to noise.

## 4.2 Applications to Vertebral Contour Identification

### 4.2.1 Experimental Results using the Gradient-based Edge Detectors

In this section, two typical gradient-based edge methods, the Canny and Laplacian of Gaussian method are chosen to show the detection performance with DVF images. Other gradient-based operators, such as the Sobel and Prewitt, will not be discussed since they performance not as good as the Canny algorithm.

The Canny operator has been widely applied to the segmentation of medical images, e.g. (Hamou,A.K. et al. 2004; Koh,H.K. et al. 2006; Li,J. et al. 2006; Xu,W. et al. 2005). The Canny edge detector was also applied to obtain the edge pixels of the lumbar spine in DVF images (Zheng,Y. 2002). However, the vertebral contour results were not good enough for the Hough transform in the next step and manual landmarking and isolating each vertebra were required. Here, we will discuss the implementation of the Canny algorithm to DVF images and show the experimental results.

In the Canny algorithm, a Gaussian filter is firstly applied to the raw images to reduce the response to noise because the Canny edge detector uses the first derivative of the Gaussian filter to obtain the edge maps and is consequently sensitive to noise present on

raw images. After that, the gradient is calculated using the first derivative of the Gaussian filter. Each edge point has an edge direction and this edge direction, together with the local gradient, gives an estimated intensity gradient at each point in the image. Given these estimated gradients, a search is then carried out to determine if the gradient magnitude assumes a local maximum in the gradient direction. This step is referred to as non-maximum suppression. The Canny algorithm uses two thresholds to detect strong and weak edges, and includes the weak edges in the output if they are connected to strong edges. The final step in Canny edge detection is called hysteresis thresholding. In hysteresis thresholding, if the gradient magnitude is below the low threshold level, it is set to zero to be a non-edge. If the magnitude is higher than the high threshold level, it is set to be an edge. If the magnitude lies between these two threshold levels, then it is regarded as a non-edge unless there is a path from this pixel to a pixel with a gradient above the high threshold level. Therefore, this method is more likely to detect true edges.

In order to select a suitable edge detection method for this project, an experiment has been conducted to apply the Canny operator to DVF images. In the experiments, a low and a high threshold were selected subjectively and by experience. The results are shown in Figures 4-5 and 4-6. When a low threshold was applied, too many unwanted edges remained and it is difficult to identify the contours of the vertebrae. However, there are too few useful edges left when a high threshold was selected. These detected vertebral boundaries will mislead the automated motion tracking in the next step of research. More detection results with different threshold values are attached in the Appendix A.

In a further experiment, the Laplacian of Gaussian (LoG) method has also been applied to DVF images. As discussed in the previous section, the Laplacian edge detector aims to find the zero crossings of the second derivative of the image, however, it is sensitive to noise. Therefore, the Gaussian operator is used before edge detection to reduce the effect

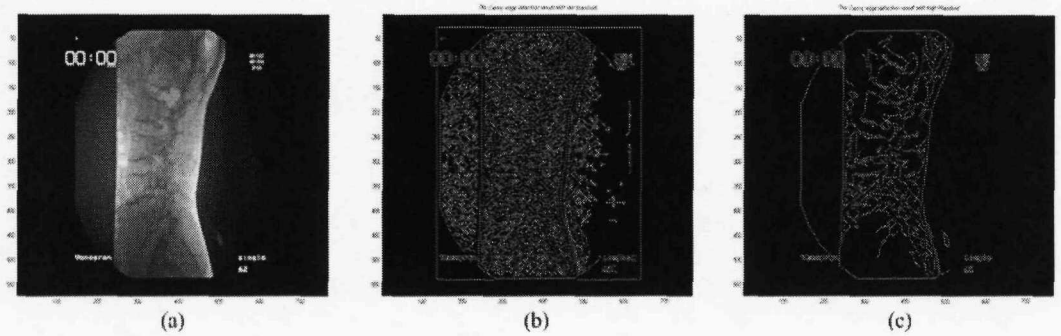


**Figure 4-5** The Canny edge detection result of the DVF image in the neutral position. (a) The original DVF image. (b) Canny with low threshold of [0.006 0.016]. (c) Canny with high threshold of [0.019 0.047].

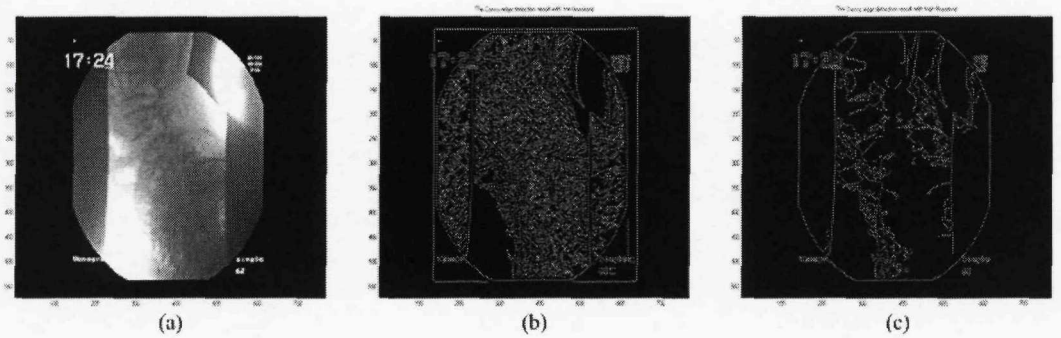


**Figure 4-6** The Canny edge detection result of the DVF image in the extreme position. (a) The original DVF image. (b) Canny with low threshold of [0.006 0.016]. (c) Canny with high threshold of [0.019 0.047].

of noise and improve the performance. Consider the Gaussian function $f(r) = -e^{-\frac{r^2}{2\sigma^2}}$, where $r^2 = x^2 + y^2$ and $\sigma$ is the standard deviation. The Laplacian of the function with respect to $r$ is $\nabla^2 f(r) = -(\frac{r^2 - \sigma^2}{\sigma^4})e^{-\frac{r^2}{2\sigma^2}}$ and it is called the Laplacian of Gaussian. Because the second derivative is a linear operator (discussed in the previous section), filtering an image with $\nabla^2 f(r)$ is the same as convolving the image with the Gaussian operator first and then computing the Laplacian of the result. Finally, locating the edges consists of finding the zero crossings of the computed results. The detection results are

shown in Figures 4-7 and 4-8. The thresholds were also set by experience and observations of edge maps at the different threshold values. It can be seen that the vertebral edges are worse than those from the Canny method. In particular, when a high threshold was applied, the edges are not good even for the manual landmarking. More detection results with different threshold values are also attached in the Appendix A.

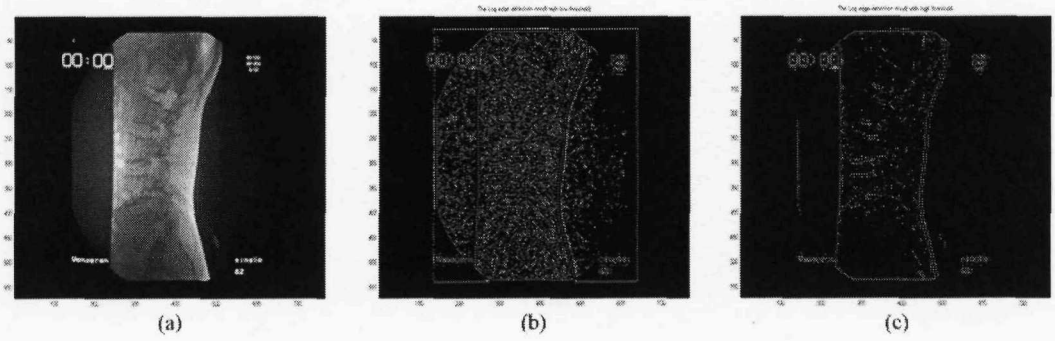


**Figure 4-7** The Laplaican of Gaussian (LoG) edge detection result of the DVF image in the neutral position. (a) The original DVF image. (b) LoG with low threshold of 0.001. (c) LoG with high threshold of 0.002.

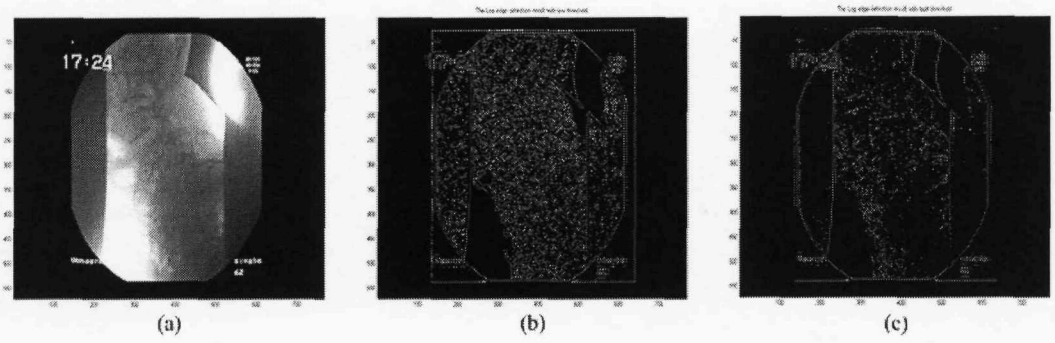


**Figure 4-8** The Laplaican of Gaussian (LoG) edge detection result of the DVF image in the extreme position. (a) The original DVF image. (b) LoG with low threshold of 0.001. (c) LoG with high threshold of 0.002.

### 4.2.2 Experimental Results using the Phase-based Edge Detector

The phase congruency edge detection approach tries to find the maximal Fourier components in phase (Morrone,M.C. et al. 1986; Morrone,M.C. et al. 1987). This has the advantages over the gradient-based methods in feature extraction because it is invariant to changes in image brightness or contrast and provides an absolute measurement of the significance of feature points with a universal threshold. Here, to test the performance of the phase congruency method to DVF images, an experiment has been conducted. The primary Matlab code is based on Kovesi's previous research which is available online (Kovesi,P. 2001). In his algorithm, the log-Gabor wavelets (Field,D.J. 1987) were used to calculate the phase congruency (see Chapter 5 for an introduction to wavelets). After the calculation, the non-maximum suppression and hysteresis thresholding were applied to locate the estimated vertebral boundaries. The experimental results are shown in Figures 4-9 and 4-10. The threshoulds are largely selected subjectively. The results are not promising though they may be good enough for manual landmarking (Zheng,Y. 2002). However, the current research aims to develop a more automated identification procedure and the vertebral edges yielded by the phase congruency cannot build the matching template good enough for the motion tracking because too many or too few vertebral contours are generated. Again, more detection results with different threshold values can be seen in Appendix A.

### 4.2.3 Experimental Results using the Active Contour Algorithm

The Active Contour method, such as the Greedy Snake algorithm (Williams,D.J. et al. 1992), was also tried as a basis for obtaining the vertebral edges. In the Greedy Snake algorithm, the *Energy Function* used in the implementation is expressed as $E_{total}=\alpha E_{cont}+\beta E_{curv}+\gamma E_{image}$, where $E_{cont}$ and $E_{curv}$ constitute the first and second order continuity constraints and form the *Internal Energy*; the third term $E_{image}$ constitutes the

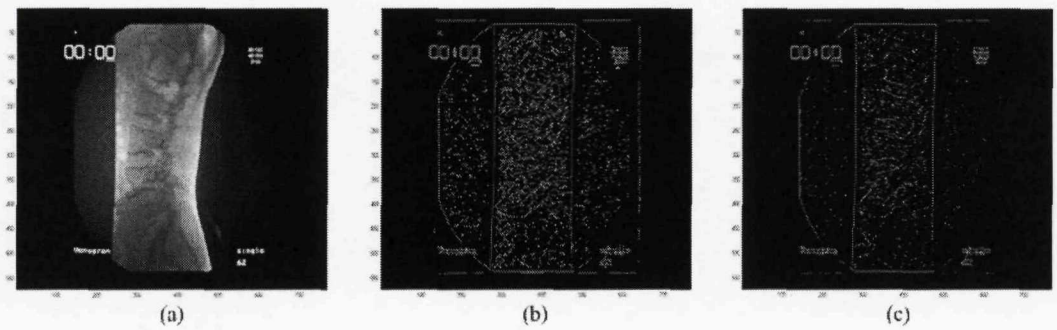

(a) (b) (c)

**Figure 4-9** The phase congruency edge detection result of the DVF image in the neutral position. (a) The original DVF image. (b) Phase congruency with low threshold of 0.1. (c) Phase congruency with high threshold of 0.4.

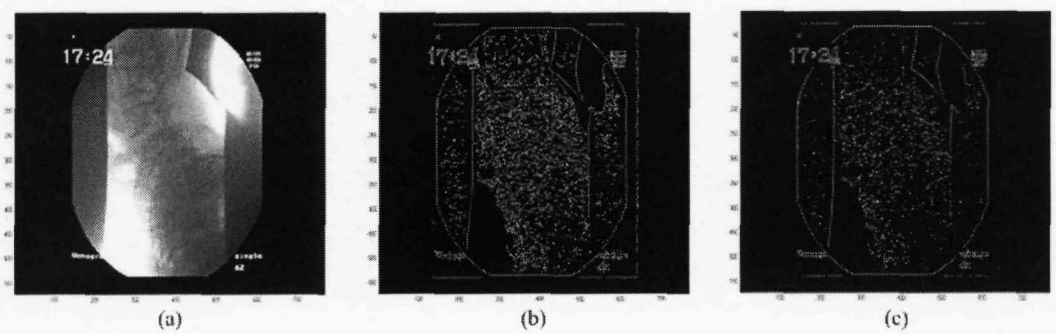

(a) (b) (c)

**Figure 4-10** The phase congruency edge detection result of the DVF image in the extreme position. (a) The original DVF image. (b) Phase congruency with low threshold of 0.1. (c) Phase congruency with high threshold of 0.4.

*External Energy* and it can be due to various features, such as lines, edges or terminations. The $E_{cont}$ corresponds to the first order continuity and it is calculated as $\overline{D}-|V_i-V_{i-1}|$, where $\overline{D}$ is the average distance between points, and $|V_i-V_{i-1}|$ means the absolute difference between the two points under consideration. The $E_{curv}$ refers to the curvature, which is calculated as $|V_{i-1}-2V_i+V_{i+1}|^2$. Finally, the $E_{image}$ is basically a normalized gradient magnitude, which can be written as $E_{image}=\frac{V_{\min}-V_{magnitude}}{V_{\max}-V_{\min}}$, where $V_{magnitude}$ represents the magnitude value of the calculated pixel, and $V_{min}$ and $V_{max}$ denote the

minimum and maximum in the neighbourhood (the 5×5 mask in the experiment) of this pixel. The parameters $\alpha$, $\beta$ and $\gamma$ are used to balance the relative influence of these three factors. In the experiments, the parameters were set as $\alpha$=1 and $\gamma$=1.2 (Williams,D.J. et al. 1992). At the end of the each iteration, a step was involved to determine the curvature at each point on the new contour. If the value was the maximum, $\beta$ was then set to 1 for the next iteration, or else it was set to 0. The different settings of the parameters cannot yield the satisfactory contours either.

The edge detection results are shown in Figures 4-11 and 4-12. The experimental results indicate that the Snake method is not suitable to yield the vertebral contour correctly in DVF images. It could be caused by the fact that the Snake algorithm is very sensitive to noise. Unfortunately, the DVF images contain a considerable amount of background noise. Furthermore, if the Gaussian operator is used to filter out the noise, the pre-processing of the Gaussian operator blurs the images and reduces the accuracy of the locations of the vertebral boundaries.

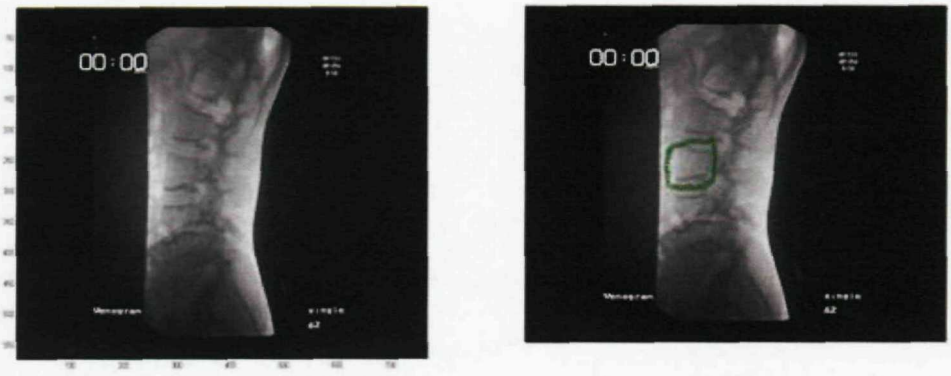


(a) (b)

**Figure 4-11** The Active Contour edge detection result of the DVF image in the neutral position. (a) The original DVF image. (b) The Greedy Snake algorithm result.

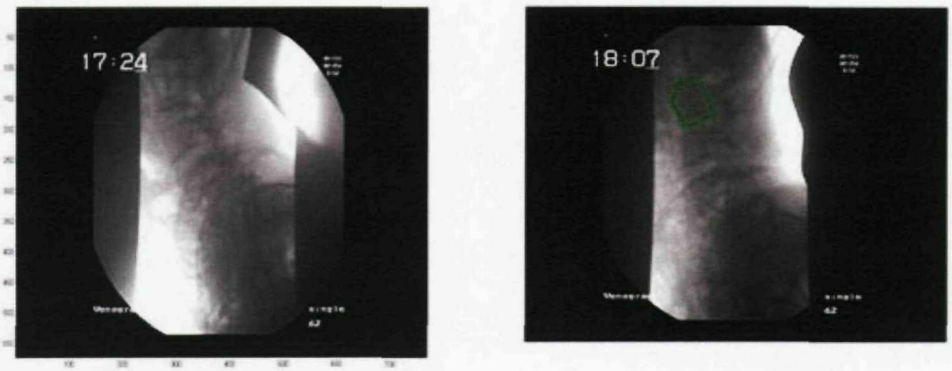


(a) (b)

**Figure 4-12** The Active Contour edge detection result of the DVF image in the extreme position. (a) The original DVF image. (b) The Greedy Snake algorithm result.

### 4.2.4 Summary

From the experimental results, the Canny edge detection method appears to be the most suitable for automated segmentation of the lumbar spine vertebrae. When a low threshold is applied, the Laplacian of Gaussian and phase congruency operators produce more vertebral contour information and too many unwanted fake edges. Therefore they would be helpful in manual landmarking of the lumbar spine but not good enough in automated segmentation. On the other hand, when a high threshold is applied, both the Laplacian of Gaussian and phase congruency lost too many details during the detection (see the Appendix A). Only the Canny operator is able to recognize the approximate contour of the lumbar spine. However, some problems, such as broken edges, would affect the tracking results in the next step. To locate better vertebral edges, a wavelet-based edge detection method is considered and will be discussed in the next chapter.

# Chapter 5

# Wavelet-based Edge Detection Method

## 5.1 Overview

From the discussion in the previous chapter, the conventional edge operators cannot yield the vertebral edges good enough for the automated tracking, a better edge detection method will be proposed in this chapter. Wavelet multiresolution analysis (MRA) offers an opportunity to investigate the edge information at the different scales. A combination of edge maps at the different scales will provide a better vertebral shape for automated tracking. The Canny edge detection algorithm has shown its potential in processing DVF images in the previous chapter and the first derivative of Gaussian (FDoG) is used as edge detector in the Canny algorithm, so the FDoG function will be the prototype of edge detector in our proposed method. The detection results at the two adjacent scales are multiplied and this method is called wavelet scale multiplication edge detection method. Each edge map has its advantages and disadvantages. Usually, the edges in small scale are more accurate, although they are more sensitive to noise so that some false edges are generated; on the other hand, with large scale, fewer wrong edges are detected but this is traded against a reduced accuracy in edge position. The multi-scale product combines the advantages at different scales together and yields the better edges. The experimental results with the DVF image from the calibration model and human subjects will be generated, shown and discussed in this chapter.

## 5.2 Introduction to Wavelet and Multiresolution Analysis

The Fourier transform (FT) is widely used in analysis of raw time-domain signals. The FT provides frequency information and the amplitude-frequency relationship. However, it does not give any information about where in space or time the frequencies occur. Therefore the FT can be used if the research is only interested in which spectral components exist in a signal but is not interested in where these occur. To overcome this problem, several methods have been developed in recent decades. The wavelet transform is a transformation to basis functions that are localized in both scale and time. It is capable of providing the time and frequency information simultaneously, hence giving a time-frequency representation of the signal. The wavelet transform was introduced by Alfred Haar in 1909. Since then the wavelet theory has developed rapidly. Recently, it is increasing apparent that image processing can gain improvements in performance by using wavelet-based approaches since Mallat's fundamental contribution to the development of the wavelet theory (Mallat,S.G. et al. 1992b). Wavelet-based edge detection approaches have been widely applied in processing biomedical images to help clinical diagnosis. In particular, due to the characteristics of multi-resolution analysis, a wavelet-based operator can have better performance than the conventional edge detectors when poor quality images are presented, such as X-ray images (Deschenes,S. et al. 2002), mammography images (Chen,C.H. et al. 1997) and ultrasound images (Kaspersen,J.H. et al. 2001; Tsantis,S. et al. 2006). This chapter will discuss the wavelet theory briefly and emphasize the wavelet scale multiplication edge detection as well as its application to DVF images.

### 5.2.1 The Definition of Wavelet Series

The wavelet series is generated from a single basic wavelet $\psi(t)$, which is also called the mother wavelet, and then scaled and translated to create a wavelet series. Because of the property of zero average in the mother wavelet, a large value of scale corresponds to low

frequency while a small scale shows the high frequencies. A series of wavelets can be derived from $\psi(t)$ by $\psi_{a,b}(t) = \frac{1}{\sqrt{a}}\psi(\frac{t-b}{a})$, $(a,b \in R, a > 0)$ (Daubechies,I. 1992). In the equation, $a$ is the scale factor, $a^{-\frac{1}{2}}$ is for energy normalization across the different scales, $b$ is the translation factor and $R$ denotes the [+]real number. For example, a Mexican Hat wavelet $\psi(t) = (1-t^2)\cdot e^{-\frac{t^2}{2}}$ is shown in Figure 5-1(a). Figure 5-1(b) shows the translated wavelet $\psi_{1,4}(t) = \psi(t-4)$ and Figure 5-1(c) shows the scaled and translated wavelet $\psi_{2,-2}(t) = \frac{1}{\sqrt{2}}\psi(\frac{t+2}{2})$.

The discrete wavelets are only scaled and translated in discrete steps. Usually the scale and translation parameters $(a,b)$ a re defined based on a pair of constants ($a_0$>1, $b_0$>0) and $(a,b) = (a_0^m, nb_0a_0^m)$, $(m,n \in Z)$, where $Z$ denotes the set of [*]integers. Then a set of discrete wavelets can be rewritten as $\psi_{m,n}(t) = \frac{1}{\sqrt{a_0^m}}\psi(\frac{t-nb_0a_0^m}{a_0^m})$, $(m,n \in Z; a_0 > 1, b_0 > 0)$.

The effect of discretizing the wavelet is that the time-scale space is now sampled at discrete intervals. Moreover the scale factor $a_0$ is usually set to be 2 so that the sampling of the frequency axis corresponds to dyadic sampling which is a very natural choice for computers. The translation factor $b_0$ is set to be 1 for dyadic sampling of the time axis. As a result $(a,b) = (2^m, n\cdot 2^m)$, $(m,n) \in Z$, and the wavelets scaled by $2^j$ are written as $\psi_{j,n}(t) = \frac{1}{\sqrt{2^j}}\psi(\frac{t-2^j n}{2^j})$, $(j,n \in Z)$.

[+]*The real number can be described as numbers that can be given by an infinite decimal representation and represented as points along an infinitely long number line.*

[*]*The integers are the set of numbers consisting of the natural number and their negatives. In non-mathematical terms, they are number that can be written without a fractional or decimal component.*

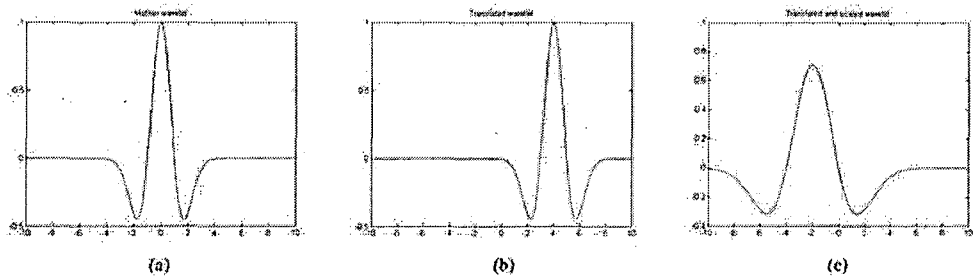

**Figure 5-1** The example of a series of the Mexican Hat wavelet. (a) The mother wavelet. (b) The translated wavelet. (c) The scaled and translated wavelet.

After discretizing the wavelets, an infinite number of scales and translations are still needed to calculate the wavelet transform. So a method to reduce the number of wavelets to analyze a signal has to be developed and this method should keep the quality of the transform. The translations of the wavelets are limited by the duration of the signal under investigation so that there is an upper boundary for the wavelets. Then the question remaining is that of how many scales are needed to analyze the signal to obtain satisfactory results.

## 5.2.2 The Scaling Function and Filter Bank

It is well known from Fourier theory that stretching in the time domain is equivalent to compressing the spectrum and shifting downwards in the frequency domain, which is shown in the equation $F\left\{f(\frac{t}{a})\right\} = |a| \cdot F(a\omega)$, where $a>1$ and $F(\omega)=F\{f(t)\}$. This means that a time stretch of the wavelet by a scale factor of 2 will compress the frequency spectrum of the wavelet by the scale factor of 2 and also shift all frequency components down by the scale factor of 2. Figure 5-2 shows an example, in which, $\psi_j$ is the Fourier transform of the mother wavelet and the others are the wavelet set derived from the mother wavelet. As a result, since one wavelet can be considered as a band-pass filter, a set of scaled wavelets can be considered as a band-pass filter bank. Moreover the ratio

between the centre frequency of a wavelet spectrum and the width of this spectrum is the same for all the wavelets in this set. This ratio is usually known as the Q factor and in this case the set of the wavelets is therefore considered as a constant Q band-pass filter bank.

The scaling function $\phi(t)$ has the characterization of $\int\phi(t)dt = 1$ (Mallat,S.G. 1989a) which means that the scaling function does not detect the difference in the signals. Furthermore, the scaling function has a low-pass spectrum and so it investigates the low frequency components of the signal. Then if the signal is analyzed by a combination of the scaling function and the wavelets, the scaling function is used to cover the remaining spectrum after the wavelet has been stretched to a suitable scale, such as scale $j+1$, shown in Figure 5-2. Since one wavelet can be considered as a band-pass filter and a scaling function can be regarded as a low-pass filter, a series of scaled wavelets together with a scaling function can be considered as a filter bank. In this way the number of the wavelets is limited from an infinite number to a finite one. The number of filters needed is actually decided by the application and selection requires trial and error.

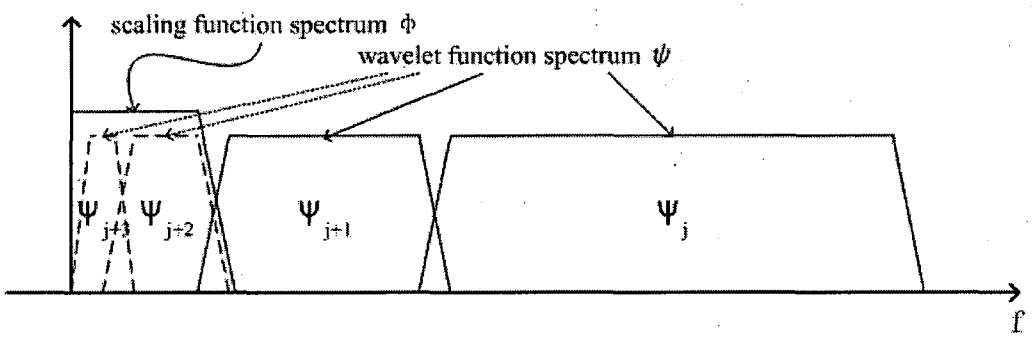


**Figure 5-2** Spectrum of a scaling function and a series of wavelet functions.

### 5.2.3 Wavelet Decomposition and Multiresolution Analysis

The decomposition of signal using the filter bank can be built in an iterative way. The first step is to split the signal spectrum in two equal components which are the output of a low-pass filter and the output of a high-pass filter. The high-pass part contains the finest details and therefore do not need a further processing. However the low-pass part contains the coarse information and needs to be split again into a higher scale level. This process is repeated until a satisfactory scale level is achieved. The process of splitting the spectrum is graphically shown in Figure 5-3(a).

From the view of block diagram (Figure 5-3(b)), when a signal *f(x)* is decomposed in the filter bank, a series of detail signals $\{W_j\}$ and a series of approximation signals $\{V_j\}$ are generated due to the characterizations of high-pass and low-pass filters. $\{W_j\}$ is usually called the detail spaces while $\{V_j\}$ are called the subspaces. And $f(x) = V_1 + W_1 = V_2 + W_2 + W_1 = \cdots = V_j + W_j + W_{j-1} + \cdots + W_2 + W_1$ . So $V_j$ is the approximation of *f(x)* in the scale of *j* and $\{V_j\} = \{V_j, V_{j-1}, \cdots, V_2, V_1\}$ is defined as a set of the multiresolution analysis (MRA) of *f(x)* (Strang,G. 1989a; Strang,G. 1993b). The sequence $\{V_j\}$ has the following properties (Cohen,A. et al. 1993; Mallat,S.G. 1989b):

(1). $V_{j+1} \subset V_j$,

(2). $f(x) \in V_j \Leftrightarrow f(x - 2^j \cdot k) \in V_j$,

(3). $f(x) \in V_j \Leftrightarrow f(\frac{x}{2}) \in V_{j+1}$,

(4). $\lim V_j = \{0\}$.

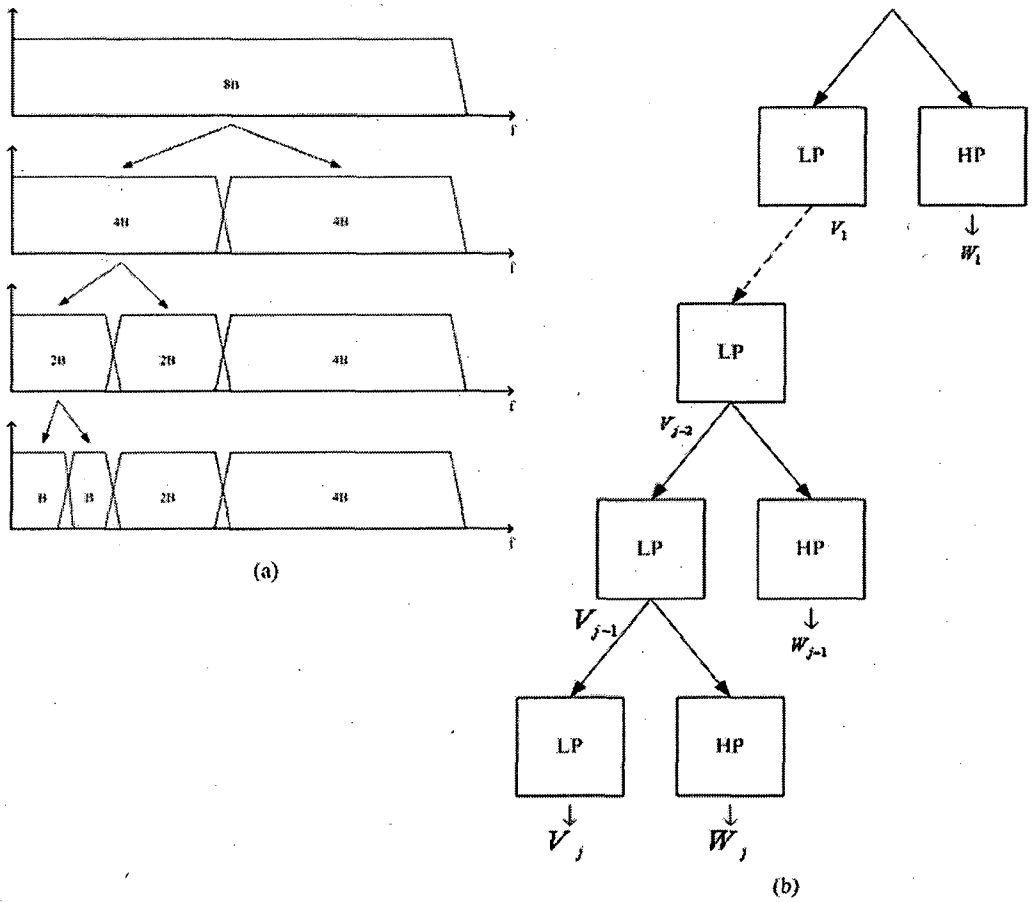


**Figure 5-3** Decomposing the signal spectrum with an iteratire filter bank. (a) The spectrum view. (b) The block diagram view.

*Property* (*1*) means than an approximation at a scale of $j$ contains all the necessary information to compute an approximation at the next scale $j+1$. *Property* (*2*), the property of self-similarity in time, indicates that $V_j$ is invariant to any translation proportional to the scale $j$. *Property* (*3*) is the characteristic of self-similarity in scale, which shows that dividing the dilating function by 2 in the time domain means that it enlarges the details by 2 in the frequency domain and it will be an approximation at the next scale $j+1$. Finally, *Property* (*4*) implies that all the details of $f(x)$ will be lost when the scale $j$ goes to infinity, which means only low pass filters are used in the decomposition.

The MRA provides a recursive algorithm to analyze a signal up to the desired details and this theory was developed in many previous research works (Herley,C. et al. 1993; Polyak,N. et al. 1998; Smith,M.J.T. et al. 1986; Vetterli,M. et al. 1992). The MRA has been widely applied in field of audio compression (Srinivasan,P. et al. 1998), image compression (Ben Amar,C. et al. 2005; Polyak,N. et al. 2000), image de-noising (De Stefano,A. et al. 2004; Humeau,A. et al. 2002; Katkovnik,V. 2004; Strela,V. et al. 1999; Zhong,J.M. et al. 2005) and pattern recognition (Chen,G.Y. et al. 2003; Zhang,L. et al. 2005). In the following part of this chapter, we will emphasize the application of wavelet decomposition and MRA to edge detection in image processing.

## 5.3 Wavelet Multiresolution in the Application of Edge Detection

### 5.3.1 Wavelet Multiresolution Decomposition in Two-Dimensions

In image processing, the one-dimensional (1-D) wavelet transform discussed in the previous section is easily extended to two-dimensional (2-D) functions. A non-standard decomposition method is usually applied to acquire the coefficients in the wavelet transform (Strang,G. 1989b; Strang,G. 1993a). In two dimensions, a 2-D scaling function $\phi(x,y)$, and three 2-D wavelets $\psi^H(x,y)$, $\psi^V(x,y)$ and $\psi^D(x,y)$ are defined as follows:

$$\phi(x,y) = \phi(x)\phi(y)$$
$$\psi^H(x,y) = \psi(x)\phi(y)$$
$$\psi^V(x,y) = \phi(x)\psi(y)$$
$$\psi^D(x,y) = \psi(x)\psi(y)$$

Here the superscripts of the wavelets mean the different directions. The $\psi^H$ measures the variations along the columns in the image so that it detects the horizontal edges; the $\psi^V$

responds to the variations along the rows, such as the vertical edges; and the $\psi^D$ examines the variations along the diagonals since it detects the edges in both the horizontal and the vertical directions. The wavelets are able to measure the variations in the intensity or grey level of the image. Moreover the definitions of the 2-D wavelets do not increase the computational complexity of the 2-D wavelet transform.

Given an image $f(x,y)$ and $J$ is the satisfactory finest scale value, which means $f(x,y)$ has been decomposed into sufficient detail. Then the $W_\phi(J)$ defines the approximation of $f(x,y)$ at the scale of $J$ and the $W_\psi^i(j), i \in \{H,V,D\}$ defines the detailed information at the horizontal ($H$), vertical ($V$) and diagonal ($D$) directions at each scale of $j$. Here the superscript index $i$ identifies the direction $H,V$ and $D$ respectively. Figure 5-4 shows the iteration procedure of 2-D wavelet decomposition into an approximation subband at the scale of $J$ and a series of detailed subbands at different resolution scales in all directions. The approximation subband consists of the so-called scaling coefficients and the detailed subbands are composed of the wavelet coefficients. In this case, an undecimated wavelet transform (Mallat,S.G. 1999) is considered where the number of the wavelet coefficients is equal at each scale. The undecimated method provides more precise information for the frequency localization since the size of the coefficients array do not diminish from level to level. As a result, it applies the wavelet decomposition at each point of the image and preserves all the information contained in the image.

### 5.3.2 Review of the Applications

The conventional edge detectors have the problem of noisy and broken edges since they depend on only one solution. A two stage edge extraction method (Shih,M.Y. et al. 2005) was introduced to solve this problem. In their method, the original images were decomposed into several subband gradient images by multiresolution wavelet theory.

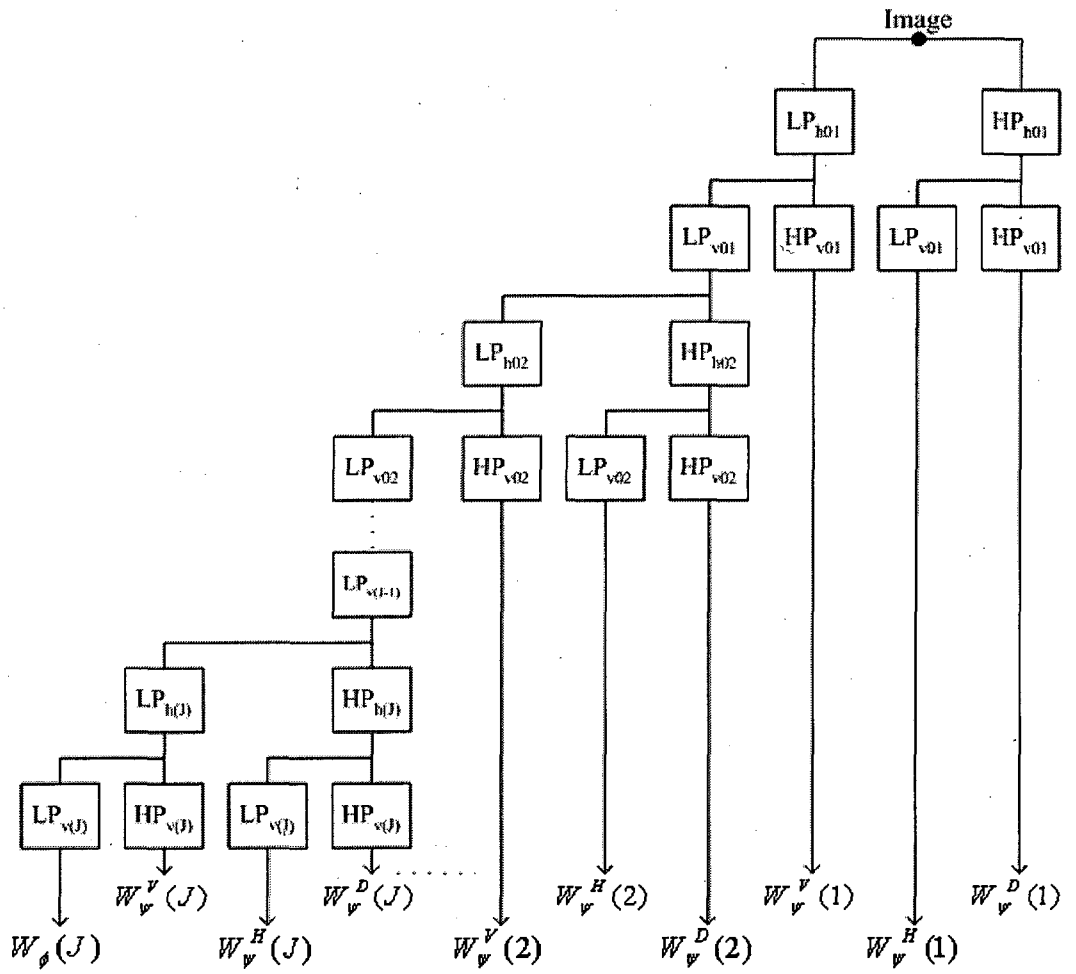


**Figure 5-4** The block diagram of 2-D undecimated wavelet decomposition.

Then a conventional edge operator was used to detect the edges in the finest-scale gradient image. Finally, they proposed an edge tracking algorithm to refine the results and reduce the noisy or blurred influences by analyzing the gradient images at different resolutions. According to the wavelet multiresolution theory, the edge information was propagated from fine scale to coarse scale. Some broken edges at the finest scale may be connected at a coarser scale. With this idea, the broken edge problem was reduced and better edge detection results were obtained. The localization criterion $P_l$ (Aydin,T. et al. 1996) of 0.9370 and detection criterion $P_e$ (Aydin,T. et al. 1996) of 0.1166 were reported

(Shih,M.Y. et al. 2005), which shows great improvement compared with the conventional edge detection methods. However, the decimated method was applied in this research and this means that some edges may be lost with the reduction of the number of the wavelet coefficients.

Another common problem in the conventional gradient-based edge detection is that corners are often missed because the gradient at corners is usually small and so a wavelet multiresolution corner detection algorithm (Lee,J.S. et al. 1995) was proposed. In their algorithm, a three-scale wavelet transform on corner orientation (Liu,H.C. et al. 1990; Rosenfeld,A. et al. 1975) was performed after the boundary of a shape was extracted. Based on both the information of local maxima and modulus of the wavelet transform results, corners and arcs were detected. The orientation ramp width, which was determined by the ratio of the transformed modulus of two scales, reveals the difference between the corner and arc and it is used in the detection of edge points. Their experimental results proved that their method was more effective than several conventional corner detection methods (Beus,H.L. et al. 1987; Cheng,F. et al. 1988; Rattarangsi,A. et al. 1992; Rosenfeld,A. et al. 1973; Rosenfeld,A. et al. 1975), insensitive to boundary noise and more computationally efficient.

Some researchers have tried to improve the accuracy of detection and reduce the effect of noise in other ways. A combined spatial- and scale-space edge detection method (Faghih,F. et al. 2002) was proposed since the spatial and wavelet-based techniques have different advantages and disadvantages. The spatial domain approach is more successful in detecting and locating the weak edges but can provide false edges in response to noise. However, the wavelet-based edge detector is less sensitive to noise although it is not accurate as the spatial domain method in locating the edges. So with the combination of the results obtained in both spatial- and scale-space, edge maps are derived are well localized as well as the successful suppression of the noise effects. However, their

method focused more on de-noising and reconstructing the images by using the edge information obtained from spatial- and scale-edge detection results.

In general, most wavelet multiresolution utilizations in edge detection are based on the combination of the multiscale wavelet transform and decomposition with the traditional edge detection approaches. This combined method has widely applied in the segmentation of poor quality images, such as camera-generated images (Qin,Q. et al. 2004; Simhadri,K.K. et al. 1998; Wang,J.Z. et al. 2001) and biomedical images (Bezerianos,A. et al. 1995; Song,Y. et al. 2004). Furthermore, this method also has good performance in the identification of the features of interest in medical images (Deschenes,S. et al. 2002; Kaspersen,J.H. et al. 2001).

From the discussion above, wavelet decomposition and multiresolution analysis help to obtain better results from the conventional edge detectors. The typical problems of the traditional edge detection method, such as broken edges and missing corners, are solved to some extent by using the combined approach. However, these method discussed above do not apply the wavelet theory to obtain the edge directly. A robust and simple wavelet-based edge detection method will be discussed in the next section. This method uses the wavelet filters to detect edges directly at various scales and combines these results together to improve the performance in detection.

# 5.4 Wavelet Scale Multiplication Edge Detection Method

## 5.4.1 Wavelet-based Edge Detection

Recall the discussion in the previous chapter, an edge in an image is a contour across which the brightness of the image changes abruptly. In image processing, an edge is often interpreted as one class of singularity. In mathematical function, singularities are able to be characterized easily as discontinuities where the gradient approaches infinity. However image data is discrete, so edges in an image are often defined as the local maxima of the gradient.

Edge detection is an important task in image processing and it is a main tool in pattern recognition and image segmentation. The classical edge detectors mentioned in the previous chapter work well with high quality images, but usually are not good enough for noisy images since they cannot distinguish edges with little difference in significance since most of them analyze an image at a single resolution. Although the Fourier transform (FT) is the main mathematical tool for analyzing singularities which represent edges in mathematics, the FT is global and not well adapted to detecting local singularities. It is hard to find the location and spatial distribution using the FT. The wavelet transform is a local analysis and it is especially suitable for time-frequency analysis (Goswami,J.C. et al. 1999), which is essential for singularity detection. This is the major motivation for the study of the wavelet theory in edge detection.

With the development of the wavelet theory, the wavelet transform has proved to be a powerful mathematical tool to examine the singularities in edge detection (Beus,H.L. et al. 1987; Lee,J.S. et al. 1995; Liu,H.C. et al. 1990; Mallat,S.G. 1999; Mallat,S.G. et al. 1992b; Mallat,S.G. et al. 1992a; Tang,Y.Y. et al. 1999; Tang,Y.Y. et al. 2000; Yang,L.H. et al. 2001). Recall the previous chapter, edge locations are related to the extreme of the

first derivative of the signal and the zero crossings of the second derivative of the signal. However, the local extreme of the first derivative wavelet function shows more advantages than the zero crossings because the magnitude of the wavelet modulus represents the relative strength of the edge (Mallat,S.G. et al. 1992b; Mallat,S.G. et al. 1992a) and is therefore able to recognize useful edges from small fluctuations cased by noise. From the discussion in the previous chapter, the Canny edge detector has a better performance in locating the vertebral edges than other gradient-based first derivative edge detectors. Basically, in the Canny algorithm, the gradient is calculated using the first derivative of Gaussian (FDoG) filter and so the FDoG function is used as the mother wavelet in the wavelet transform. Given an image $f(x,y)$ and the Gaussian function $\theta(x,y)$, edge points can be located from the two components $W_s^1 f(x,y)$ and $W_s^2 f(x,y)$ of the wavelet coefficients at a certain scale level of $s$ and these two components are calculated as:

$$\begin{pmatrix} W_s^1 f(x,y) \\ W_s^2 f(x,y) \end{pmatrix} = s \begin{pmatrix} \frac{\partial}{\partial x}(f * \theta_s)(x,y) \\ \frac{\partial}{\partial y}(f * \theta_s)(x,y) \end{pmatrix} = s\vec{\nabla}(f * \theta_s)(x,y).$$

At each scale $s$, the wavelet modulus of the gradient vector is proportional to

$$M_s f(x,y) = \sqrt{\left|W_s^1 f(x,y)\right|^2 + \left|W_s^2 f(x,y)\right|^2}.$$

And the angle of the gradient vector with the horizontal direction is given by

$$A_s f(x,y) = \tan^{-1} \frac{W_s^2 f(x,y)}{W_s^1 f(x,y)}.$$

The direction of gradient vector at a point $(x,y)$ indicates the direction in the image along which the directional derivative of the image has the largest absolute value. An edge point (local maxima) can be detected as point $(x_0,y_0)$ such that the modulus of the gradient vector is of maximum value in the image.

In this way, the wavelet transform yields the edges of images at various resolutions and thereby offers a multiresolution edge detection method to investigate the image singularities more effectively. Based on Mallat's fundamental contributions to the wavelet-based edge detection, the edge information in several scales can be combined for consideration to compensate for the shortcomings of the results at single resolutions. For example, Teager's energy operator (Kaiser,J.F. 1990) was used to combine the edge results at different resolutions to improve the performance of edge detection (Aydin,T. et al. 1996). In 1-D, the operator is defined as $\Gamma[f(s)] = f^2(s) - f(s+1)f(s-1)$, where $s$ means the $s^{th}$ scale. Although their approach improved edge detection in noisy images, they employed a complex algorithm. Some simpler methods exist and will be discussed in the following section.

## 5.4.2 Background of the Wavelet Scale Multiplication

Using the wavelet edge detection filter, edges can be detected at different scales. Each edge map has its advantages and disadvantages. Generally speaking, the edge map in small scale is more accurate, but it is also more sensitive to noise so that some false edges are produced; on the other hand, with large scale, less wrong edge information is detected but this is traded against a reduced accuracy in edge location. The idea here is that a better edge map will be obtained if multi-scale correlation combines the advantages at different scales together. This idea was first put forward by Rosenfeld and his colleagues who used the multi-scale products to enhance multi-scale peaks due to edges (Rosenfeld.A 1970; Rosenfeld.A et al. 1971). The direct multiplication of the detection results of images at different scales locates important edges very efficiently and quite accurately. Similar research was conducted by Sadler,B.M. et al. (1999), and an odd number multi-scale products was considered because it made the edges unbiased and preserved edge-polarity information. They also noticed that with the increase of scale, the growth of the region of support will reduce the interference of neighbouring edges. Moreover, considering the shifts of edge position at different scales could improve the

accuracy of the wavelet scale multiplication results (Lee,Y. et al. 2000). However, much more simple methods were proposed to employ the wavelet edge detector at only two adjacent scales and then multiply the edge results (Bao,P. et al. 2005; Zhang,L. et al. 2002). The final edge maps were determined by finding the local maxima directly in the multi-scale product.

Since the wavelet scale multiplication amplifies edge structures while diluting noise, these approaches have been tested in applications of denoising in Magnetic Resonance Images (Bao,P. et al. 2003; Xu,Y.S. et al. 1994). The direct spatial correlation of the wavelet transform at several adjacent scales was calculated to remove noise and preserve edges. Xu and his colleagues indicated that their denoising technique can remove over 80% of the noise from the images while maintaining at least 80% of the original value of the gradient at most edges (Xu,Y.S. et al. 1994). Moreover, Bao and his colleagues proposed a nonlinear thresholding algorithm and imposed it on the wavelet scale multiplication results for noise suppression. Their experimental results also showed improved performance. From what has been discussed above, potentially enhanced results are expected if the wavelet scale multiplication edge detection method is applied to DVF images.

### 5.4.3 One-Dimensional Analysis

To clarify the scale multiplication method, we first pose the edge detection in 1-D. In previous studies (Bao,P. et al. 2003; Sadler,B.M. et al. 1999; Xu,Y.S. et al. 1994; Zhang,L. et al. 2002), the non-orthogonal Mallat wavelet set (Mallat,S.G. et al. 1992a) was used. Canny first presented the first derivative of Gaussian (FDoG) as an optimal edge detector for isolating edges (Canny,J. 1986) and the Mallat wavelet set is very close to the FDoG (see Figure 5-5). Moreover, the Mallat wavelet set can be designed to obtain the multiresolution edges so it is more powerful than the Canny edge detector. Recall the definition of wavelet, a function $\psi(x)$ is called a wavelet if it has a finite length or fast

decaying oscillating waveform, and its average is equal to zero. A quadratic spline function $\psi(x)$ as the mother wavelet and the region of support (RoS) is usually set to be greater than 4 units of $x$ since the Gaussian function decays rapidly (Bao,P. et al. 2005; Sadler,B.M. et al. 1999). In this project, we set the RoS to be [-4,4], therefore the Mallat wavelet can be written as:

$$\psi(x)=\begin{cases}0 & |x|\geq 4\\ -\psi(-x) & 0\leq x\leq 4\\ -\frac{3}{32}x^2-\frac{1}{4}x & -2\leq x\leq 0\\ \frac{1}{32}(x+4)^2 & -4\leq x\leq -2\end{cases}.$$

In Figure 5-5, $\psi(x)$ is plotted as well as the FDoG function. It can be seen that $\psi(x)$ approximates the FDoG function closely. Therefore the Mallat wavelet set is $\psi_s(x)=\frac{\psi(\frac{x}{s})}{s}$ and the RoS is [-4$s$,4$s$], where $s$ denotes the scale. The Mallat wavelet is adopted in this project because it shows better performance than the Canny edge detector which showed potential in Chapter 4. Moreover, we choose the Mallat wavelet due to the fact that it is a real function (some wavelets are complex functions) and for the ease of implementation. Bao, Zhang and their colleagues have proved that scale multiplication using only two adjacent scales works simply and effectively (Bao,P. et al. 2005; Zhang,L. et al. 2002), so we actually utilize the Mallat wavelet at two scales and here $s_2=2s_1$.

Recall the discussion in Chapter 4 that, in practice, a sub-image, which is also called a mask, is used in edge detection. This process is similar to a finite impulse filter (FIR) convoluted with the image. A pair of masks, $h_x$ and $h_y$ gives two directional gradient images $G_x$ and $G_y$ respectively. The gradient image is traditionally calculated as $\nabla f=|G_x|+|G_y|$. This method is much more attractive computationally and still preserves relative changes in grey level of the image. The Mallat wavelet should be discretized

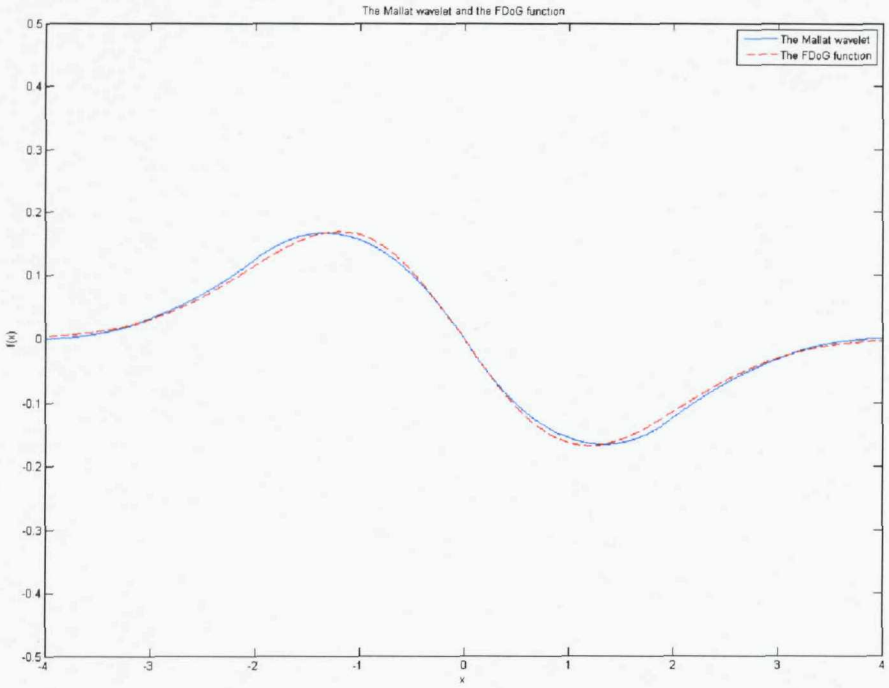


**Figure 5-5** The Mallat wavelet (blue solid line) and the first derivative of Gaussian function (red dashed line).

before implementation. In Mallat theory, the discrete filter length of the discrete Mallat wavelet is $l_j = 2^{j+2} - 2$, where $j$ denotes the $j^{th}$ scale. In discretizing the Mallat wavelet, we basically choose the equal number $\frac{l_j}{2}$ of the points at the positive and negative parts of the wavelet and these points have equal spacing. As a result, these points are symmetric and require the condition that wavelets have the mean value of zero. For example, in Figure 5-6, we discretize the Mallat wavelet FIR filter to be $f_1 = \psi_1(x = \pm 2) = [0.125, -0.125]$ at the finest scale $s=2^0=1$. At the second scale $s=2^1=2$, the discrete filter is then

$$f_2 = \psi_2(x = \pm 2, \pm 4, \pm 6) = [0.0156, 0.0625, 0.0781, -0.0781, -0.0625, -0.0156].$$

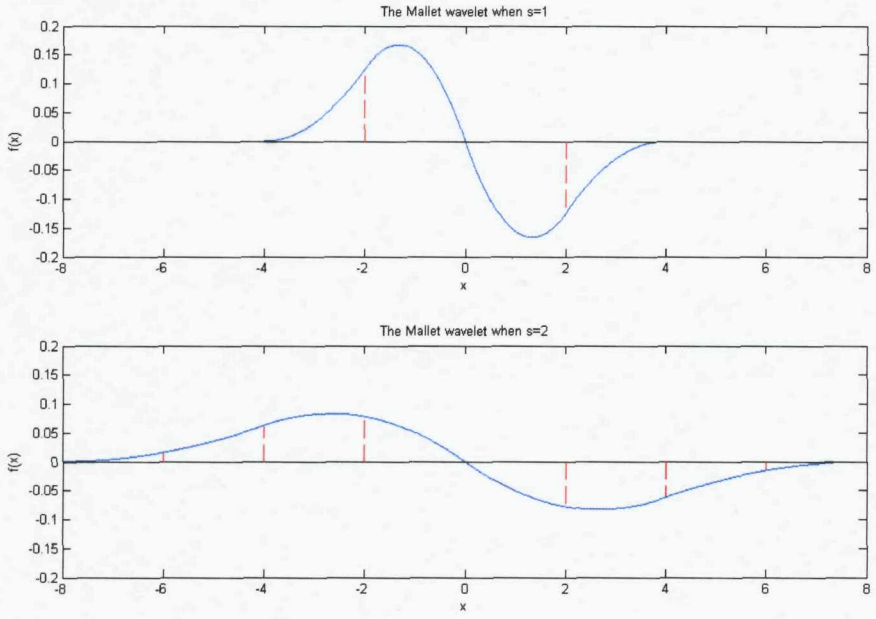


**Figure 5-6** The discrete Mallat wavelet FIR filter at the scales of 1 (top) and 2 (bottom).

After discretizing the Mallat wavelet, we can use it as an FIR filter in edge detection in one-dimension. In simulation, we suppose the signal to be detected is composed of several step edges and impulse edges, as well as additive unit-variance white Gaussian noise. Figure 5-7(b) shows an example of 1-D signal $W(x) = G(x) + n(x)$, where $n(x) \sim N(0, \sigma^2)$ is white Gaussian noise and $G(x)$ is the signal without noise shown in Figure 5-7(a). Here we let $G(x) = A[s(x) + \delta(x)]$, where $A$ is a constant. $G(x)$ takes the value of $A$ in the ranges [51, 150], [201, 250], [301, 320], [350, 360] and [401, 405], as well as the impulse edges given by $\delta(x-440)$, $\delta(x-470)$ and $\delta(x-473)$. The signal-to-noise ratio (SNR) is 12dB, defined as $10\log_{10}\frac{A^2}{\sigma^2}$, where $A$=4. We suppose the step edges represent the real image edges and the impulse edges as well as the white Gaussian noise are the background noise. From Figure 5-7(b), it can be seen that the edge information is seriously affected by the noise under the condition of low SNR. This causes the problem in edge detection, which is shown in Figure 5-8.

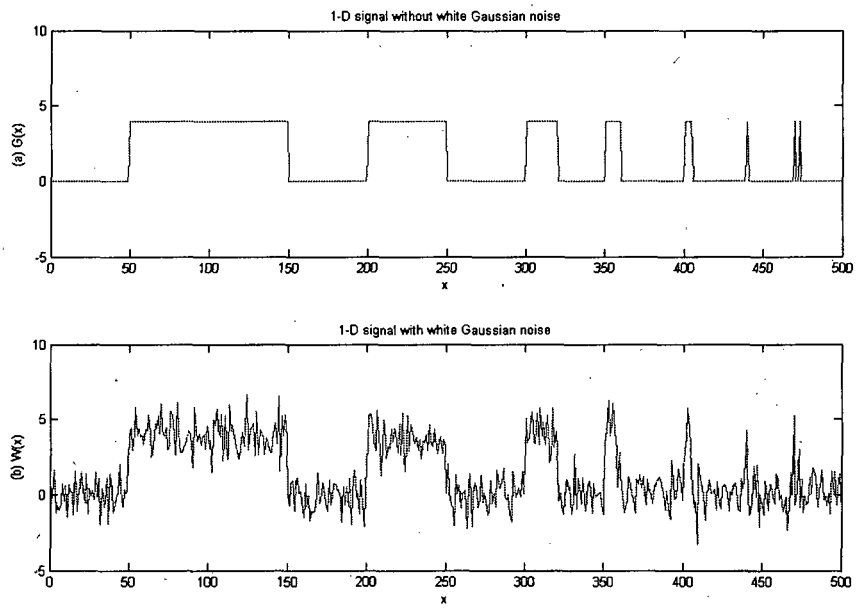


**Figure 5-7** An example of a 1-D signal without and with white Gaussian noise.

Figure 5-8(b)-(e) show the edge detection results using the discrete Mallat wavelet FIR filter at the first four scales respectively. Due to low SNR, the edge is difficult to distinguish from the background noise when a fine scale is used, which is shown in Figure 5-8(b) and (c). In the figures, there is a lot of false edge information generated by noise and they have similar values to those of the real edges. Therefore it is hard to detect edges accurately in this situation. When a coarse scale is utilized, the false edges are restrained and the real edges can be detected with a thresholding technique.

However, large scale decreases the accuracy of the edge location, which can be seen in Figure 5-8(d) and (e). To improve the performance of the edge detection, multi-scale products are introduced. Figure 5-9(c)-(e) show the multi-scale products generated by the edge map at the $1^{st}$ and $2^{nd}$ scales, the $2^{nd}$ and $3^{rd}$ scales, as well as the $3^{rd}$ and $4^{th}$ scales respectively. It can be seen that most of the Gaussian noise has been suppressed and the real edges can be recognized relatively easily at the correct locations. Furthermore, all

edges are now identified as positive changes in the edge maps due to the multiplication. Considering DVF images suffer the problem with high noise interference, the scale multiplication method should help us in identifying the vertebral edges.

To investigate the feasibility of the application of multi-scale products in the edge detection of DVF images, we analyze a DVF image in the horizontal direction (the $x$ direction). Firstly, we select a small part from an original DVF image. The project target is to identify the contour of spinal vertebrae in DVF images, so the small part of the image we choose consists of a whole vertebra, as shown in Figure 5-10(b). From this we can explore the performance of the scale multiplication method on the DVF image. From Figure 5-10(b), it can be seen that the image has low contrast and high noise interference, which can also be seen when the image is expanded in the horizontal direction row by row. Figure 5-10(c) shows a single line of the DVF image (b) in the horizontal direction.

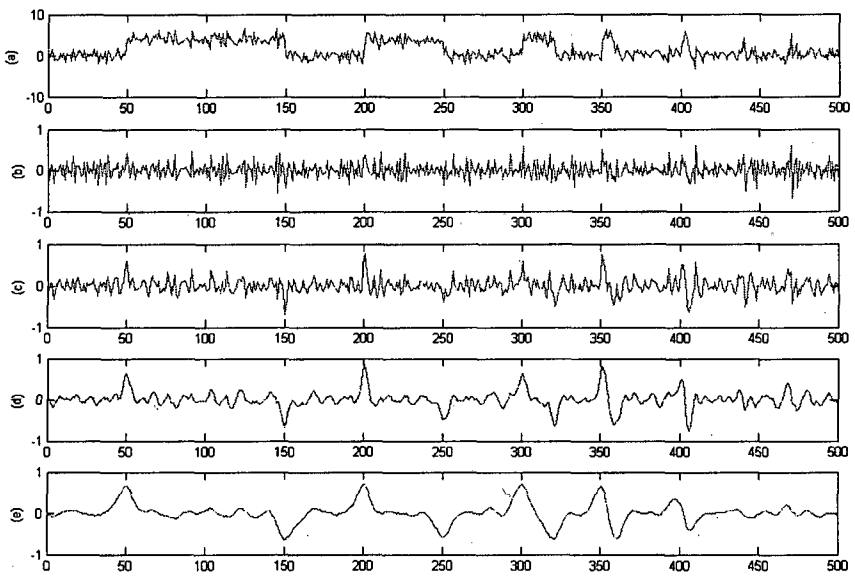


**Figure 5-8** The Mallat wavelet edge detection results. (a) The 1-D signal shown in Figure 5-7(b). (b)-(e). The results of applying the discrete Mallat wavelet FIR filter at the first four scales.

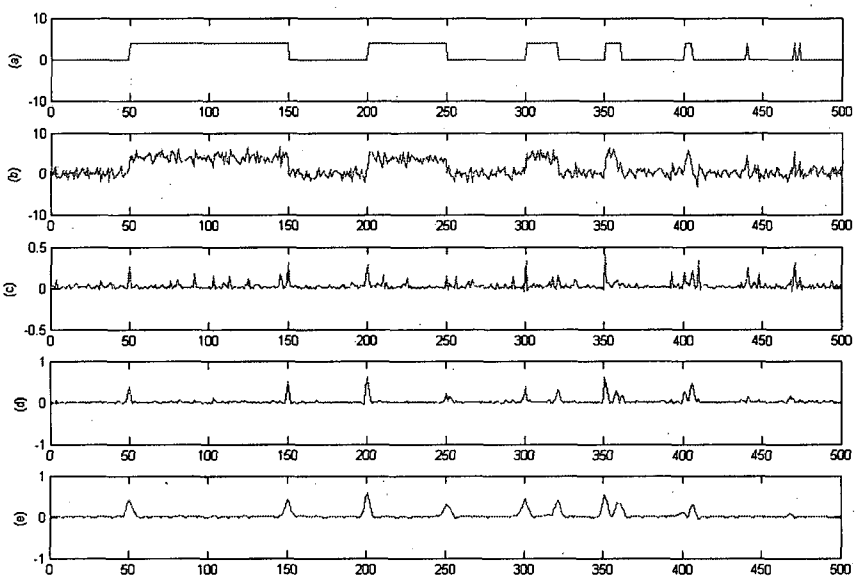


**Figure 5-9** The wavelet scale multiplication results. (a)-(b) The 1-D signals shown in Figure 5-7. (c)-(e) the results of wavelet scale multiplication.

This figure shows five selected cycles which means that it displays five rows of the DVF image (b). For each cycle, the selections having low values represent the vertebra body which is dark in colour. The selection with a high value represents the adjacent structures around the vertebra, such as soft issues, and can be treated here as noise. Like the simulation discussed above, we applied the discrete Mallat wavelet FIR filter to this 1-D DVF image signal and analyze the results of different scales and scale-products. Figure 5-11(b) and (c) show the edge detection results at the scales of $2^1$ and $2^2$ respectively. It can be seen that the edge information is difficult to detect because a number of peaks are present, which means that edges in the image are mixed with the erroneous edges caused by noise and some peaks are too insignificant to be distinguished. However, after multiplying the two results, much clearer edge information is obtained in Figure 5-11(d). By detecting the peaks in the figure, the real edge can be identified correctly. In conclusion, from the 1-D noisy signal simulation and the analysis of part of a real DVF image in 1-D, the wavelet scale multiplication edge detection method appears to be able

to solve the problems we encounter in the utilization of the traditional edge detectors. The multi-scale product can avoid detecting erroneous edges caused by noise and can identify the real edges in the correct location. So the scale multiplication can be applied in our project and is expected to provide the information of spinal vertebrae edges and hence vertebral contour, rotation angle and inter-vertebral angle, for the diagnosis of low back pain.

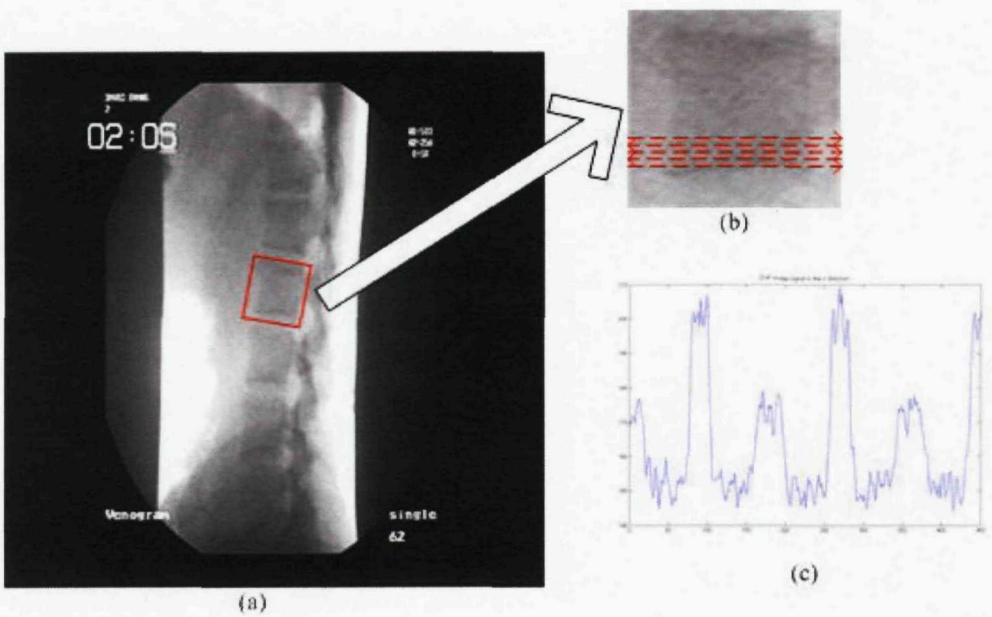


**Figure 5-10** An illustration of DVF image in 1-D. (a) An DVF image. (b) A small part of the DVF image (a). A part of the DVF image in the $x$ direction.

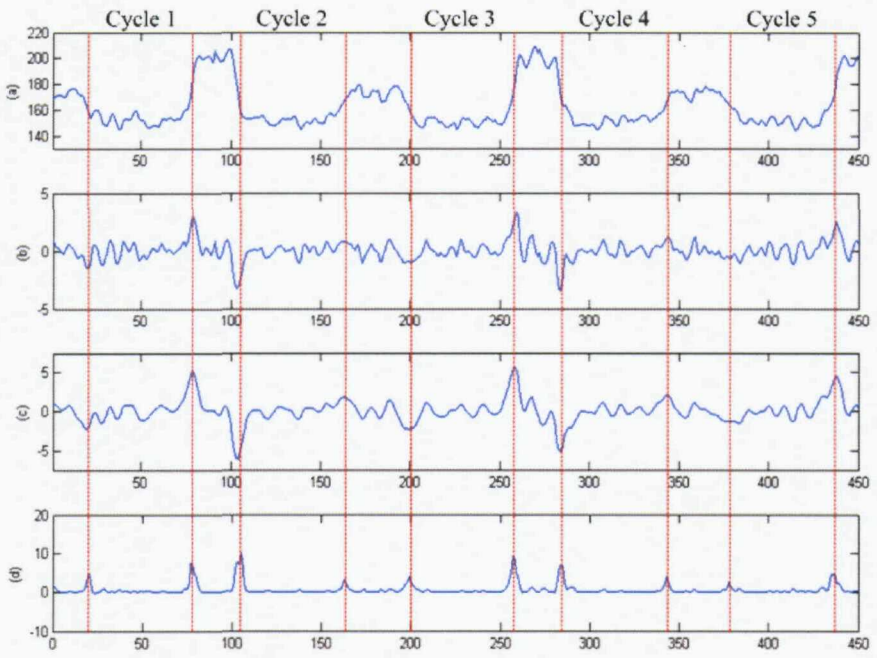


**Figure 5-11** The edge locating results of 1-D DVF signal. (a) 1-D DVF image signal shown in Figure 5-10(c). (b)-(c) The Mallat wavelet edge detection results at the scale of $2^1$ and $2^2$. (d) The result of scale multiplication of (b) and (c).

## 5.4.4 Two-Dimensional Analysis

Recall that in Section 5.4.1, the calculation of the wavelet modulus was presented. Now, suppose the image $f(x,y)$ is filtered by a discrete Mallat wavelet FIR filter at a small scale $s_1$ and a large scale $s_2$ in the $x$ direction and the responses are $H_{s_1}^x(x,y)$ and $H_{s_2}^x(x,y)$ respectively. So the multi-scale product in the $x$ direction is defined as $P_{\text{Im}}^x = H_{s_1}^x(x,y) \cdot H_{s_2}^x(x,y)$. Similarly in the $y$ direction, $H_{s_1}^y(x,y)$ and $H_{s_2}^y(x,y)$ are calculated and then the scale multiplication $P_{\text{Im}}^y = H_{s_1}^y(x,y) \cdot H_{s_2}^y(x,y)$ can be obtained. So combining the result in both horizontal and vertical direction, the filtered result of the whole image is $P_{\text{Im}} = P_{\text{Im}}^x + P_{\text{Im}}^y$.

Figure 5-12(a) shows a noisy synthetic image $f(x,y)$. This image is composed of several plain edges superimposed with white Gaussian noise. From Figure 5-12(a), it can be seen that the synthetic image has the steps at [51, 150], [201, 250], [301, 320], [351, 360] and [401, 405]. We suppose that the step edges represent the real edges and the white Gaussian noise is the background image noise. The image is filtered at a fine scale ($2^1$) and at a coarse scale ($2^2$) respectively, and shown in Figure 5-12(b)-(c). Due to the low SNR, the edges are difficult to distinguish from the background noise when a fine scale is applied, which is shown in Figure 5-12(b). In the figure, the real edges are seriously affected by false edge information.

Therefore it is hard to detect edges accurately in this situation. On the other hand, in Figure 5-12(c), when a large scale is utilized, the edges appear but the large scale decreases the accuracy of the edge location. To improve the performance, a multi-scale product of (b) and (c) is introduced. Figure 5-12(d) shows the result of the wavelet scale multiplication. It has the much sharper edges than Figure 5-12(c) and the noise is better suppressed than in Figure 5-12(b). Most of the false edges are suppressed effectively and real edges can be recognized relatively easily at the correct locations. Again this example of the synthetic image indicates the good performance of the scale multiplication method under high noise interference conditions. Moreover, in general, an improved result would be expected after thresholding.

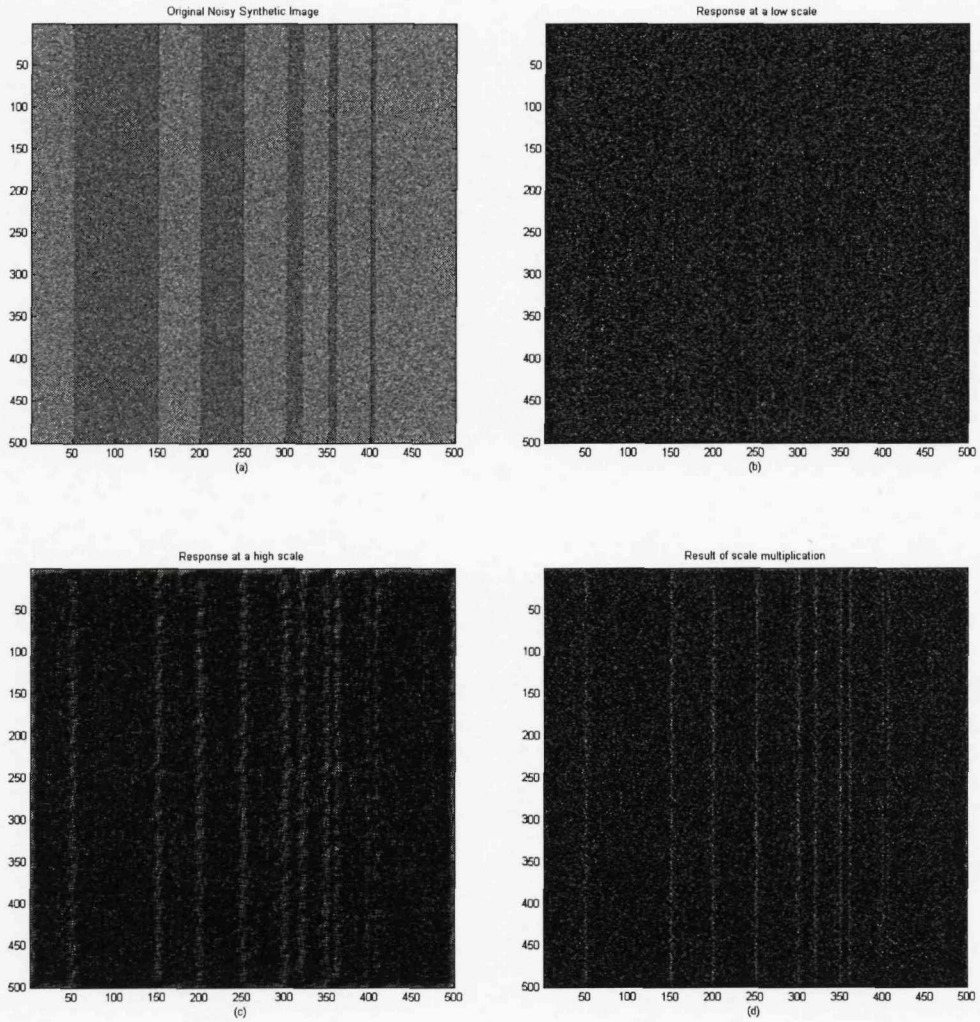


**Figure 5-12** A 2-D simulation for the swavelet scale multiplication edge detection method. (a) A noisy synthetic image. (b) Response at a low scale. (c) Response at a high scale. (d) Results of the scale multiplication.

## 5.4.5 Thresholding

In edge detection, the gradient image should be thresholded to eliminate false edges generated by noise. Then a problem very commonly faced is the choice of threshold values. When a single threshold is adopted, some false edges may appear if the single

threshold value is too small. On the other hand, some true edges may be eliminated if the value is too large. Canny proposed a double thresholding algorithm (Canny,J. 1986), in which a low threshold and a high threshold are applied to obtain double threshold edge maps. The double thresholding algorithm can also be applied in this project because of the characteristics of low contrast and high noise interference. In DVF images, the areas of interest have low contrast while the areas of less interest have a higher contrast. This means that the areas of interest have much lower gradient values than the others after filtering by the discrete Mallat wavelet filter. Hence the real vertebral edge information will be missed if a large threshold is applied. Moreover, the edge detection results are susceptible to noise and pick up of irrelevant features from images if a low threshold value is adopted. As a result, the double thresholding method is applied after edge detection on the DVF images.

In our project, the low threshold value can be calculated using an algorithm controlled by the standard deviation of the noise in the image. Hence the threshold value is adaptive to the noise level for the different DVF images. To calculate the low threshold $t_l$, *Bao* and his colleagues proposed the following algorithm,

$$t_l = c \cdot \sqrt{1+2\rho^2} \cdot \sigma_1 \cdot \sigma_2,$$

$$\rho = \sqrt{\frac{2^3 s_1^3 s_2^3}{(s_1^2 + s_2^2)^3}},$$

$$\sigma_1 = \sqrt[4]{\frac{\pi}{4s_1^2}} \cdot \sigma \text{ and } \sigma_2 = \sqrt[4]{\frac{\pi}{4s_2^2}} \cdot \sigma;$$

where $c$ is a constant, $s_i$ *(i=1,2)* is the scale value, and $\sigma$ is the standard deviation of the noise in DVF images. To estimate the standard deviation of the noise in the DVF image, we expanded the DVF images in the $x$-direction in the way shown in Figure 5-13(a), and then we have the 1-D signal which is shown in Figure 5-13(b). By analyzing the power spectral density (PSD) of this signal, we can learn about the cut-off frequency of the

signal of interest. Then we can design a high-pass filter to estimate the noise distribution in the $x$-direction and calculate the standard deviation $\sigma_x$. For example, the PSD of the noise in the $x$-direction is shown in Figure 5-14(a) and the probability density function (pdf) is plotted in Figure 5-14(b). Similarly, we estimate the noise distribution of the noise in the $y$-direction and calculate $\sigma_y$. The corresponding PSD and pdf are shown in Figure 5-14(c) and (d) respectively. Denote the threshold in the $x$-direction as $t_l^x$ and in the y-direction as $t_l^y$, then the threshold for the 2-D image is set to be $t_l = \frac{t_l^x + t_l^y}{2}$.

Furthermore, in order to eliminate the erroneous edges generated by the DVF system, a high threshold $t_h$ is applied. Because these system-generated edges have similar values, an identical threshold can be applied to all DVF images. By analyzing the histogram of the gradient image after wavelet filtering, the high threshold value can be selected. Finally the edges belonging to the range $[t_l,t_h]$ are treated as the edge of interest and the other edges are discarded.

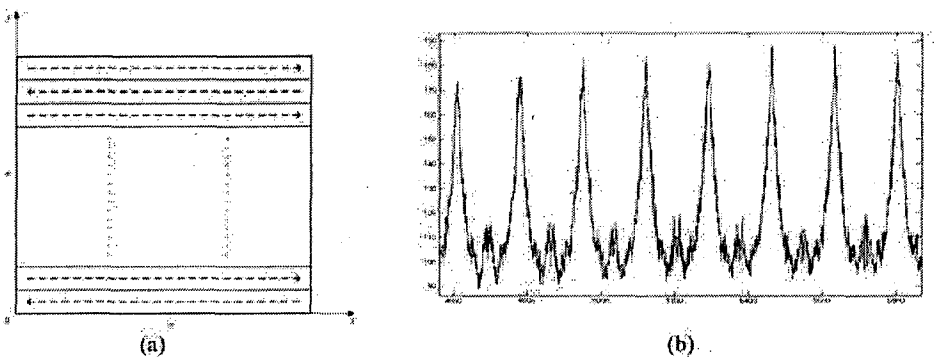


**Figure 5-13** The illustration of a 2-D image in 1-D. (a) The expanding of a 2-D image to a 1-D signal in the $x$-direction. (b) A part of the 1-D DVF image signal.

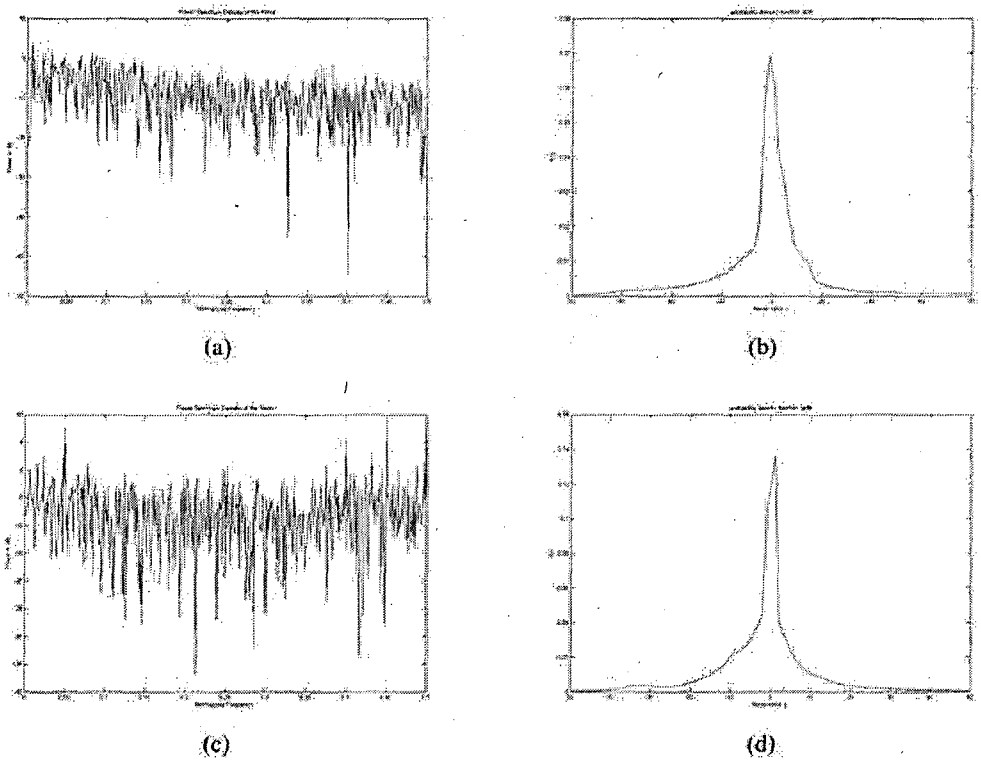


**Figure 5-14** The PSD and pdf of the noise of the DVF image. (a) The noise PSD in the *x*-direction. (b) The noise pdf in the *x*-direction. (c) The noise PSD in the *y*-direction. (b) The noise pdf in the *y*-direction.

## 5.5 Experimental Results

We applied the Mallat wavelet for edge detection with the small scale $s_1$ equal to $2^1$, and the large scale $s_2$ to $2^2$. Hence we have the two Mallat wavelets $\psi_{s_1=2}(x)$ and $\psi_{s_2=4}(x)$, which are written as:

$$\psi_{s_1=2}(x)=\frac{1}{2^8}\begin{cases}0 & |x|\geq 8\\ -(x-8)^2 & 4\leq x\leq 8\\ 3x^2-16x & 0\leq x\leq 4\\ -3x^2-16x & -4\leq x\leq 0\\ (x+8)^2 & -8\leq x\leq -4\end{cases}$$

$$\psi_{s_2=4}(x)=\frac{1}{2^{11}}\begin{cases}0 & |x|\geq 16\\ -(x-16)^2 & 8\leq x\leq 16\\ 3x^2-32x & 0\leq x\leq 8\\ -3x^2-32x & -8\leq x\leq 0\\ (x+16)^2 & -16\leq x\leq -8.\end{cases}$$

From section 5.4.3, when discretizing the Mallat wavelets to FIR filters, the length of the FIR filter is decided based upon $l_i=2^{i+2}-2\ \ (i=1,2)$. So finally, the discrete Mallat wavelet FIR filter can be written as:

$$f_1=\psi_{s_1=2}(x=\pm 2,\pm 4,\pm 6)=[0.0156,0.0625,0.0781,-0.0781,-0.0625,-0.0156],$$

$$f_2=\psi_{s_2=4}(x=\pm 2,\pm 4,\pm 6,\pm 8,\pm 10,\pm 12,\pm 14)=[0.0020,0.0078,0.0176,0.0313,0.0410,$$
$$0.0391,0.0254,-0.0254,-0.0391,-0.0410,-0.0313,-0.0176,-0.0078,-0.0020].$$

We filter DVF images using these two discrete Mallat wavelet FIR filters respectively and then multiply them together. The pixel shift caused by FIR filtering in both horizontal and vertical directions is considered, and then we shift the filtered image in the inverse direction to avoid the error in edge position so that the vertebral contour can be

detected at the correct location. A detection result after thresholding is shown in Figure 5-15, from which it can be seen that the result shows the clear lumbar vertebrae edges in the correct locations. This is an example of a DVF image taken from the lateral side. Another example using an anterior-posterior view is shown in Figure 5-16. Both of these results are achieved under the same parameter settings.

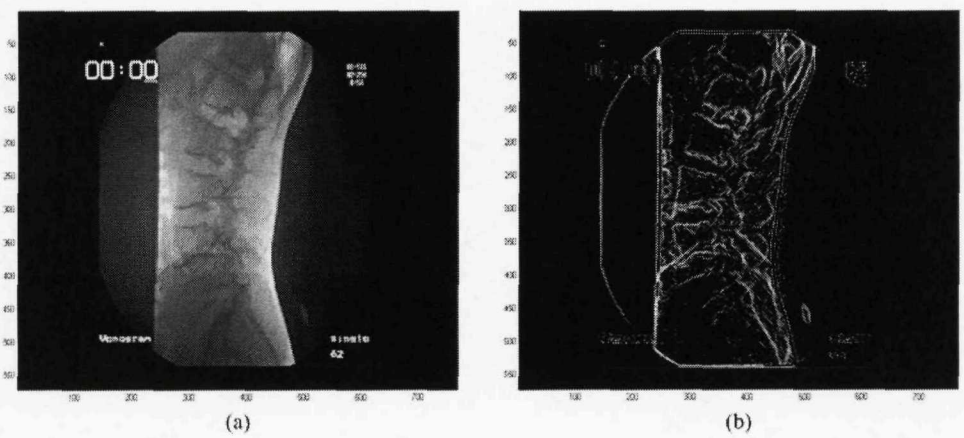

**Figure 5-15** The wavelet scale multiplication edge detection of the lateral view. (a) An original lateral DVF image. (b) Edge detection by the scale multiplication method.

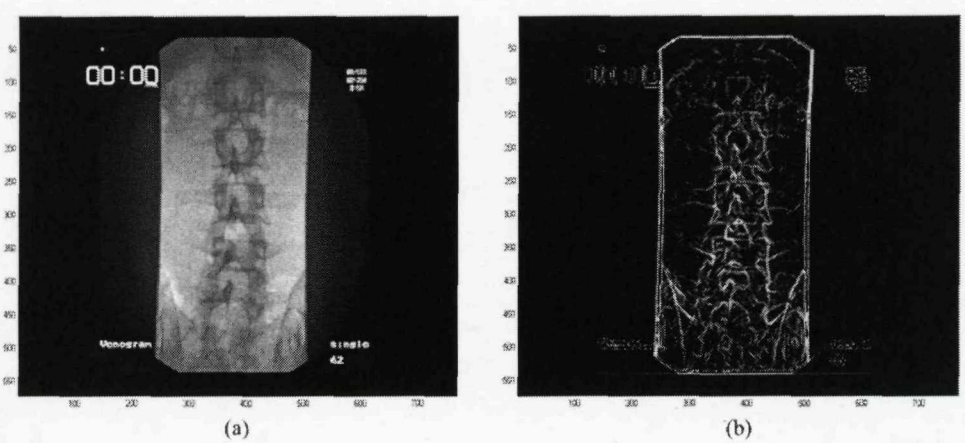

**Figure 5-16** The wavelet scale multiplication edge detection of the posterior view. (a) An original posterior DVF image. (b) Edge detection by the scale multiplication method.

To conduct the initial test prior to real data and measure the precision of this method, a calibration model (Breen,A. et al. 1988) has been introduced. The model is shown in Figure 5-17 and consists of two human lumbar vertebrae (L3 and L4) hinged at the disc centrum by a universal joint. A computerized numerically controlled machine was used to accurately locate the angular positions in 2-D. The step change in the rotation angle is 5° and the useable range is 30°.

Figure 5-18 shows DVF images of the calibration model at rotation angles from -20° to 10°. The definition of rotation angle has been given in Section 2.3.3. Vertebra L4 remains stationary while the vertebra L3 is rotated. The edge detection results of Figure 5-18 is shown in Figure 5-19 and indicate the clarity of spine vertebral edges. The rotation angles were then calculated (based on the definition of rotation angle discussed in Section 2.3.3) to examine the accuracy of the scale multiplication approach. From Table 5-1, it can be seen that the rotation angles are observed with considerable accuracy, which is well within the limits that would be necessary for clinical application. However, in this case, the distorting effects of soft tissues were not included. So the quality of these images is better than the real DVF images and the better detection results are therefore expected.

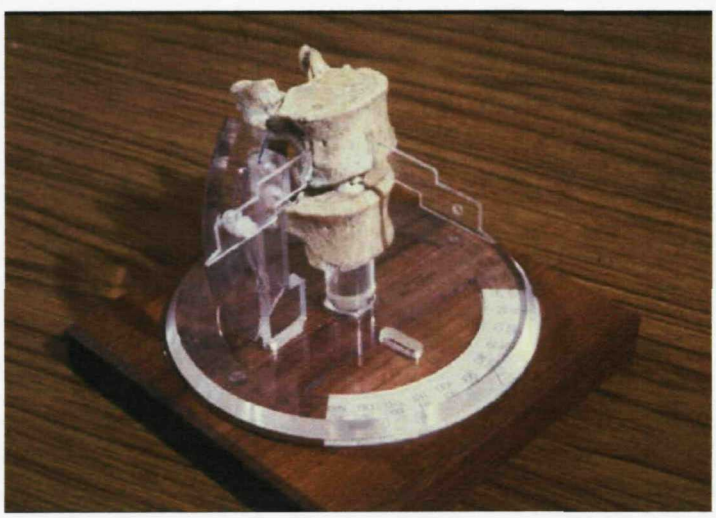

**Figure 5-17** The calibration model.

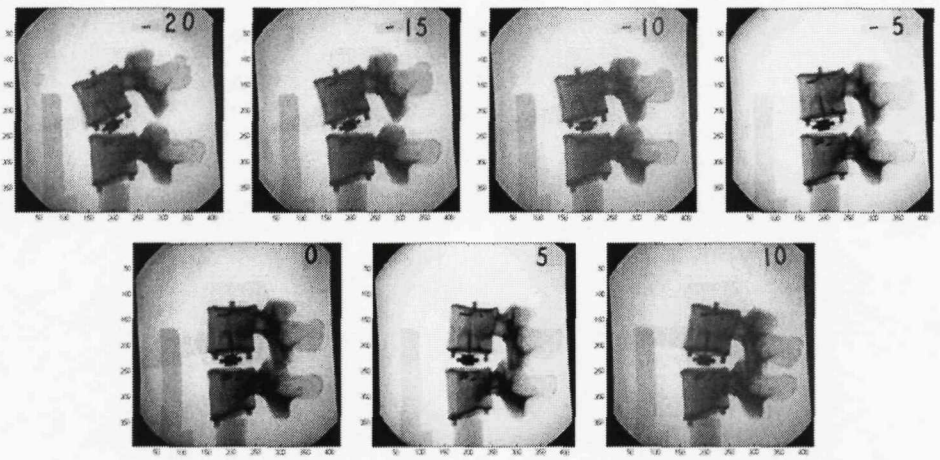


**Figure 5-18** The calibration model with changes in inter-vertebral angle.

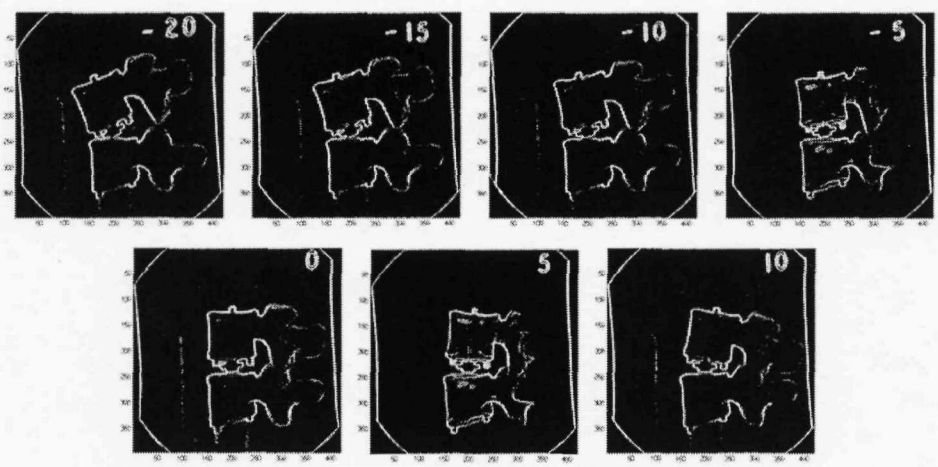


**Figure 5-19** The detection results of the edges of the calibration model.

We then attempted to track the vertebral position and measure the changes of rotation and intervertebral angles over the spinal vertebrae motion sequence. The tracking for this study was carried out by manual landmarking the corner positions for every vertebra in each frame after the wavelet multiplication edge detector was applied. An example of the manual landmarking process is shown in Figure 5-20 and vertebral corners are marked as the yellow points in the figure. After the four corners of the lumbar vertebra are located,

the midplane of the vertebra body can be obtained. Recall the section 2.3.3, the angle between the midplane and the horizontal reference line is defined as the rotation angle and the angle between two adjacent vertebrae is defined as the intervertebral angle. In computation of the intervertebral angle, midplanes of the two adjacent vertebrae are obtained first. After that, the angle between two midplanes is measured to get the intervertebral angle.

In the measurement of rotation angles, we set the starting frame as the initial neutral position of the motion sequence and normalize to zero. The measurements can then be expressed as changes relative to this starting position. An example of the rotation angle of the spinal vertebrae for a spine motion sequence is shown in Figure 5-21. In the motion sequence, each flexion/extension begins from the initial neutral position. The subjects proceed to full flexion and are then taken into full extension using the articulating table. Moreover, the relative movement of one vertebra and its neighbour is also studied because the movement of the vertebrae in the image sequence is not fixed to a reference point. Figure 5-22 shows the changes of the intervertebral angles of the spine movement in Figure 5-21. Only the lateral rotation images are shown here since the spinal motion of the subjects is side bending in this case.

**Table 5-1** The results of the rotation of the calibration model.

| L3 | | |
|---|---|---|
| Presented Angle (degree) | Results of the scale multiplication (degree) | Error (degree) |
| -20 | -21 | 1 |
| -15 | -16 | 1 |
| -10 | -10 | 0 |
| -5 | -5 | 0 |
| 0 | 0 | 0 |
| 5 | 4 | 1 |
| 10 | 9 | 1 |

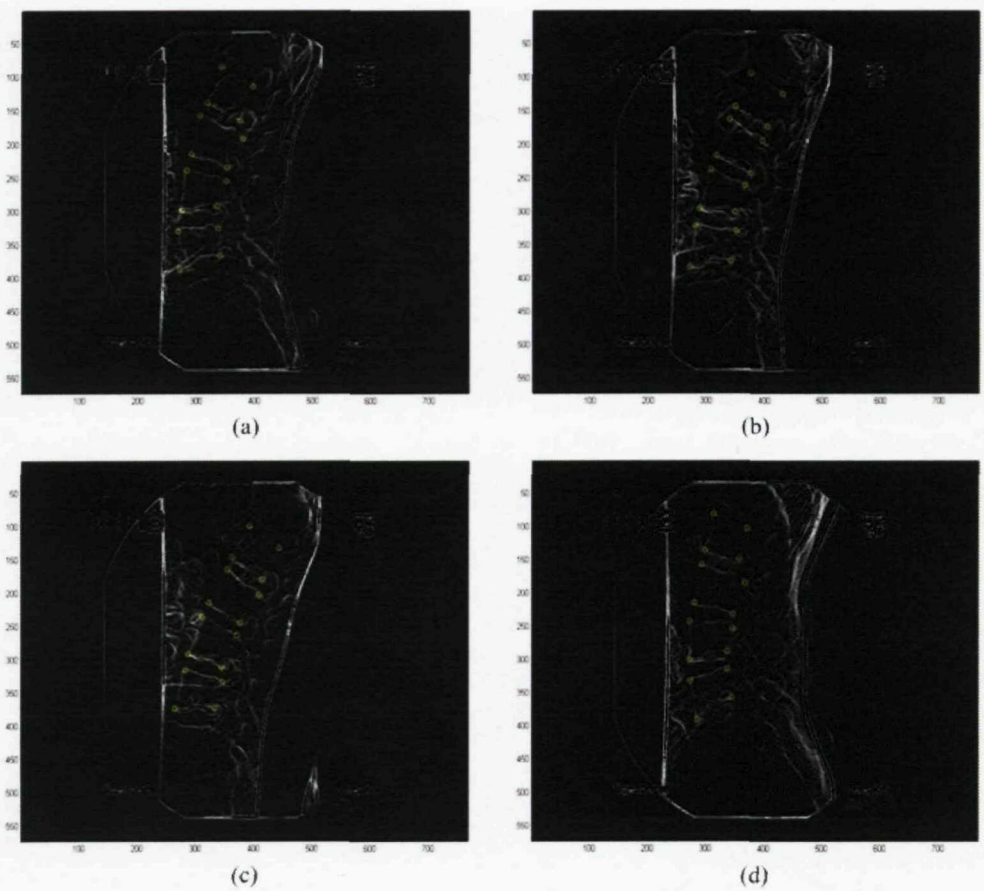


**Figure 5-20** An illustration of the manual landmarking process of the lateral edge maps.

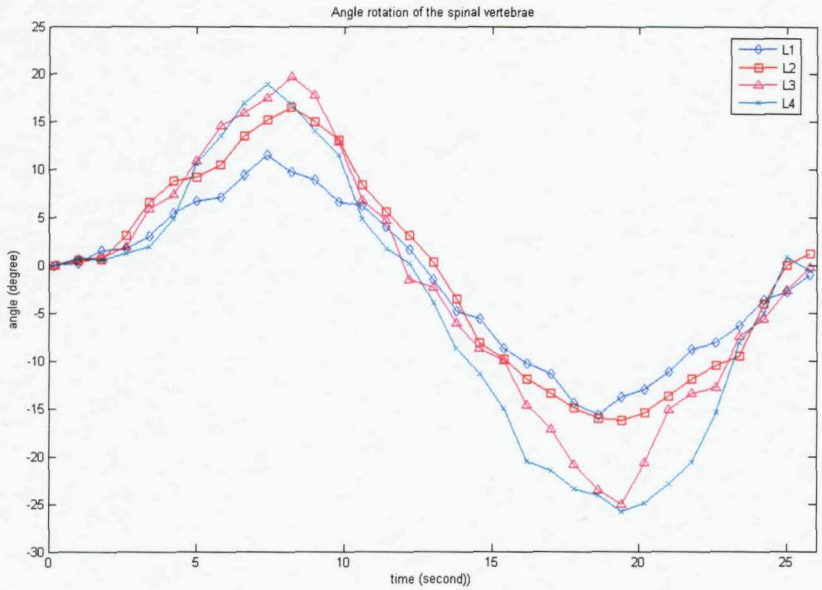


**Figure 5-21** The lateral angle of rotation of the spinal vertebrae in the spine flexion/extension.

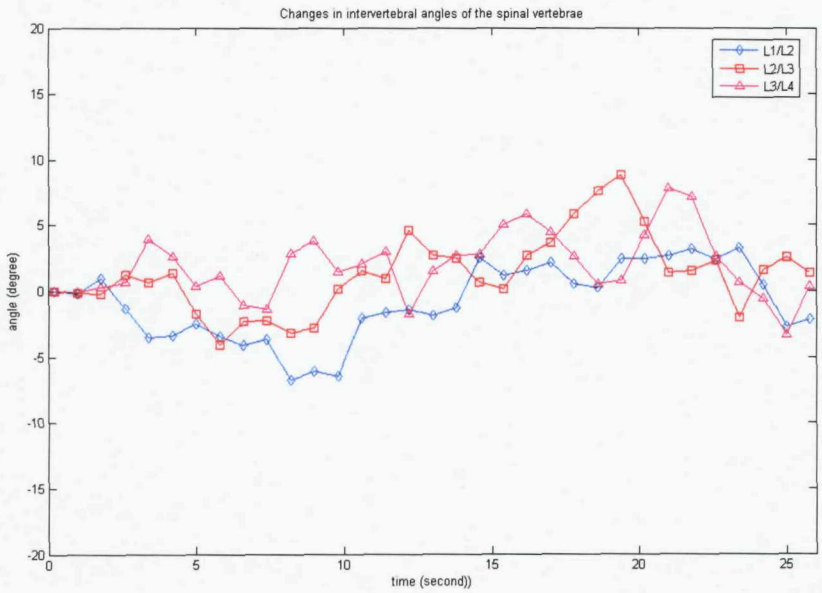


**Figure 5-22** The changes in the lateral intervertebral angles of the spinal vertebrae in the spine flexion/extension.

## 5.6 Discussions

Detection of the lumbar spine edges is the most difficult part of the motion analysis, primarily due to the low contrast and large amount of noise in DVF images. Conventional edge detection approaches, such as the Canny edge detector or phase congruency, cannot adequately extract the vertebral shapes from poor quality DVF images for the automated tracking of the spine movement (Zheng,Y. 2002). Therefore, the wavelet multi-scale product edge detector was developed for detection of the true edges from the noisy background. The main peaks in the wavelet multi-scale product are used to locate the correct vertebral shapes. The experimental results from the calibration model images show that the calculated rotation angles are very close to the pre-set values and the error is in the range of 0° to 1°. It is much better than that established in some similar studies where an average error of from 4° to 10° was reported (Tezmol,A. et al. 2002; Wong,S.F. et al. 2004). The standard error $s_{\bar{d}}$ is 0.28 according the following calculation equation

$$s_{\bar{d}} = \frac{s_d}{\sqrt{N}} = \frac{\sqrt{\frac{\sum_{i=1}^{N}(x_i - \hat{x}_i)^2}{N-1}}}{\sqrt{N}}, \qquad \text{Equation 5.1}$$

where $s_d$ is the sample standard deviation, $N$ is the number of the frames in the DVF sequence, $x_i$ is the calculated result and $\hat{x}_i$ is the pre-set value. Furthermore, the experimental results from the human DVF image sequence from the lateral bending motion shows the expected approximately sinusoidal motion pattern and it can be seen that L4 has the most significant changes in the rotation angle while L1 has the least changes. This is because the subjects lay on the passive motion table (PMT), have their upper body fixed on the articulating table and their lower body bends in each flexion/extension (see Section 2.2)

However, the tracking discussed above is completed manually and it is very tedious and time consuming. Moreover, inter- and intra-observer repeatability should be carried out

to assess the accuracy when using the new edge detection method and compared with previous reliability studies (Breen,A. et al. 1988; Breen,A.C. et al. 1989a). Further work is aimed at automated identification of the vertebrae and hence the kinematic analysis. A more automated tracking method has been developed based on the Hough transform algorithm and described in the next chapter.

# Chapter 6

# Generalized Hough Transform

## 6.1 Introduction

In the previous chapter, the intervertebral angle of the calibration model was calculated based on the manual landmark position of four corners of the vertebra. The changes of vertebral rotations and intervertebral angles over the spine motion were also measured by manual landmarking the corner positions for every vertebra in each frame. Although the measurement results show potential in clinical application, this measurement progress is very tedious and time consuming. Moreover, this would be compounded if inter- and intra-observer repeatability were carried out to. So a more automated method is required to track the vertebrae movement by taking the advantage of the wavelet edge detection results.

Generally speaking, extraction of the key features, such as lines, edges and curves, from images, is a key step in an image analysis procedure. The most popular technique for feature extraction is the Hough transform (HT). It was devised by Paul Hough to look for particle tracks in bubble chambers rather than shapes in images (Hough,P.V.C. 1962). In 1969, Rosenfeld found that the Hough transform, as well as the Radon transform (Deans,S.R. 1983), has the potential for curve detection (Rosenfeld,A. 1969). Subsequently, the Hough transform was applied to detecting lines in images (Duda,R.O. et al. 1972) and since then it has been developed considerably. Dana Ballard extended the classical Hough transform to identify arbitrary shapes (Ballard,D.H. 1981). This modified

Hough transform is known as the Generalized Hough transform (GHT). The GHT combines the HT with the principle of the template matching. This combination enables the HT to not only be used to detect features which can be described by equations, such as lines or circles, but also can be applied to extract arbitrary objects which are described using a model. Moreover the GHT is more efficient compared with the normal template matching methods (Stockman,G.C. et al. 1977). The Generalized Hough transform is therefore used to track the vertebrae movement in this project.

The Hough transform firstly defines a mapping from the image points into an accumulator space (or Hough space). The HT can then be achieved by reformulating the template matching process and gathering the evidence to locate the position of the peak value in the accumulator space. In the Generalized Hough transform, the problem of finding the object described using a model can be solved by detecting the reference position of the model in an image. When the location of the reference point is known, the object can be extracted using a reference table (see the later part of this chapter for detail). In this chapter, a review of the Hough transform is conducted briefly and the Generalized Hough transform is then described in more detail. Based on the wavelet edge detection results, the experimental results in which the GHT has been applied to the calibration model data are presented. The measurements have yielded promising results. Finally, the GHT is applied to wavelet edge detection maps of real DVF image sequences and the extraction results are analysed and reported.

## 6.2 The Hough Transform

### 6.2.1 The Hough transform for Lines

The basic function of the Hough transform is to find lines in an image. A straight line can be expressed as $y=mx+c$ in the Cartesian parameterisation, where $(x,y)$ are the co-ordinates of a point on the line, $m$ is the slope of the line and $c$ is the intercept on the $y$ axis. Thus, a line can be defined by a pair of parameters $(m,c)$ since all the points on the line have the same value of the parameter set, such as $(x_i,y_i)$ and $(x_j,y_j)$, which is shown in Figure 6-1(a). We can also re-write the equation of a line in the slope-intercept form as $c=-mx+y$. This equation shows that each point $(x,y)$ corresponds to a line in the $(m,c)$ space. In Figure 6-1(b), the $mc$-space yields the equation of a single line for the point $(x_i,y_i)$. Moreover, the other point $(x_j,y_j)$ also has a line in the $mc$-space and these two lines intersect at a point $(m_0,c_0)$. Here, $m_0$ is the slope and $c_0$ is the intercept of the line containing both $(x_i,y_i)$ and $(x_j,y_j)$ in the $xy$-space. Actually, all points contained on this line have lines in the $mc$-space that intersect at $(m_0,c_0)$. As a result, the line can be extracted by finding this point in the $mc$-space.

In the computation of the Hough transform, the $mc$-space is called the accumulator space or Hough space. The accumulator space is divided into so-called accumulator cells, which is illustrated in Figure 6-2, where $(m_{min},m_{max})$ and $(c_{min},c_{max})$ are the expected ranges of the slope and intercept values. Each cell at co-ordinate $(i,j)$ corresponds to an accumulator value $A_{(i,j)}$ and these cells are initially set to zero. Then, for every point $(x,y)$ in the image, the parameter $m$ is set to equal to each of the allowed subdivision values on the $m$-axis and then the corresponding $c$ can be calculated using the equation $c=-mx+y$. After that, the results are rounded to the nearest allowed value in the $c$-axis. When a choice of $m$ results in a solution of $c$, $A_{(i,j)}$ is replaced by $A_{(i,j)}+1$. At the end of this procedure, a value in $A_{(i,j)}$ represents the number of points lying on the line $y=mx+c$ in the

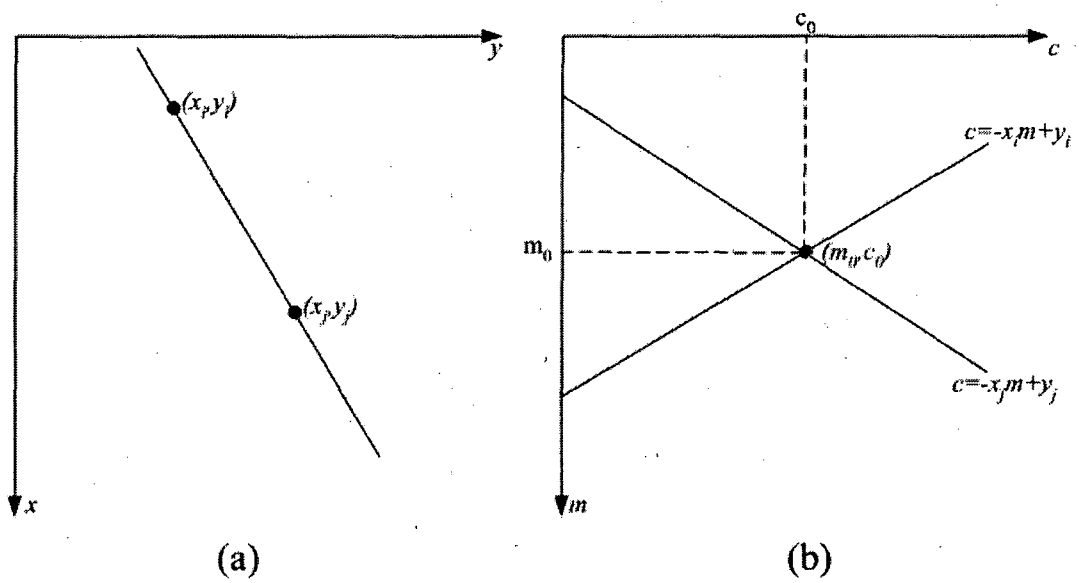


**Figure 6-1** An illustration of the line extraction. (a) A line in the *xy*-space. (b) Lines in the *mc*-space.

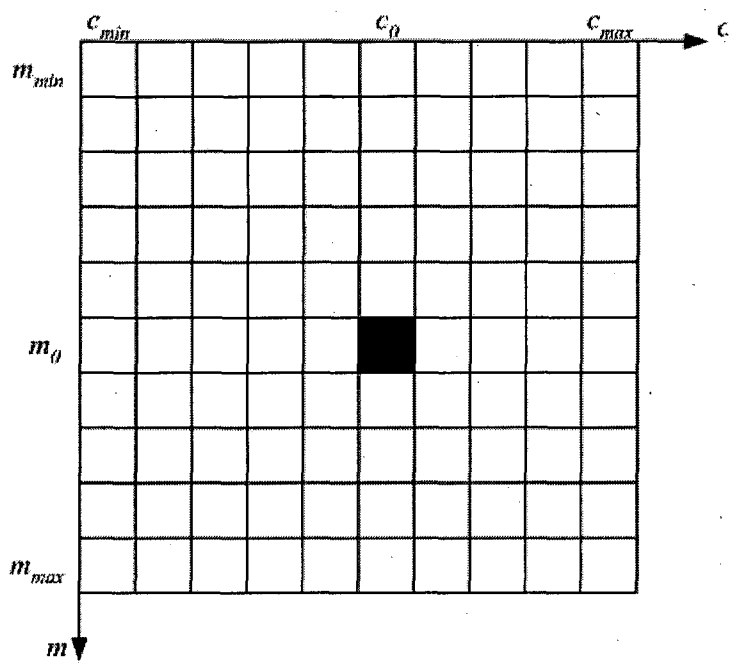


**Figure 6-2** Subdivision of the accumulator space for use in the Hough transform

*xy*-space. The peak value in the accumulator space provides the strong evidence that a corresponding straight line exists in the searched image.

A problem with using the Cartesian parameterisation is that the slope $m$ may approach to infinity when the straight line becomes more and more vertical. In that case, it is impractical to describe the line in the Cartesian parameterisation. This problem was solved by using polar parameterisation. In polar parameterisation, a line is represented as $\rho=x\cos\theta+y\sin\theta$, where $\theta$ is the angle of the line normal to the line in an image and $\rho$ is the length between the origin and the point where the lines intersect, as illustrated in Figure 6-3(a). Thus, by considering the geometry of the arrangement in Figure 6-3(a), $c=\frac{\rho}{\sin\theta}$ and $m=\tan\varphi=-\frac{1}{\tan\theta}$ can be obtained. Figure 6-3(b) shows the subdivision of the accumulator space. The basic idea of constructing the accumulator cells is identical to the method discussed for the slope-intercept representation. However, the *mc*-space is replaced by the $\theta\rho$-space and the polar representation yields sinusoidal curves in the $\theta\rho$-space. Based on the polar representation, $\theta$ can be defined in the range between -90° to 90°.

Figure 6-4 shows two simulation examples of locating lines using the polar Hough transform. In Figure 6-4(a), there is a single line which generates the peak shown in Figure 6-4(c). The magnitude of the peak is proportional to the number of pixels in the line from which it was generated. Figure 6-4(b) contains an image of a line with salt and pepper noise added with a noise density of 0.5. The detection result is illustrated in Figure 6-4(d), in which the peak value is still detected despite of the occurrence of the interference. These two simulation examples indicate that the HT is able to deliver a correct response to extract the line, as long as the number of co-linear points along the line exceeds the number of the other pixels in the image.

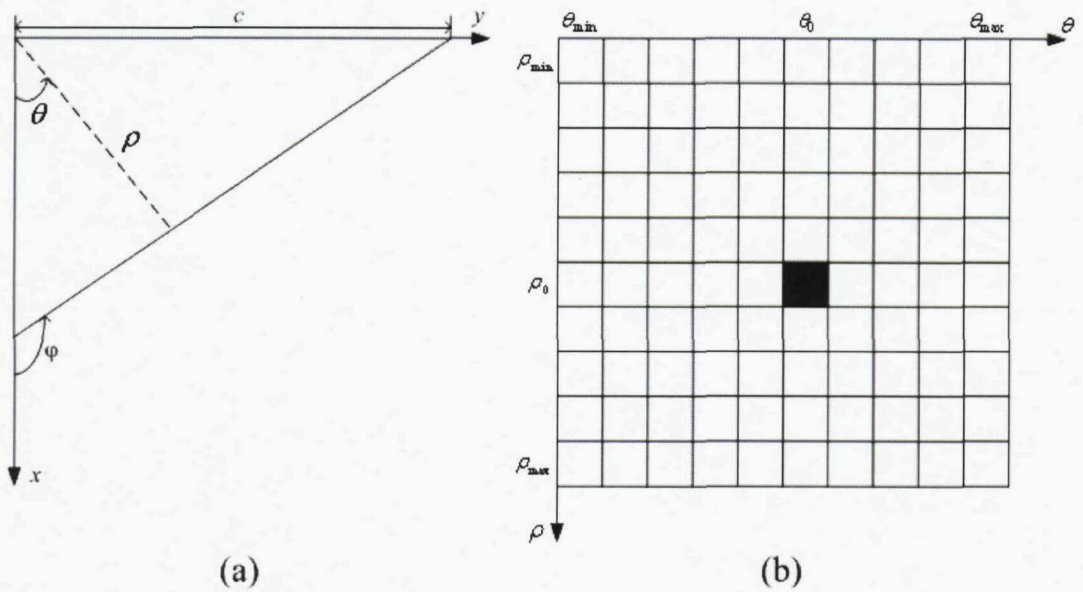


**Figure 6-3** Polar parameterization of a line. (a) Polar definition of a line. (b) Subdivision of the $\theta\rho$-space into cells.

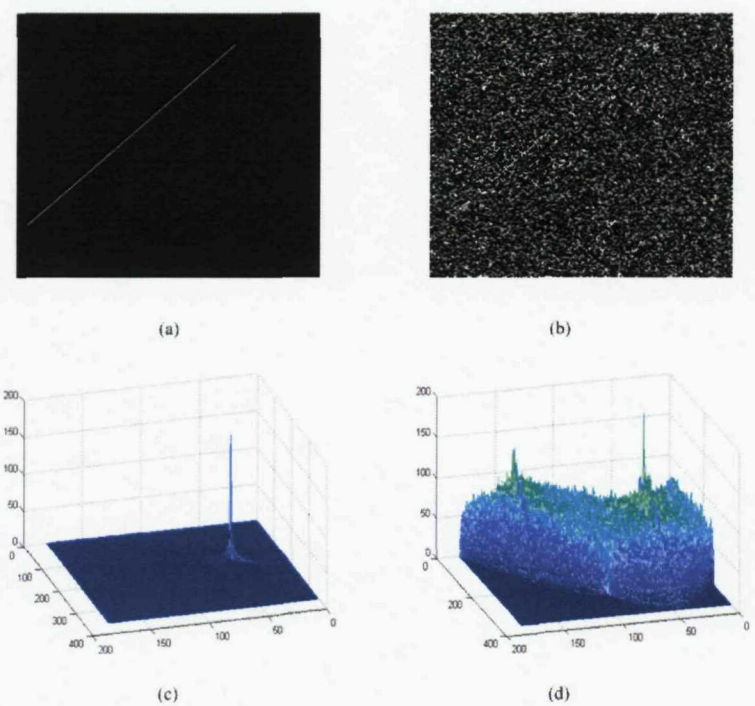


**Figure 6-4** Implementation of the polar Hough transform to detect a line.

### 6.2.2 The Hough transform for circles and ellipses

The idea of the HT can be extended to the application of other analytical shapes, such as circles and ellipses. The implementation for circle extraction is realized by modifying the representation functions to $(x-x_0)^2+(y-y_0)^2=r^2$, where $(x_0,y_0)$ is the origin and $r$ is the radius. Because this representation has three parameters, two for the centre of the circle and the other one for the radius of the circle, a three-dimensional accumulator space $(x_0,y_0,r)$ is needed in extraction. Furthermore, this three-dimensional accumulator space can be reduced to a two-dimensional space by using the polar definition for circles. In polar representation, the co-ordinates of a point on a circle can be written as $\begin{cases} x = x_0 + r\cos\theta \\ y = y_0 + r\sin\theta \end{cases}$, and the centre of the circle can then be defined as $\begin{cases} x_0 = x - r\cos\theta \\ y_0 = y - r\sin\theta \end{cases}$. Therefore, circles can be extracted from images by locating their centre points by trying every possible parameter combination of $\theta$ and $r$ for each point in images.

Circle extraction is crucial in shape detection since many objects have a circular shape. However, circles are usually deformed to ellipses due to several reasons, such as the viewpoint of the camera. Based on the definition of an ellipse $\frac{(x-x_0)^2}{a^2}+\frac{(y-y_0)^2}{b^2}=1$, a four-dimensional accumulator space $(x_0,y_0,a,b)$ is needed. Aguado and his colleagues represented the ellipse in a different way by using the differentiable vector-valued function (Aguado,A.S. et al. 1996b). In their definition, an ellipse can be written as $z(\theta)=xU_x+yU_y$ for $U_x=[1,0]$, $U_y=[0,1]$ and $\begin{cases} x = x_0 + a_x\cos\theta + b_x\sin\theta \\ y = y_0 + a_y\cos\theta + b_y\sin\theta \end{cases}$. This equation corresponds to the polar representation of an ellipse. It contains six parameters $(x_0,y_0,a_x,b_x,a_y,b_y)$ that build the shape of ellipse. Here $\theta$ is not a free parameter but only a position index in a reference table. Moreover, because $a_xb_x+a_yb_y=0$ is one of the well-known properties of an ellipse, an ellipse can be extracted by finding its centre point $(x_0,y_0)$ in a three-dimensional accumulator space, which can be written as

$$\begin{cases} x_0 = x - a_x \cos\theta - b_x \sin\theta \\ y_0 = y - a_y \cos\theta - b_y \sin\theta. \end{cases}$$

From the discussion above, it can be seen that the complexity of determining the maximal vote increases with the increase of the dimensionality needed to extract the shape of interest.

## 6.3 The Generalized Hough transform

### 6.3.1 Overview

In the Hough transform for circles and ellipses, the polar representation is used to reduce the dimensionality of the accumulator space. Moreover, it introduces the idea that every point on the features of interest can be represented as a parameter set $(r,\theta)$ based on a reference point, such as the centre point in the above examples. Here, $r$ is the distance between the reference point and the point lying on the feature curve and $\theta$ is the angle between these two points. As a result, this representation can be used to describe arbitrary shapes without an analytical expression. The method to extract arbitrary shapes with unknown position, size and orientation was firstly introduced by (Merlin,P.M. et al. 1975) and was finally developed into a full template mapping approach, called the Generalized Hough transform by (Ballard,D.H. 1981). Furthermore, some researchers have extended the Hough transform to extract shapes in three-dimensional (3-D) space (Bhattacharya,P. et al. 2000; Hu,G. 1995).

To improve the performance of the Hough transform, some researchers have tried to improve its computational efficiency since it requires much storage and computation time

with the increase in the complexity of the features of interest. The fast Hough transform (Guil,N. et al. 1995; Li,H.W. et al. 1986) and the adaptive Hough transform (Cao,X. et al. 1988; Chau,C.P. et al. 2004; Ecabert,O. et al. 2004) are widely used to reduce storage and computation time to locate an object in images. Alternatively, some researchers have tried to improve the performance by using a better description of the contour of the object. In this way, for example, the Fourier descriptor was introduced (Kuhl,F.P. et al. 1982; Persoon,E. et al. 1986; Staib,L.H. et al. 1992) and was applied in object identification with the Hough transform technique (Aguado,A.S. et al. 1996a; Aguado,A.S. et al. 1998; Yuen,S.Y. et al. 1997).

Simultaneously, a different idea was proposed to save storage and computation time in the Hough transform. It is called the randomized Hough transform (RHT) (Xu,L. et al. 1990; Xu,L. et al. 1993). In the RHT, instead of taking every single point in an image, this algorithm only picks up a randomly chosen sample set of input points. The evidence vote stops when the peak value of the accumulator space is greater than a pre-defined threshold value. The randomized Hough transform is widely used in the extraction of lines, circles and ellipses (Basca,C.A. et al. 2005; Chen,T.C. et al. 2001; Cheng,Z. et al. 2004; Mao,J. et al. 2006; McLaughlin,R.A. 1996; McLaughlin,R.A. 1998; Yao,J. et al. 2004). Moreover, it can be applied in the detection of the arbitrary shapes (Fung,P.F. et al. 1996), motion (Kalviainen,H. et al. 1992; Kalviainen,H. 1996) and in medical image processing (Behrens,T. et al. 2003; Lu,W. et al. 2005). However, the disadvantage of the inversed RHT cannot be completed since lots of information is lost during the transform. It is also difficult to set an appropriate thresholding value. Therefore, the randomized Hough transform is not used in this project.

Here the Generalized Hough transform is selected to track the vertebral movement. The GHT has been widely applied in motion extraction (Grant,M.G. et al. 2002; Li,H.L. et al. 1996; Montret,L. et al. 1994; Ulrich,M. et al. 2003) because of its properties of invariance to translation and robustness to occlusion. Furthermore, the Generalized Hough transform

and its modified extensions have been applied to detect features in medical images in both good quality images (Brejl,M. et al. 2000; Zana,F. et al. 1999) and poor quality images (Kobatake,H. et al. 1996; Scales,N. et al. 2004). In particular, a GHT based approach has been used to locate rib borders in posterior chest radiographs (Yue,Z.J. et al. 1995). In this approach, a knowledge based GHT finds the approximate location of the rib borders after pre-determining the thoracic cage boundary to restrict the searching area. This pre-processing is able to improve the accuracy and reduce computation time. Because the GHT can only find the approximate locations of the ribs, the active contour method (Kass,M. et al. 1988) was used to finally locate the rib borders. The accuracy of this approach was tested by comparing the detection results with those made by the experienced radiologist. Another modified GHT method, called the Customized Hough transform, was developed to locate the cervical vertebrae in X-ray images (Tezmol,A. et al. 2002). In this method a template was obtained by averaging 50 manually landmarked lateral cervical X-rays images. With the template image, the Customized Hough transform was able to identify the cervical vertebrae and measure the variations of the cervical vertebral shapes. However, the reported orientation error was 4.16° on average which indicated that the accuracy was not good enough for spine biomechanical studies in our project because the maximum rotation angle is about 30°. A much more accurate result was obtained in locating the position of the lumbar spine vertebrae in DVF image sequences (Zheng,Y. et al. 2003; Zheng,Y.L. et al. 2004). In their methods, binary template edge information was acquired by using manual landmarking of the edge detection results obtained from using the Sobel edge detector or phase congruency. The Fourier descriptor was then used to describe the edge template mathematically. Finally, the GHT was applied to track the lumbar spine motion and the measured accuracy was much better than that established by (Tezmol,A. et al. 2002). However, manual landmarking and isolating each vertebra are required in their methods and approximately five minutes is needed to extract vertebrae in one DVF frame, so it is very time consuming to process about 150 frames in a typical DVF sequence.

In summary, the Generalized Hough transform is powerful in object identification and motion tracking. Moreover, the GHT shows great potential to detect the shapes of interest in the medical images, even in some poor quality images, such as in a mammogram or DVF images. However, it has problems such as manual landmarking, unacceptable errors and is time consuming. Since better edge information is obtained by using the wavelet based edge detector in this project, a promising tracking result is expected after applying the edge information directly to the generalized Hough transform.

### 6.3.2 Description of the Algorithm

The first problem in the Generalized Hough transform is how to determine the position of an arbitrary object in an image. For a known 2-D object with a closed contour, its reference point is usually defined as the centre of mass, like $O$ in Figure 6-5(a). Thus, given an edge point $A$ in the image, it can belong to an infinite number of different contours of the object, for example, some contours without considering rotation and scaling are shown in Figure 6-5(b) and there is a possible centre $O_i$ for each possible contour. By repeating this procedure until all possible contours are considered, the most likely position of the reference point of the translated object can be obtained by locating the maximal number of votes in the accumulator space, shown in Figure 6-5(c). Moreover, if rotation and scaling are considered, shown in Figure 6-5(d), the evidence gathering procedure in the Generalized Hough transform can be extended to more complex problems. This means that more parameters are needed to be considered and more dimensions are needed for the accumulator space.

After locating the reference point of the arbitrary object, a reference table, which is called the R-Table, was introduced to describe the arbitrary contour in the generalized Hough transform. From the discussion in Section 6.2.2, any point on a given 2-D arbitrary contour can be represented as a parameter set $(r,\theta)$ based on a reference point, where $r$ is the distance between the reference point and the point lying on the feature curve of

interest and $\theta$ is the angle between these two points. Moreover, the edge direction $\beta$ of this point is used to index the parameter set $(r,\theta)$. In this way, the R-Table is built by arranging the points with the same edge direction values in the same row, as shown in Figure 6-6. It should be noticed that the number of the elements in each row may be larger than one and be different since some points may have the same edge direction (e.g. Table 6-1).

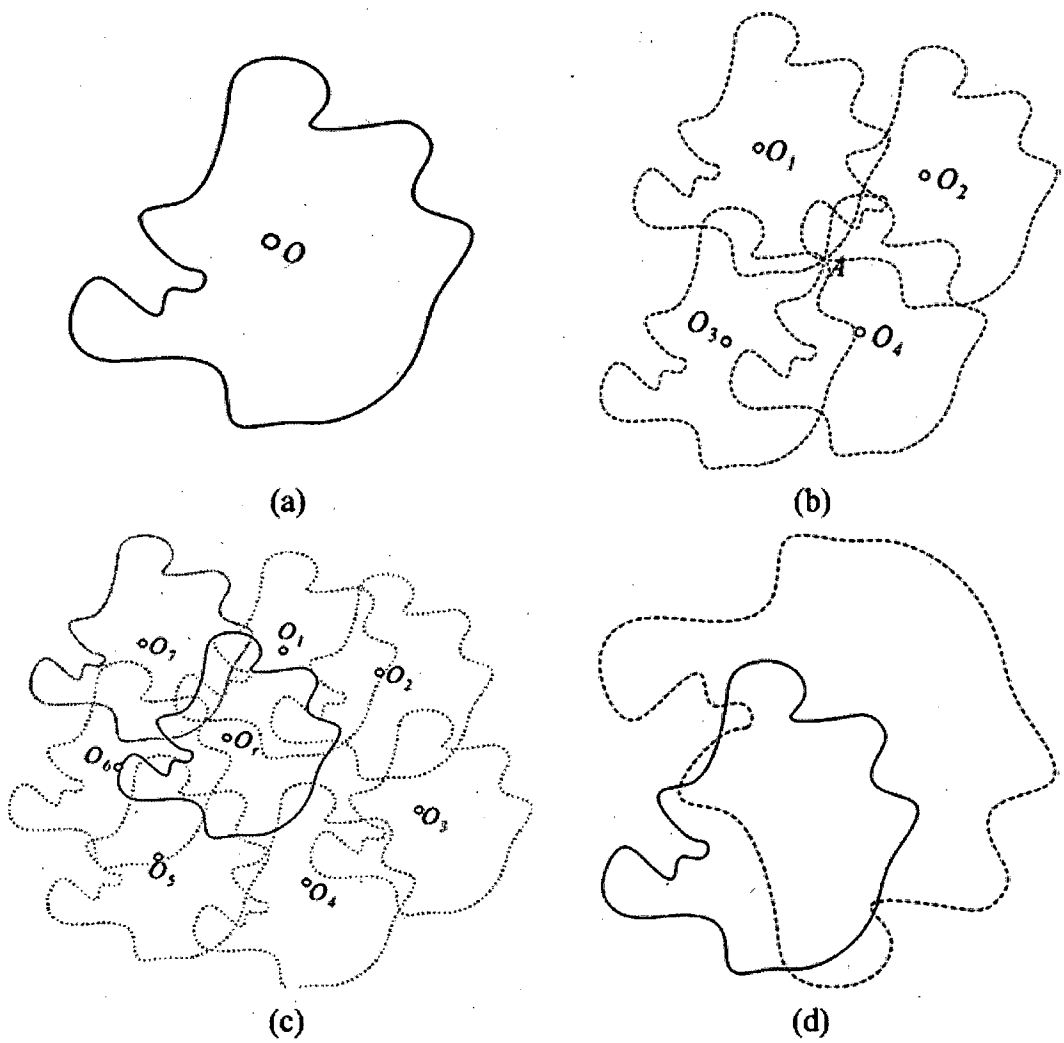


**Figure 6-5** An illustration of arbitrary shape extraction using the Generalized Hough transform. (a) An object and its reference point. (b) Some possible contours that fit edge point *A*. (c) Evidence gathering in the accumulator space. (d) The object contour and possible rotated and scaled contour.

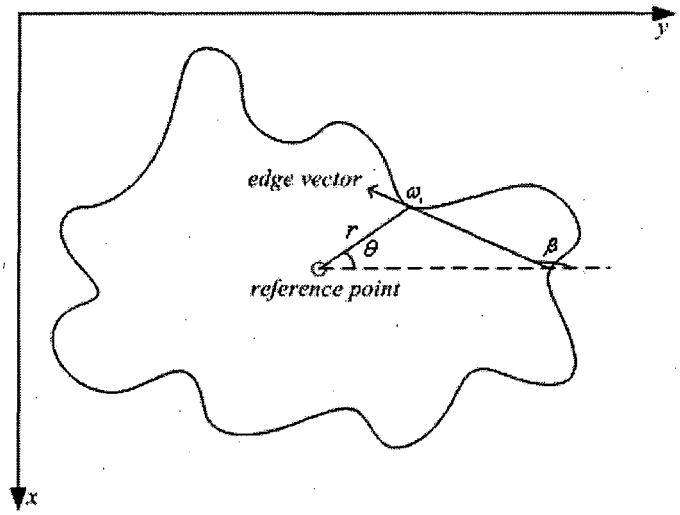


**Figure 6-6** An illustration of building the R-Table.

Thus, the shape in the image can be defined by its two components $(r,\theta')$ and the reference point in the $x$ and $y$ directions, $\begin{bmatrix} x_{curve} \\ y_{curve} \end{bmatrix} = \begin{bmatrix} x_r + sr\sin\theta' \\ y_r + sr\cos\theta' \end{bmatrix}$, where $[x_r,y_r]$ is the coordinates of the reference point, $s$ is the scale factor, $\theta'=\theta+\varphi$ and $\varphi$ is the rotation angle. In the cases of no scaling and rotation ($s$=1 and $\varphi$=0), the description of the shape is written as $\begin{bmatrix} x_{curve} \\ y_{curve} \end{bmatrix} = \begin{bmatrix} x_r + r\sin\theta \\ y_r + r\cos\theta \end{bmatrix}$, which matches the definition of the R-Table. However, when scaling and rotation happen, the shape is expressed as:

$$\begin{bmatrix} x_{curve} \\ y_{curve} \end{bmatrix} = \begin{bmatrix} x_r + sr\sin\theta' \\ y_r + sr\cos\theta' \end{bmatrix}$$
$$= \begin{bmatrix} x_r + sr\sin(\theta+\varphi) \\ y_r + sr\cos(\theta+\varphi) \end{bmatrix} = \begin{bmatrix} x_r + sr(\sin\theta\cos\varphi + \cos\theta\sin\varphi) \\ y_r + sr(\cos\theta\cos\varphi - \sin\theta\sin\varphi) \end{bmatrix}$$
$$= \begin{bmatrix} x_r \\ y_r \end{bmatrix} + s\begin{bmatrix} \cos\varphi & \sin\phi \\ -\sin\varphi & \cos\varphi \end{bmatrix}\begin{bmatrix} r\sin\theta \\ r\cos\theta \end{bmatrix}.$$

As a result, the curve depends on four parameters. Two parameters $x_r$ and $y_r$ define the new position of the reference point on the curve, which means the translations in the $x$

and $y$ directions. So the new position of the reference point on the curve can be obtained as $\begin{bmatrix} x_r \\ y_r \end{bmatrix} = \begin{bmatrix} x_{curve} \\ y_{curve} \end{bmatrix} - s \begin{bmatrix} \cos\varphi & \sin\phi \\ -\sin\varphi & \cos\varphi \end{bmatrix} \begin{bmatrix} r\sin\theta \\ r\cos\theta \end{bmatrix}$.

Moreover, the lumbar spine vertebrae are assumed to remain the same shape and have no out-of-plane motion during the whole movement, which means the scale factor $s$ is equal to 1 in our project. The assumption of absence of out-of-plane motion is reasonable for spine flexion/extension movements, but it is erroneous for spine lateral bending motion where a couple of spine axial rotation is present (White,A.A. et al. 1978). So, the new position of the reference point can finally be expressed as:

$$\begin{cases} x_r = x_{curve} - r\sin\theta\cos\varphi - r\cos\theta\sin\varphi \\ y_r = y_{curve} + r\sin\theta\sin\varphi - r\cos\theta\cos\varphi \end{cases}.$$

In our Generalized Hough transform algorithm, the R-Table is firstly built to describe the template vertebra edge obtained from the wavelet-based edge detector. Then for each edge point in the edge detected images, the parameter sets $(r,\theta)$ are checked by indexing its edge direction angle $\beta$. For every possible rotation angle $\varphi$ and each value of the parameter set $(r,\theta)$, the possible values of the $(x_r,y_r)$ are calculated and then voted for to find the peak, which represents the most likely position of the reference point on the vertebra. Moreover, because the vertebrae move in a fairly tight range during the spine motion, the possible values of the curve points and the rotation angles can be reduced to a certain range to improve the efficiency and increase the accuracy. This will be discussed later.

### 6.3.3 Applications to the Calibration Model

In the previous chapter, a calibration model (Breen,A. et al. 1988) was used to measure the precision of the wavelet-based edge detector results. However, the measurement was

carried out by manual landmarking the four corners of the vertebrae L3 and L4. In this chapter, the precision of the wavelet-based edge detector is tested again and the test is completed by using the Generalized Hough transform to locate the reference point (centre point of the template model, CTM) and then calculate the rotation angle of the vertebra L3. For the GHT, the likely rotation is from -90° to +90° and the original size of the calibration model image is 396×420. During the GHT feature extraction, the changes of unknown parameters $x_{curve}$, $y_{curve}$ and $\theta$ are limited to a small range in order to reduce the computational cost and requirement on storage. In the example of the calibration model, the range of $x_{curve}$ and $y_{curve}$ are 150 pixels (from 100 to 250) and for $\theta$ is 40° (from -25° to +15°). This limitation leads to a size of the accumulator space (Hough space) of 151×151×41, which is much smaller than the original Hough space 396×420×181.

As described in the GHT algorithm, a template was chosen first. Because the vertebra L3 moves from -20° to +10° in this case and -5° is the mean value of the rotation angles, the frame of -5° is selected as the template frame, as shown in Figure 6-7(a). A small area which contains the whole L3 is selected as the template model. After that, our wavelet multiplication edge detection method was applied to obtain the edge map of the template model. The R-Table (Table 6-1) was built based on this edge map. Every edge point in the edge map is represented as the combinations of $r$ and $\theta$ indexed by edge direction $\beta$. For some edge directions, more than one combination exist, e.g. the edge direction with 0°. The reference point was calculated and shown as a cyan circle in Figure 6-7(b). Thus, we aimed to track the reference point during the motion sequence and then calculate the rotation angle of each frame and compare the results with the pre-set results to measure the precision. Finally, in order to show the tracking results more clearly, the four vertebral corners were manual marked and are shown as the green points in Figure 6-7(b). The new positions of these four corners were also able to be tracked and displayed as the green points in the image sequence after the application of the GHT with the wavelet edge detection results.

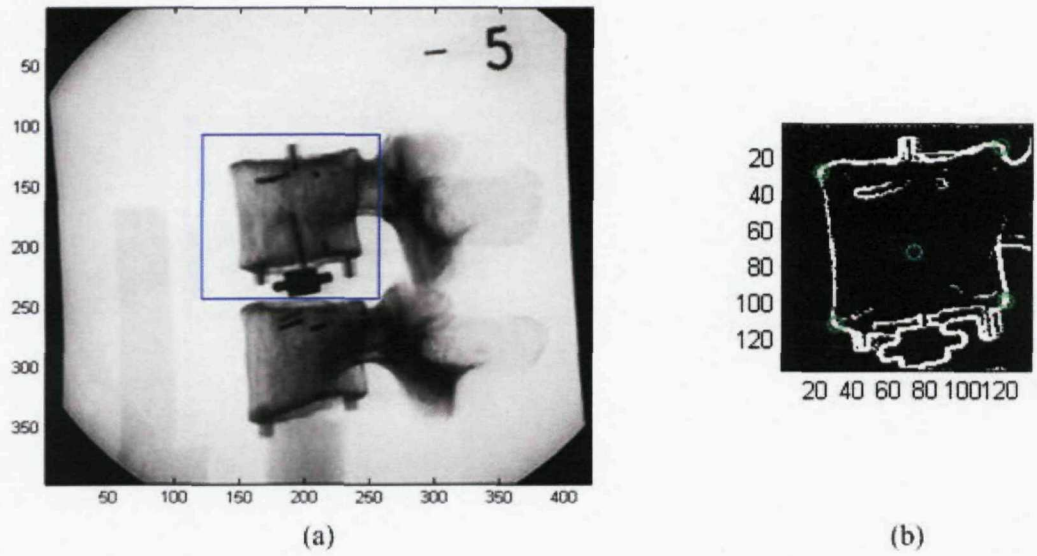


**Figure 6-7** An illustration of the template selection and extraction. (a) The template frame in which L3 rotates -5° and the selection of the template model. (b) The wavelet edge detection result of the template model and the GHT of the template model corners and center point.

**Table 6-1** The R-Table for the calibration model tracking.

| $\beta$ | $(r,\theta)$ |
|---|---|
| 0° | (85.45, 0.96), (83.22, 0.99), (82.68, 1.01), (79.18, 1.08), … , (50.45, -1.33) |
| 1° | (0, 0) |
| 2° | (0, 0) |
| … | … |
| 90° | (94.11, 0.82), (93.38, 0.81), (91.93, 0.80), (91.22, 0.79), … , (63.29 -1.48) |
| … | … |
| 180° | (94.18, 0.84), (93.51, 0.85), (91.55, 0.87), (90.27, 0.89), … , (62.01, -1.55) |

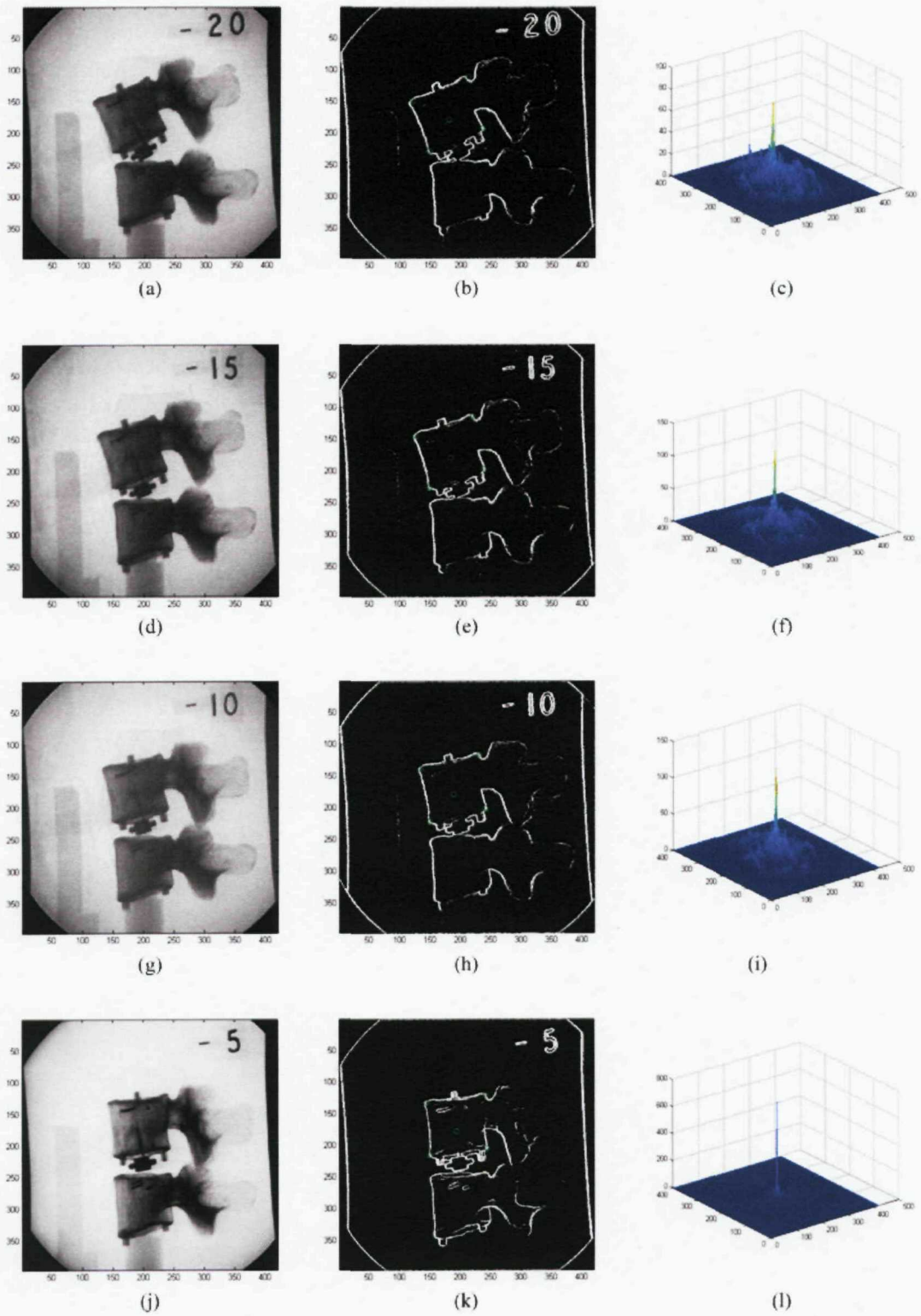


(a) (b) (c)

(d) (e) (f)

(g) (h) (i)

(j) (k) (l)

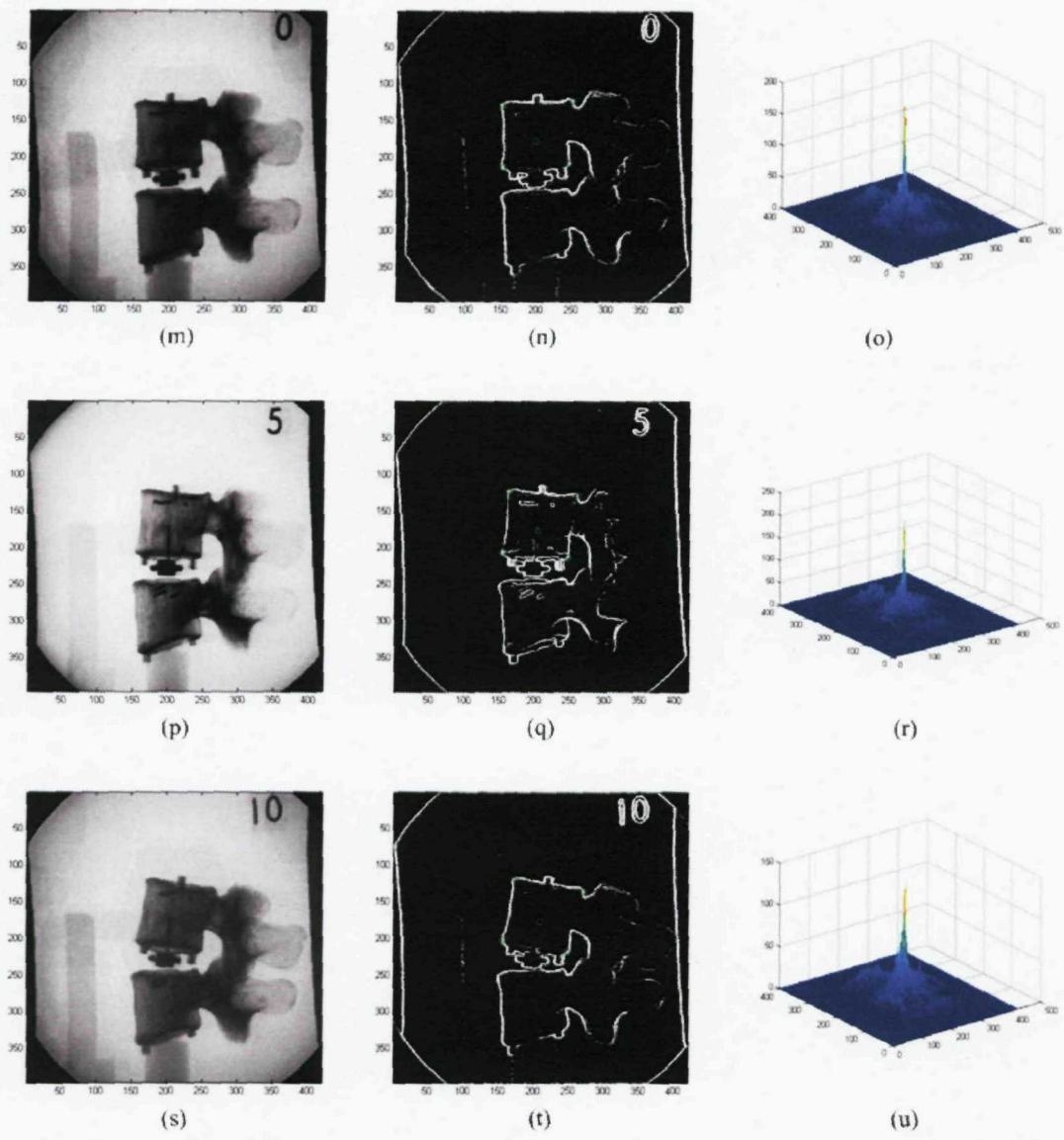


**Figure 6-8** The edge detection and tracking results of the calibration model DVF sequence.

The edge detection and tracking results are shown in Figure 6-8. The left column shows the original DVF images of the calibration model, in which the L3 was pre-set to rotate from -20° to 10°. The extraction results were superimposed on the edge detection results and illustrated in the middle column. Corresponding to the template model in Figure 6-7(b), the green point means the corner point of the vertebrae and the cyan point indicates the reference point of L3. The right-hand column shows the maps of the

accumulator space (Hough space). Table 6-2 compares the GHT extraction results with the pre-set rotation values and the previous manual landmarking results. Note that the initial angle is -5° due to the template model selection, so this should be considered when the rotation angles are finally calculated. It can be seen that the calculated rotation angles from the GHT method are very close to the pre-set values and the error is in the range of -1° to +1°. Although the accuracy of the automated tracking is very slightly worse than the manual landmarking method, it is much better than that established in a similar study where an average error of from 4° to 10° was reported (Tezmol,A. et al. 2002; Wong,S.F. et al. 2004). The standard error $s_{\bar{d}}$ is 0.345 according the standard error calculation equation, which is Equation 5.1 expressed in Section 5.5. Furthermore, the interval values for the parameters are 1° for rotation and 1 pixel for translation in this example, more accurate results are expected when a finer interval is applied. However, this will increase the computation cost and storage.

### 6.3.4 Applications to the DVF Images

After testing the accuracy of the Generalized Hough transform using the calibration model, we applied the GHT to the real DVF image sequences to analysis the lumbar spine motion. The DVF images we used here were collected from normal healthy subjects without any lumbar spine problems (Kondracki,M. 2001). Based on these image data, the normal lumbar spine movement and its several relative biomechanical parameters can be studied with the application of the GHT. However, only the tracking results will be discussed in this section and the study of the lumbar spine kinematics will be discussed in the next chapter.

**Table 6-2** The GHT extraction results compared with the pre-set values and the manual landmarking results.

| L3 | | | | |
|---|---|---|---|---|
| | The manual landmarking results | | The GHT extraction results | |
| Pre-set rotation angles (°) | Calculated rotation angles (°) | Errors (°) | Calculated rotation angles (°) | Errors (°) |
| -20 | -21 | -1 | -19 | 1 |
| -15 | -16 | -1 | -14 | 1 |
| -10 | -10 | 0 | -10 | 0 |
| -5 | -5 | 0 | -4 | 1 |
| 0 | 0 | 0 | 0 | 0 |
| 5 | 4 | -1 | 4 | -1 |
| 10 | 9 | -1 | 9 | -1 |

### 6.3.4.1 Vertebra L3 Extraction

Generally speaking, the vertebra L3 area has the best display quality in DVF images because the X-rays are usually focused on this area during the DVF acquisition. As a result, we aimed to apply the GHT to track the L3 movement as a first step.

Similar to the tracking process in the calibration model, a template frame was first selected. From the studies in the previous chapter, the rotation angles are normalized to start from zero degrees and are distributed in an approximately sinusoidal way. Therefore, we chose a frame with the neutral position as the template frame, shown in Figure 6-9(a), and a small area containing the whole L3 was selected as the template model. After that, our wavelet multiplication edge detector was applied to obtain the binary edge map for the template model (Figure 6-9(b)). The R-Table was then built based on this edge map and the reference point (centre point of the template model, CTM) was calculated as

shown as a cyan circle in Figure 6-9(b). As described in the GHT algorithm, we aimed to track this reference point during the whole motion sequence and calculate the rotation angle of each frame. Moreover, in order to show the tracking results more clearly, four corners of L3 were manual marked as shown as the green points in Figure 6-9(b). The new positions of these four corners were also able to be tracked and displayed as the green points in the image sequence after the application of the GHT.

For the GHT, the all likely rotations are from -90° to +90° and the original size of the DVF images is 572×768. So theoretically, the size of the accumulator space (Hough space) is about 572×768×181. Apparently, it is unnecessary and unpractical in the computation. During the GHT feature extraction, only the small areas containing L3 vertebrae were analyzed in order to reduce the computational cost and improve the efficiency. By experience, we set the range of $x_{curve}$ and $y_{curve}$ from 200 to 350, and from 250 to 400, respectively and it is guaranteed that the L3 vertebrae are located in the range during the whole sequence. Furthermore, with the previous studies of the manual landmarking results, and the rotation angle of L3, we also reduced the range of $\theta$ from -15° to +30°. Thus, the size of the accumulator space (Hough space) was reduced to 151×151×46 rather than the full original size.

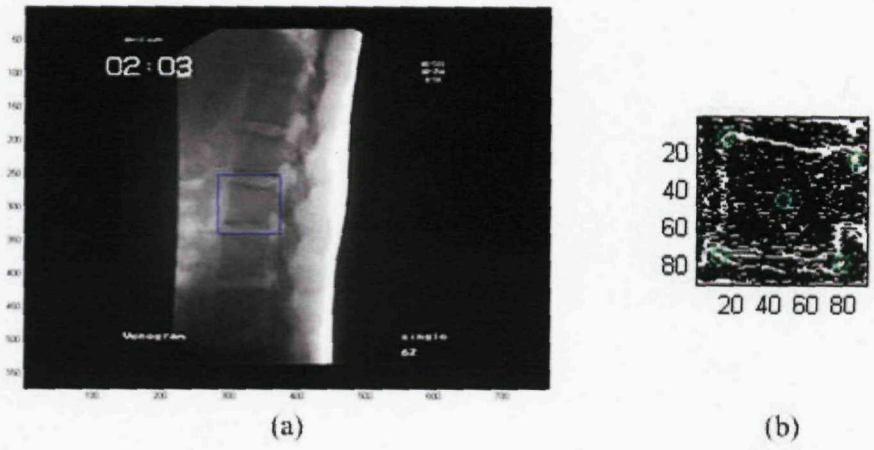


**Figure 6-9** An illustration of the template selection and edge extraction. (a) The template frame with the neutral position and the selection of the template model. (b) The wavelet edge detection result of the template model as well as the reference point (center point) determination and the corner marking of the template model edges.

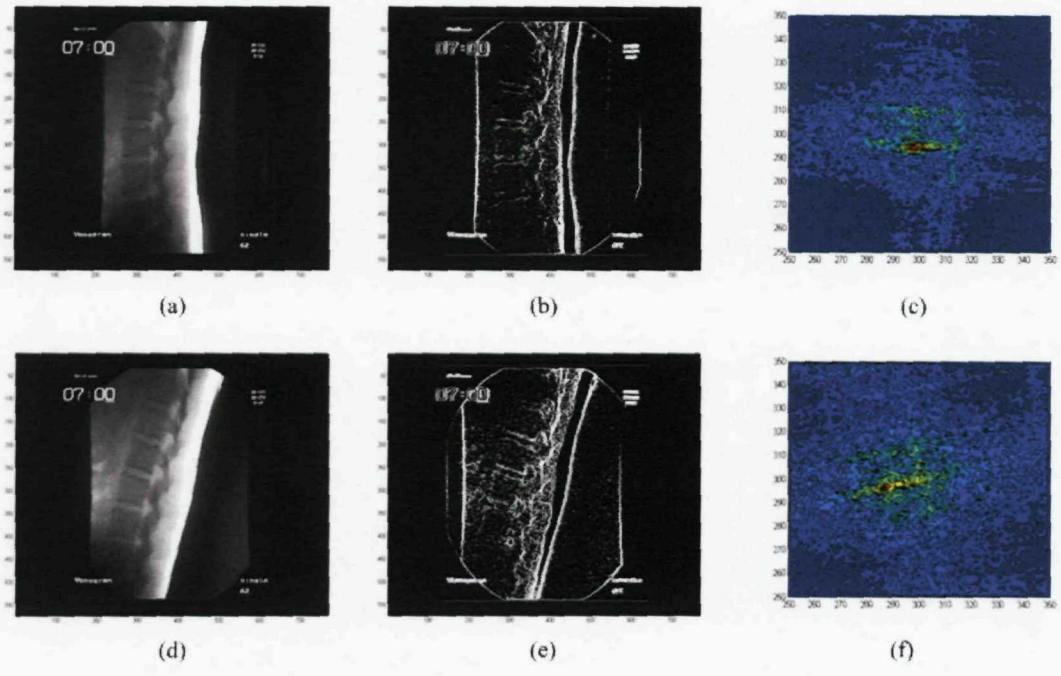


**Figure 6-10** The edge detection and GHT results on L3 of two DVF frames. The first column shows the original DVF images. The second column shows the wavelet edge detection results as well as the findings of the reference points (centre points) and the corners. The third column shows the accumulator space (Hough space) in 2-D of the GHT.

Two examples of the tracking results are illustrated in Figure 6-10. The first example (the top row) shows the tracking of a frame of the neutral position and the second example (the bottom row) shows the tracking of a frame of an extreme position. In Figure 6-10, the first column shows the original DVF images and the tracking results superimposed on the edge detection results derived from the wavelet multiplication method are shown in the second column. Corresponding to the template model in Figure 6-9(b), the green points mean the corner points of the L3 and the cyan points indicate the reference points (centre points) of the L3. Moreover, the accumulator space (Hough space) in 2-D is shown in the third column, in which the coordinates of the reference points (centre points) can be easily located by finding the peaks.

### 6.3.4.2 Other Lumbar Spine Vertebrae Extraction

The GHT was applied to other lumbar vertebrae L1, L2 and L4 within the same neutral and extreme images using the same template frame. However, different thresholding values in the edge detection were chosen by experience since the vertebrae have different definition in DVF images.

Figures 6-11 to 6-13 show the L1, L2 and L4 results respectively. In the figures, the first row shows the template frame, the template model and its edges generated using the wavelet multiplication edge detection method. The second and third rows show the tracking results of the frames in the neutral and extreme position respectively.

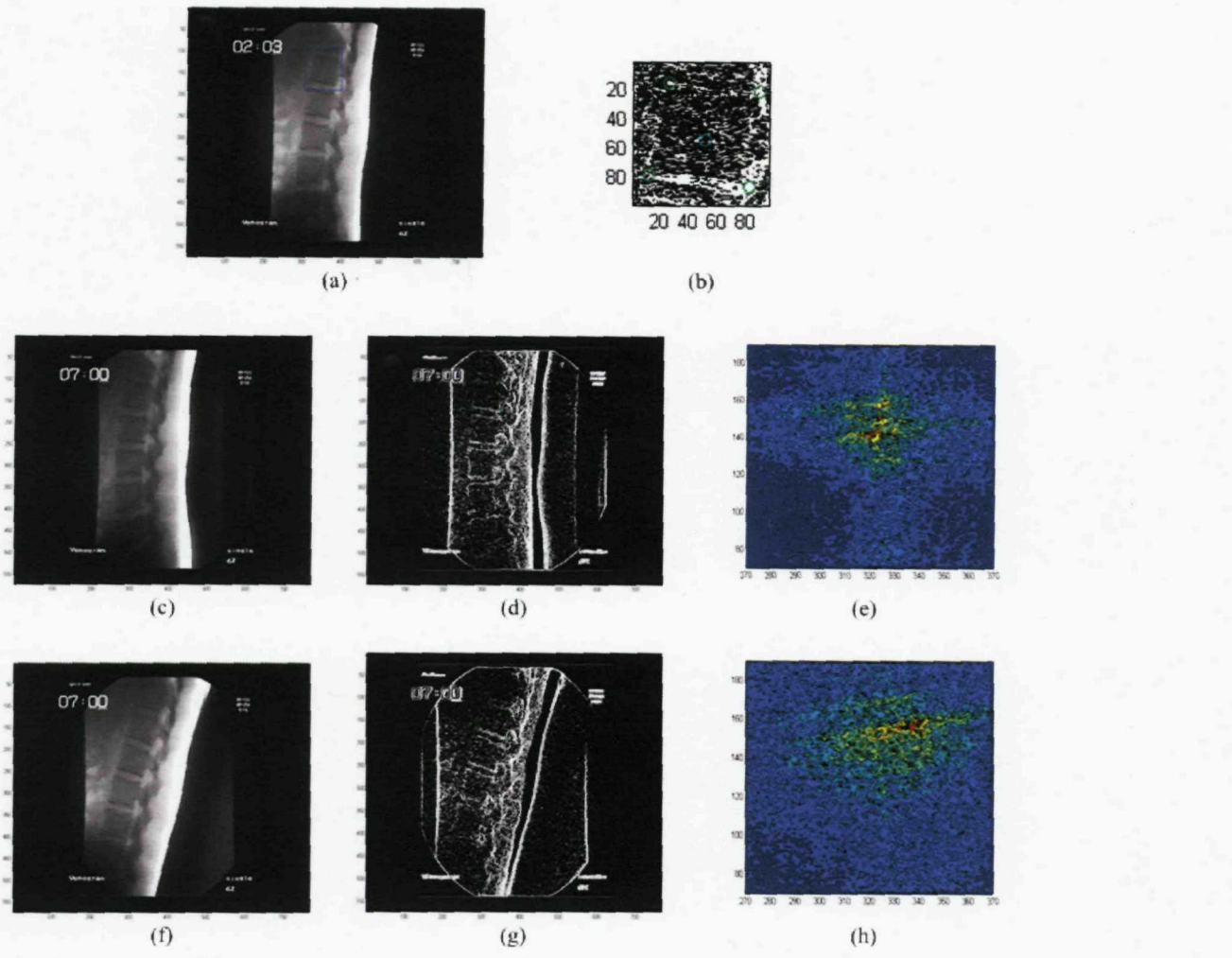


**Figure 6-11** The template model selection and extraction as well as the edge detection and the GHT results on the L1. The first row shows the template frame, the template model and its edges. The second row shows the tracking result of the frame in the neutral position. The third row shows the tracking result of the frame in the extreme position.

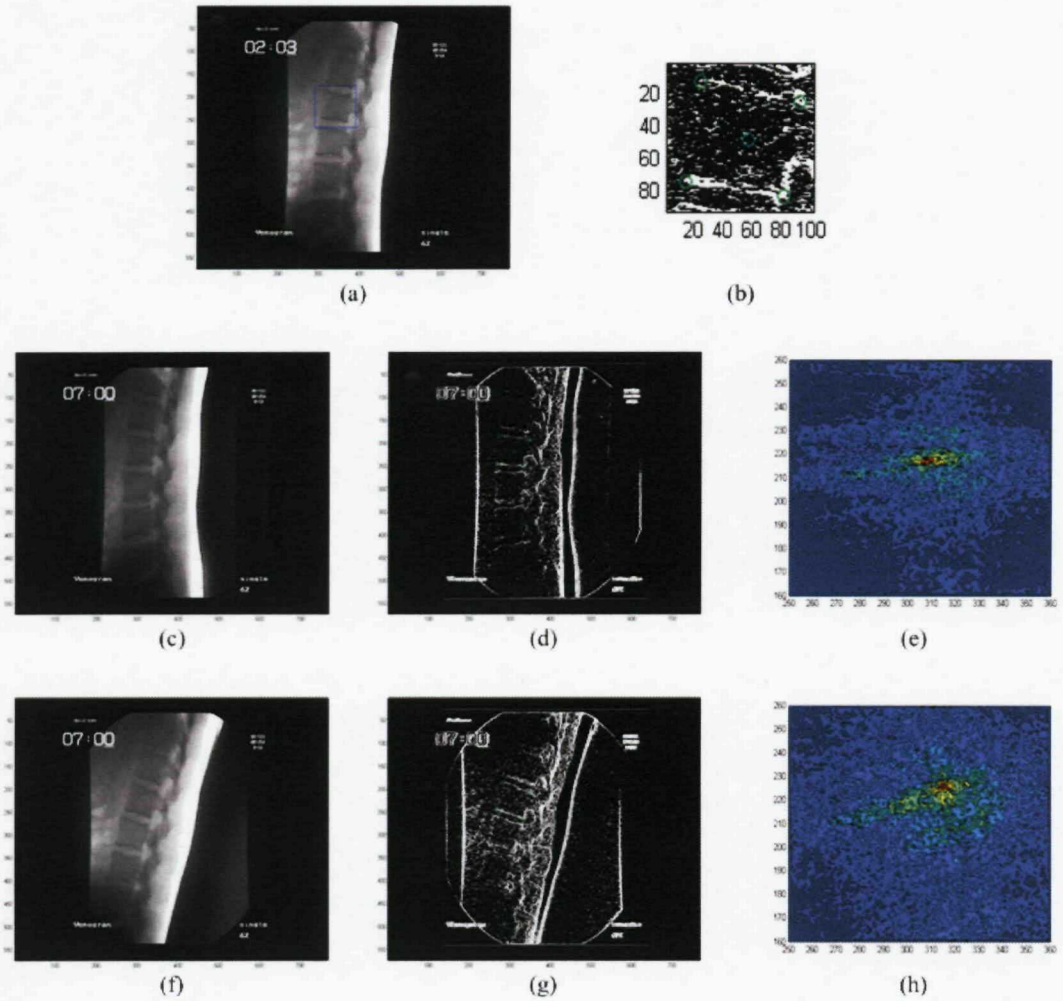


**Figure 6-12** The template model selection and extraction as well as the edge detection and the GHT results on the L2. The first row shows the template frame, the template model and its edges. The second row shows the tracking result of the frame in the neutral position. The third row shows the tracking result of the frame in the extreme position.

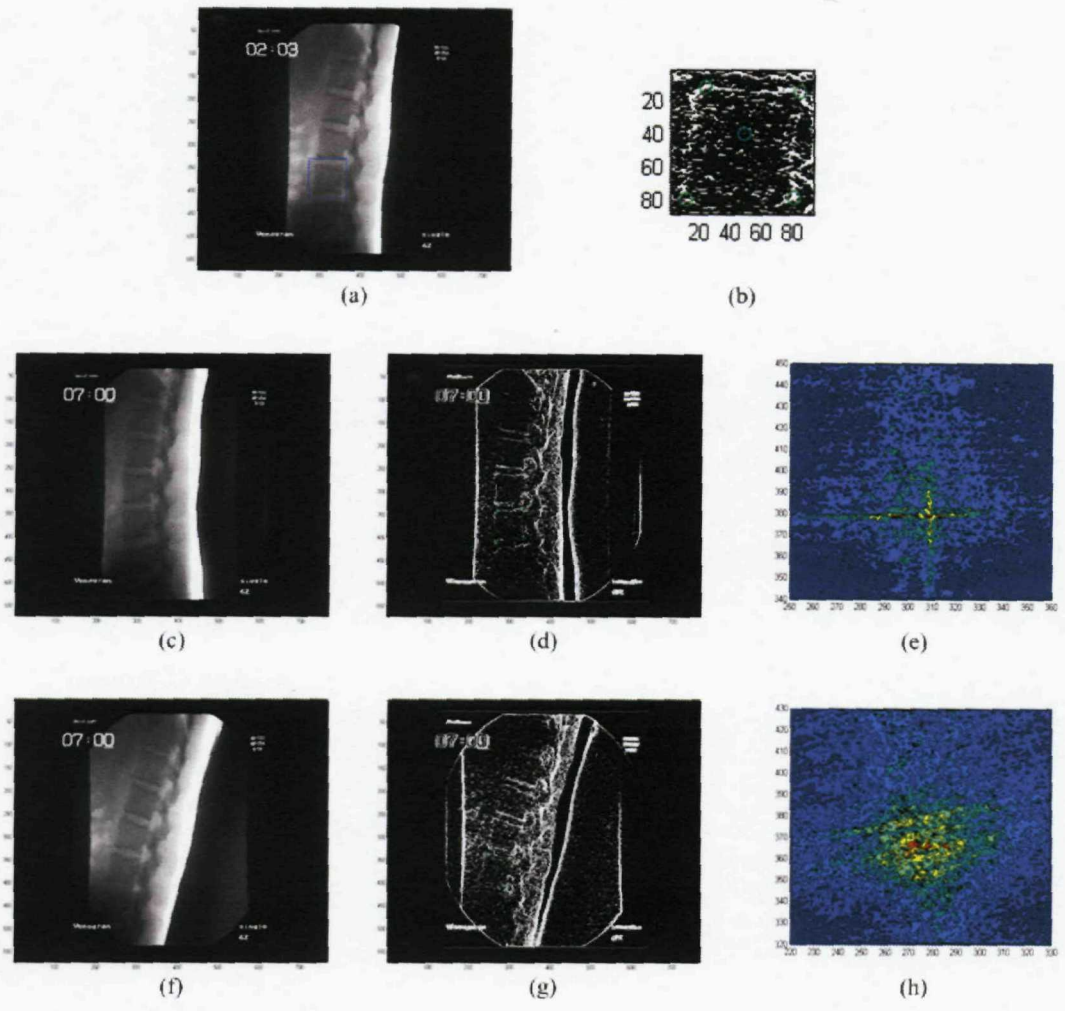


**Figure 6-13** The template model selection and extraction as well as the edge detection and the GHT results on the L4. The first row shows the template frame, the template model and its edges. The second row shows the tracking result of the frame in the neutral position. The third row shows the tracking result of the frame in the extreme position.

From what we have showed above, it can be seen that the GHT has good performance in vertebral extraction. However, it sometimes fails to locate the L1 and L4 correctly, which is shown in Figure 6-14. This situation happens when some part of L1 or L4 are covered by other structures, such as the pelvis, during the whole motion sequence. The structure overlapping causes the edge maps of L1 and L4 to have edge lines crossing the vertebral body in different positions. The lines have strong energy and generate different energy

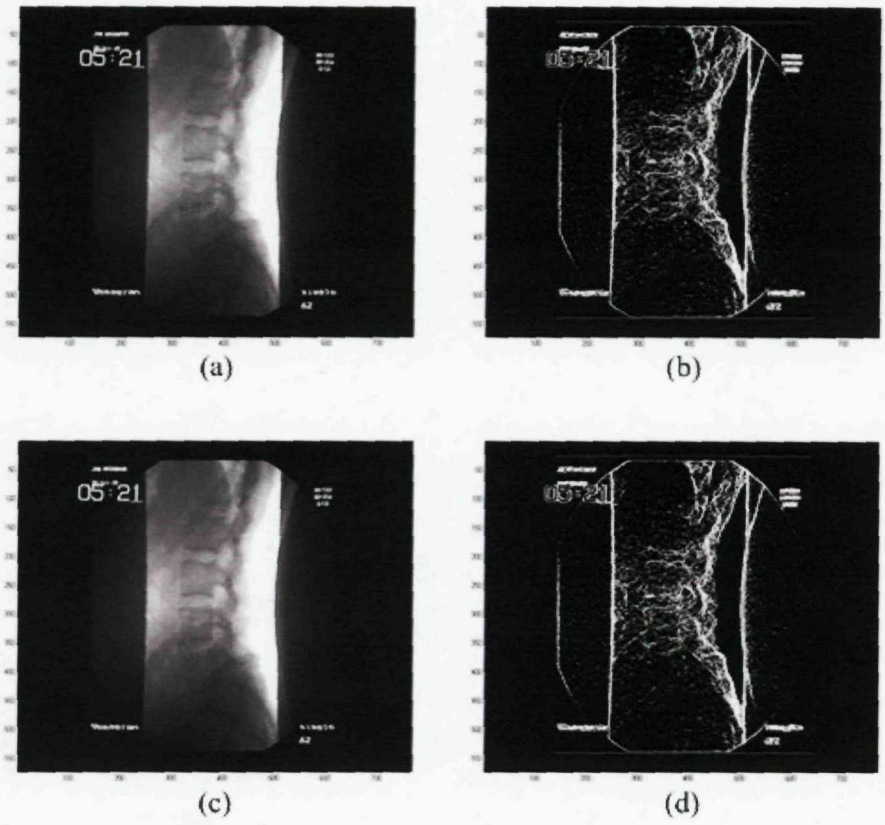


**Figure 6-14** An examples of erroneous tracking. The first row shows the poor tracking of the L1. The second row shows the problem of tracking of the L4.

distribution. Therefore the R-Table generated by the template model cannot describe the vertebra L1 and L4 well and this causes the fault in tracking.

### 6.3.4.3 Vertebral Extraction from the A/P View Images

In previous research, manual input was needed to initialize the template model shape and to form the chain code, from which the Fourier Descriptors can be derived (Zheng,Y. et al. 2003; Zheng,Y.L. et al. 2004). However, the edge maps generated from the anterior/posterior (A/P) view images have no clear vertebral bodies because the vertebral

body edge map is confused due to other structures of the spine, such as lamina, spinous process and transverse process. Therefore, it is difficult to manual mark the vertebral body shapes in the A/P view images after edge detection. As described in our GHT algorithm, the R-Table is generated directly from the edges of the template model. As a result, it is possible to apply the GHT to the DVF images taken from the A/P side to track the lumbar spine motion.

The tracking process is the same as for tracking the lateral images. In the GHT, the size of the accumulator space (Hough space) is also reduced by observation in order to increase the computation efficiency and save the computation time. Some feature extraction results of the L1, L2, L3 and L4 are shown in Figures 6-15 to 6-18 respectively. Moreover, the four corners of the vertebra are manual marked in order to show the tracking results more clearly. The neutral and extreme positions are chosen as the examples, as for the lateral images.

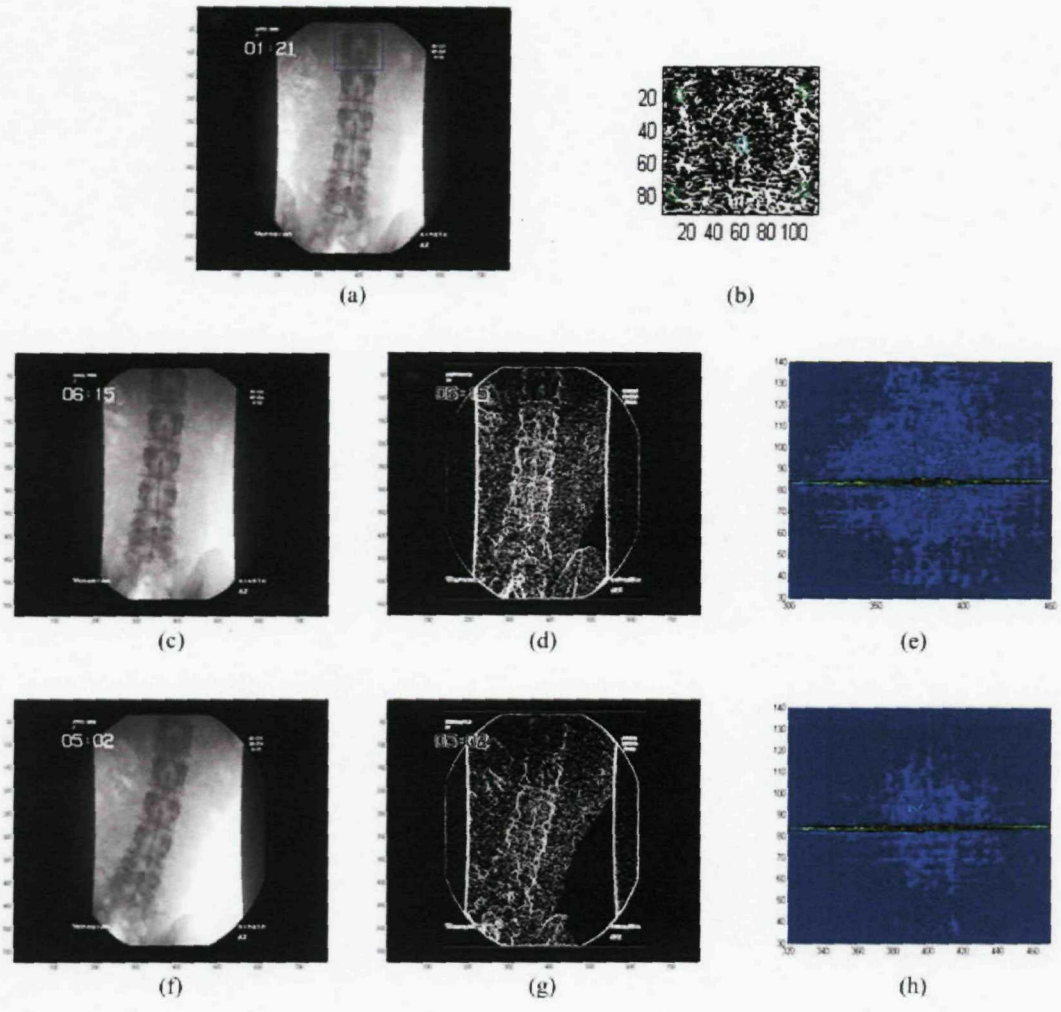


**Figure 6-15** The template model selection and extraction as well as the edge detection and the GHT results for L1 from the A/P view. The first row shows the template frame, the template model and its edges. The second row shows the tracking result of the frame in the neutral position. The row column shows the tracking result of the frame in the extreme position.

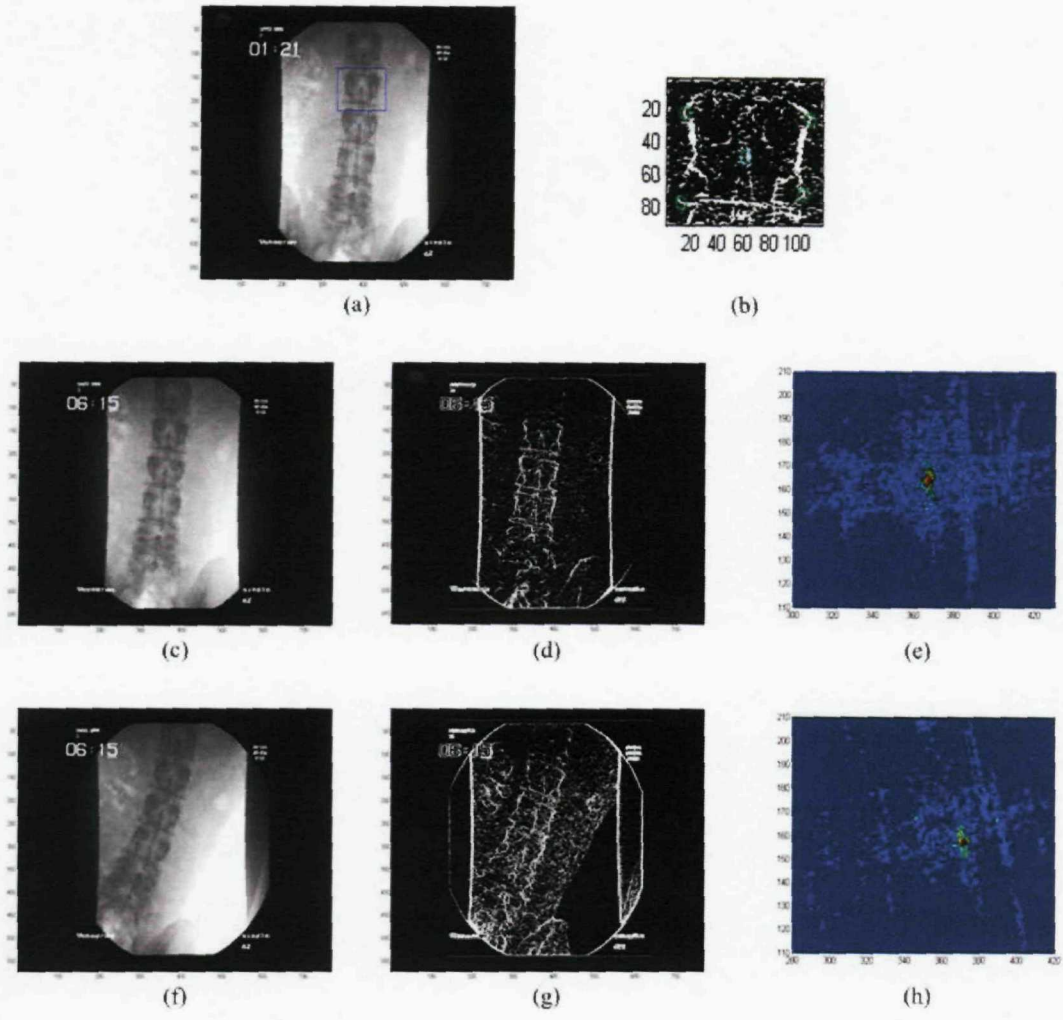


**Figure 6-16** The template model selection and extraction as well as the edge detection and the GHT results for L2 from the A/P view. The first row shows the template frame, the template model and its edges. The second row shows the tracking result of the frame in the neutral position. The third row shows the tracking result of the frame in the extreme position.

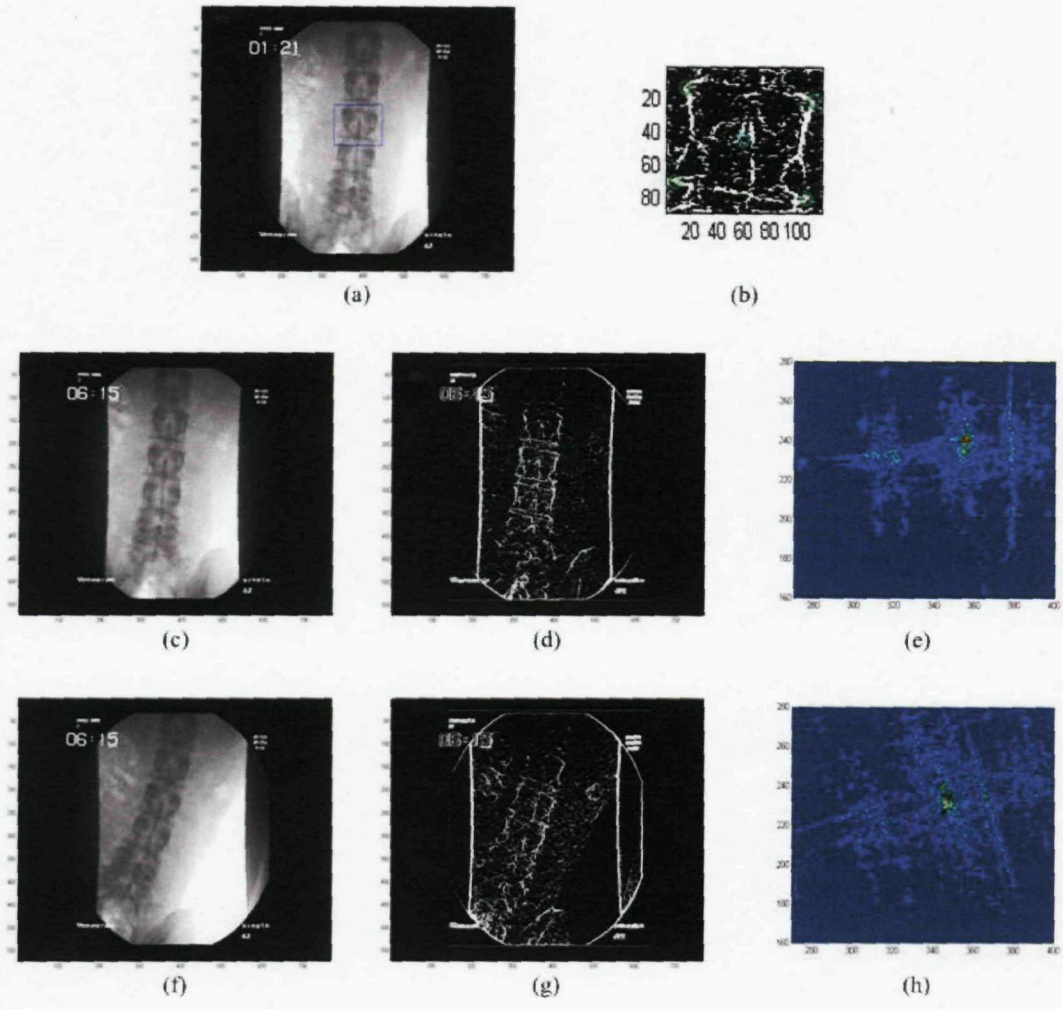


**Figure 6-17** The template model selection and extraction as well as the edge detection and the GHT results for L3 from the A/P view. The first row shows the template frame, the template model and its edges. The second row shows the tracking result of the frame in the neutral position. The third row shows the tracking result of the frame in the extreme position.

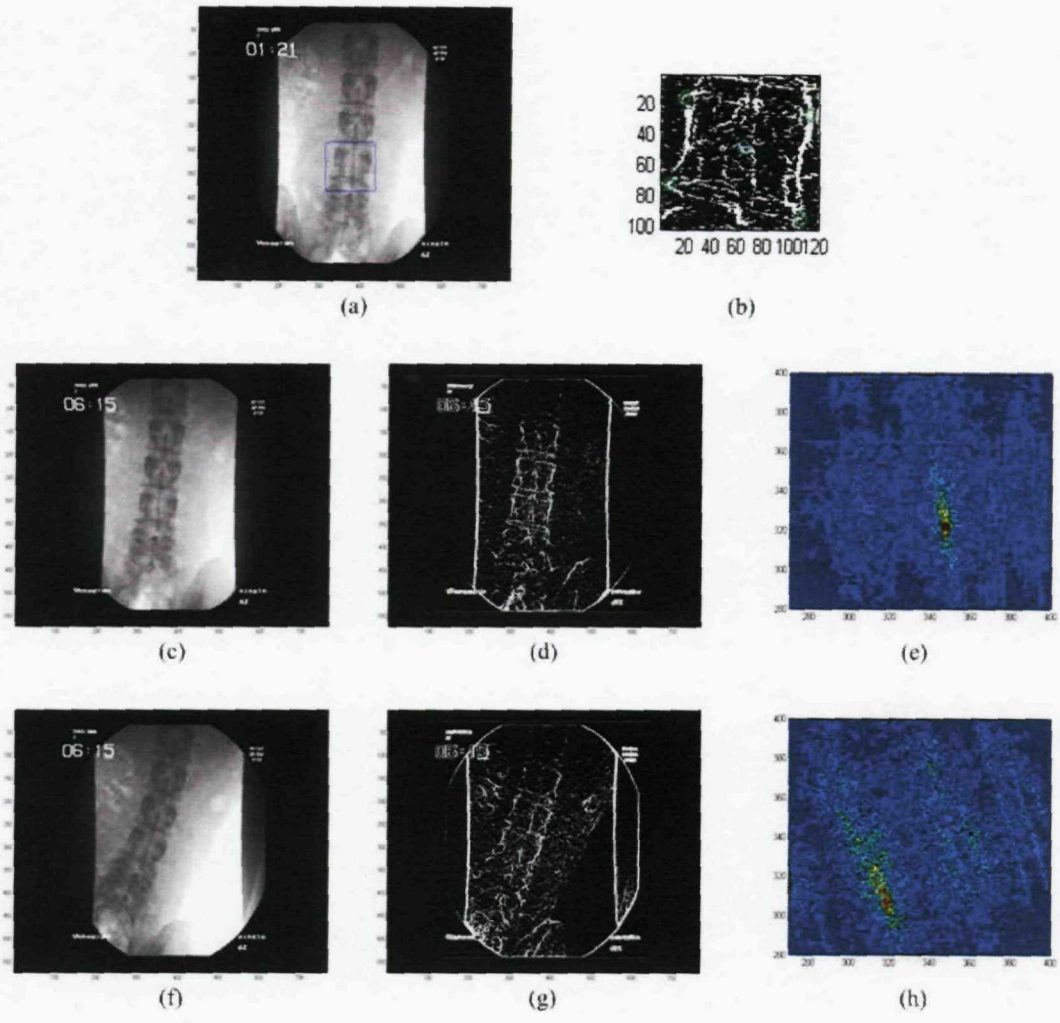


**Figure 6-18** The template model selection and extraction as well as the edge detection and the GHT results for L4 from the A/P view. The first row shows the template frame, the template model and its edges. The second row shows the tracking result of the frame in the neutral position. The third row shows the tracking result of the frame in the extreme position.

From the figures, it can be seen that the GHT has a good performance on the A/P images. Although the vertebral shapes are not easy to be distinguished by human eyes in the edge maps, the GHT is able to track the vertebral movement correctly, even in the L4 tracking. In this way, some characteristics of the normal spine motion can be studied based on the DVF images taken from the A/P view and these studies do not require manual landmarking. However, it sometimes fails to extract L1 correctly, which is shown in

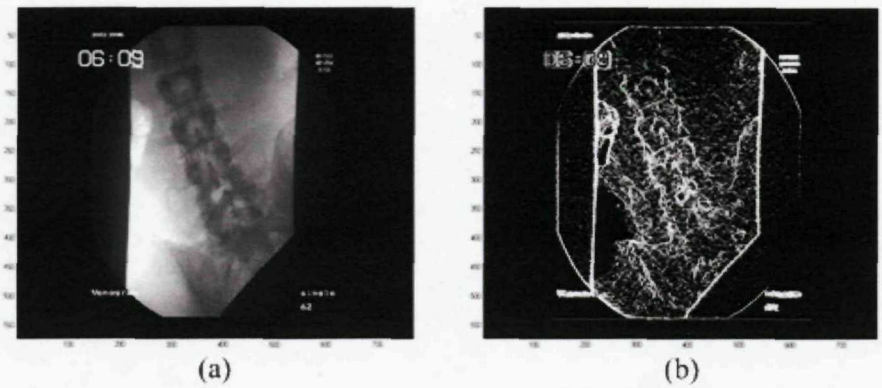


**Figure 6-19** An example of erroneous tracking of L1.

Figure 6-19. This situation happens when the whole vertebral body of L1 does not appear in the image. The lack of integrity of the vertebra body causes the enormous description of the shape of target.

## 6.4 Tracking using the Edge Results from the Canny Edge Detector

Recall the discussions in Chapter 4, of the conventional edge detection methods the Canny algorithm can yield the best vertebral contours. In order to investigate the tracking results using the edge map generated by the Canny edge detector and compare it with that from the wavelet scale multiplication edge detector, an experiment was designed to apply the edge results from the Canny operator in the Generalized Hough transform. An example of tracking results is shown in Figure 6-20. From the template model (Figure 6-20(b)), the fake edges contained inside the vertebral boundary affect the generation of a reliable R-Table for the GHT tracking. Furthermore, in the edge map (Figure 6-20(d)), there are also lots of fake edges existing inside the vertebral areas, which causes the problem with matching to the template model. In conclusion, the tracking results show

that the limitations of the edge results from the Canny edge detection method cause the Canny operator not suitable in this project.

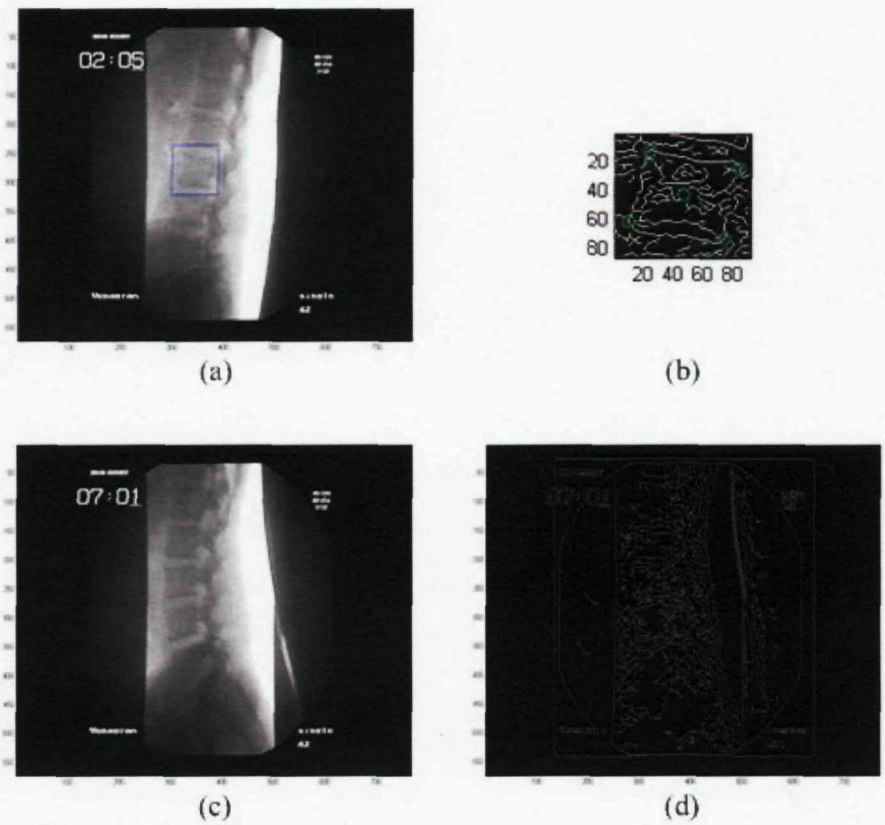


**Figure 6-20** The template model selection and extraction as well as the edge detection and the GHT results on the L3, using the edge map generated from the Canny edge detector. The first row shows the template frame, the template model and its edges. The second row shows an example of the tracking results.

## 6.5 Summary

In this chapter, an overview of the Hough transform was given, and the basic idea of the Generalized Hough transform was introduced in detail followed by a brief review on the previous studies of the GHT and its application to medical images. After that, the GHT

algorithm used in tracking the vertebrae in DVF images was described. In order to measure the performance and accuracy, the GHT was applied to the calibration model images and the results look promising. Finally, the GHT was applied to the real DVF images from the both lateral and A/P views. The results are still encouraging although the method sometimes fails to track the L1 and L4 in the lateral images, or the L1 in A/P images. This problem would be solved by the future efforts in several possible directions which will be mentioned in the last chapter.

# Chapter 7

# Automated Tracking of Vertebrae in DVF Sequences

## 7.1 Introduction

All of the ten healthy subject files, which were listed in Chapter 3, were involved in the tracking study. In the motion tracking, the generalized Hough transform was applied to the vertebral shapes generated by using the wavelet scale multiplication edge detector. For the DVF images taken from the lateral view, only the movements of the vertebrae L2 and L3 were investigated since not all the vertebral motion of L1 and L4 can be tracked correctly due to missing sections from some images. However, for the DVF images taken from the anterior/posterior (A/P) view, the spinal movement of L2 to L4 were studied due to the good performance of the GHT in tracking motion on the A/P view images because the edge maps contain more integrated vertebral shapes even though they are confused with other structures of human body. For each DVF sequence, the rotation angle, the intervertebral angle and the translation of the centre point of the vertebrae were calculated. Only some results will be displayed in this chapter but all tracking results are presented in Appendix B-K.

Furthermore, the biomechanical tracking results, such as the rotation angles and intervertebral angles, were compared with *Kondracki*'s research (Kondracki,M. 2001)

based on the same image frames in the same DVF sequences. He manual landmarked the DVF sequences to calculate the biomedical parameters and, as an experienced clinician, these results are regarded as the "gold standard" in our project. We aimed to evaluate our edge detection and motion tracking method by comparing our results with the "gold standard" data. The error and range of distribution were calculated and will be discussed. *Kondracki* investigated every three or four image frames in each DVF sequence in his research, so we also tracked the same frames. However, in the first few frames in every DVF sequence, the octagonal edges (shown in Figure 7-1) generated by the DVF acquisition system to aid focusing for the radiographer would affect the tracking results because of their strong energy distribution. As a result, we actually tracked from about the $13^{th}$ or $14^{th}$ frame and we therefore tracked a total of 34-46 image frames in every DVF sequence.

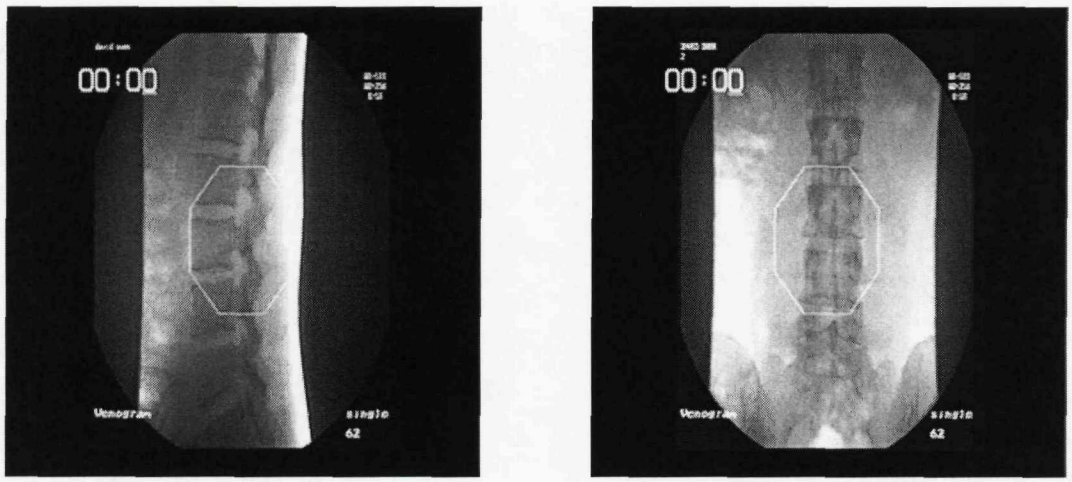


(a) (b)

**Figure 7-1** The DVF images contain the octagonal frames. (a) The lateral view. (b) The A/P view.

## 7.2 Motion Tracking of the DVF Images from the Lateral View

### 7.2.1 Rotation Angles of the Spine in Flexion/Extension

In the flexion/extension study, there are two sets from the lateral view ('*laton*' and '*latwo*') of DVF sequences for each subject. However *Kondracki* did not provide the data of the rotation angles for subject RM and recorded only 1 set ('*laton*') of the rotation angles for subject JM in his research (Kondracki,M. 2001). Our algorithm was successfully tested with 10 sets of the lateral images from 8 healthy subjects. These 10 data sets are BM '*laton*', CR '*latwo*', DE '*laton*', DO '*laton*', DO '*latwo*', GP '*latwo*', JM '*laton*', JW '*laton*', JW '*latwo*', and NW '*laton*'. Figure 7-2 shows a part of the tracking results and Figure 7-3 shows the estimated rotation angles over a DVF sequence. For each subject, we calculated the statistical values of mean and standard deviation for our measurements and compared them with *Kondracki*'s results. The Range of Motion (ROM) of the rotation angles was also calculated and compared. Finally, to investigate the accuracy of our method, the mean of the error, the standard deviation of the error and the standard error (SE) were calculated. Here, the results of *Kondracki* are set to be the 'true' values and our measurements are set to be the estimated values. The standard error (SE) $s_{\bar{d}}$ is expressed in Equation5.1. The statistical analysis of subject DO is shown in Table 7-1. The errors of the ROM are in the range of 0°-3°. The absolute values of the mean of the error are less than 1.25° and the standard deviations of the error are controlled within 1.6°. Moreover, the figures of estimated rotation angles over DVF sequences and the tables of the statistical analysis of all 10 data sets can be found in Appendix B-J.

# Chapter 7

# Automated Tracking of Vertebrae in DVF Sequences

## 7.1 Introduction

All of the ten healthy subject files, which were listed in Chapter 3, were involved in the tracking study. In the motion tracking, the generalized Hough transform was applied to the vertebral shapes generated by using the wavelet scale multiplication edge detector. For the DVF images taken from the lateral view, only the movements of the vertebrae L2 and L3 were investigated since not all the vertebral motion of L1 and L4 can be tracked correctly due to missing sections from some images. However, for the DVF images taken from the anterior/posterior (A/P) view, the spinal movement of L2 to L4 were studied due to the good performance of the GHT in tracking motion on the A/P view images because the edge maps contain more integrated vertebral shapes even though they are confused with other structures of human body. For each DVF sequence, the rotation angle, the intervertebral angle and the translation of the centre point of the vertebrae were calculated. Only some results will be displayed in this chapter but all tracking results are presented in Appendix B-K.

Furthermore, the biomechanical tracking results, such as the rotation angles and intervertebral angles, were compared with *Kondracki*'s research (Kondracki,M. 2001)

based on the same image frames in the same DVF sequences. He manual landmarked the DVF sequences to calculate the biomedical parameters and, as an experienced clinician, these results are regarded as the "gold standard" in our project. We aimed to evaluate our edge detection and motion tracking method by comparing our results with the "gold standard" data. The error and range of distribution were calculated and will be discussed. *Kondracki* investigated every three or four image frames in each DVF sequence in his research, so we also tracked the same frames. However, in the first few frames in every DVF sequence, the octagonal edges (shown in Figure 7-1) generated by the DVF acquisition system to aid focusing for the radiographer would affect the tracking results because of their strong energy distribution. As a result, we actually tracked from about the $13^{th}$ or $14^{th}$ frame and we therefore tracked a total of 34-46 image frames in every DVF sequence.

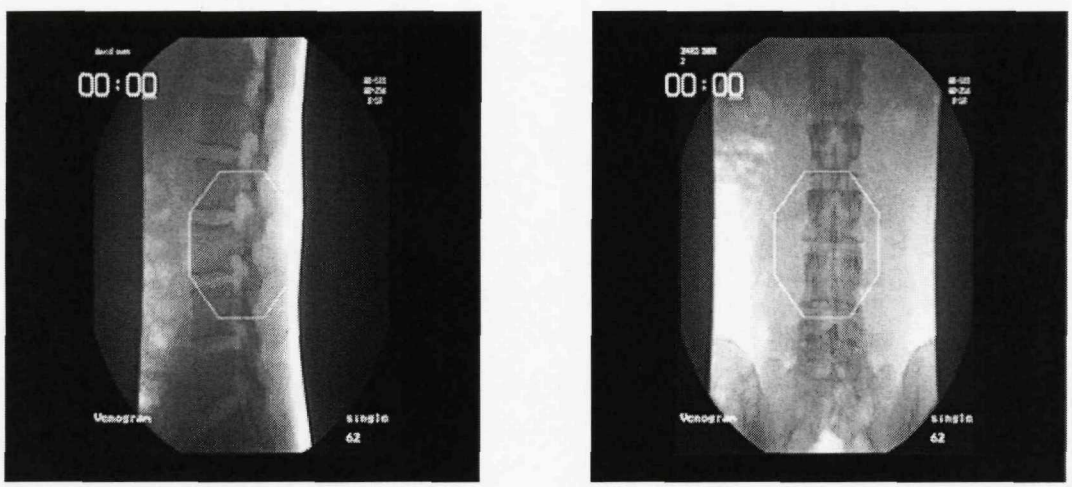


(a) (b)

**Figure 7-1** The DVF images contain the octagonal frames. (a) The lateral view. (b) The A/P view.

## 7.2 Motion Tracking of the DVF Images from the Lateral View

### 7.2.1 Rotation Angles of the Spine in Flexion/Extension

In the flexion/extension study, there are two sets from the lateral view ('*laton*' and '*latwo*') of DVF sequences for each subject. However *Kondracki* did not provide the data of the rotation angles for subject RM and recorded only 1 set ('*laton*') of the rotation angles for subject JM in his research (Kondracki,M. 2001). Our algorithm was successfully tested with 10 sets of the lateral images from 8 healthy subjects. These 10 data sets are BM '*laton*', CR '*latwo*', DE '*laton*', DO '*laton*', DO '*latwo*', GP '*latwo*', JM '*laton*', JW '*laton*', JW '*latwo*', and NW '*laton*'. Figure 7-2 shows a part of the tracking results and Figure 7-3 shows the estimated rotation angles over a DVF sequence. For each subject, we calculated the statistical values of mean and standard deviation for our measurements and compared them with *Kondracki*'s results. The Range of Motion (ROM) of the rotation angles was also calculated and compared. Finally, to investigate the accuracy of our method, the mean of the error, the standard deviation of the error and the standard error (SE) were calculated. Here, the results of *Kondracki* are set to be the 'true' values and our measurements are set to be the estimated values. The standard error (SE) $s_{\bar{a}}$ is expressed in Equation5.1. The statistical analysis of subject DO is shown in Table 7-1. The errors of the ROM are in the range of 0°-3°. The absolute values of the mean of the error are less than 1.25° and the standard deviations of the error are controlled within 1.6°. Moreover, the figures of estimated rotation angles over DVF sequences and the tables of the statistical analysis of all 10 data sets can be found in Appendix B-J.

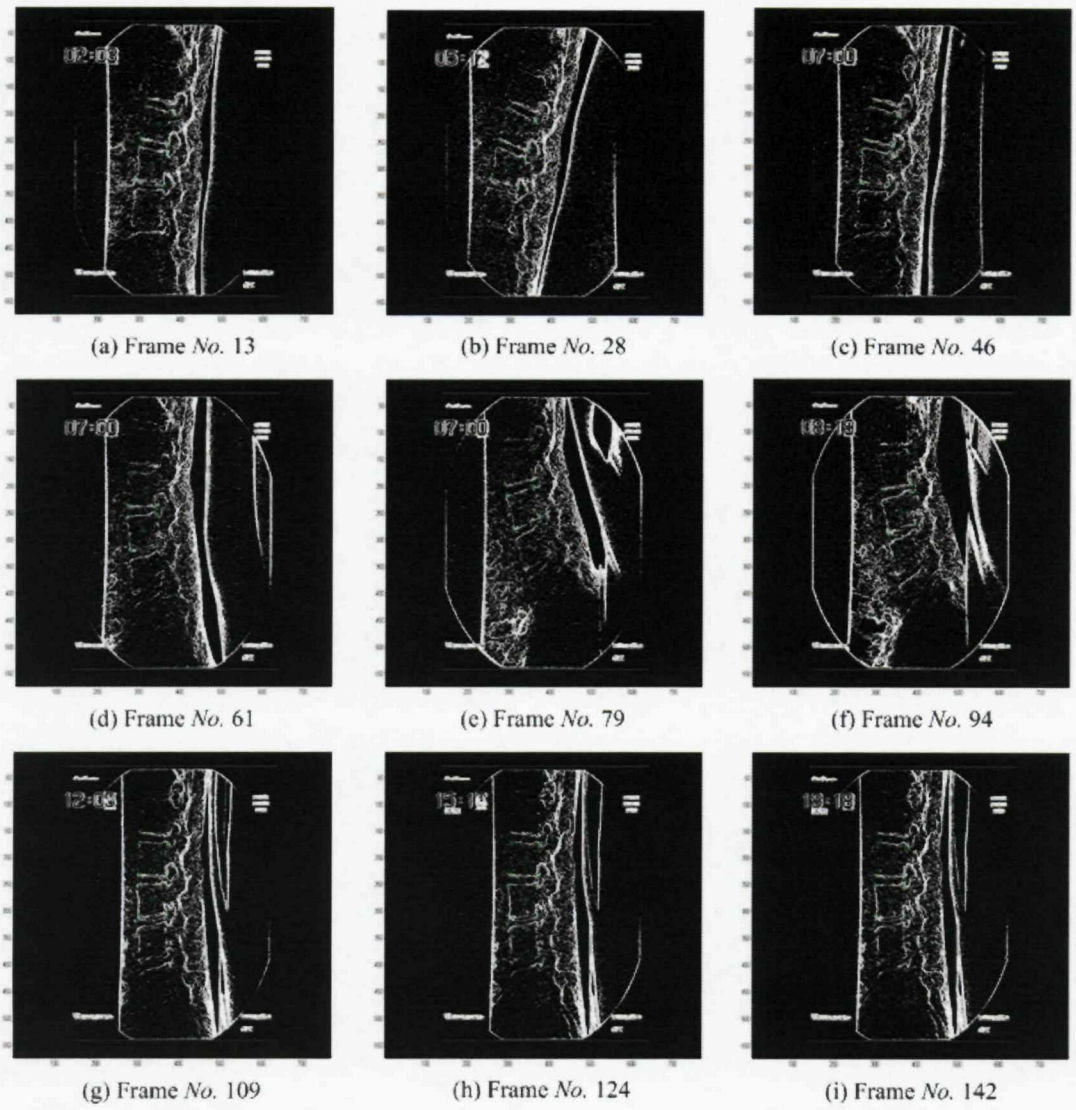

(a) Frame *No.* 13 (b) Frame *No.* 28 (c) Frame *No.* 46

(d) Frame *No.* 61 (e) Frame *No.* 79 (f) Frame *No.* 94

(g) Frame *No.* 109 (h) Frame *No.* 124 (i) Frame *No.* 142

**Figure 7-2** The tracking results of a healthy subject DO flexion/extension sequence in the lateral view.

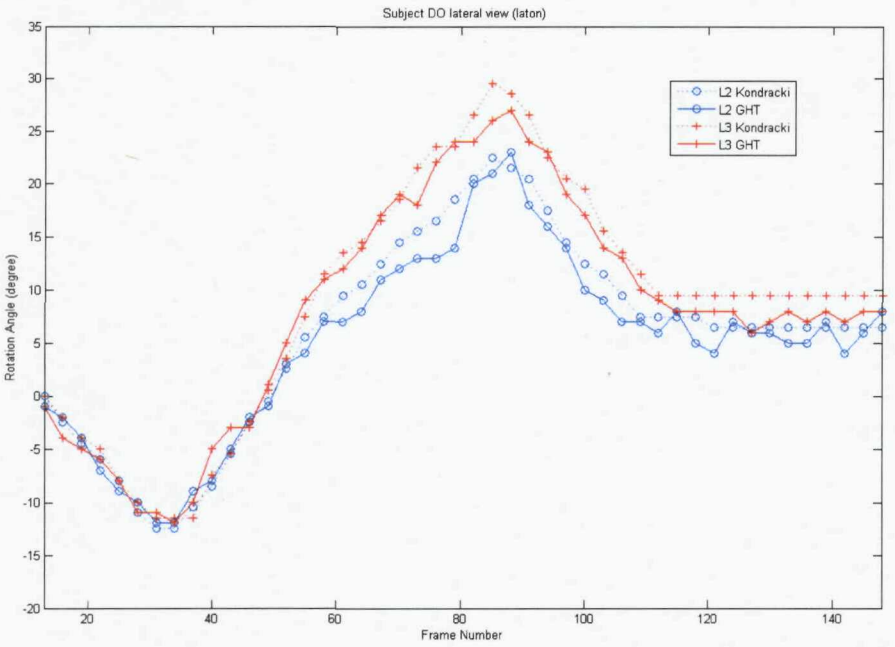


**Figure 7-3** The rotation angles of the vertebrae L2 and L3 versus frame number. Extension is positive in the graph.

Based on the comparisons of all 10 data sets, the mean value of the mean of error (MME), the mean value of the standard deviation of error (MSDE) and the mean value of the standard error (MSE) were calculated and are shown in Table 7-2. The calculation of '*laton*' data are based on 6 sets of DVF sequences while the calculation of '*latwo*' data are based on 4 sets of DVF sequences. From the table, it can be seen that the experimental results from our method are close to *Kondracki*'s manual method result. Moreover, the overall error of the vertebra L3 tracking is generally smaller than that of L2 because the focus of DVF system is on L3 during the image acquisition and L3 consequently has the better image quality than L2.

All the discussion above is based on the tracking of only the vertebrae L2 and L3.

**Table 7-1** The rotation angle measurement of flexion/extension of subject DO.

| | | | | mean of the rotation (°) | std of the rotation (°) | Range of Motion (°) | mean of the error (°) | std of the error (°) | SE |
|---|---|---|---|---|---|---|---|---|---|
| Subject DO | laton | L2 | *Kondracki* | 5.96 | 9.44 | 35 | -0.91 | 1.45 | 0.253 |
| | | | GHT | 5.04 | 8.73 | 35 | | | |
| | | L3 | *Kondracki* | 8.98 | 11.44 | 41 | -0.93 | 1.46 | 0.256 |
| | | | GHT | 8.04 | 10.83 | 39 | | | |
| | latwo | L2 | *Kondracki* | 5.37 | 8.01 | 28 | -1.23 | 1.28 | 0.302 |
| | | | GHT | 4.14 | 7.59 | 25 | | | |
| | | L3 | *Kondracki* | 7.54 | 10.71 | 37 | -0.80 | 1.55 | 0.296 |
| | | | GHT | 6.74 | 10.15 | 35 | | | |

[+]*std is the standard deviation.*

[+]*SE is the standard error.*

**Table 7-2** The statistical analysis of the tracking results of the rotation angle from the lateral view of 10 DVF sequences from 8 human subjects.

| | laton | | latwo | |
|---|---|---|---|---|
| | L2 | L3 | L2 | L3 |
| MME (°) | -0.820 | -0.772 | -0.568 | -0.523 |
| MSDE (°) | 1.190 | 1.298 | 1.230 | 1.053 |
| MSE | 0.2482 | 0.2560 | 0.2620 | 0.2488 |

[+]*MME is the mean value of the mean of error.*

[+]*MSDE is the mean value of the standard deviation of error.*

[+]*MSE is the mean value of the standard error.*

## 7.2.2 Intervertebral Angles of the Spine in Flexion/Extension

The relative movement of one vertebra and its neighbour was also studied in this project because the movement of the vertebrae in the image sequence is not fixed to a reference point. With the 10 tracking results discussed above, we can calculate the intervertebral angles over the motion sequence. For example, Figure 7-4 shows the changes of the intervertebral angles of the spine movement in Figure 7-3. Similar to the rotation angle measurement, the statistical and biomechanical parameters were investigated and are shown in Table 7-3. All the statistical measurements of these 10 data sets can be found in the Appendix B-J. Finally, the MME, MSDE and MSE of the intervertebral angle measurement were calculated and shown in Table 7-4. The MME is close to 0°, the MSDE is around 1.5° and the MSE value ranges from 0.22 to 0.28. Again, promising tracking results were obtained, which suggests that the method is reliable and robust.

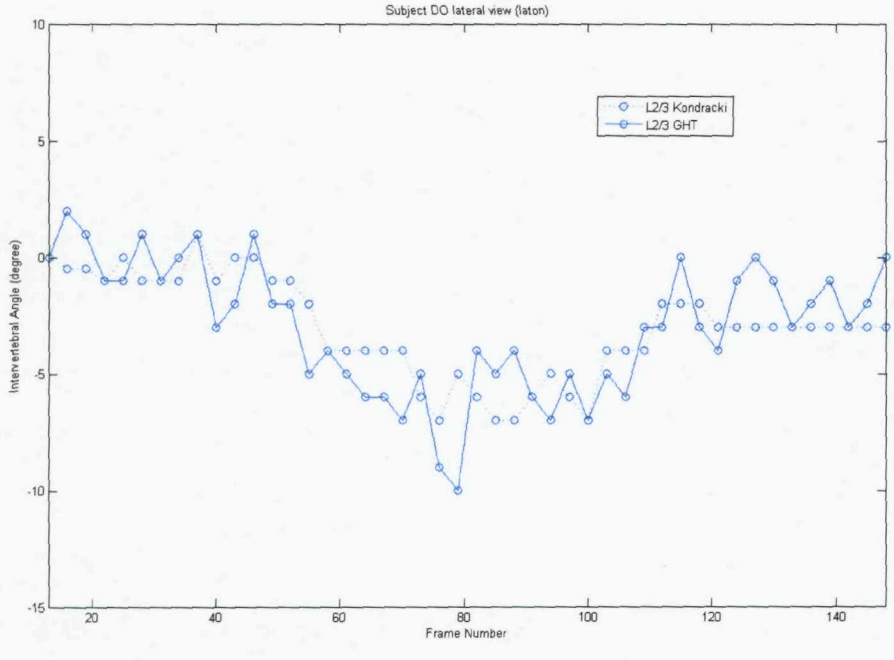


**Figure 7-4** The intervertebral angles of the vertebrae L2/3 versus frame number.

**Table 7-3** The intervertebral angle measurement of flexion/extension of subject DO.

| | | | | mean of the IVA (°) | std of the IVA (°) | Range of Motion (°) | mean of the error (°) | std of the error (°) | SE |
|---|---|---|---|---|---|---|---|---|---|
| Subject DO | L2/3 | laton | *Kondracki* | -3.02 | 2.17 | 7 | 0.02 | 1.82 | 0.269 |
| | | | GHT | -3.00 | 2.83 | 11 | | | |
| | | latwo | *Kondracki* | -2.17 | 2.99 | 8.5 | -0.43 | 1.60 | 0.280 |
| | | | GHT | -2.60 | 2.90 | 10 | | | |

[+] *IVA is the intervertebral angle.*

[+]*std is the standard deviation.*

[+]*SE is the standard error.*

**Table 7-4** The statistical analysis of the tracking results of the intervertebral angle from the lateral view of 10 DVF sequences from 8 human subjects.

| | L2/3 | |
|---|---|---|
| | laton | latwo |
| MME (°) | -0.072 | -0.045 |
| MSDE (°) | 1.328 | 1.628 |
| MSE | 0.2287 | 0.2800 |

[+]*MME is the mean value of the mean of error.*

[+]*MSDE is the mean value of the standard deviation of error.*

[+]*MSE is the mean value of the standard error.*

## 7.2.3 Translations of the Spine in Flexion/Extension

In addition to the rotation angle, our Generalized Hough algorithm also provides the translation of the centre point of the template model (CTM). However, the CTM cannot be used directly to study the translation of the vertebrae in the spinal motion because the CTM does not represent the centre point of the vertebra. Here, we define the centre point

of the vertebra (CV) $(x_{CV},y_{CV})$ as $x_{CV} = \frac{\sum_{i=1}^{4} x_{c,i}}{4}$ and $y_{CV} = \frac{\sum_{i=1}^{4} y_{c,i}}{4}$, where $(x_c,y_c)$ is the coordinates of the four vertebral corners. To avoid the confusion, we show only the CTMs as the cyan points in the tracking result sequences in Figure 7-2 while only the distribution of CVs is displayed in this section. Figures 7-5 and 7-6 show the *x*- and *y*-translation of the centre points of the vertebrae L2 and L3. Moreover, the 2-D illustration of the translation of the CVs of the vertebrae L2 and L3 is shown in Figure 7-7. From these figures, it can be seen that the vertebrae do not return to the starting position of the movement, which match the tracking results of the rotation angle. Again, all 10 tracking results of the translation can be found in the Appendix B-J.

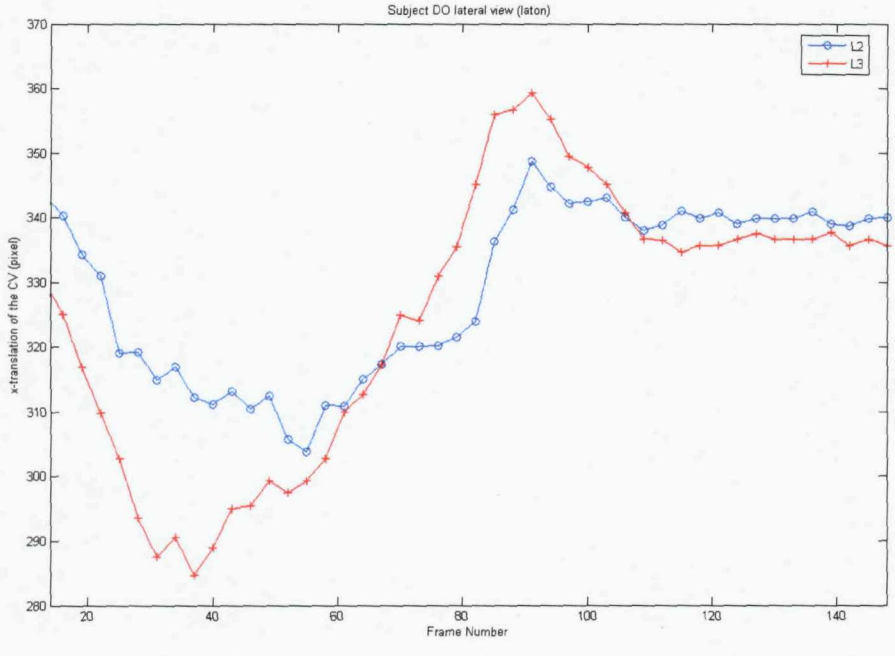


**Figure 7-5** The *x*-translation of the CVs of the vertebrae L2 and L3 versus frame number.

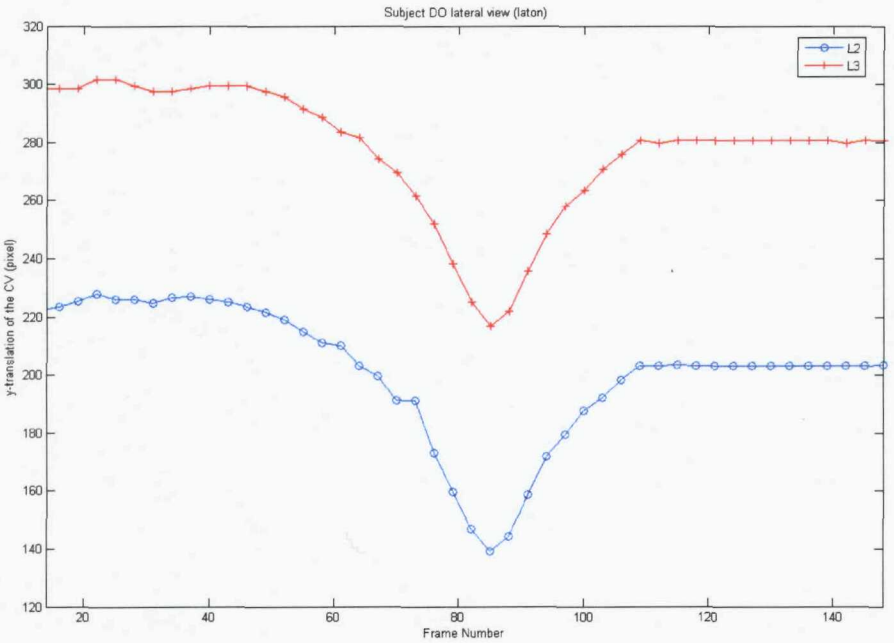


**Figure 7-6** The *y*-translation of the CVs of the vertebrae L2 and L3 versus frame number.

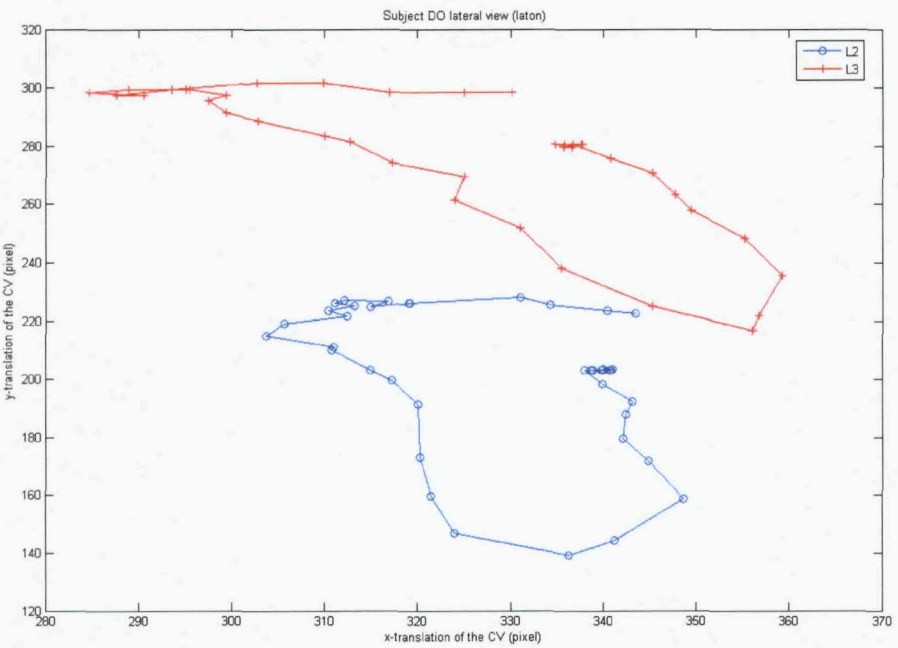


**Figure 7-7** The translation of the CVs of the vertebrae L2 and L3 in 2-D illustration.

## 7.3 Motion Tracking of the DVF Images from the Anterior/Posterior View

### 7.3.1 Rotation Angles of the Spine in Lateral Bending

In the lateral bending study, there are also two sets from the A/P view ('*paone*' and '*patwo*') of DVF sequences for each subject. However *Kondracki* did not provide the rotation angles for the '*paone*' data sequences of subject CR, GD and NW and recorded the rotation angles for only the '*paone*' data set sequence of subject DE and JM in his research (Kondracki,M. 2001). Moreover, the DVF sequence RM '*paone*' does not include the entire image frames for tracking. Our algorithm was successfully tested with the remaining 14 sets of the lateral images from 10 healthy subjects. Figure 7-8 shows a part of the tracking results and Figure 7-9 shows the estimated rotation angles over a DVF sequence. For each subject we calculated the same statistical values as what we did for the lateral image sequences, for our measurements and compared them with *Kondracki*'s results. The Range of Motion (ROM) of the rotation angles was also calculated and compared. Finally, to investigate the accuracy of our method, the mean of error, the standard deviation of error and the standard error (SE) were calculated. Here, the results of *Kondracki* are set to be the 'true' values and our measurements are set to be the estimated values. The standard error (SE) $s_{\bar{d}}$ is expressed in Equation 5.1. The statistical analysis of a subject is shown in Table 7-5. The errors of the ROM are in the range of 0°-4°. The absolute values of the mean of the error are less than 1.35° and the standard deviations of the error are controlled under 1.5°. In addition, the figures of estimated rotation angles over DVF sequences and the tables of the statistical analysis of all 10 data sets can be found in Appendix B-K.

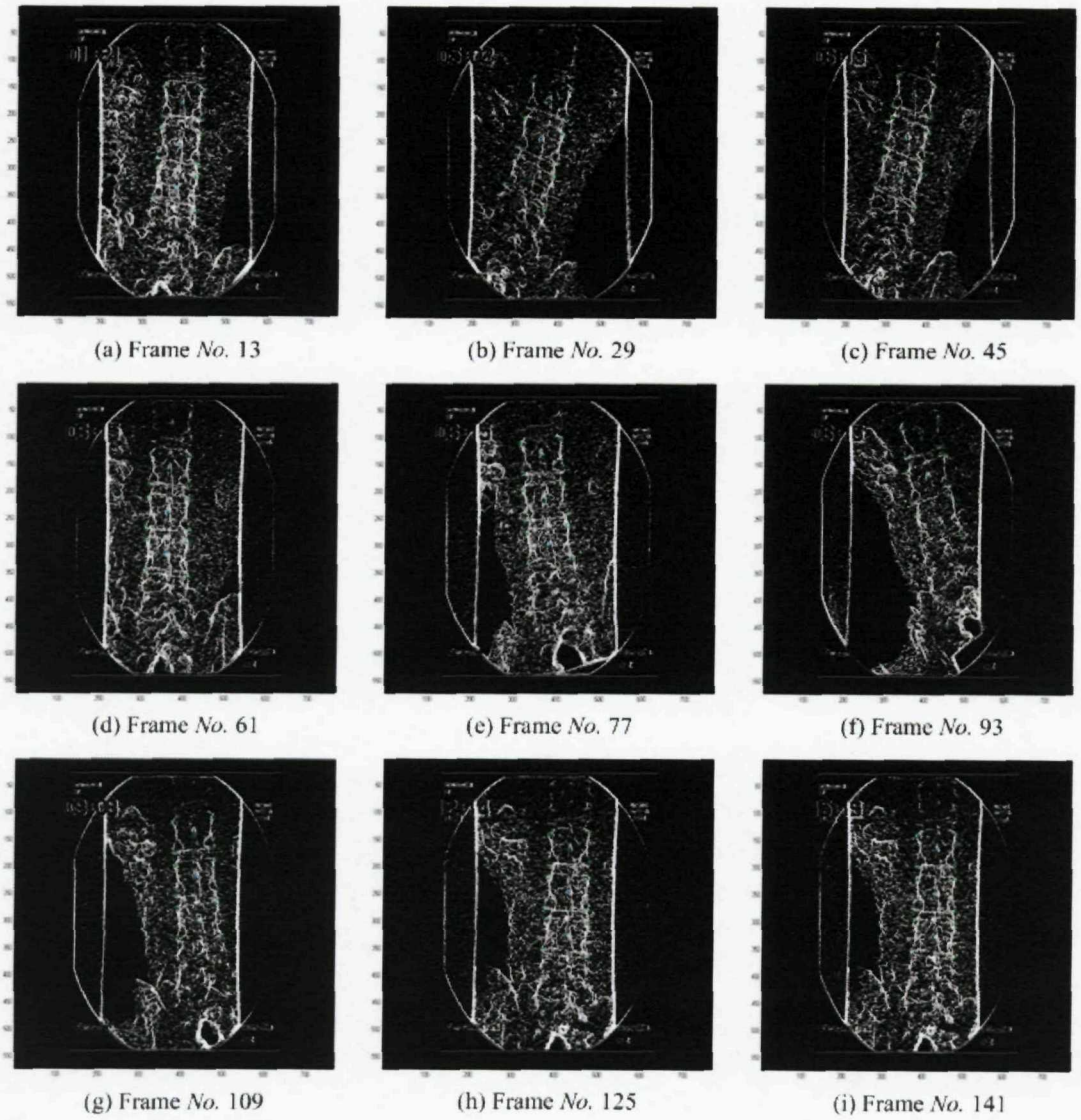

(a) Frame *No.* 13 (b) Frame *No.* 29 (c) Frame *No.* 45

(d) Frame *No.* 61 (e) Frame *No.* 77 (f) Frame *No.* 93

(g) Frame *No.* 109 (h) Frame *No.* 125 (i) Frame *No.* 141

**Figure 7-8** The tracking results of a healthy subject DO lateral bending sequence in the A/P view.

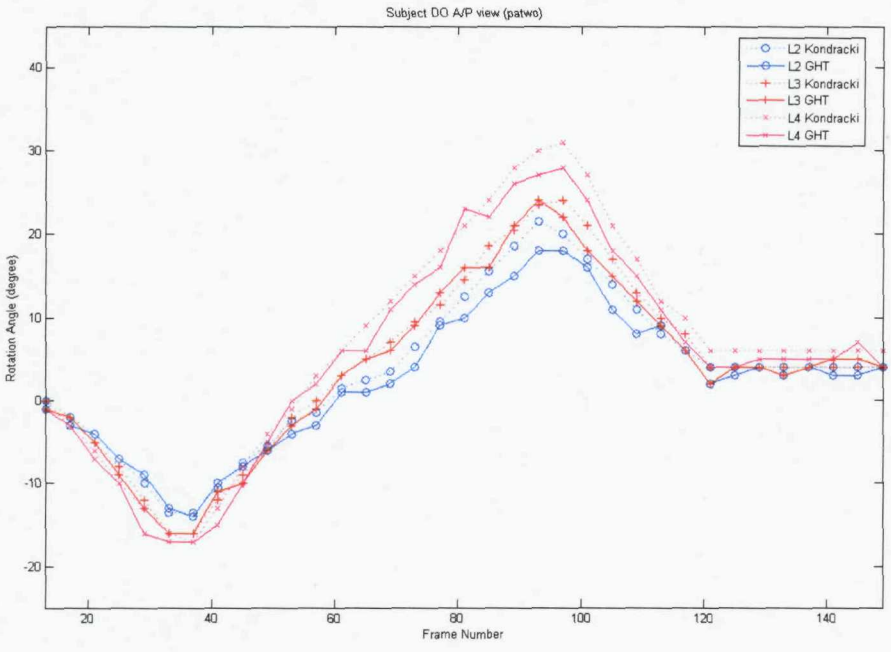


**Figure 7-9** The rotation angles of the vertebrae L2, L3 and L4 versus frame number. Left side lateral bending is positive in the graph.

As discussed for the lateral view sequences, the mean value of the mean of error (MME), the mean value of the standard deviation of error (MSDE) and the mean value of the standard error (MSE) were calculated based on the comparisons of all 14 data sets. The results are shown in Table 7-6. The calculation of '*paone*' data are based on 6 sets of DVF sequences while the calculation of '*patwo*' data are based on 8 sets of DVF sequences. From Table 7-6, it can be seen that the experimental results of our method are close to *Kondracki*'s, which is regarded as the 'gold standard' in this research. The ROM of lateral bending tends to be larger than that of flexion/extension but this probably reflects the experiment design of *Kondracki*. In general, L4 has the worst tracking accuracy because it has the largest range of movement of the three vertebrae followed.

All the discussion above is based on the tracking of only the vertebrae L2, L3 and L4.

**Table 7-5** The rotation angle measurement of lateral bending of subject DO.

| | | | | mean of the rotation (°) | std of the rotation (°) | Range of Motion (°) | mean of the error (°) | std of the error (°) | SE |
|---|---|---|---|---|---|---|---|---|---|
| Subject DO | paone | L2 | *Kondracki* | 3.08 | 10.36 | 38 | -0.64 | 1.36 | 0.292 |
| | | | GHT | 2.43 | 9.37 | 34 | | | |
| | | L3 | *Kondracki* | 5.63 | 12.95 | 47 | -0.89 | 1.45 | 0.331 |
| | | | GHT | 4.74 | 12.01 | 44 | | | |
| | | L4 | *Kondracki* | 6.57 | 14.34 | 51 | -0.61 | 1.38 | 0.294 |
| | | | GHT | 5.97 | 13.57 | 47 | | | |
| | patwo | L2 | *Kondracki* | 3.49 | 9.24 | 35 | -1.06 | 1.21 | 0.273 |
| | | | GHT | 2.43 | 8.46 | 32 | | | |
| | | L3 | *Kondracki* | 4.29 | 10.80 | 40 | -0.49 | 1.10 | 0.204 |
| | | | GHT | 3.80 | 10.60 | 40 | | | |
| | | L4 | *Kondracki* | 6.89 | 13.20 | 48 | -1.34 | 1.26 | 0.314 |
| | | | GHT | 5.54 | 12.85 | 45 | | | |

[+]*std is the standard deviation.*

[+]*SE is the standard error.*

**Table 7-6** The statistical analysis of the tracking results of the rotation angle from the A/P view of 14 DVF sequences from 10 human subjects.

| | paone | | | patwo | | |
|---|---|---|---|---|---|---|
| | L2 | L3 | L4 | L2 | L3 | L4 |
| MME | -0.390 | -0.518 | -0.668 | -0.634 | -0.646 | -0.844 |
| MSDE | 1.278 | 1.428 | 1.51 | 1.173 | 1.291 | 1.425 |
| MSE | 0.2345 | 0.2690 | 0.2890 | 0.2330 | 0.2476 | 0.2831 |

[+]*MME is the mean value of the mean of error.*

[+]*MSDE is the mean value of the standard deviation of error.*

[+]*MSE is the mean value of the standard error.*

## 7.3.2 Intervertebral Angles of the Spine in Lateral Bending

The relative movement of one vertebra and its neighbour was also studied in this project because the movement of the vertebrae in the image sequence is not fixed to a reference point. With the 14 tracking results discussed above, we can calculate the intervertebral angles over the motion sequence. For example, Figure 7-10 shows the relative changes of the intervertebral angles of the spine movement in Figure 7-9. Similar to the rotation angle measurement, the statistical and biomechanical parameters were investigated and shown in Table 7-7. All the statistical analysis of these 14 data sets can be found in the Appendix B-K. Finally, the MME, MSDE and MSE of the intervertebral angle measurement were calculated and are shown in Table 7-8. The MME is less than 0.2°, the MSDE is around 1.2° and the MSE value ranges from 0.19 to 023. Again, promising tracking results were also obtained, which means that our method is reliable and robust.

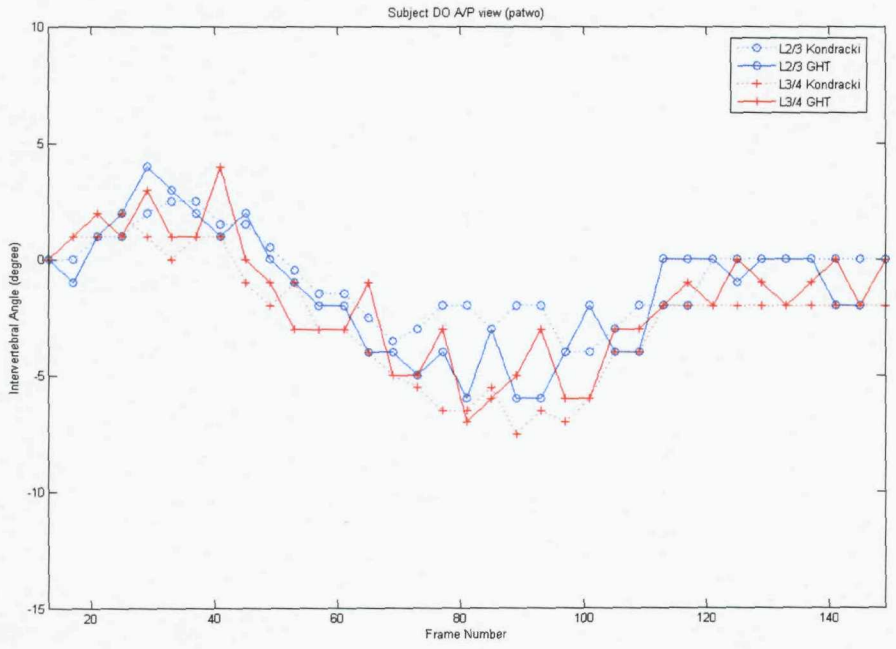


**Figure 7-10** The intervertebral angles of the vertebrae L2/3 and L3/4 versus frame number.

**Table 7-7** The intervertebral angle measurement of lateral bending of subject DO.

| | | | | mean of the IVA (°) | std of the IVA (°) | Range of Motion (°) | mean of the error (°) | std of the error (°) | SE |
|---|---|---|---|---|---|---|---|---|---|
| Subject DO | paone | L2/3 | *Kondracki* | -2.55 | 2.87 | 10 | 0.25 | 1.18 | 0.234 |
| | | | GHT | -2.30 | 3.00 | 13 | | | |
| | | L3/4 | *Kondracki* | -0.93 | 2.30 | 8 | -0.28 | 1.30 | 0.258 |
| | | | GHT | -1.21 | 2.75 | 12 | | | |
| | patwo | L2/3 | *Kondracki* | -0.80 | 1.81 | 6.5 | -0.57 | 1.54 | 0.279 |
| | | | GHT | -1.37 | 2.62 | 10 | | | |
| | | L3/4 | *Kondracki* | -2.6 | 2.65 | 9.5 | 0.86 | 1.27 | 0.260 |
| | | | GHT | -1.74 | 2.67 | 11 | | | |

[+] *IVA is the intervertebral angle.*

[+]*std is the standard deviation.*

[+]*SE is the standard error.*

**Table 7-8** The statistical analysis of the tracking results of the intervertebral angle from the A/P view of 14 DVF sequences from 10 human subjects.

| | laton | | latwo | |
|---|---|---|---|---|
| | L2/3 | L3/4 | L2/3 | L3/4 |
| MME (°) | 0.130 | 0.148 | 0.014 | 0.199 |
| MSDE (°) | 1.193 | 1.263 | 1.133 | 1.153 |
| MSE | 0.2100 | 0.2242 | 0.1971 | 0.2050 |

[+]*MME is the mean value of the mean of error.*

[+]*MSDE is the mean value of the standard deviation of error.*

[+]*MSE is the mean value of the standard error.*

### 7.3.3 Translations of the Spine in Lateral Bending

In addition to the information of rotation angle, our Generalized Hough algorithm also provides the translation of the centre point of the template model (CTM). However, the CTM cannot be used directly to study the translation of the vertebrae in the spinal motion because the CTM does not represent the centre point of the vertebra. Here, we applied the definition of the centre point of the vertebra CV ($x_{CV}$,$y_{CV}$) as mentioned in Section 7.2.3. To avoid the confusion, we show only the CTMs as the cyan points in the tracking result sequences in Figure 7-8 while only the distribution of CVs is displayed in this section. Figures 7-11 and 7-12 show the $x$- and $y$-translation of the centre points of the vertebrae L2, L3 and L4. In addition, the 2-D illustration of the translation of the CVs of the vertebrae L2, L3 and L4 is shown in Figure 7-13. From these figures, it can be seen that the vertebrae do not return to the starting position of the movement, which match as the tracking results for the rotation angle. Again, all 14 tracking results of the translation can be found in the Appendix B-K.

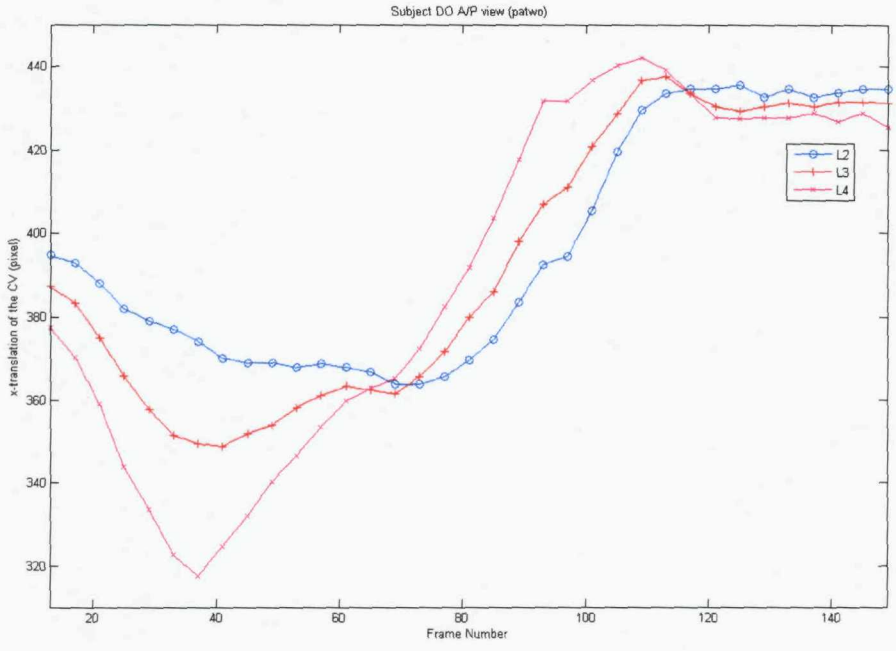


**Figure 7-11** The *x*-translation of the CVs of the vertebrae L2, L3 and L4 versus frame number.

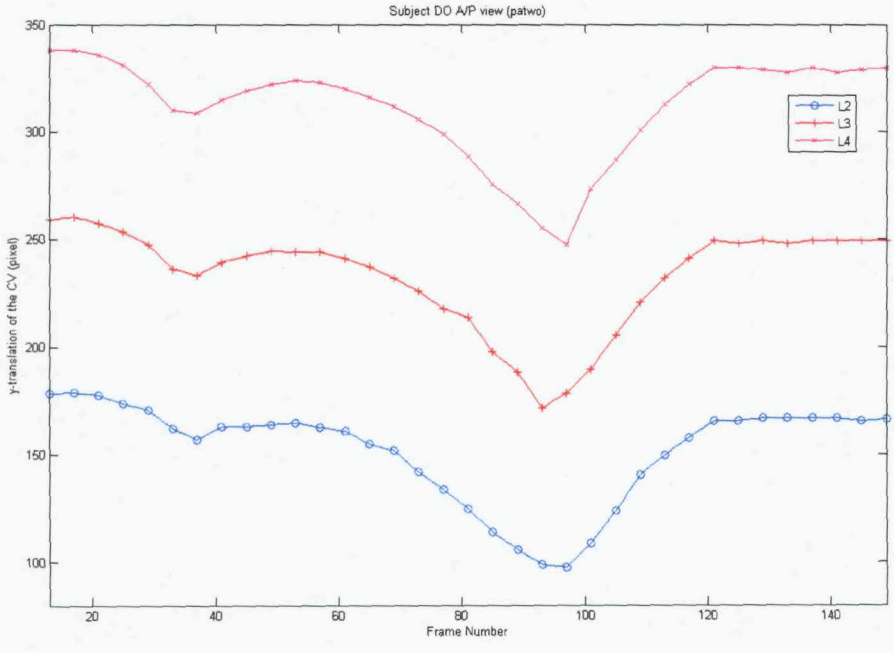


**Figure 7-12** The *y*-translation of the CVs of the vertebrae L2, L3 and L4 versus frame number.

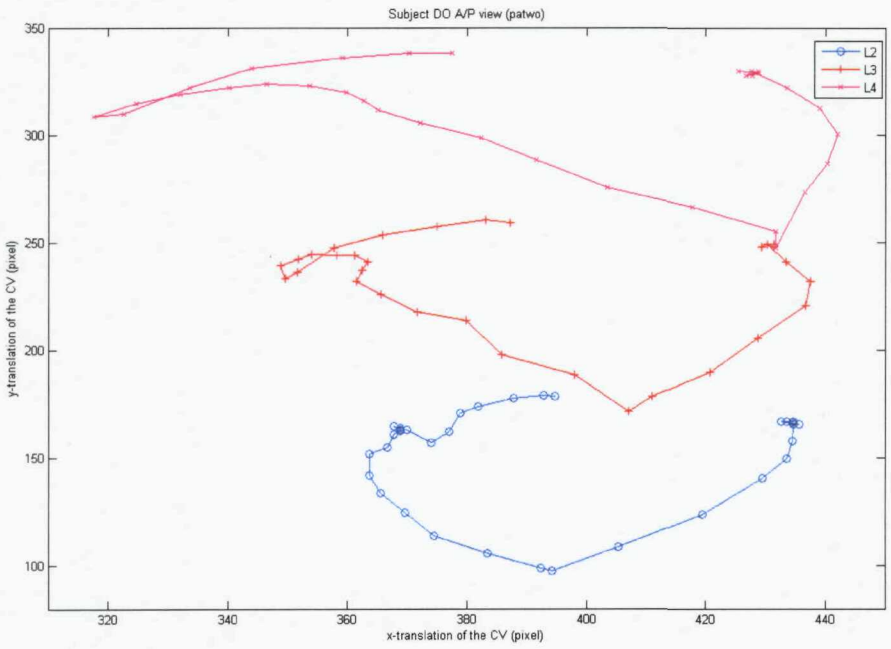


**Figure 7-13** The translation of the CVs of the vertebrae L2, L3 and L4 in 2-D illustration.

## 7.4 Summary

The full tracking results of our method have been shown and discussed in this chapter. Furthermore, the tracking results were compared with those of an experienced clinician, *Kondracki*, manual approach (Kondracki,M. 2001). In his research, he showed that the average values of rotation angles obtained in his study were broadly in agreement with those found in the established literature for *in vivo* studies (Dvorak,J. et al. 1991; Frobin,W. et al. 1996; Hayes,M.A. et al. 1989; Lin,R.M. et al. 1994; Pearcy,M.J. 1985; White,A.A. et al. 1990; Yamamoto,I. et al. 1989). So the rotation data of *Kondracki*'s manual tracking method is assumed to be the 'gold standard' in our research. From the figures and tables shown in this chapter as well as in the Appendix B-K, our results are promising and close to the 'gold standard', which indicates the reliability and robustness of our algorithm. Our method has been successfully tested on 24 sets of sequences out of

40 DVF sequences. In our tracking, the image quality of the vertebral bodies affects the accuracy as expected. So in the tracking of the flexion/extension sequences, the vertebra L3 generally has smaller error values than L2. On the other hand, the range of motion of the vertebrae reduces the precision of the tracking results. So in the tracking of the lateral bending sequences, the vertebra L4 has the lowest accuracy in all three vertebrae since L4 moves in the largest range, generally about 1.5 times that of the L2's range due to the using of the passive motion table where the upper lumbar spine moves less than the bottom parts of the lumbar spine.

# Chapter 8

# Conclusions and Future Work

## 8.1 Conclusions

Low back pain has become one of the serious problems in developed countries and its cost, both economic and social, is enormous. Although low back pain occurs commonly, its diagnosis remains difficult. The reasons could be that low back pain is caused by many different sources and the analysis and diagnosis is difficult due to the complicated structure of the human spine. Research has shown that low back pain is often related to mechanical disorders of the human spine. As a result, the study of spine motion would be very useful in diagnosis low back pain. To date, digital videofluoroscopy (DVF) is currently the only practical technique to obtain continuous spine motion sequences. However due to the low radiation dosage, DVF images have a poorer quality than other medical images and the quality varies across the images.

This research aims to develop a method of automated segmentation and motion tracking for the analysis of lumbar spine motion for low back pain diagnosis. Characterization of the normal motion of the lumbar spine would form the basis for locating a source of damage by identifying any abnormal motion at the vertebral level. The identification of the vertebral contour is the first step in our research. In Chapter 4, we investigated the edge detection results using some conventional edge operators. Both the gradient- and phase-based edge detection methods were tested with DVF images. The edge maps after thresholding from the neutral and extreme positions were presented. The Canny operator

showed the most potential although it cannot yield the vertebral contours of sufficient quality for automated tracking.

In Chapter 5, we applied a wavelet scale multiplication based approach as the edge detector to DVF images of the lumbar spine. Since the previous studies showed that the Canny edge detection has a better performance and the first derivative of Gaussian (FDoG) function is used as edge detector in the Canny algorithm, we used the Mallat wavelet, which is close to the FDoG function, as the mother wavelet to generate the wavelet filter for edge detection. The experimental results on the artificial edge images and on the spine calibration model images were shown to demonstrate the promise of this method. It has been shown that the contour of the spinal vertebrae can be detected automatically in DVF images. The wavelet-based approach was also tested with DVF sequences from human asymptomatic, healthy subjects. With the edge information, biomechanical parameters, such as rotation angle and intervertebral angle, were calculated based on manual landmarking the four corners of each vertebra.

However, manual landmarking is a laborious, time consuming and error-prone procedure. An automated system is desired to reduce the workload and hence creat the possibility of clinical implementation. Chapter 6 addressed the development of an automated tracking technique for spine motion using the Generalized Hough transform. The procedure for the selection of the template model, the building of the Reference Table and the tracking algorithm were described. By locating the maximum value in the Hough space, we obtained the rotation and translation parameters of the spine motion. The proposed method was tested by the DVF image sequences of the calibration model and of the human subjects. In the tracking of the calibration model sequences, the calculated rotation angles were very close to the pre-set values. The error was in the range of -1° to +1° and the standard error was 0.345. For the human subject sequences, our algorithm was successful in tracking the vertebrae L2 and L3 in the lateral images while it had a better performance in the A/P images, where L2-L4 were successfully tracked.

Chapter 7 presented the further results of the tracking with the human subject sequences. Twenty-four out of forty DVF image sequences of 10 healthy subjects were analyzed. Considering some sequences have no 'true' rotation angle values for comparison with the tracking results from our approach, we actually completed nearly 80% (24 out of 31 sequences) of motion analysis. Moreover, we compared our results with those from 'gold standard' measurements made manually by the experienced clinician. The errors of the rotation angles and intervertebral angles were small. The absolute value of MME was less than 1°, and the MSDE was controlled within 1.6°. Furthermore, the standard error generally ranged between 0.22 and 0.30. Finally, the translations of the centre of the vertebrae were also plotted.

## 8.2 Future Work

### 8.2.1 Improvement of the Generalized Hough Transform

The efficiency of our algorithm could be improved for clinical practice. The computational cost and memory required depend on the total number of edge points in the target area of the images, the size of the target area, the possible range of the rotation and translation parameters, and the intervals used for quantizing these parameters. In this project, the Matlab programme requires about two minutes to extract one vertebra in one DVF image frame on a 3GHz PC with 1GB memory. This includes the time consumed by the wavelet scale multiplication method to detect the edge maps. Moreover, considering the usage of the memory, the tracking procedure has to be separated into 3-4 parts for each vertebra due to limitation of the memory available. Therefore, it is necessary to optimize the source code with respect to the computational cost. This improvement would benefit the real-time, clinical application.

There are two main limitations existing in the Generalized Hough transform (GHT) in analyzing motion sequences. First, for an image containing multiple objects, the GHT has to extract them separately. The possible relationships (referred to as spatial information), such as the position constraints, are not taken into account within the implementation of the GHT. Second, for object extraction in a motion sequence, the GHT algorithm is applied frame by frame. This means that the GHT does not take the advantage of the possible relationships between frames (referred to as temporal information) in a motion sequence. A new version of the Hough transform, the Spatio-Temporal Hough transform (STHT), is designed to extend the ability of the Hough transform to handle motion analysis by combining the spatio-temporal information (Zheng,Y. 2002). Thus, it is expected to be more robust for motion analysis with an improved ability to process the poor quality DVF image sequences more quickly. Previous research (Sarkar,S. et al. 2002) has shown promising results on a large variety of motion sequences by using the Hough transform combining the spatio-temporal space. This algorithm would be worth further study in the next stage of this project.

### 8.2.2 Refined Description of Transformation Model and Image Registration Method

In our tracking algorithm, the building of the Reference Table and the matching of the Hough transform do not require manual landmarking. All the calculations are based directly on the edge map obtained from our wavelet-based operator. So the obtaining of good and clear edge maps will greatly benefit the motion tracking. The current study does not succeed in tracking all five lumbar vertebrae due to the lack of integrity of vertebral contour. For example, the tracking of L1 suffers from the low contrast and missing sections of the vertebral contour in many raw images. In the flexion/extension tracking, L4 is usually behind the line of the pelvis which lies across the vertebral body.

Vertebral shape gives crucial cues for accurate tracking. Vertebral contour may be better described using more sophisticate mathematical tools, such as the affine transformation (Cyganski,D. et al. 1987; Sapiro,G. et al. 1993). Because the deformation of vertebral bodies does happen in DVF images, a technique, called the diffeomorphisms (Banyaga,A. 1997; Christensen,G.E. et al. 1996), provides support in the representation of the transformation model. The diffeomorphisms technique has been applied in some research on MRI and CT images (Joshi,S.C. et al. 2000; Marsland,S. et al. 2004) and may be considered as a possible direction in the further development of this project.

With the transformation model, an image registration approach could be applied in motion tracking. The *Lucas-Kanade* method (Lucas,B.D. et al. 1981; Lucas,B.D. 1984) is still one of the most popular techniques of two-frame differential methods for motion estimation, which is also called optical flow. Several researchers have tested the *Lucas-Kanade* algorithm and obtained favorable results in medical image analysis (Zou,X.C. et al. 2007), even in heart echocardiographic image sequences with poor image quality (Baraldi,P. et al. 1996). Another potential technique is the Automated Image Registration (AIR) algorithm (Woods,R.P. et al. 1993). The AIR algorithm has been used in image registration in positron emission tomography (PET), CT and MRI images (Tohka,J. et al. 2004; Vaquero,J.J. et al. 2001) and may be applicable to DVF images.

### 8.2.3 Motion Modelling and Clinical Applications

Another possible area would be the understanding the relationship between the distribution of biomechanical parameters and the spine motion. First, more biomechanical analysis of the spine motion would be of great interest. For example, the instantaneous axis of rotation (IAR) could be studied and the centrode can be built as demonstrated in Section 2.3.3.4. At present, only DVF image sequences from ten healthy subjects were analyzed. In the future, more healthy subjects would be involved in order to build a larger

database of normal spine motion if possible. And then the quantitative analysis and modelling tools would then be used to model the normal spine movement.

Our algorithm has the potential to automate image processing of DVF images from other clinical investigations and so could be also applied to other clinical biomechanical studies, such as the cervical spine, the fingers, or the knee.

Finally, a new imaging technique, which can yield the motion sequence in real time with better image quality and low radiation exposure, is still desired. When this appears or is expected that the techniques developed for the DVF image sequences will achieve even better results.

# References

Adams,M.A. & Dolan,P. (2005) Spine biomechanics. Journal of Biomechanics. 38, 10. 1972-1983.

Aguado,A.S.; Montiel,M.E.; & Nixon,M.S. (1996a) Extracting arbitrary geometric primitives represented by Fourier descriptors. Proceedings of the 13th International Conference on Pattern Recognition 1996. 2, 25-29. 547-551.

Aguado,A.S.; Montiel,M.E.; & Nixon,M.S. (1996b) On using directional information for parameter space decomposition in ellipse detection. Pattern Recognition. 29, 3. 369-381.

Aguado,A.S.; Nixon,M.S.; & Montiel,M.E. (1998) Parameterizing arbitrary shapes via Fourier descriptors for evidence-gathering extraction. Computer Vision and Image Understanding. 69, 2. 202-221.

Allen,R.; Simonis,C.; & Breen,A. (1992) Spine kinematic analysis using digital videofluoroscopy and image processing. IEE Colloquium on Image Processing for Disabled People. 6/1-6/4.

Aydin,T.; Yemez,Y.; Anarim,E.; & Sankur,B. (1996) Multidirectional and multiscale edge detection via M-band wavelet transform. Ieee Transactions on Image Processing. 5, 9. 1370-1377.

Ballard,D.H. (1981) Generalizing the Hough Transform to Detect Arbitrary Shapes. Pattern Recognition. 13, 2. 111-122.

Banyaga,A. (1997) The Structure of Classical Diffeomorphism Groups (Mathematics and Its Applications). 1st edition, Springer.

Bao,P. & Zhang,L. (2003) Noise reduction for magnetic resonance images via adaptive multiscale products thresholding. Ieee Transactions on Medical Imaging. 22, 9. 1089-1099.

Bao,P.; Zhang,L.; & Wu,X.L. (2005) Canny edge detection enhancement by scale multiplication. Ieee Transactions on Pattern Analysis and Machine Intelligence. 27, 9. 1485-14U1.

Baraldi,P.; Sarti,A.; Lamberti,C.; Prandini,A.; & Sgallari,F. (1996) Evaluation of differential optical flow techniques on synthesized echo images. Ieee Transactions on Biomedical Engineering. 43, 3. 259-272.

Basca,C.A.; Talos,M.; & Brad,R. (2005) Randomized Hough Transform for Ellipse Detection with Result Clustering. The International Conference on Computer as a tool 2005, EUROCON 2005. 2, 1397-1400.

Behrens,T.; Rohr,K.; & Stiehl,H.S. (2003) Robust segmentation of tubular structures in 3-D medical images by parametric object detection and tracking. Ieee Transactions on Systems Man and Cybernetics Part B-Cybernetics. 33, 4. 554-561.

Ben Amar,C.; Zaied,M.; & Alimi,A. (2005) Beta wavelets. Synthesis and application to lossy image compression. Advances in Engineering Software. 36, 7. 459-474.

Bergman,R.A.; Afifi,A.K.; & Heidger,P.M. (1989) Atlas of Microscopic Anatomy - A Functional Approach: Companion to Histology and Neuroanatomy. 2Rev Ed, Saunders (W.B.) Co Ltd.

Beus,H.L. & Tiu,S.S.H. (1987) An improved corner detection algorithm based on chain-coded plane curves. Pattern Recognition. 20, 3. 291-296.

Bezerianos,A.; Munteanu,A.; Alexopoulos,D.; Panayiotakis,G.; & Cristea,P. (1995) Wavelet Based Edge Detection Method for Analysis of Coronary Angiograms. Computers in Cardiology 1995. 573-576.

Bhattacharya,P.; Liu,H.Y.; Rosenfeld,A.; & Thompson,S. (2000) Hough-transfonn detection of lines in 3-D space. Pattern Recognition Letters. 21, 9. 843-849.

Bogduk,N. (2005) Clinical anatomy of the lumbar spine and sacrum. 4th ed., Edinburgh: Elsevier Churchill Livingstone.

Booth,S. & Clausi,D.A. (2001) Image segmentation using MRI vertebral cross-sections. Canadian Conference on Electrical and Computer Engineering. 2, 1303-1307.

Breen,A.; Allen,R.; & Morris,A. (1988) An Image-Processing Method for Spine Kinematics - Preliminary Studies. Clinical Biomechanics. 3, 1. 5-10.

Breen,A.C. (1991) The measurement of the kinematics of the human spine using videofluoroscopy and image processing. PhD Thesis, University of Southampton, UK.

Breen,A.C. & Allen,R. (1989a) A digital videofluoroscopy technique for spine kinematics. Journal of Medical Engineering & Technology. 13, 1/2. 109-113.

Breen,A.C. & Allen,R. (1989b) Image presentations for spinal kinematic analysis using digital videofluoroscopy. Third International Conference on Image Processing and its Applications. 343-347.

Breen,A.C.; Allen,R.; & Morris,A. (1987) A computer/X-ray method for measuring spinal segmental movement: a feasibility study. Transactions of the Pacific Consortium for Chiropractic Research. E3.1-3.7.

Breen,A.C.; Brydges,R.; Nunn,H.; Kause,J.; & Allen,R. (1993) Quantitative analysis of lumbar spine intersegmental motion. European Journal of Physical Medicine & Rehabilitation. 3, 5. 182-190.

Breen,A.C.; Humphries,K.; Rice,S.; Cheung,P.; Osborne,A.; & Allen,R. (1991) The analysis of spine kinematics using digital videofluoroscopy. Journal of Biomechanics. 24, 6. 480-

Brejl,M. & Sonka,M. (2000) Object localization and border detection criteria design in edge-based image segmentation: Automated learning from examples. Ieee Transactions on Medical Imaging. 19, 10. 973-985.

Bushberg,J.T. (2002) The essential physics of medical imaging. 2nd ed., Philadelphia: Lippincott Williams & Wilkins.

Canny,J. (1986) A Computational Approach to Edge-Detection. Ieee Transactions on Pattern Analysis and Machine Intelligence. 8, 6. 679-698.

Cao,G.T.; Shi,P.F.; & Hu,B. (2006) Ultrasonic liver discrimination using 2-D phase congruency. Ieee Transactions on Biomedical Engineering. 53, 10. 2116-2119.

Cao,X.; Rodd,M.G.; Deravi,F.; & Wu,Q.M. (1988) Modified Hough transforms for object feature extraction. Engineering Applications of Artificial Intelligence. 1, 2. 97-101.

Chau,C.P. & Siu,W.C. (2004) Adaptive dual-point Hough transform for object recognition. Computer Vision and Image Understanding. 96, 1. 1-16.

Chen,C.H. & Lee,G.G. (1997) On digital mammogram segmentation and microcalcification detection using multiresolution wavelet analysis. Graphical Models and Image Processing. 59, 5. 349-364.

Chen,G.Y.; Bui,T.D.; & Krzyzak,A. (2003) Contour-based handwritten numeral recognition using multiwavelets and neural networks. Pattern Recognition. 36, 7. 1597-1604.

Chen,T.C. & Chung,K.L. (2001) An efficient randomized algorithm for detecting circles. Computer Vision and Image Understanding. 83, 2. 172-191.

Cheng,F. & Hsu,W. (1988) Parallel algorithm for corner finding on digital curves. Pattern Recognition Letters. 8, 1. 47-53.

Cheng,Z. & Liu,Y. (2004) Efficient technique for ellipse detection using restricted randomized Hough transform. Proceedings of the International Conference on Information Technology: Coding and Computing, ICTT 2004. 2, 714-718.

Cho,Z.H. (1993) Foundations of medical imaging. London: Wiley.

Cholewicki,J. & Mcgill,S.M. (1992) Lumbar spine kinematics obtained from videofluoroscopy. Journal of Biomechanics. 25, 7. 801-

Cholewicki,J.; Mcgill,S.M.; Wells,R.P.; & Vernon,H. (1991) Method for Measuring Vertebral Kinematics from Videofluoroscopy. Clinical Biomechanics. 6, 2. 73-78.

Christensen,G.E.; Rabbitt,R.D.; & Miller,M.I. (1996) Deformable templates using large deformation kinematics. Ieee Transactions on Image Processing. 5, 10. 1435-1447.

Cohen,A. & Daubechies,I. (1993) Orthonormal Bases of Compactly Supported Wavelets .3. Better Frequency Resolution. Siam Journal on Mathematical Analysis. 24, 2. 520-527.

Cyganski,D.; Cott,T.A.; Orr,J.A.; & Dodson,R.J. (1987) Development, Implementation, testing and application of an affine transform invariant curvature function. Proceeding of the 1st International Conference of Computer Vision, London. 496-500.

Daubechies,I. (1992) Ten Lectures on Wavelets. 1 edition, SIAM: Society for Industrial and Applied Mathematics.

De Stefano,A.; Allen,R.; & White,P.R. (2004) Noise reduction in spine videofluoroscopic images using the undecimated wavelet transform. Computerized Medical Imaging and Graphics. 28, 8. 453-459.

Deans,S.R. (1983) The Radon Transform and Some of Its Applications. New York: John Wiley & Sons.

Deschenes,S. & Guise,J.D. (2002) Wavelet-based automatic segmentation of the vertebral bodies in digital radiographs. IEEE International Conference on Acoustics, Speech, and Signal Processing (ICASSP '02). 4, 3868-3871.

Duda,R.O. & Hart,P.E. (1972) Use of Hough Transformation to Detect Lines and Curves in Pictures. Communications of the Acm. 15, 1. 11-&.

Dvorak,J.; Panjabi,M.M.; Chang,D.G.; Theiler,R.; & Grob,D. (1991) Functional Radiographic Diagnosis of the Lumbar Spine - Flexion Extension and Lateral Bending. Spine. 16, 5. 562-571.

Dykes,M.I. (2002) Anatomy. 2nd ed., London: Mosby.

Ebraheim,N.A.; Hassan,A.; Lee,M.; & Xu Rongming (2005) Functional anatomy of the lumbar spine. Seminars in Pain Medicine. 2, 3. 131-137.

Ecabert,O. & Thiran,J.P. (2004) Adaptive Hough transform for the detection of natural shapes under weak affine transformations. Pattern Recognition Letters. 25, 12. 1411-1419.

Faghih,F. & Smith,M. (2002) Combining spatial and scale-space techniques for edge detection to provide a spatially adaptive wavelet-based noise filtering algorithm. Ieee Transactions on Image Processing. 11, 9. 1062-1071.

FDA Public Health Advisory (1994) Avoidance of Serious X-Ray-Induced Skin Injuries to Patients During Fluoroscopically-Guided Procedures. http://www.fda.gov/cdrh/fluor.html.

Field,D.J. (1987) Relations Between the Statistics of Natural Images and the Response Properties of Cortical-Cells. Journal of the Optical Society of America A-Optics Image Science and Vision. 4, 12. 2379-2394.

Frobin,W.; Brinckmann,P.; Leivseth,G.; Biggemann,M.; & Reikeras,O. (1996) Precision measurement of segmental motion from flexion-extension radiographs of the lumbar spine. Clinical Biomechanics. 11, 8. 457-465.

Fung,P.F.; Lee,W.S.; & King,I. (1996) Randomized generalized Hough transform for 2-D gray scale object detection. Proceedings of the 13th International Conference on Pattern Recognition 1996. 2, 25-29. 511-515.

Gertzbein,S.D.; Seligman,J.; Holtby,R.; Chan,K.W.; Ogston,N.; Kapasouri,A.; & Tile,M. (1986) Centrode Characteristics of the Lumbar Spine As A Function of Segmental Instability. Clinical Orthopaedics and Related Research. 208. 48-51.

Giles,L.G.F. & Singer,K.P. (2003) Clinical Anatomy and Management of Low Back Pain. Vol. 1, Oxford: Butterworth-Heinemann.

Gonzalez,R.C. (1992) Digital image processing. 3rd ed., Reading, Mass.: Addison-Wesley.

Goswami,J.C. & Chan,A.K. (1999) Fundamentals of Wavelets: Theory, Algorithms, and Applications. NJ: John Wiley & Sons, Inc.

Grant,M.G.; Nixon,M.S.; & Lewis,P.H. (2002) Extracting moving shapes by evidence gathering. Pattern Recognition. 35, 5. 1099-1114.

Guil,N.; Villalba,J.; & Zapata,E.L. (1995) A Fast Hough Transform for Segment Detection. Ieee Transactions on Image Processing. 4, 11. 1541-1548.

Hainline,B. (1995) Low-Back Injury. Clinics in Sports Medicine. 14, 1. 241-265.

Hamou,A.K. & El-Sakka,M.R. (2004) A novel segmentation technique for carotid ultrasound images. Proceedings of IEEE International Conference on Acoustics, Speech, and Signal Processing, 2004.ICASSP '04. 3, 521-524.

Hart,D. & Wall,B.F. (2004) UK population dose from medical X-ray examinations. European Journal of Radiology. 50, 3. 285-291.

Harvey,S.B. & Hukin,D.W.L. (1998) Measurement of lumbar spinal flexion-extension kinematics from lateral radiographs: simulation of the effects of out-of-plane movement and errors in reference point placement. Medical Engineering & Physics. 20, 6. 403-409.

Hayes,M.A.; Howard,T.C.; Gruel,C.R.; & Kopta,J.A. (1989) Roentgenographic Evaluation of Lumbar Spine Flexion-Extension in Asymptomatic Individuals. Spine. 14, 3. 327-331.

Herley,C. & Vetterli,M. (1993) Wavelets and Recursive Filter Banks. Ieee Transactions on Signal Processing. 41, 8. 2536-2556.

Hochamn,M. & Tuli,S. (2005) Cervical Spondylotic Myelopathy: A Review. The Internet Journal of Neurology. 4, 1.

Hough,P.V.C. (1962) Method and Means for Recognising Complex Patterns. US Patent 3969654.

Hu,G. (1995) 3-D object matching in the Hough space. IEEE International Conference on System, Man and Cybernetics."Intelliqent Systems for the 21st Century". 3, 22-25. 2718-2723.

Hubal,M.J.; Ingalls,C.P.; Allen,M.R.; Wenke,J.C.; Hogan,H.A.; & Bloomfield,S.A. (2005) Effects of eccentric exercise training on cortical bone and muscle strength in the estrogen-deficient mouse. Journal of Applied Physiology. 98, 5. 1674-1681.

Humeau,A.; Koitka,A.; Saumet,J.L.; & L'Huillier,J.P. (2002) Wavelet de-noising of laser Doppler reactive hyperemia signals to diagnose peripheral arterial occlusive diseases. Ieee Transactions on Biomedical Engineering. 49, 11. 1369-1371.

Jin,J.S.; Wang,Y.; & Hiller,J. (2000) An adaptive nonlinear diffusion algorithm for filtering medical images. Ieee Transactions on Information Technology in Biomedicine. 4, 4. 298-305.

Joshi,S.C. & Miller,M.I. (2000) Landmark matching via large deformation diffeomorphisms. Ieee Transactions on Image Processing. 9, 8. 1357-1370.

Kaiser,J.F. (1990) On a simple algorithm to calculate the "energy" of a signal. Proceeding of IEEE International Conference of Acoustic Speech Signal Processing. 381-384.

Kalviainen,H. (1996) Motion detection using the randomised Hough transform: exploiting gradient information and detecting multiple moving objects. IEE Proceedings of the Vision, Image and Signal Processing. 143, 6. 361-369.

Kalviainen,H.; Oja,E.; & Xu,L. (1992) Randomized Hough transform applied to translational and rotational motion analysis. Proceedings of the 11th International Conference on Pattern Recognition 1992. 1, 672-675.

Kaspersen,J.H.; Lango,T.; & Lindseth,F. (2001) Wavelet-based edge detection in ultrasound images. Ultrasound in Medicine and Biology. 27, 1. 89-99.

Kass,M.; Witkin,A.; & Terzopoulos,D. (1988) Snakes: Active contour models. International Journal of Computer Vision. 1, 4. 321-331.

Katkovnik,V. (2004) A multiresolution nonparametric regression for spatially adaptive image de-noising. Ieee Signal Processing Letters. 11, 10. 798-801.

Kobatake,H. & Yoshinaga,Y. (1996) Detection of spicules on mammogram based on skeleton analysis. Ieee Transactions on Medical Imaging. 15, 3. 235-245.

Koh,H.K.; Shen,W.; Shuter,B.; & Kassim,A.A. (2006) Segmentation of Kidney Cortex in MRI Studies using a Constrained Morphological 3D H-maxima Transform. The 9th International Conference on Control, Automation, Robotics and Vision 2006. 1-5.

Kondracki,M. (1991) Source of error: an estimation of instantaneous axes of rotation in spinal joints. Msc Thesis, University of Strathclyde.

Kondracki,M. (2001) Clinical applications of digitised videofluoroscopy in the lumbar spine. PhD Thesis, University of Southampton, UK.

Kovesi,P. (1999) Image Features From Phase Congruency. Videre: A Journal of Computer Vision Research. 1, 3. MIT Press: 1-27.

Kovesi,P. (2001) Invariant Measures of Image Features From Phase Information. http://www.csse.uwa.edu.au/~pk/Research/research.html.

Kuhl,F.P. & Giardina,C.R. (1982) Elliptic Fourier Features of A Closed Contour. Computer Graphics and Image Processing. 18, 3. 236-258.

Kyan,M.J.; Guan,L.; Arnison,M.R.; & Cogswell,C.J. (2001) Feature extraction of chromosomes from 3-D confocal microscope images. Ieee Transactions on Biomedical Engineering. 48, 11. 1306-1318.

Lee,J.S.; Sun,Y.N.; & Chen,C.H. (1995) Multiscale Corner Detection by Using Wavelet Transform. Ieee Transactions on Image Processing. 4, 1. 100-104.

Lee,Y. & Kozaitis,S.P. (2000) Multiresolution gradient-based edge detection in noisy images using wavelet domain filters. Optical Engineering. 39, 9. 2405-2412.

Li,H.L. & Chakrabarti,C. (1996) Motion estimation of two-dimensional objects based on the straight line Hough transform: A new approach. Pattern Recognition. 29, 8. 1245-1258.

Li,H.W.; Lavin,M.A.; & Lemaster,R.J. (1986) Fast Hough Transform - A Hierarchical Approach. Computer Vision Graphics and Image Processing. 36, 2-3. 139-161.

Li,J.; Zhou,L.; Yu,H.; & Liang,H. (2006) Multi-region Segmentation of CT Images Based on Information Fusion. The 1st Conference on Industrial Electronics and Applications, 2006. 1-6.

Lin,R.M.; Yu,C.Y.; Chang,Z.J.; Lee,C.C.; & Su,F.C. (1994) Flexion-Extension Rhythm in the Lumbosacral Spine. Spine. 19, 19. 2204-2209.

Linton,S.J. (2000) A review of psychological risk factors in back and neck pain. Spine. 25, 9. 1148-1156.

Littlewood,C. & May,S. (2007) Measurement of range of movement in the lumbar spine-what methods are valid? A systematic review. Physiotherapy. 93, 3. 201-211.

Liu,H.C. & Srinath,M.D. (1990) Partial Shape Classification Using Contour Matching in Distance Transformation. Ieee Transactions on Pattern Analysis and Machine Intelligence. 12, 11. 1072-1079.

Liu,Z.; Forsyth,D.S.; Marincak,A.; & Vesley,P. (2006) Automated rivet detection in the EOL image for aircraft lap joints inspection. Ndt & e International. 39, 6. 441-448.

Lu,W.; Tan,J.L.; & Floyd,R. (2005) Automated fetal head detection and measurement in ultrasound images by iterative randomized Hough transform. Ultrasound in Medicine and Biology. 31, 7. 929-936.

Lucas,B.D. (1984) Generalized Image Matching by the Method of Differences. Doctoral dissertation, Robotics Institute, Carnegie Mellon University.

Lucas,B.D. & Kanade,T. (1981) An iterative image registration technique with an application to stereo vision. Proceedings of Imaging understanding workshop. 121-130.

Mallat,S.G. (1999) A wavelet tour of signal processing. 2nd ed., San Diego, Ca.: Academic.

Mallat,S.G. (1989a) A Theory for Multiresolution Signal Decomposition - the Wavelet Representation. Ieee Transactions on Pattern Analysis and Machine Intelligence. 11, 7. 674-693.

Mallat,S.G. (1989b) Multifrequency Channel Decompositions of Images and Wavelet Models. Ieee Transactions on Acoustics Speech and Signal Processing. 37, 12. 2091-2110.

Mallat,S.G. & Hwang,W.L. (1992a) Singularity Detection and Processing with Wavelets. Ieee Transactions on Information Theory. 38, 2. 617-643.

Mallat,S.G. & Zhong,S. (1992b) Characterization of Signals from Multiscale Edges. Ieee Transactions on Pattern Analysis and Machine Intelligence. 14, 7. 710-732.

Mao,J.; Xiong,R.; & Ding,W. (2006) A Compound and Robust Algorithm for Ellipse Detection. The 16th International Conference on Artificial Reality and Telexistence Workshops 2006, ICAT '06. 381-386.

Marsland,S. & Twining,C.J. (2004) Constructing diffeomorphic representations for the groupwise analysis of nonrigid registrations of medical images. Ieee Transactions on Medical Imaging. 23, 8. 1006-1020.

McLaughlin,R.A. (1996) Randomized Hough transform: better ellipse detection. Proceedings of IEEE TENCON Digital Signal Processing Applications 1996, TENCON '96. 1, 26-29. 409-414.

McLaughlin,R.A. (1998) Randomized Hough Transform: Improved ellipse detection with comparison. Pattern Recognition Letters. 19, 3-4. 299-305.

Merlin,P.M. & Farber,D.J. (1975) Parallel Mechanism for Detecting Curves in Pictures. Ieee Transactions on Computers. C 24, 1. 96-98.

Montret,L.; Ekerol,H.; & Hodgson,D.C. (1994) Object Tracking at Field Rate Using the Hough Transform. Mechatronics. 4, 3. 331-337.

Morrone,M.C. & Owens,R.A. (1987) Feature Detection from Local Energy. Pattern Recognition Letters. 6, 5. 303-313.

Morrone,M.C.; Ross,J.; Burr,D.C.; & Owens,R. (1986) Mach Bands Are Phase Dependent. Nature. 324, 6094. 250-253.

Muggleton,J.M. & Allen,R. (1997) Automatic location of vertebrae in digitized videofluoroscopic images of the lumbar spine. Medical Engineering & Physics. 19, 1. 77-89.

Muggleton,J.M. & Allen,R. (1998) Insights into the measurement of vertebral translation in the sagittal plane. Medical Engineering & Physics. 20, 1. 21-32.

Nixon,M.S. & Aguado,A.S. (2002) Feature extraction and image processing. Oxford: Newnes.

Novosad,J.; Cheriet,F.; Petit,Y.; & Labelle,H. (2004) Three-dimensional (3-D) reconstruction of the spine from a single X-ray image and prior vertebra models. Ieee Transactions on Biomedical Engineering. 51, 9. 1628-1639.

Oliver,J. & Middleditch,A. (1995) Function Anatomy of the Spine. Oxford: Butterworth-Heinemann.

Oxford Radfliffe Hospital (1995) Back Pain. Bandolier Journal, http://www.jr2.ox.ac.uk/bandolier/band19/b19-1/html.

Patel,A.T. & Ogle,A.A. (2000) Diagnosis and Management of Acute Low Back Pain. American Academy of Family Physcians. 6, 6.

Pearcy,M.J. (1985) Stereo radiography of lumbar spine motion. Acta Orthopaedica Scandinavica. 56, 45 p.

Persoon,E. & Fu,K.S. (1986) Shape-Discrimination Using Fourier Descriptors. Ieee Transactions on Pattern Analysis and Machine Intelligence. 8, 3. 388-397.

Phillips,D.L. (2004) The Economic Costs of Low Back Pain.

Polyak,N. & Pearlman,W.A. (1998) Filters and filter banks for periodic signals, the Zak transform and fast wavelet decomposition. Ieee Transactions on Signal Processing. 46, 857-873.

Polyak,N. & Pearlman,W.A. (2000) A new flexible bi-orthogonal filter design for multiresolution filterbanks with application to image compression. Ieee Transactions on Signal Processing. 48, 8. 2279-2288.

Popov,T.V. (2006) EPR imaging characterization of natural and synthetic materials. Joint Advanced Student School (JASS), Course 6: Molecular Imaging in Natural Science and Medicine.

Qin,Q.; Wang,W.; & Chen Sijin (2004) The application of dyadic wavelet in the RS building image edge detection. International Conference on Image Processing, 2004.ICIP '04. 3, 1731-1734.

RadiologyInfo (2007) Radiation Exposure in X-ray Examinations . http://www.radiologyinfo.org/en/pdf/sfty_xray.pdf.

Rakesh,R.R.; Chaudhuri,P.; & Murthy,C.A. (2004) Thresholding in edge detection: A statistical approach. Ieee Transactions on Image Processing. 13, 7. 927-936.

Rattarangsi,A. & Chin,R.T. (1992) Scale-Based Detection of Corners of Planar Curves. Ieee Transactions on Pattern Analysis and Machine Intelligence. 14, 4. 430-449.

Rosenfeld,A. (1969) Picture Processing by Computer. London, UK: Academic Press.

Rosenfeld,A. & Johnston,E. (1973) Angle Detection on Digital Curves. Ieee Transactions on Computers. C 22, 9. 875-878.

Rosenfeld,A. & Weszka,J.S. (1975) An improved method of angle detection on digital curve. IEEE Transactions on Computer. 24, 940-941.

Rosenfeld.A (1970) A Nonlinear Edge Detection Technique. Proceedings of the Institute of Electrical and Electronics Engineers. 58, 5. 814-&.

Rosenfeld.A & Thurston,M. (1971) Edge and Curve Detection for Visual Scene Analysis. Ieee Transactions on Computers. C 20, 5. 562-&.

Sadler,B.M. & Swami,A. (1999) Analysis of multiscale products for step detection and estimation. Ieee Transactions on Information Theory. 45, 3. 1043-1051.

Sapiro,G. & Tannenbaum,A. (1993) Affine Invariant Scale-Space. International Journal of Computer Vision. 11, 1. 25-44.

Sarkar,S.; Majchrzak,D.; & Korimilli,K. (2002) Perceptual organization based computational model for robust segmentation of moving objects. Computer Vision and Image Understanding. 86, 3. 141-170.

Scales,N.; Kerry,C.; & Prize,M. (2004) Automated image segmentation for breast analysis using infrared images. Proceedings of the 26th Annual International Conference on the Engineering in Medicine and Biology Society, 2004.EMBC 2004. 3, 1737-1740.

Shih,M.Y. & Tseng,D.C. (2005) A wavelet-based multiresolution edge detection and tracking. Image and Vision Computing. 23, 4. 441-451.

Shrimpton,P.C.; Miller,H.C.; Lewis,M.A.; & Dunn,M. (2003) Doses from Computed Tomography (CT) examinations in the UK - 2003 Review. National Radiological Protection Board (NRPB) Report. NRPB-W67,

Simhadri,K.K.; Iyengar,S.S.; Holyer,R.J.; Lybanon,M.; & Zachary,J.M. (1998) Wavelet-based feature extraction from oceanographic images. Ieee Transactions on Geoscience and Remote Sensing. 36, 3. 767-778.

Simonis,C. & Allen,R. (1992) Determination Of Instantaneous Centres Of Rotation: Parallel Application In Spine Kinematics. Proceedings of the Annual International Conference of the IEEE Engineering in Medicine and Biology Society. 1, 39-40.

Smith,M.J.T. & Barnwell,T.P. (1986) Exact Reconstruction Techniques for Tree-Structured Subband Coders. Ieee Transactions on Acoustics Speech and Signal Processing. 34, 3. 434-441.

Song,Y.; He,K.; Zhou,J.; Liu,Z.; & Li,K. (2004) Multi-resolution Feature Extraction in Human Face. Proceedings of International Conference on Information Acquisition, 2004. 417-421.

Sonka,M.; Hlavac,V.; & Boyle,R. (1993) Image processing, analysis and machine vision. London: Chapman & Hall.

Srinivasan,P. & Jamieson,L.H. (1998) High-quality audio compression using an adaptive wavelet packet decomposition and psychoacoustic modeling. Ieee Transactions on Signal Processing. 46, 4. 1085-1093.

Staib,L.H. & Duncan,J.S. (1992) Boundary Finding with Parametrically Deformable Models. Ieee Transactions on Pattern Analysis and Machine Intelligence. 14, 11. 1061-1075.

Stockman,G.C. & Agrawala,A.K. (1977) Equivalence of Hough Curve Detection to Template Matching. Communications of the Acm. 20, 11. 820-822.

Strang,G. (1989a) Wavelets and Dilation Equations: A Brief Introduction. Saim Review. 31, 613-627.

Strang,G. (1989b) Wavelets and Dilation Equations: A Brief Introduction. Saim Review. 31, 613-627.

Strang,G. (1993a) Wavelet Transforms Versus Fourier-Transforms. Bulletin of the American Mathematical Society. 28, 2. 288-305.

Strang,G. (1993b) Wavelet Transforms Versus Fourier-Transforms. Bulletin of the American Mathematical Society. 28, 2. 288-305.

Strela,V.; Heller,P.N.; Strang,G.; Topiwala,P.; & Heil,C. (1999) The application of multiwavelet filterbanks to image processing. Ieee Transactions on Image Processing. 8, 4. 548-563.

Takahashi,S.; Passuti,N.; & Delecrin,J. (1997) Interpretation and utility of traction radiography in scoliosis surgery - Analysis of patients treated with Cotrel-Dubousset instrumentation. Spine. 22, 21. 2542-2546.

Tang,Y.Y.; Yang,L.H.; Liu,J.; & Ma,H. (1999) Wavelet Theory and Its Application to Pattern Recognition. Singapore: World Scientific.

Tang,Y.Y.; Yang,L.H.; & Liu,J.M. (2000) Characterization of Dirac-structure edges with wavelet transform. Ieee Transactions on Systems Man and Cybernetics Part B-Cybernetics. 30, 1. 93-109.

Tezmol,A.; Sari-Sarraf,H.; Mitra,S.; Long,R.; & Gururajan,A. (2002) Customized Hough transform for robust segmentation of cervical vertebrae from X-ray images. The 5th IEEE Southwest Symposium on Image Analysis and Interpretation, 2002. 7-9. 224-228.

Tohka,J.; Kivimaki,A.; Reilhac,A.; Mykkanen,J.; & Ruotsalainen,U. (2004) Assessment of brain surface extraction from PET images using Monte Carlo simulations. Ieee Transactions on Nuclear Science. 51, 5. 2641-2648.

Tsantis,S.; Dimitropoulos,N.; Cavouras,D.; & Nikiforidis,G. (2006) A hybrid multi-scale model for thyroid nodule boundary detection on ultrasound images. Computer Methods and Programs in Biomedicine.

Ulrich,M.; Steger,C.; & Baumgartner,A. (2003) Real-time object recognition using a modified generalized Hough transform. Pattern Recognition. 36, 11. 2557-2570.

Van Herp,G.; Rowe,P.; Salter,P.; & Paul,J.P. (2000) Three-dimensional lumbar spinal kinematics: a study of range of movement in 100 healthy subjects aged 20 to 60+ years. Rheumatology. 39, 12. 1337-1340.

Vaquero,J.J.; Desco,M.; Pascau,J.; Santos,A.; Lee,I.; Seidel,J.; & Green,M.V. (2001) PET, CT, and MR image registration of the rat brain and skull. Ieee Transactions on Nuclear Science. 48, 4. 1440-1445.

Vaughan,J.J.; Winter,R.B.; & Lonstein,J.E. (1996) Comparison of the use of supine bending and traction radiographs in the selection of the fusion area in adolescent idiopathic scoliosis. Spine. 21, 21. 2469-2473.

Vetterli,M. & Herley,C. (1992) Wavelets and filter banks: Theory and design. Ieee Transactions on Signal Processing. 40, 2207-2232.

Wang,J.Z.; Li,J.; Gray,R.M.; & Wiederhold,G. (2001) Unsupervised multiresolution segmentation for images with low depth of field. Ieee Transactions on Pattern Analysis and Machine Intelligence. 23, 1. 85-90.

White,A.A. & Panjabi,M.M. (1978) The basic kinematics of the human spine. A review of past and current knowledge. Spine. 3, 1. 12-20.

White,A.A. & Panjabi,M.M. (1990) Clinical biomechanics of the spine. 2nd ed., Philadelphia: J.B. Lippincott.

Williams,D.J. & Shah,M. (1992) A Fast Algorithm for Active Contours and Curvature Estimation. Cvgip-Image Understanding. 55, 1. 14-26.

Wong,A. & Clausi,D.A. (2007) ARRSI: Automatic registration of remote-sensing images. Ieee Transactions on Geoscience and Remote Sensing. 45, 5. 1483-1493.

Wong,S.F.; Wong,K.Y.K.; Wong,W.N.K.; Leong,C.Y.J.; & Luk,D.K.K. (2004) Tracking lumbar vertebrae in digital videofluoroscopic video automatically. Medical Imaging and Augmented Reality, Proceedings. 3150, 154-162.

Woods,R.P.; Mazziotta,J.C.; & Cherry,S.R. (1993) Mri-Pet Registration with Automated Algorithm. Journal of Computer Assisted Tomography. 17, 4. 536-546.

Xu,L. & Oja,E. (1993) Randomized Hough Transform (Rht) - Basic Mechanisms, Algorithms, and Computational Complexities. Cvgip-Image Understanding. 57, 2. 131-154.

Xu,L.; Oja,E.; & Kultanen,P. (1990) A New Curve Detection Method - Randomized Hough Transform (Rht). Pattern Recognition Letters. 11, 5. 331-338.

Xu,W.; Xia,S.; Xiao,M.; & Duan,H. (2005) A Model-based Algorithm for Mass Segmentation in Mammograms. The 27th Annual International Conference of the Engineering in Medicine and Biology Society 2005.IEEE-EMBS 2005. 2543-2546.

Xu,Y.S.; Weaver,J.B.; Healy,D.M.; & Lu,J. (1994) Wavelet Transform Domain Filters - A Spatially Selective Noise Filtration Technique. Ieee Transactions on Image Processing. 3, 6. 747-758.

Yamamoto,I.; Panjabi,M.M.; Crisco,T.; & Oxland,T. (1989) Three-dimensional movements of the whole lumbar spine and lumbosacral joint. Spine. 14, 1256-1260.

Yang,L.H.; You,X.; Haralick,R.M.; & Phillips,I.T. (2001) Characterization of Dirac edge with new wavelet transform. Proceedings of the 2nd International Conference of Wavelet Applications. 1, 872-878.

Yao,J.; Kharma,N.; & Grogono,P. (2004) Fast robust GA-based ellipse detection. Proceedings of the 17th International Conference on Pattern Recognition 2004, ICPR 2004. 2, 23-26. 859-862.

Yezzi,A.; Kichenassamy,S.; Kumar,A.; Olver,P.; & Tannenbaum,A. (1997) A geometric snake model for segmentation of medical imagery. Ieee Transactions on Medical Imaging. 16, 2. 199-209.

Yue,Z.J.; Goshtasby,A.; & Ackerman,L.V. (1995) Automatic Detection of Rib Borders in Chest Radiographs. Ieee Transactions on Medical Imaging. 14, 3. 525-536.

Yuen,S.Y. & Ma,C.H. (1997) An investigation of the nature of parameterization for the Hough transform. Pattern Recognition. 30, 6. 1009-1040.

Zana,F. & Klein,J.C. (1999) A multimodal registration algorithm of eye fundus images using vessels detection and Hough transform. Ieee Transactions on Medical Imaging. 18, 5. 419-428.

Zhang,L. & Bao,P. (2002) Edge detection by scale multiplication in wavelet domain. Pattern Recognition Letters. 23, 14. 1771-1784.

Zhang,L.; Bao,P.; & Wu,X.L. (2005) Multiscale LMMSE-based image denoising with optimal wavelet selection. Ieee Transactions on Circuits and Systems for Video Technology. 15, 4. 469-481.

Zheng,Y. (2002) Automated segmentation of lumbar vertebrae for the measurement of spine kinematics. PhD Thesis, University of Southampton, UK.

Zheng,Y.; Nixon,M.S.; & Allen,R. (2001) Automatic lumbar vertebrae segmentation in fluoroscopic images via optimised concurrent Hough transform. Proceedings of the 23rd Annual International Conference of the IEEE Engineering in Medicine and Biology Society. 3, 2653-2656.

Zheng,Y.; Nixon,M.S.; & Allen,R. (2003) Lumbar spine visualisation based on kinematic analysis from videofluoroscopic imaging. Medical Engineering & Physics. 25, 3. 171-179.

Zheng,Y.L.; Nixon,M.S.; & Allen,R. (2004) Automated segmentation of lumbar vertebrae in digital videofluoroscopic images. Ieee Transactions on Medical Imaging. 23, 1. 45-52.

Zhong,J.M. & Ning,R.L. (2005) Image denoising based on wavelets and multifractals for singularity detection. Ieee Transactions on Image Processing. 14, 10. 1435-1447.

Zou,X.C.; Zhao,X.B.; & Feng,Y. (2007) An Efficient Medical Image Registration Algorithm Based on Gradient Descent. IEEE/ICME International Conference on Complex Medical Engineering, 2007.CME 2007. 363-369.

# Appendices

## Appendix A. Edge Detection Results

### A.1 Canny Edge Detector

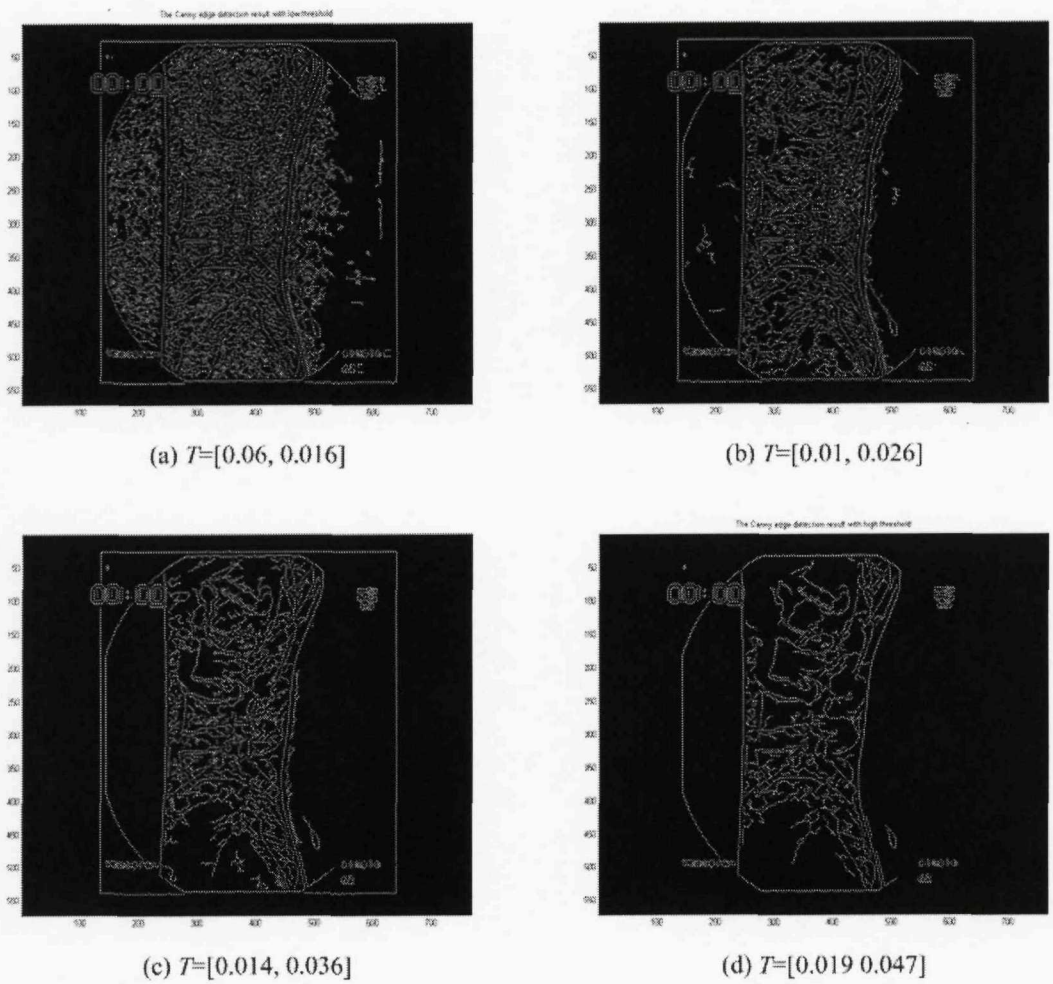

(a) $T$=[0.06, 0.016]

(b) $T$=[0.01, 0.026]

(c) $T$=[0.014, 0.036]

(d) $T$=[0.019 0.047]

**Figure Appendix-1** Edge maps using Canny edge detector.

## A.2 Laplaican of Gaussian Edge Detector

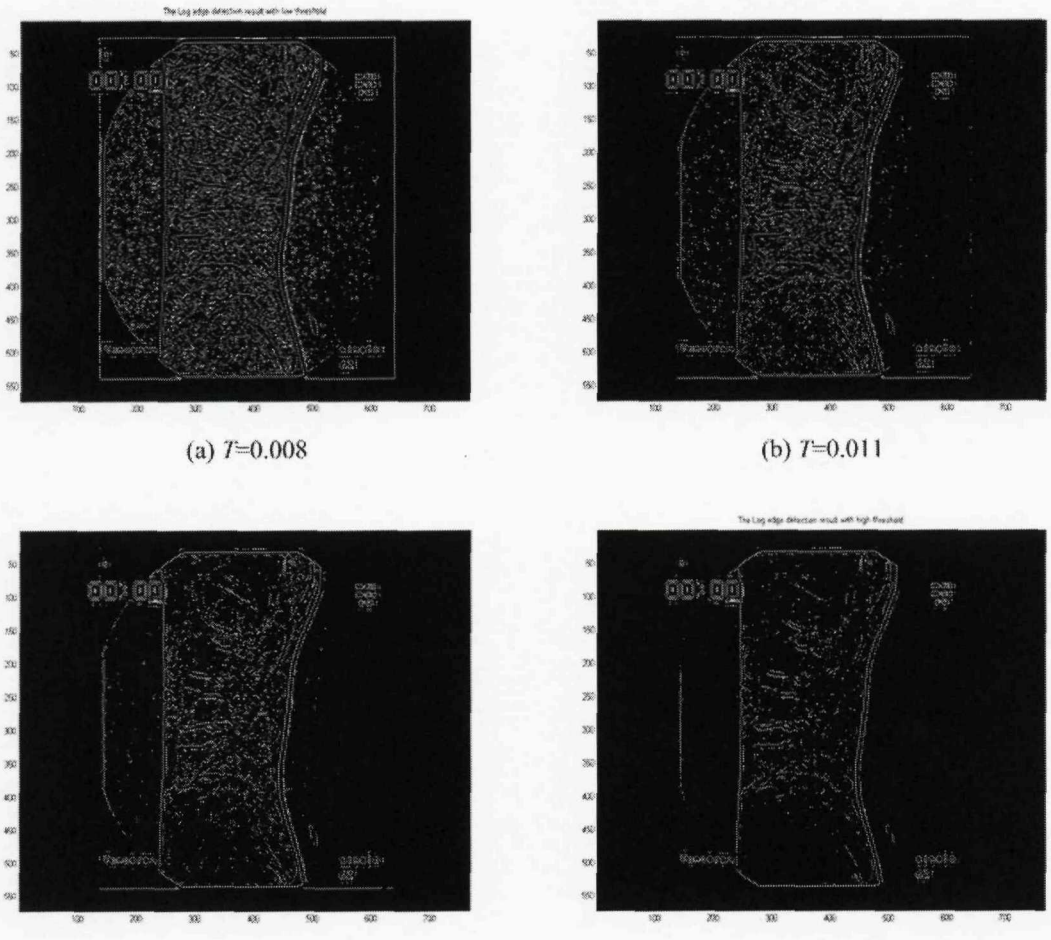

(a) $T$=0.008 (b) $T$=0.011

(c) $T$=0.014 (d) $T$=0.017

**Figure Appendix-2** Edge maps using Laplacian of Gaussian edge detector.

## A.3 Phase Congruency Edge Detector

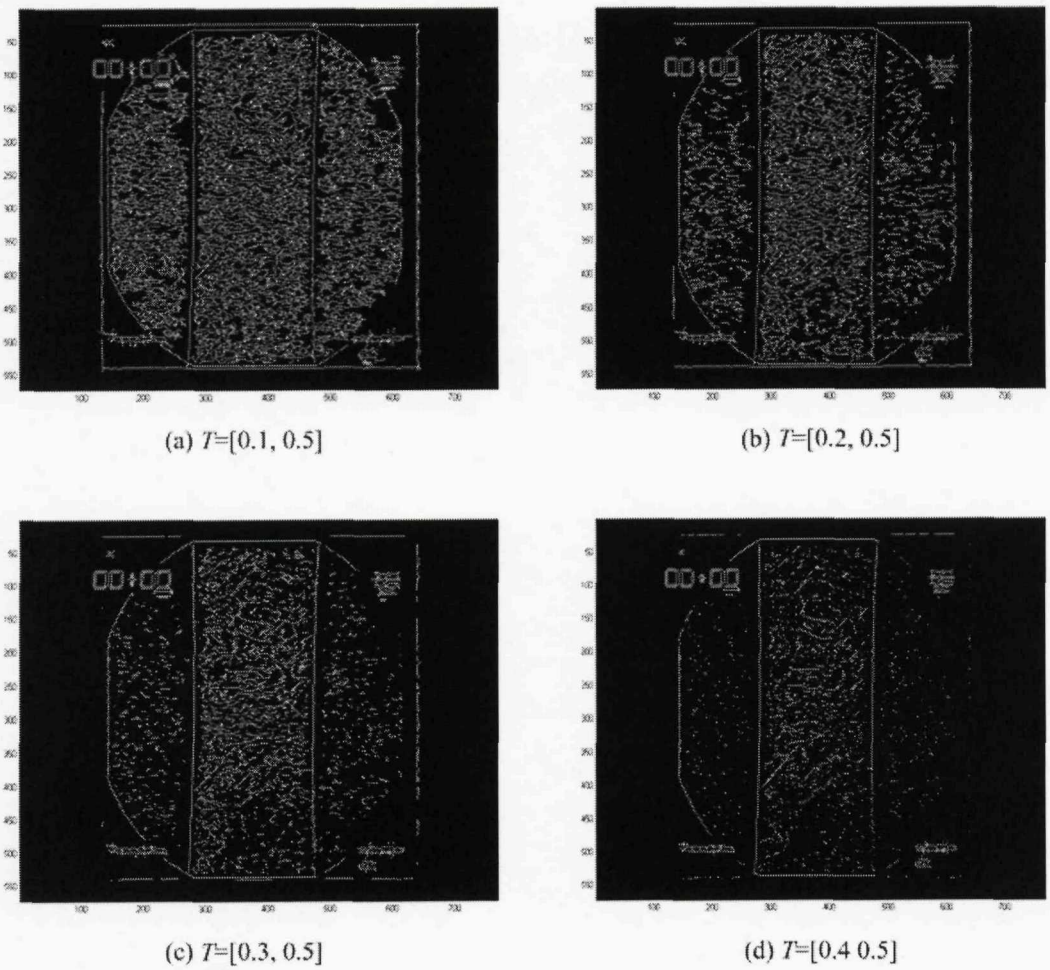

(a) $T$=[0.1, 0.5] (b) $T$=[0.2, 0.5]

(c) $T$=[0.3, 0.5] (d) $T$=[0.4 0.5]

**Figure Appendix-3** Edge maps using Phase congruency edge detector.

# Appendix B. Subject BM

## B.1 Motion Tracking of the DVF Images from the Lateral View

**Table Appendix-1** The measurement of rotation angles of subject BM.

| | | | | mean of the rotation (°) | std of the rotation (°) | Range of Motion (°) | mean of the error (°) | std of the error (°) | SE |
|---|---|---|---|---|---|---|---|---|---|
| Subject BM | laton | L2 | *Kondracki* | 3.37 | 6.26 | 24.5 | -1.46 | 0.83 | 0.287 |
| | | | GHT | 1.91 | 5.90 | 22 | | | |
| | | L3 | *Kondracki* | 5.83 | 8.92 | 31.5 | -0.80 | 1.07 | 0.227 |
| | | | GHT | 5.03 | 8.75 | 30 | | | |

[+]*std is the standard deviation.*

[+]*SE is the standard error.*

**Table Appendix-2** The measurement of intervertebral angles of subject BM.

| | | | | mean of the IVA (°) | std of the IVA (°) | Range of Motion (°) | mean of error (°) | std of the error (°) | SE |
|---|---|---|---|---|---|---|---|---|---|
| Subject BM | L2/3 | laton | *Kondracki* | -2.46 | 3.07 | 11 | -0.80 | 0.93 | 0.208 |
| | | | GHT | -3.26 | 3.48 | 11 | | | |

[+] *IVA is the intervertebral angle.*

[+]*std is the standard deviation.*

[+]*SE is the standard error.*

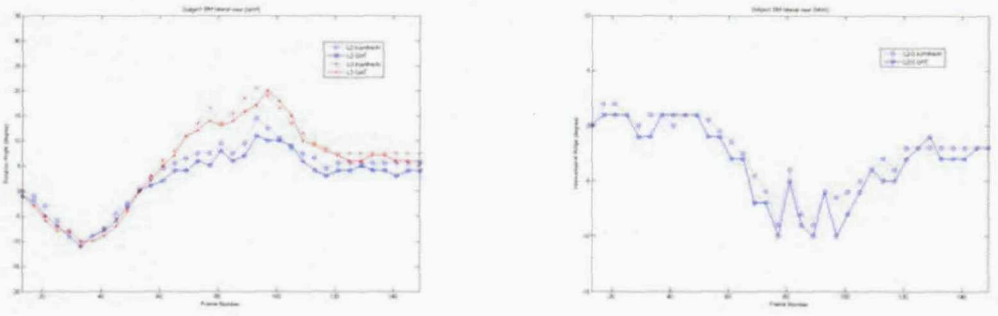

(a) (b)

**Figure Appendix-4** The rotation and intervertebral angles of the vertebrae L2 and L3 versus frame number of subject BM '*laton*'. (a) The rotation angles. (b) The intervertebral angles.

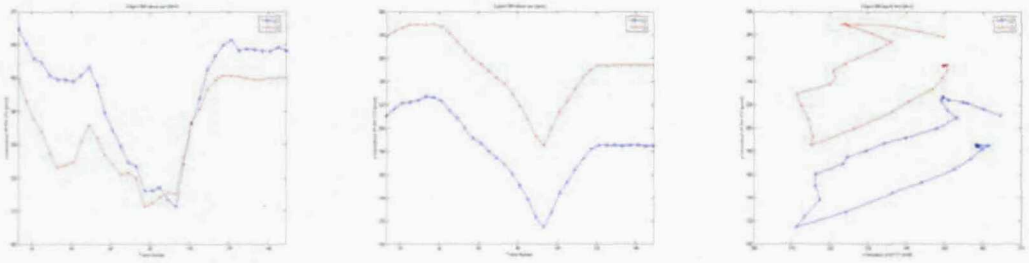

(a) (b) (c)

**Figure Appendix-5** The translation of the vertebrae L2 and L3 versus frame number of subject BM '*laton*'. (a) *x*-translation of the centre points of the vertebrae. (b) *y*-translation of the centre point of the vertebrae. (c) The translation of the centre points of the vertebrae in 2-D.

## B.2 Motion Tracking of the DVF Images from the Anterior/Posterior View

**Table Appendix-3** The measurement of rotation angles of subject BM.

| | | | | mean of the rotation (°) | std of the rotation (°) | Range of Motion (°) | mean of the error (°) | std of the error (°) | SE |
|---|---|---|---|---|---|---|---|---|---|
| Subject BM | paone | L2 | *Kondracki* | 5.48 | 13.48 | 46.5 | -0.63 | 1.38 | 0.258 |
| | | | GHT | 4.83 | 12.65 | 42 | | | |
| | | L3 | *Kondracki* | 5.63 | 15.30 | 55 | -0.60 | 1.54 | 0.280 |
| | | | GHT | 5.03 | 14.29 | 51 | | | |
| | | L4 | *Kondracki* | 9.87 | 17.94 | 63.5 | -1.04 | 1.47 | 0.306 |
| | | | GHT | 8.83 | 16.88 | 59 | | | |
| | patwo | L2 | *Kondracki* | 8.89 | 14.06 | 48 | -1.31 | 1.08 | 0.290 |
| | | | GHT | 7.57 | 13.38 | 46 | | | |
| | | L3 | *Kondracki* | 9.66 | 15.46 | 55 | -1.14 | 1.19 | 0.281 |
| | | | GHT | 8.51 | 14.76 | 51 | | | |
| | | L4 | *Kondracki* | 9.80 | 18.22 | 65 | -0.77 | 1.44 | 0.277 |
| | | | GHT | 9.03 | 17.50 | 60 | | | |

[+]*std is the standard deviation.*

[+]*SE is the standard error.*

**Table Appendix-4** The measurement of intervertebral angles of subject BM.

| | | | | mean of the IVA (°) | std of the IVA (°) | Range of Motion (°) | mean of the error (°) | std of the error (°) | SE |
|---|---|---|---|---|---|---|---|---|---|
| Subject BM | paone | L2/3 | *Kondracki* | -0.17 | 2.21 | 8.5 | -0.03 | 1.24 | 0.209 |
| | | | GHT | -0.20 | 2.10 | 9 | | | |
| | | L3/4 | *Kondracki* | -4.24 | 2.98 | 9.5 | 0.44 | 1.20 | 0.216 |
| | | | GHT | -3.80 | 3.11 | 12 | | | |
| | patwo | L2/3 | *Kondracki* | -0.77 | 1.80 | 8 | -0.17 | 0.95 | 0.164 |
| | | | GHT | -0.94 | 2.15 | 9 | | | |
| | | L3/4 | *Kondracki* | -0.14 | 2.92 | 11 | -0.37 | 1.17 | 0.207 |
| | | | GHT | -0.51 | 3.05 | 10 | | | |

† *IVA is the intervertebral angle.*

† *std is the standard deviation.*

† *SE is the standard error.*

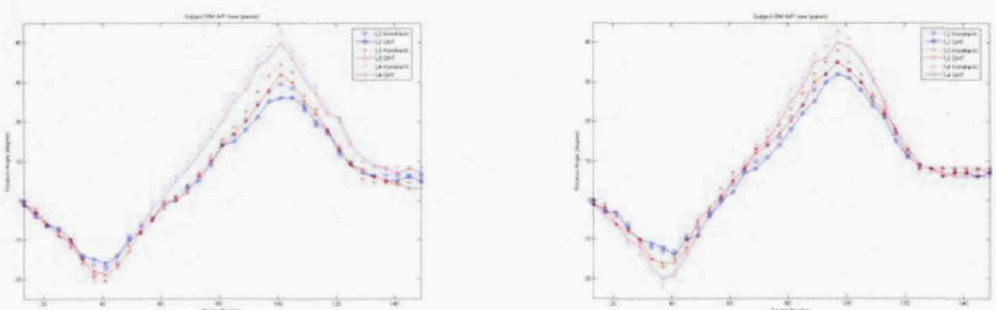

(a) (b)

**Figure Appendix-6** The rotation angles of the vertebrae L2, L3 and L4 versus frame number of subject BM. (a) Data set '*paone*'. (b) Data set '*patwo*'.

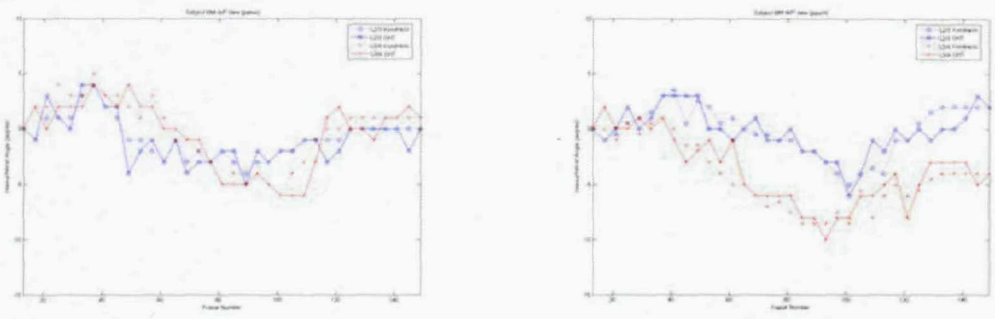

(a) (b)

**Figure Appendix-7** The intervertebral angles of the vertebrae L2/3 and L3/4 versus frame number of subject BM. (a) Data set '*paone*'. (b) Data set '*patwo*'.

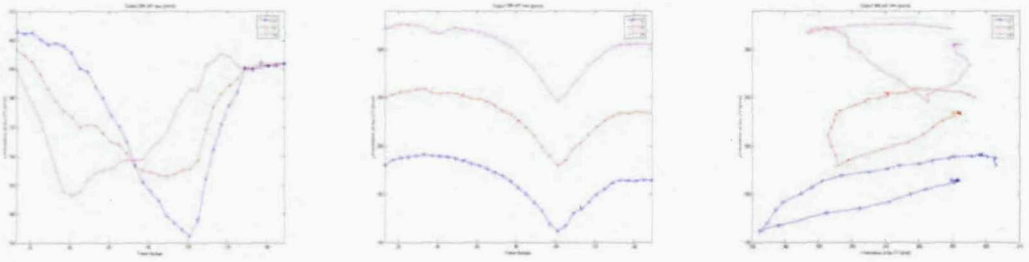

(a) (b) (c)

**Figure Appendix-8** The translation of the vertebrae L2, L3 and L4 versus frame number of subject BM '*paone*'. (a) *x*-translation of the centre points of the vertebrae. (b) *y*-translation of the centre point of the vertebrae. (c) The translation of the centre points of the vertebrae in 2-D.

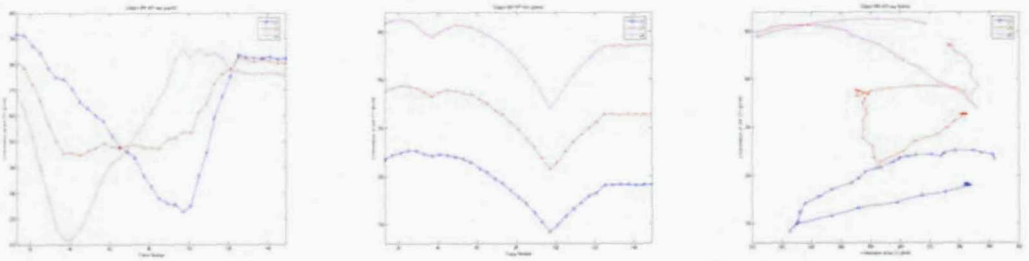

(a) (b) (c)

**Figure Appendix-9** The translation of the vertebrae L2, L3 and L4 versus frame number of subject BM '*patwo*'. (a) *x*-translation of the centre points of the vertebrae. (b) *y*-translation of the centre point of the vertebrae. (c) The translation of the centre points of the vertebrae in 2-D.

# Appendix C. Subject CR

## C.1 Motion Tracking of the DVF Images from the Lateral View

**Table Appendix-5** The measurement of rotation angles of subject CR.

| | | | | mean of the rotation (°) | std of the rotation (°) | Range of Motion (°) | mean of the error (°) | std of the error (°) | SE |
|---|---|---|---|---|---|---|---|---|---|
| Subject CR | latwo | L2 | *Kondracki* | 4.51 | 5.93 | 20.5 | -0.46 | 1.68 | 0.295 |
| | | | GHT | 4.06 | 6.80 | 24 | | | |
| | | L3 | *Kondracki* | 5.63 | 9.82 | 32 | -0.63 | 1.40 | 0.259 |
| | | | GHT | 5.00 | 9.47 | 30 | | | |

[+]*std is the standard deviation.*

[+]*SE is the standard error.*

**Table Appendix-6** The measurement of intervertebral angles of subject CR.

| | | | | mean of the IVA (°) | std of the IVA (°) | Range of Motion (°) | mean of error (°) | std of the error (°) | SE |
|---|---|---|---|---|---|---|---|---|---|
| Subject CR | L2/3 | latwo | *Kondracki* | -1.11 | 4.20 | 13.5 | 0.17 | 2.16 | 0.366 |
| | | | GHT | -0.94 | 3.10 | 13 | | | |

[+] *IVA is the intervertebral angle.*

[+]*std is the standard deviation.*

[+]*SE is the standard error.*

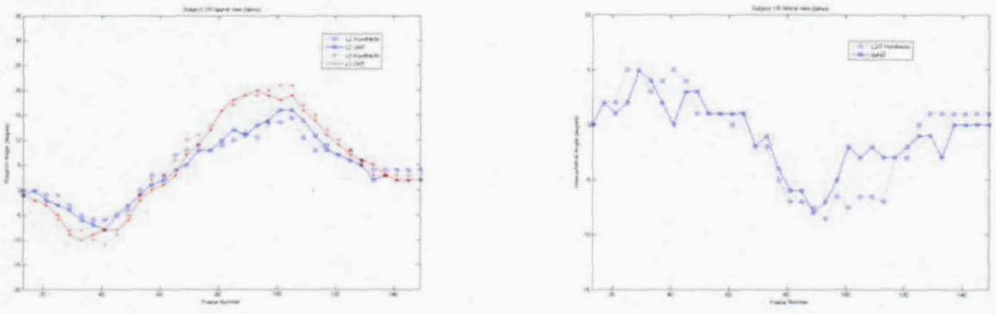

(a) (b)

**Figure Appendix-10** The rotation and intervertebral angles of the vertebrae L2 and L3 versus frame number of subject CR '*latwo*'. (a) The rotation angles. (b) The intervertebral angles.

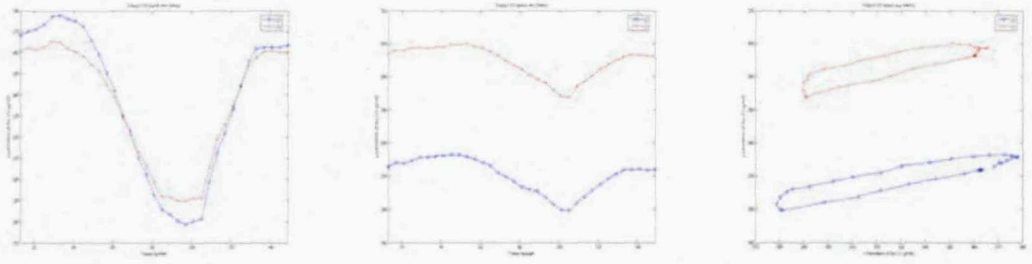

(a) (b) (c)

**Figure Appendix-11** The translation of the vertebrae L2 and L3 versus frame number of subject CR '*latwo*'. (a) *x*-translation of the centre points of the vertebrae. (b) *y*-translation of the centre point of the vertebrae. (c) The translation of the centre points of the vertebrae in 2-D.

## C.2 Motion Tracking of the DVF Images from the Anterior/Posterior View

**Table Appendix-7** The measurement of rotation angles of subject CR.

| | | | | mean of the rotation (°) | std of the rotation (°) | Range of Motion (°) | mean of the error (°) | std of the error (°) | SE |
|---|---|---|---|---|---|---|---|---|---|
| Subject CR | patwo | L2 | *Kondracki* | 2.39 | 9.54 | 32.5 | -0.30 | 1.30 | 0.227 |
| | | | GHT | 2.09 | 8.59 | 29 | | | |
| | | L3 | *Kondracki* | 5.43 | 14.52 | 48 | -0.69 | 1.44 | 0.270 |
| | | | GHT | 4.74 | 13.31 | 45 | | | |
| | | L4 | *Kondracki* | 4.71 | 16.77 | 55 | -0.77 | 1.52 | 0.288 |
| | | | GHT | 3.94 | 15.71 | 52 | | | |

[+]*std is the standard deviation.*

[+]*SE is the standard error.*

**Table Appendix-8** The measurement of intervertebral angles of subject CR.

| | | | | mean of the IVA (°) | std of the IVA (°) | Range of Motion (°) | mean of the error (°) | std of the error (°) | SE |
|---|---|---|---|---|---|---|---|---|---|
| Subject CR | patwo | L2/3 | *Kondracki* | -3.04 | 5.05 | 16.5 | 0.39 | 0.99 | 0.180 |
| | | | GHT | -2.66 | 4.83 | 17 | | | |
| | | L3/4 | *Kondracki* | 0.71 | 2.78 | 8.5 | 0.09 | 1.06 | 0.180 |
| | | | GHT | 0.80 | 3.00 | 10 | | | |

[+] *IVA is the intervertebral angle.*

[+]*std is the standard deviation.*

[+]*SE is the standard error.*

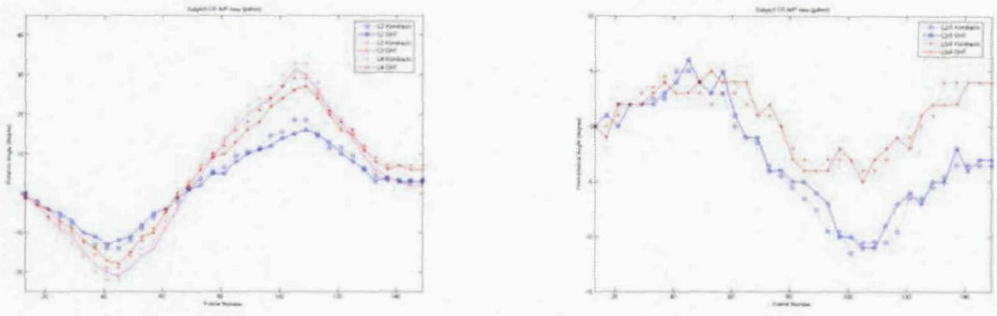

(a) (b)

**Figure Appendix-12** The rotation and intervertebral angles of the vertebrae L2, L3 and L4 versus frame number of subject CR '*patwo*'. (a) The rotation angles. (b) The intervertebral angles.

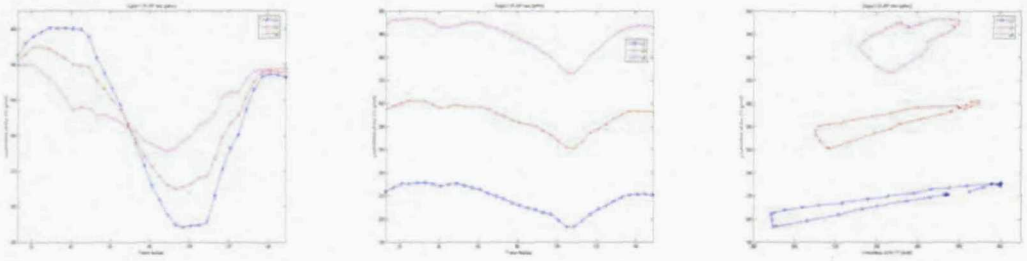

(a) (b) (c)

**Figure Appendix-13** The translation of the vertebrae L2, L3 and L4 versus frame number of subject CR '*patwo*'. (a) *x*-translation of the centre points of the vertebrae. (b) *y*-translation of the centre point of the vertebrae. (c) The translation of the centre points of the vertebrae in 2-D.

# Appendix D. Subject DE

## D.1 Motion Tracking of the DVF Images from the Lateral View

**Table Appendix-9** The measurement of rotation angles of subject DE.

| | | | | mean of the rotation (°) | std of the rotation (°) | Range of Motion (°) | mean of the error (°) | std of the error (°) | SE |
|---|---|---|---|---|---|---|---|---|---|
| Subject DE | laton | L2 | *Kondracki* | 3.86 | 6.59 | 23 | -1.09 | 1.09 | 0.263 |
| | | | GHT | 2.77 | 6.60 | 24 | | | |
| | | L3 | *Kondracki* | 7.53 | 9.48 | 30.5 | -1.50 | 1.36 | 0.345 |
| | | | GHT | 6.03 | 8.75 | 30 | | | |

[+]*std is the standard deviation.*

[+]*SE is the standard error.*

**Table Appendix-10** The measurement of intervertebral angles of subject DE.

| | | | | mean of the IVA (°) | std of the IVA (°) | Range of Motion (°) | mean of error (°) | std of the error (°) | SE |
|---|---|---|---|---|---|---|---|---|---|
| Subject DE | L2/3 | laton | *Kondracki* | -3.67 | 3.22 | 10.5 | 0.41 | 1.48 | 0.255 |
| | | | GHT | -3.26 | 2.58 | 10 | | | |

[+] *IVA is the intervertebral angle.*

[+]*std is the standard deviation.*

[+]*SE is the standard error.*

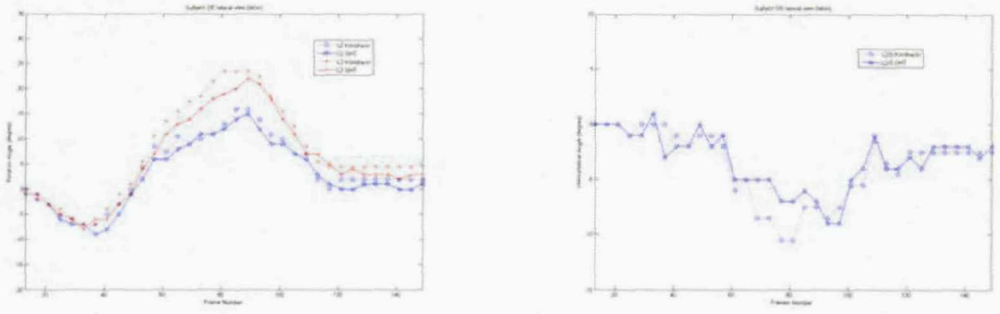

(a) (b)

**Figure Appendix-14** The rotation and intervertebral angles of the vertebrae L2 and L3 versus frame number of subject DE '*laton*'. (a) The rotation angles. (b) The intervertebral angles.

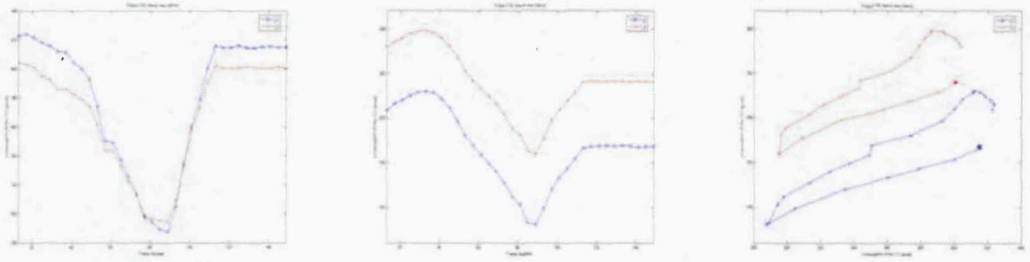

(a) (b) (c)

**Figure Appendix-15** The translation of the vertebrae L2 and L3 versus frame number of subject DE '*laton*'. (a) *x*-translation of the centre points of the vertebrae. (b) *y*-translation of the centre point of the vertebrae. (c) The translation of the centre points of the vertebrae in 2-D.

## D.2 Motion Tracking of the DVF Images from the Anterior/Posterior View

**Table Appendix-11** The measurement of rotation angles of subject DE.

| | | | | mean of the rotation (°) | std of the rotation (°) | Range of Motion (°) | mean of the error (°) | std of the error (°) | SE |
|---|---|---|---|---|---|---|---|---|---|
| Subject DE | paone | L2 | *Kondracki* | 2.46 | 10.28 | 38.5 | -0.31 | 1.21 | 0.212 |
| | | | GHT | 2.14 | 9.83 | 35 | | | |
| | | L3 | *Kondracki* | 5.69 | 13.61 | 51 | -0.74 | 1.29 | 0.252 |
| | | | GHT | 4.94 | 12.64 | 48 | | | |
| | | L4 | *Kondracki* | 6.83 | 16.50 | 62 | -0.77 | 1.53 | 0.291 |
| | | | GHT | 6.06 | 15.61 | 59 | | | |

[+]*std is the standard deviation.*

[+]*SE is the standard error.*

**Table Appendix-12** The measurement of intervertebral angles of subject DE.

| | | | | mean of the IVA (°) | std of the IVA (°) | Range of Motion (°) | mean of the error (°) | std of the error (°) | SE |
|---|---|---|---|---|---|---|---|---|---|
| Subject DE | paone | L2/3 | *Kondracki* | -3.23 | 3.58 | 12.5 | 0.43 | 1.13 | 0.205 |
| | | | GHT | -2.80 | 3.21 | 13 | | | |
| | | L3/4 | *Kondracki* | -1.14 | 3.12 | 11 | 0.03 | 1.14 | 0.192 |
| | | | GHT | -1.11 | 3.29 | 11 | | | |

[+] *IVA is the intervertebral angle.*

[+]*std is the standard deviation.*

[+]*SE is the standard error.*

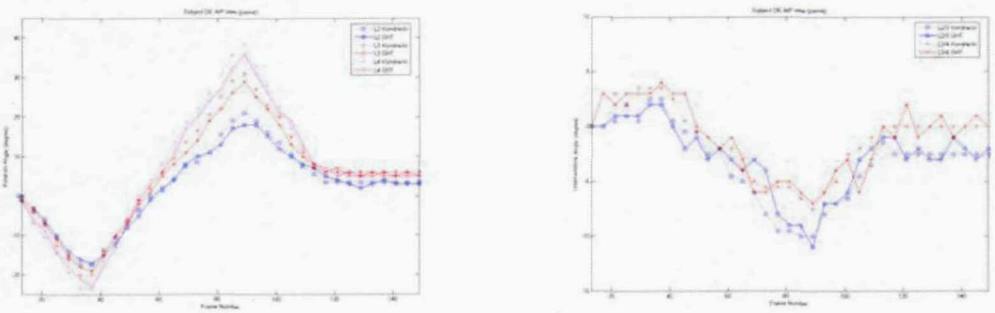

(a) (b)

**Figure Appendix-16** The rotation and intervertebral angles of the vertebrae L2, L3 and L4 versus frame number of subject DE '*paone*'. (a) The rotation angles. (b) The intervertebral angles.

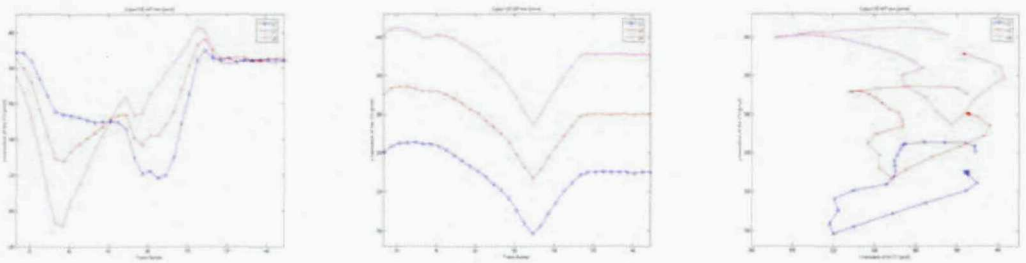

(a) (b) (c)

**Figure Appendix-17** The translation of the vertebrae L2, L3 and L4 versus frame number of subject DE '*paone*'. (a) *x*-translation of the centre points of the vertebrae. (b) *y*-translation of the centre point of the vertebrae. (c) The translation of the centre points of the vertebrae in 2-D.

# AppendixE. Subject DO

## E.1 Motion Tracking of the DVF Images from the Lateral View

**Table Appendix-13** The measurement of rotation angles of subject DO.

| | | | | mean of the rotation (°) | std of the rotation (°) | Range of Motion (°) | mean of the error (°) | std of the error (°) | SE |
|---|---|---|---|---|---|---|---|---|---|
| Subject DO | laton | L2 | *Kondracki* | 5.96 | 9.44 | 35 | -0.91 | 1.45 | 0.253 |
| | | | GHT | 5.04 | 8.73 | 35 | | | |
| | | L3 | *Kondracki* | 8.98 | 11.44 | 41 | -0.93 | 1.46 | 0.256 |
| | | | GHT | 8.04 | 10.83 | 39 | | | |
| | latwo | L2 | *Kondracki* | 5.37 | 8.01 | 28 | -1.23 | 1.28 | 0.302 |
| | | | GHT | 4.14 | 7.59 | 25 | | | |
| | | L3 | *Kondracki* | 7.54 | 10.71 | 37 | -0.80 | 1.55 | 0.296 |
| | | | GHT | 6.74 | 10.15 | 35 | | | |

[+]*std is the standard deviation.*

[+]*SE is the standard error.*

**Table Appendix-14** The measurement of intervertebral angles of subject DO

| | | | | mean of the IVA (°) | std of the IVA (°) | Range of Motion (°) | mean of error (°) | std of the error (°) | SE |
|---|---|---|---|---|---|---|---|---|---|
| Subject DO | L2/3 | laton | *Kondracki* | -3.02 | 2.17 | 7 | 0.02 | 1.82 | 0.269 |
| | | | GHT | -3.00 | 2.83 | 11 | | | |
| | | latwo | *Kondracki* | -2.17 | 2.99 | 8.5 | -0.43 | 1.60 | 0.280 |
| | | | GHT | -2.60 | 2.90 | 10 | | | |

[+] *IVA is the intervertebral angle.*

[+] *std is the standard deviation.*

[+] *SE is the standard error.*

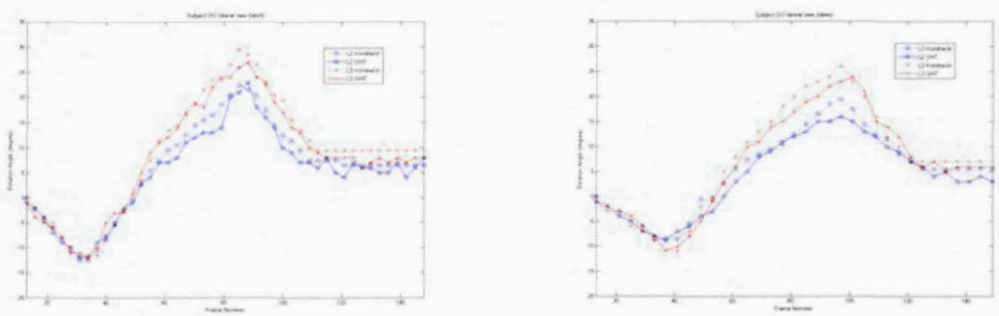

(a) (b)

**Figure Appendix-18** The rotation angles of the vertebrae L2 and L3 versus frame number of subject DO. (a) Data set '*laton*'. (b) Data set '*latwo*'.

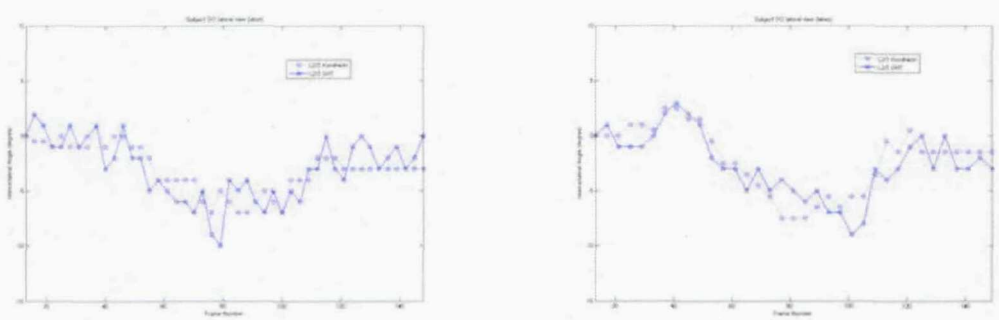

(a) (b)

**Figure Appendix-19** The intervertebral angles of the vertebrae L2/3 versus frame number of subject DO. (a) Data set '*laton*'. (b) Data set '*latwo*'.

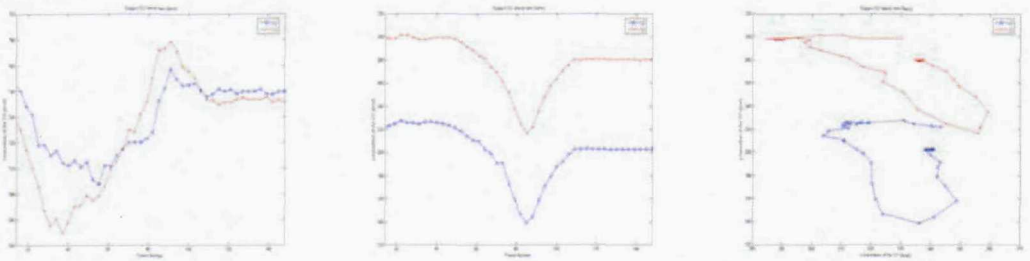

(a) (b) (c)

**Figure Appendix-20** The translation of the vertebrae L2 and L3 versus frame number of subject DO '*laton*'. (a) *x*-translation of the centre points of the vertebrae. (b) *y*-translation of the centre point of the vertebrae. (c) The translation of the centre points of the vertebrae in 2-D.

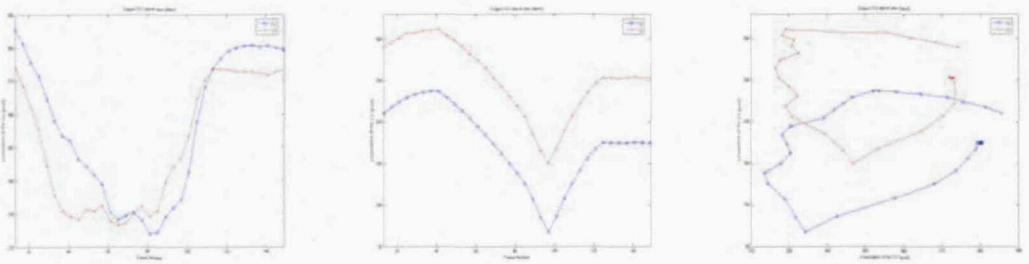

(a) (b) (c)

**Figure Appendix-21** The translation of the vertebrae L2 and L3 versus frame number of subject DO '*latwo*'. (a) *x*-translation of the centre points of the vertebrae. (b) *y*-translation of the centre point of the vertebrae. (c) The translation of the centre points of the vertebrae in 2-D.

## E.2 Motion Tracking of the DVF Images from the Anterior/Posterior View

**Table Appendix-15** The measurement of rotation angles of subject DO.

| | | | | mean of the rotation (°) | std of the rotation (°) | Range of Motion (°) | mean of the error (°) | std of the error (°) | SE |
|---|---|---|---|---|---|---|---|---|---|
| Subject DO | paone | L2 | *Kondracki* | 3.08 | 10.36 | 38 | -0.64 | 1.36 | 0.292 |
| | | | GHT | 2.43 | 9.37 | 34 | | | |
| | | L3 | *Kondracki* | 5.63 | 12.95 | 47 | -0.89 | 1.45 | 0.331 |
| | | | GHT | 4.74 | 12.01 | 44 | | | |
| | | L4 | *Kondracki* | 6.57 | 14.34 | 51 | -0.61 | 1.38 | 0.294 |
| | | | GHT | 5.97 | 13.57 | 47 | | | |
| | patwo | L2 | *Kondracki* | 3.49 | 9.24 | 35 | -1.06 | 1.21 | 0.273 |
| | | | GHT | 2.43 | 8.46 | 32 | | | |
| | | L3 | *Kondracki* | 4.29 | 10.80 | 40 | -0.49 | 1.10 | 0.204 |
| | | | GHT | 3.80 | 10.60 | 40 | | | |
| | | L4 | *Kondracki* | 6.89 | 13.20 | 48 | -1.34 | 1.26 | 0.314 |
| | | | GHT | 5.54 | 12.85 | 45 | | | |

[+]*std is the standard deviation.*

[+]*SE is the standard error.*

**Table Appendix-16** The measurement of intervertebral angles of subject DO.

| | | | | mean of the IVA (°) | std of the IVA (°) | Range of Motion (°) | mean of the error (°) | std of the error (°) | SE |
|---|---|---|---|---|---|---|---|---|---|
| Subject DO | paone | L2/3 | *Kondracki* | -2.55 | 2.87 | 10 | 0.25 | 1.18 | 0.234 |
| | | | GHT | -2.30 | 3.00 | 13 | | | |
| | | L3/4 | *Kondracki* | -0.93 | 2.30 | 8 | -0.28 | 1.30 | 0.258 |
| | | | GHT | -1.21 | 2.75 | 12 | | | |
| | patwo | L2/3 | *Kondracki* | -0.80 | 1.81 | 6.5 | -0.57 | 1.54 | 0.279 |
| | | | GHT | -1.37 | 2.62 | 10 | | | |
| | | L3/4 | *Kondracki* | -2.6 | 2.65 | 9.5 | 0.86 | 1.27 | 0.260 |
| | | | GHT | -1.74 | 2.67 | 11 | | | |

[+] *IVA is the intervertebral angle.*

[+] *std is the standard deviation.*

[+] *SE is the standard error.*

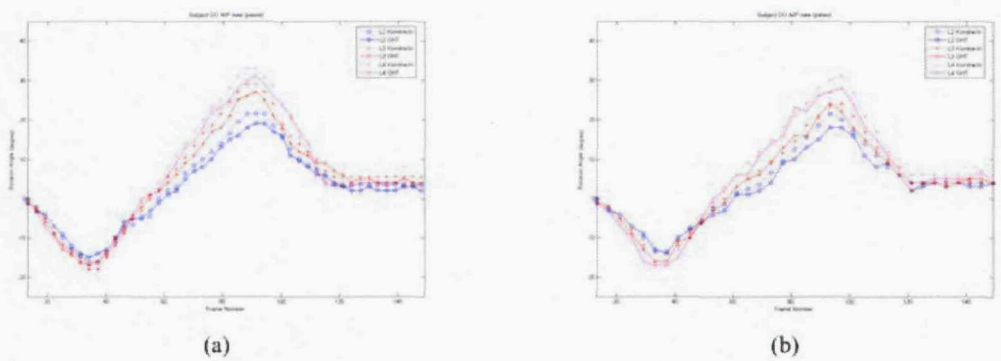

(a) (b)

**Figure Appendix-22** The rotation angles of the vertebrae L2, L3 and L4 versus frame number of subject DO. (a) Data set '*paone*'. (b) Data set '*patwo*'.

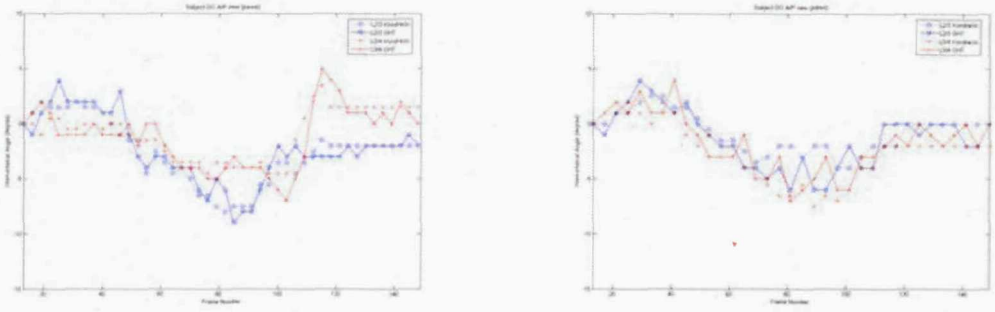

(a) (b)

**Figure Appendix-23** The intervertebral angles of the vertebrae L2/3 and L3/4 versus frame number of subject DO. (a) Data set '*paone*'. (b) Data set '*patwo*'.

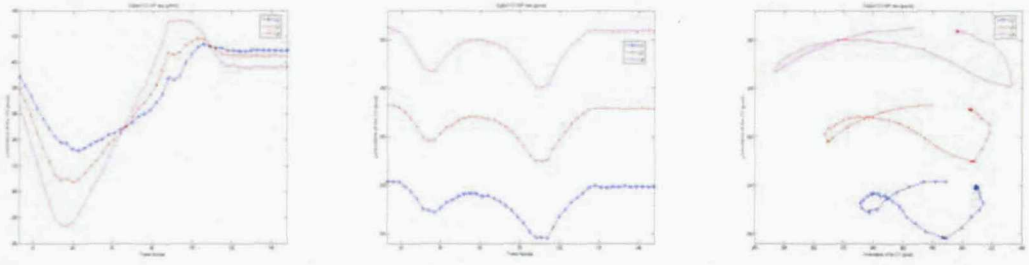

(a) (b) (c)

**Figure Appendix-24** The translation of the vertebrae L2, L3 and L4 versus frame number of subject DO '*paone*'. (a) *x*-translation of the centre points of the vertebrae. (b) *y*-translation of the centre point of the vertebrae. (c) The translation of the centre points of the vertebrae in 2-D.

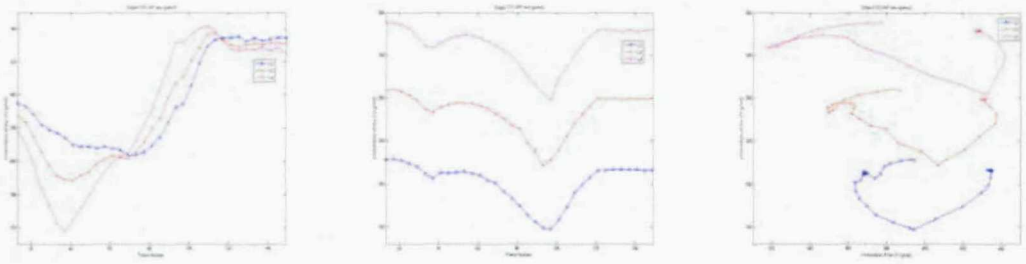

(a) (b) (c)

**Figure Appendix-25** The translation of the vertebrae L2, L3 and L4 versus frame number of subject DO '*patwo*'. (a) *x*-translation of the centre points of the vertebrae. (b) *y*-translation of the centre point of the vertebrae. (c) The translation of the centre points of the vertebrae in 2-D.

# Appendix F. Subject GD

## F.1 Motion Tracking of the DVF Images from the Anterior/Posterior View

**Table Appendix-17** The measurement of rotation angles of subject GD.

| | | | | mean of the rotation (°) | std of the rotation (°) | Range of Motion (°) | mean of the error (°) | std of the error (°) | SE |
|---|---|---|---|---|---|---|---|---|---|
| Subject GD | patwo | L2 | *Kondracki* | 3.99 | 8.57 | 31 | -0.33 | 1.15 | 0.202 |
| | | | GHT | 3.66 | 7.91 | 29 | | | |
| | | L3 | *Kondracki* | 7.99 | 13.80 | 49 | -0.70 | 1.37 | 0.260 |
| | | | GHT | 7.29 | 13.14 | 46 | | | |
| | | L4 | *Kondracki* | 9.46 | 16.44 | 57 | -0.69 | 1.43 | 0.268 |
| | | | GHT | 8.77 | 15.35 | 54 | | | |

[+]*std is the standard deviation.*

[+]*SE is the standard error.*

**Table Appendix-18** The measurement of intervertebral angles of subject GD.

| | | | | mean of the IVA (°) | std of the IVA (°) | Range of Motion (°) | mean of the error (°) | std of the error (°) | SE |
|---|---|---|---|---|---|---|---|---|---|
| Subject GD | patwo | L2/3 | *Kondracki* | -4.00 | 5.44 | 18 | 0.37 | 1.13 | 0.200 |
| | | | GHT | -3.63 | 5.49 | 18 | | | |
| | | L3/4 | *Kondracki* | -1.47 | 2.84 | 11 | -0.01 | 1.43 | 0.241 |
| | | | GHT | -1.49 | 2.67 | 12 | | | |

[+] *IVA is the intervertebral angle.*

[+]*std is the standard deviation.*

[+]*SE is the standard error.*

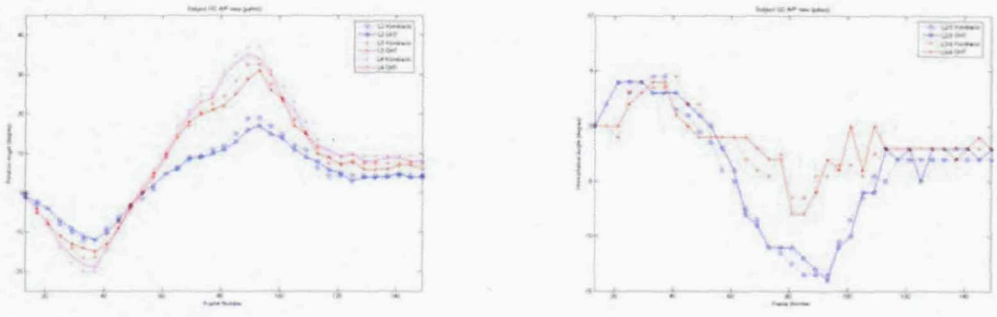

(a) (b)

**Figure Appendix-26** The rotation and intervertebral angles of the vertebrae L2, L3 and L4 versus frame number of subject GD '*patwo*'. (a) The rotation angles. (b) The intervertebral angles.

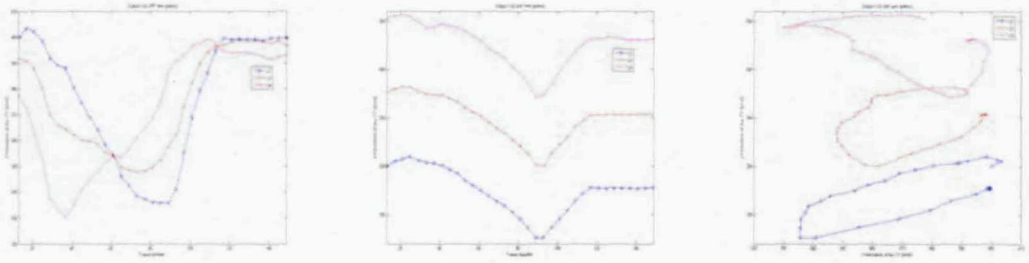

(a) (b) (c)

**Figure Appendix-27** The translation of the vertebrae L2, L3 and L4 versus frame number of subject GD '*patwo*'. (a) *x*-translation of the centre points of the vertebrae. (b) *y*-translation of the centre point of the vertebrae. (c) The translation of the centre points of the vertebrae in 2-D.

# Appendix G. Subject GP

## G.1 Motion Tracking of the DVF Images from the Lateral View

**Table Appendix-19** The measurement of rotation angles of subject GP.

| | | | | mean of the rotation (°) | std of the rotation (°) | Range of Motion (°) | mean of the error (°) | std of the error (°) | SE |
|---|---|---|---|---|---|---|---|---|---|
| Subject GP | latwo | L2 | *Kondracki* | 4.00 | 4.82 | 17 | -0.49 | 0.89 | 0.172 |
| | | | GHT | 3.51 | 4.93 | 18 | | | |
| | | L3 | *Kondracki* | 4.29 | 7.03 | 26 | -0.26 | 1.20 | 0.207 |
| | | | GHT | 4.03 | 6.75 | 23 | | | |

[+]*std is the standard deviation.*

[+]*SE is the standard error.*

**Table Appendix-20** The measurement of intervertebral angles of subject GP.

| | | | | mean of the IVA (°) | std of the IVA (°) | Range of Motion (°) | mean of error (°) | std of the error (°) | SE |
|---|---|---|---|---|---|---|---|---|---|
| Subject GP | L2/3 | latwo | *Kondracki* | -0.29 | 2.52 | 10 | -0.23 | 1.27 | 0.219 |
| | | | GHT | -0.51 | 2.38 | 8 | | | |

[+] *IVA is the intervertebral angle.*

[+]*std is the standard deviation.*

[+]*SE is the standard error.*

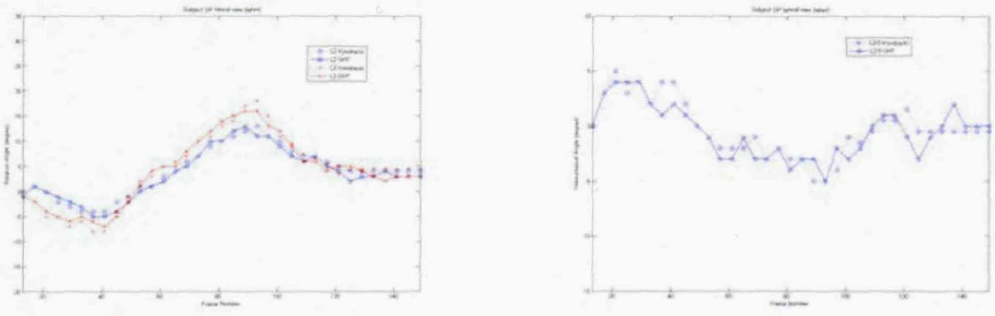

(a) (b)

**Figure Appendix-28** The rotation and intervertebral angles of the vertebrae L2 and L3 versus frame number of subject GP '*latwo*'. (a) The rotation angles. (b) The intervertebral angles.

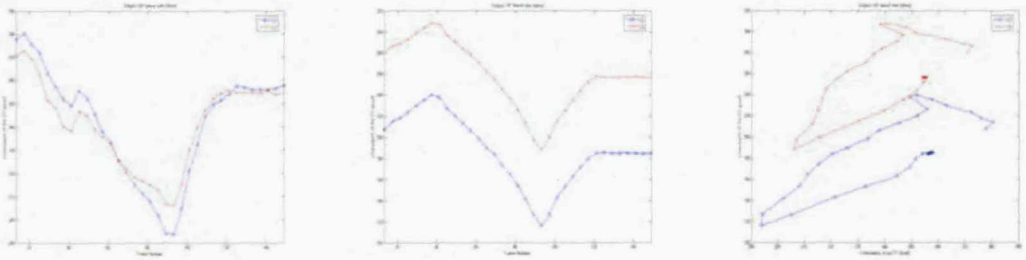

(a) (b) (c)

**Figure Appendix-29** The translation of the vertebrae L2 and L3 versus frame number of subject GP '*latwo*'. (a) *x*-translation of the centre points of the vertebrae. (b) *y*-translation of the centre point of the vertebrae. (c) The translation of the centre points of the vertebrae in 2-D.

## G.2 Motion Tracking of the DVF Images from the Anterior/Posterior View

**Table Appendix-21** The measurement of rotation angles of subject GP.

| | | | | mean of the rotation (°) | std of the rotation (°) | Range of Motion (°) | mean of the error (°) | std of the error (°) | SE |
|---|---|---|---|---|---|---|---|---|---|
| Subject GP | paone | L2 | *Kondracki* | 5.60 | 11.16 | 41 | -0.43 | 1.28 | 0.228 |
| | | | GHT | 5.17 | 10.29 | 36 | | | |
| | | L3 | *Kondracki* | 9.03 | 14.34 | 50.5 | -0.63 | 1.34 | 0.251 |
| | | | GHT | 8.40 | 13.45 | 48 | | | |
| | | L4 | *Kondracki* | 11.14 | 16.93 | 60 | -0.80 | 1.43 | 0.278 |
| | | | GHT | 10.34 | 16.36 | 56 | | | |
| | patwo | L2 | *Kondracki* | 6.56 | 12.06 | 43 | -0.76 | 1.14 | 0.232 |
| | | | GHT | 5.80 | 11.28 | 40 | | | |
| | | L3 | *Kondracki* | 7.50 | 14.94 | 53.5 | -0.64 | 1.22 | 0.234 |
| | | | GHT | 6.86 | 14.10 | 50 | | | |
| | | L4 | *Kondracki* | 11.33 | 18.61 | 63.5 | -0.81 | 1.62 | 0.307 |
| | | | GHT | 10.51 | 17.25 | 60 | | | |

[+]*std is the standard deviation.*

[+]*SE is the standard error.*

**Table Appendix-22** The measurement of intervertebral angles of subject GP.

| | | | | mean of the IVA (°) | std of the IVA (°) | Range of Motion (°) | mean of the error (°) | std of the error (°) | SE |
|---|---|---|---|---|---|---|---|---|---|
| Subject GP | paone | L2/3 | *Kondracki* | -3.43 | 3.66 | 12 | 0.20 | 1.17 | 0.200 |
| | | | GHT | -3.23 | 3.76 | 13 | | | |
| | | L3/4 | *Kondracki* | -2.11 | 2.81 | 10.5 | 0.17 | 1.37 | 0.234 |
| | | | GHT | -1.94 | 3.40 | 11 | | | |
| | patwo | L2/3 | *Kondracki* | -0.94 | 3.13 | 10.5 | -0.11 | 1.12 | 0.190 |
| | | | GHT | -1.06 | 3.27 | 12 | | | |
| | | L3/4 | *Kondracki* | -3.83 | 3.84 | 12 | 0.17 | 1.07 | 0.183 |
| | | | GHT | -3.66 | 3.41 | 11 | | | |

† *IVA is the intervertebral angle.*

† *std is the standard deviation.*

† *SE is the standard error.*

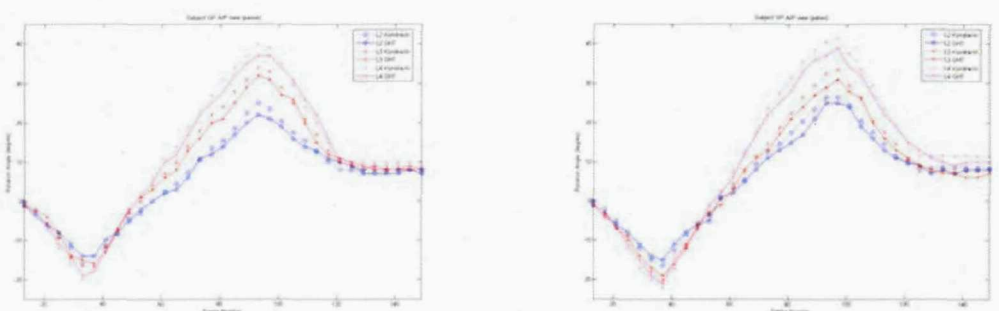

(a) (b)

**Figure Appendix-30** The rotation angles of the vertebrae L2, L3 and L4 versus frame number of subject GP. (a) Data set '*paone*'. (b) Data set '*patwo*'.

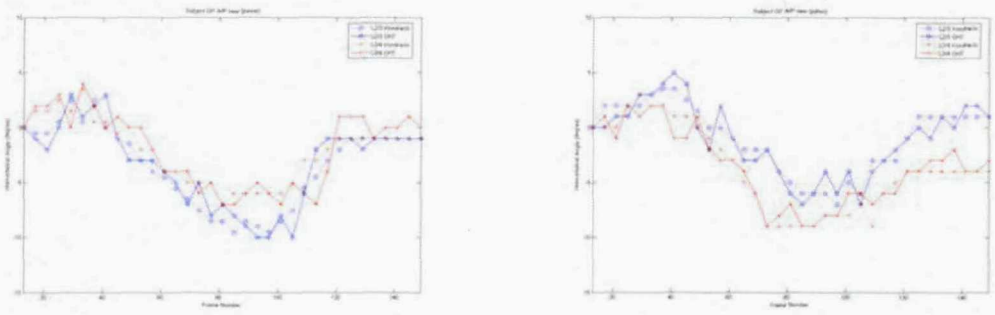

(a) (b)

**Figure Appendix-31** The intervertebral angles of the vertebrae L2/3 and L3/4 versus frame number of subject GP. (a) Data set '*paone*'. (b) Data set '*patwo*'.

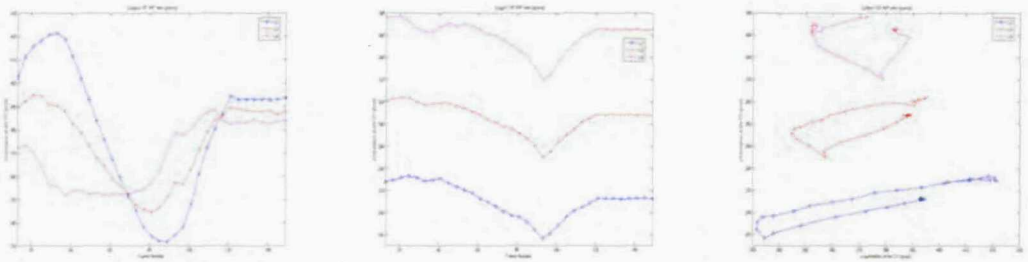

(a) (b) (c)

**Figure Appendix-32** The translation of the vertebrae L2, L3 and L4 versus frame number of subject GP '*paone*'. (a) *x*-translation of the centre points of the vertebrae. (b) *y*-translation of the centre point of the vertebrae. (c) The translation of the centre points of the vertebrae in 2-D.

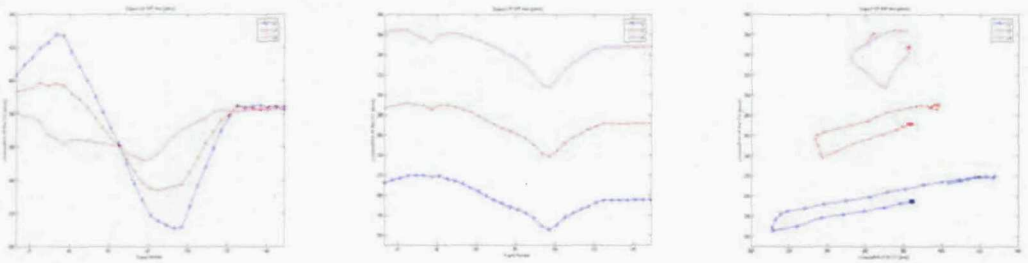

(a) (b) (c)

**Figure Appendix-33** The translation of the vertebrae L2, L3 and L4 versus frame number of subject GP '*patwo*'. (a) *x*-translation of the centre points of the vertebrae. (b) *y*-translation of the centre point of the vertebrae. (c) The translation of the centre points of the vertebrae in 2-D.

# Appendix H. Subject JM

## H.1 Motion Tracking of the DVF Images from the Lateral View

**Table Appendix-23** The measurement of rotation angles of subject JM.

| | | | | mean of the rotation (°) | std of the rotation (°) | Range of Motion (°) | mean of the error (°) | std of the error (°) | SE |
|---|---|---|---|---|---|---|---|---|---|
| Subject JM | laton | L2 | *Kondracki* | 2.99 | 8.43 | 30 | -0.59 | 1.12 | 0.215 |
| | | | GHT | 2.40 | 7.71 | 28 | | | |
| | | L3 | *Kondracki* | 0.91 | 9.80 | 37 | -0.31 | 1.43 | 0.248 |
| | | | GHT | 0.60 | 8.98 | 34 | | | |

[+]*std is the standard deviation.*

[+]*SE is the standard error.*

**Table Appendix-24** The measurement of intervertebral angles of subject JM.

| | | | | mean of the IVA (°) | std of the IVA (°) | Range of Motion (°) | mean of error (°) | std of the error (°) | SE |
|---|---|---|---|---|---|---|---|---|---|
| Subject JM | L2/3 | laton | *Kondracki* | 2.07 | 1.69 | 8 | -0.27 | 1.20 | 0.209 |
| | | | GHT | 1.80 | 1.91 | 9 | | | |

[+] *IVA is the intervertebral angle.*

[+]*std is the standard deviation.*

[+]*SE is the standard error.*

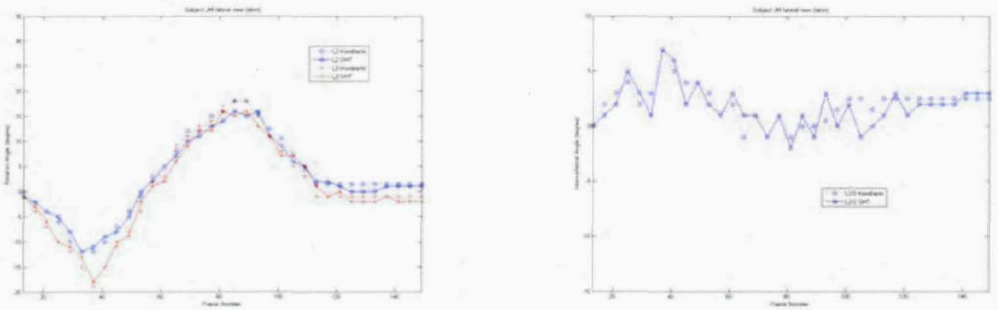

(a) (b)

**Figure Appendix-34** The rotation and intervertebral angles of the vertebrae L2 and L3 versus frame number of subject JM '*laton*'. (a) The rotation angles. (b) The intervertebral angles.

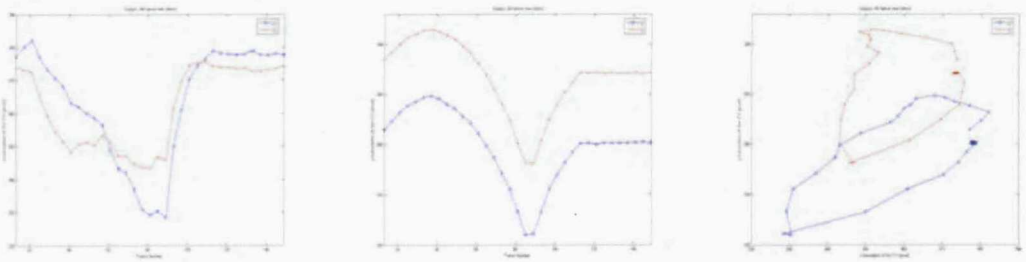

(a) (b) (c)

**Figure Appendix-35** The translation of the vertebrae L2 and L3 versus frame number of subject JM '*laton*'. (a) $x$-translation of the centre points of the vertebrae. (b) $y$-translation of the centre point of the vertebrae. (c) The translation of the centre points of the vertebrae in 2-D.

## H.2 Motion Tracking of the DVF Images from the Anterior/Posterior View

**Table Appendix-25** The measurement of rotation angles of subject JM.

| | | | | mean of the rotation (°) | std of the rotation (°) | Range of Motion (°) | mean of the error (°) | std of the error (°) | SE |
|---|---|---|---|---|---|---|---|---|---|
| Subject JM | paone | L2 | *Kondracki* | 0.03 | 10.63 | 39 | -0.17 | 1.22 | 0.209 |
| | | | GHT | -0.14 | 10.17 | 36 | | | |
| | | L3 | *Kondracki* | 3.06 | 13.04 | 48 | -0.11 | 1.40 | 0.237 |
| | | | GHT | 2.94 | 12.34 | 45 | | | |
| | | L4 | *Kondracki* | 4.71 | 16.17 | 58 | -0.40 | 1.54 | 0.269 |
| | | | GHT | 4.31 | 15.25 | 54 | | | |

[+]*std is the standard deviation.*

[+]*SE is the standard error.*

**Table Appendix-26** The measurement of intervertebral angles of subject JM.

| | | | | mean of the IVA (°) | std of the IVA (°) | Range of Motion (°) | mean of the error (°) | std of the error (°) | SE |
|---|---|---|---|---|---|---|---|---|---|
| Subject JM | paone | L2/3 | *Kondracki* | -3.03 | 3.39 | 11.5 | -0.06 | 1.22 | 0.207 |
| | | | GHT | -3.09 | 3.59 | 10 | | | |
| | | L3/4 | *Kondracki* | -1.66 | 3.34 | 12.5 | 0.29 | 1.39 | 0.241 |
| | | | GHT | -1.37 | 3.34 | 11 | | | |

[+] *IVA is the intervertebral angle.*

[+]*std is the standard deviation.*

[+]*SE is the standard error.*

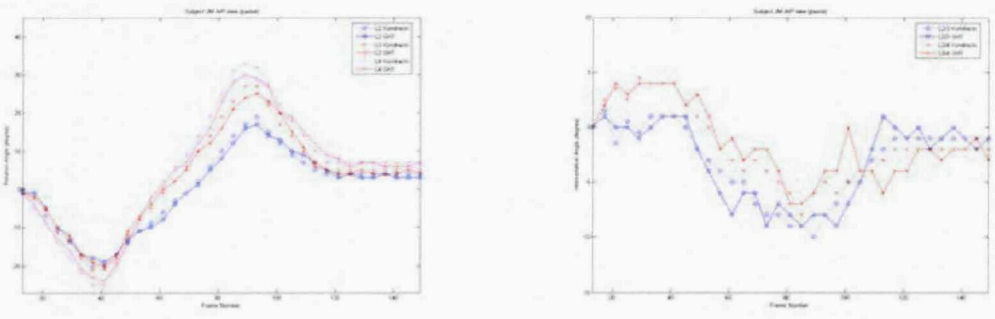

(a) (b)

**Figure Appendix-36** The rotation and intervertebral angles of the vertebrae L2, L3 and L4 versus frame number of subject JM '*paone*'. (a) The rotation angles. (b) The intervertebral angles.

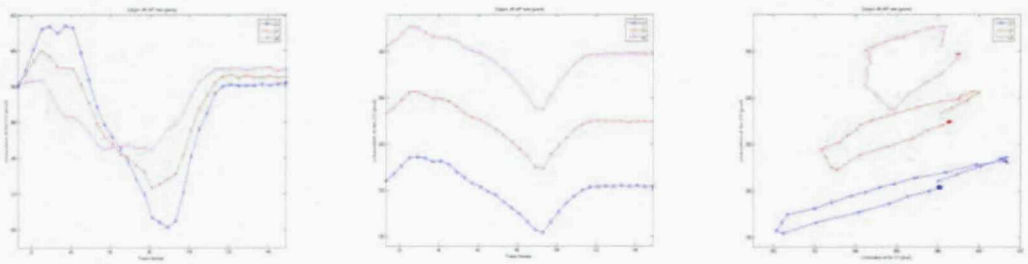

(a) (b) (c)

**Figure Appendix-36** The translation of the vertebrae L2, L3 and L4 versus frame number of subject JM '*paone*'. (a) *x*-translation of the centre points of the vertebrae. (b) *y*-translation of the centre point of the vertebrae. (c) The translation of the centre points of the vertebrae in 2-D.

# Appendix I. Subject JW

## I.1 Motion Tracking of the DVF Images from the Lateral View

**Table Appendix-27** The measurement of rotation angles of subject JW.

| | | | | mean of the rotation (°) | std of the rotation (°) | Range of Motion (°) | mean of the error (°) | std of the error (°) | SE |
|---|---|---|---|---|---|---|---|---|---|
| Subject JW | laton | L2 | *Kondracki* | 1.93 | 7.01 | 26.5 | -0.41 | 1.22 | 0.217 |
| | | | GHT | 1.51 | 6.50 | 24 | | | |
| | | L3 | *Kondracki* | 3.06 | 9.92 | 36 | -0.43 | 1.31 | 0.234 |
| | | | GHT | 2.63 | 9.52 | 32 | | | |
| | latwo | L2 | *Kondracki* | 3.17 | 6.46 | 25 | -0.09 | 1.07 | 0.181 |
| | | | GHT | 3.09 | 6.17 | 23 | | | |
| | | L3 | *Kondracki* | 4.49 | 9.07 | 33.5 | -0.40 | 1.32 | 0.233 |
| | | | GHT | 4.09 | 8.33 | 30 | | | |

[+]*std is the standard deviation.*

[+]*SE is the standard error.*

**Table Appendix-28** The measurement of intervertebral angles of subject JW.

| | | | | mean of the IVA (°) | std of the IVA (°) | Range of Motion (°) | mean of error (°) | std of the error (°) | SE |
|---|---|---|---|---|---|---|---|---|---|
| Subject JW | L2/3 | laton | *Kondracki* | -1.13 | 3.39 | 10.5 | 0.01 | 1.28 | 0.216 |
| | | | GHT | -1.11 | 3.42 | 10 | | | |
| | | latwo | *Kondracki* | -1.31 | 2.83 | 10 | 0.31 | 1.48 | 0.255 |
| | | | GHT | -1.00 | 2.61 | 9 | | | |

*IVA is the intervertebral angle.*

*std is the standard deviation.*

*SE is the standard error.*

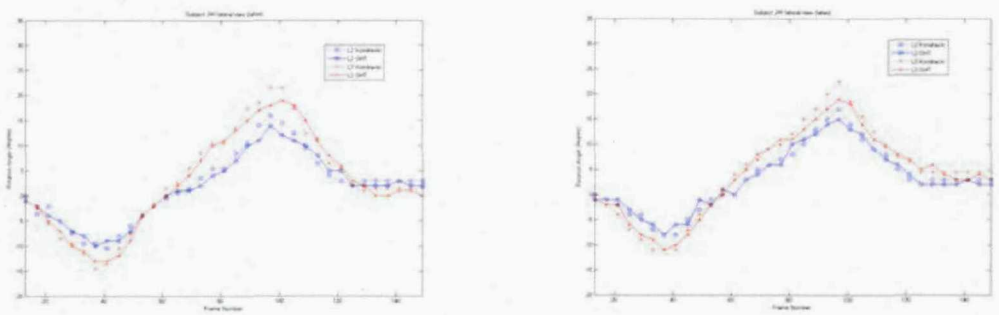

(a) (b)

**Figure Appendix-37** The rotation angles of the vertebrae L2 and L3 versus frame number of subject JW. (a) Data set '*laton*'. (b) Data set '*latwo*'.

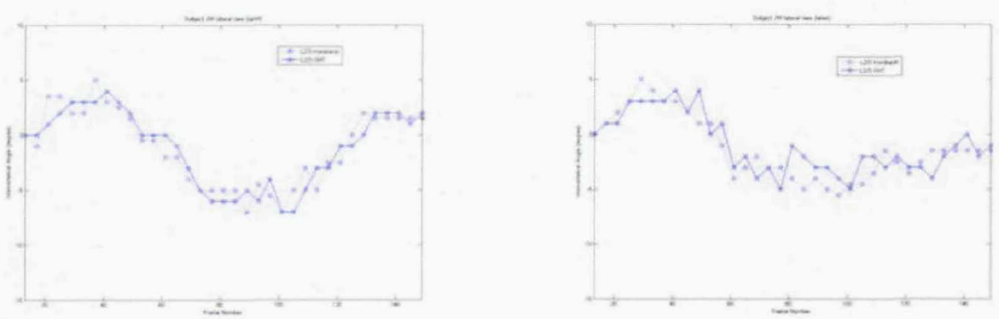

(a) (b)

**Figure Appendix-38** The intervertebral angles of the vertebrae L2/3 versus frame number of subject JW. (a) Data set '*laton*'. (b) Data set '*latwo*'.

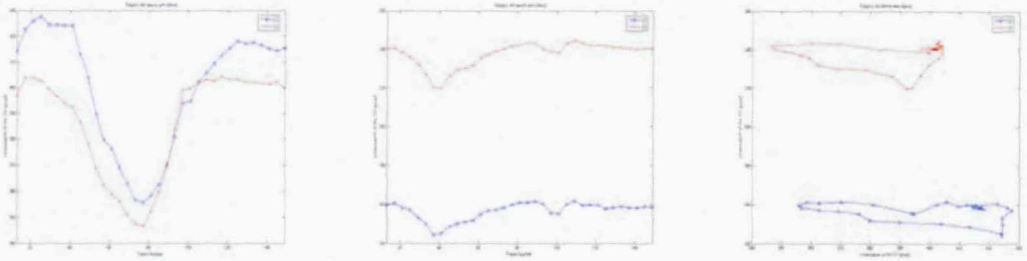

(a) (b) (c)

**Figure Appendix-39** The translation of the vertebrae L2 and L3 versus frame number of subject JW '*laton*'. (a) *x*-translation of the centre points of the vertebrae. (b) *y*-translation of the centre point of the vertebrae. (c) The translation of the centre points of the vertebrae in 2-D.

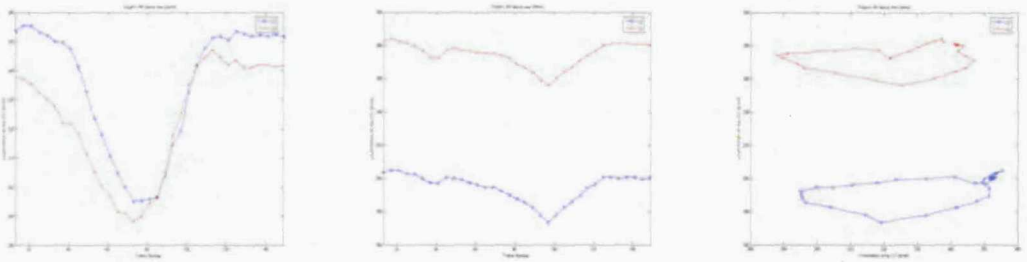

(a) (b) (c)

**Figure Appendix-40** The translation of the vertebrae L2 and L3 versus frame number of subject JW '*latwo*'. (a) *x*-translation of the centre points of the vertebrae. (b) *y*-translation of the centre point of the vertebrae. (c) The translation of the centre points of the vertebrae in 2-D.

## I.2 Motion Tracking of the DVF Images from the Anterior/Posterior View

**Table appendix-29** The measurement of rotation angles of subject JW.

| | | | | mean of the rotation (°) | std of the rotation (°) | Range of Motion (°) | mean of the error (°) | std of the error (°) | SE |
|---|---|---|---|---|---|---|---|---|---|
| Subject JW | paone | L2 | *Kondracki* | 2.56 | 11.15 | 42 | -0.16 | 1.22 | 0.208 |
| | | | GHT | 2.40 | 10.43 | 38 | | | |
| | | L3 | *Kondracki* | 2.86 | 13.57 | 51 | -0.14 | 1.55 | 0.263 |
| | | | GHT | 2.71 | 12.31 | 46 | | | |
| | | L4 | *Kondracki* | 5.13 | 17.02 | 63.5 | -0.39 | 1.71 | 0.296 |
| | | | GHT | 4.74 | 15.75 | 58 | | | |
| | patwo | L2 | *Kondracki* | 1.03 | 7.99 | 31 | -0.20 | 1.18 | 0.203 |
| | | | GHT | 0.83 | 7.24 | 26 | | | |
| | | L3 | *Kondracki* | 1.66 | 11.21 | 42 | -0.31 | 1.32 | 0.230 |
| | | | GHT | 1.34 | 10.30 | 39 | | | |
| | | L4 | *Kondracki* | 6.03 | 14.87 | 55 | -0.86 | 1.38 | 0.275 |
| | | | GHT | 5.17 | 13.77 | 51 | | | |

[+]*std is the standard deviation.*

[+]*SE is the standard error.*

**Table Appendix-30** The measurement of intervertebral angles of subject JW.

| | | | | mean of the IVA (°) | std of the IVA (°) | Range of Motion (°) | mean of the error (°) | std of the error (°) | SE |
|---|---|---|---|---|---|---|---|---|---|
| Subject JW | paone | L2/3 | *Kondracki* | -0.30 | 3.11 | 9.5 | -0.01 | 1.22 | 0.205 |
| | | | GHT | -0.31 | 2.68 | 9 | | | |
| | | L3/4 | *Kondracki* | -2.27 | 3.54 | 13 | 0.24 | 1.18 | 0.204 |
| | | | GHT | -2.03 | 3.75 | 16 | | | |
| | patwo | L2/3 | *Kondracki* | -0.63 | 3.61 | 12 | 0.11 | 1.23 | 0.209 |
| | | | GHT | -0.51 | 3.38 | 13 | | | |
| | | L3/4 | *Kondracki* | -4.37 | 3.93 | 13 | 0.54 | 1.31 | 0.241 |
| | | | GHT | -3.83 | 3.84 | 13 | | | |

- *IVA is the intervertebral angle.*
- *std is the standard deviation.*
- *SE is the standard error.*

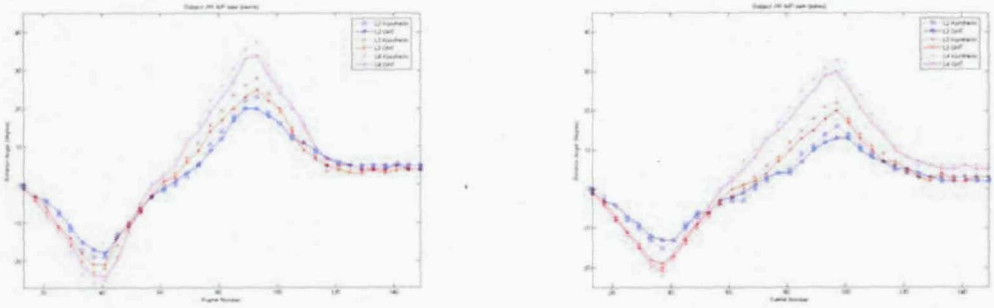

(a) (b)

**Figure Appendix-41** The rotation angles of the vertebrae L2, L3 and L4 versus frame number of subject JW. (a) Data set '*paone*'. (b) Data set '*patwo*'.

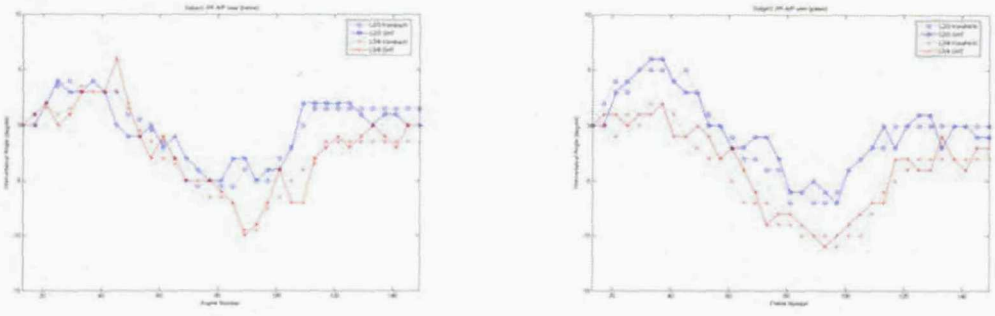

(a) (b)

**Figure Appendix-42** The intervertebral angles of the vertebrae L2/3 and L3/4 versus frame number of subject JW. (a) Data set '*paone*'. (b) Data set '*patwo*'.

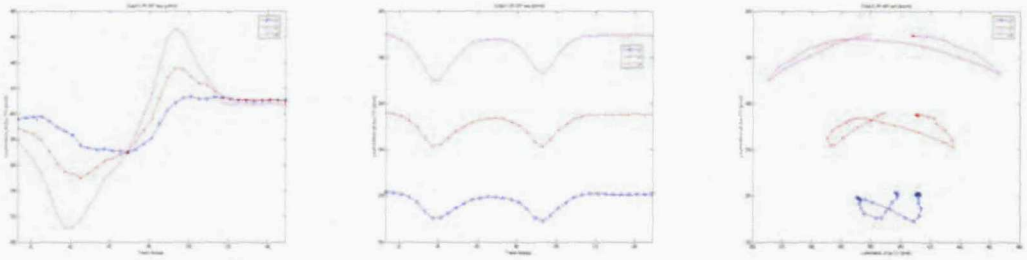

(a) (b) (c)

**Figure Appendix-43** The translation of the vertebrae L2, L3 and L4 versus frame number of subject JW '*paone*'. (a) *x*-translation of the centre points of the vertebrae. (b) *y*-translation of the centre point of the vertebrae. (c) The translation of the centre points of the vertebrae in 2-D.

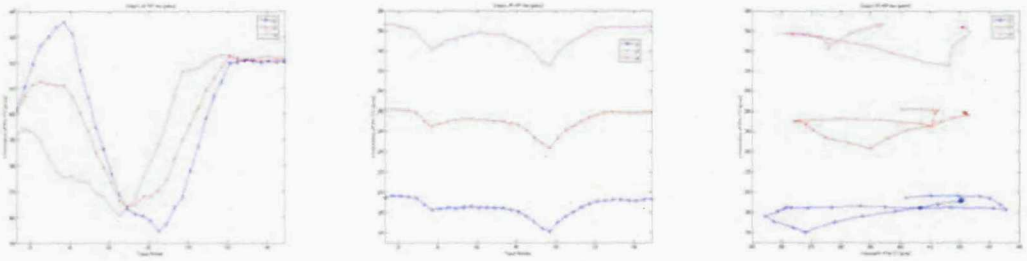

(a) (b) (c)

**Figure Appendix-44** The translation of the vertebrae L2, L3 and L4 versus frame number of subject JW '*patwo*'. (a) *x*-translation of the centre points of the vertebrae. (b) *y*-translation of the centre point of the vertebrae. (c) The translation of the centre points of the vertebrae in 2-D.

# Appendix J. Subject NW

## J.1 Motion Tracking of the DVF Images from the Lateral View

**Table Appendix-31** The measurement of rotation angles of subject NW.

| | | | | mean of the rotation (°) | std of the rotation (°) | Range of Motion (°) | mean of the error (°) | std of the error (°) | SE |
|---|---|---|---|---|---|---|---|---|---|
| Subject NW | laton | L2 | *Kondracki* | 1.74 | 7.62 | 30.5 | -0.46 | 1.43 | 0.254 |
| | | | GHT | 1.29 | 6.81 | 27 | | | |
| | | L3 | *Kondracki* | 1.89 | 9.17 | 34 | -0.66 | 1.16 | 0.226 |
| | | | GHT | 1.23 | 8.86 | 32 | | | |

[+]*std is the standard deviation.*

[+]*SE is the standard error.*

**Table Appendix-32** The measurement of intervertebral angles of subject NW.

| | | | | mean of the IVA (°) | std of the IVA (°) | Range of Motion (°) | mean of error (°) | std of the error (°) | SE |
|---|---|---|---|---|---|---|---|---|---|
| Subject NW | L2/3 | laton | *Kondracki* | -0.14 | 1.83 | 7 | 0.20 | 1.26 | 0.215 |
| | | | GHT | 0.06 | 2.45 | 10 | | | |

[+] *IVA is the intervertebral angle.*

[+]*std is the standard deviation.*

[+]*SE is the standard error.*

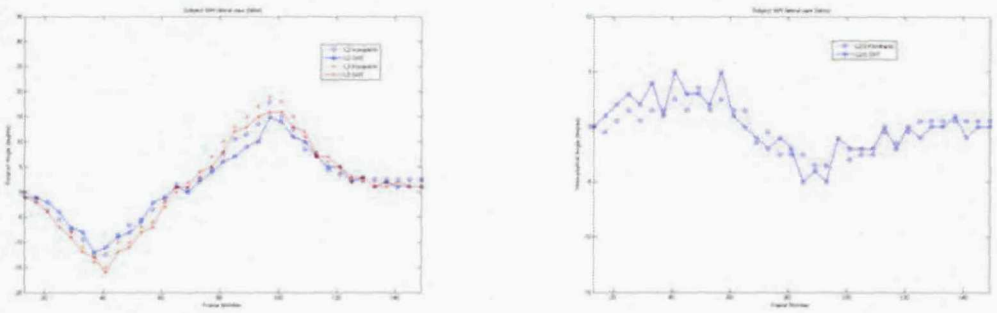

(a) (b)

**Figure Appendix-45** The rotation and intervertebral angles of the vertebrae L2 and L3 versus frame number of subject RM '*laton*'. (a) The rotation angles. (b) The intervertebral angles.

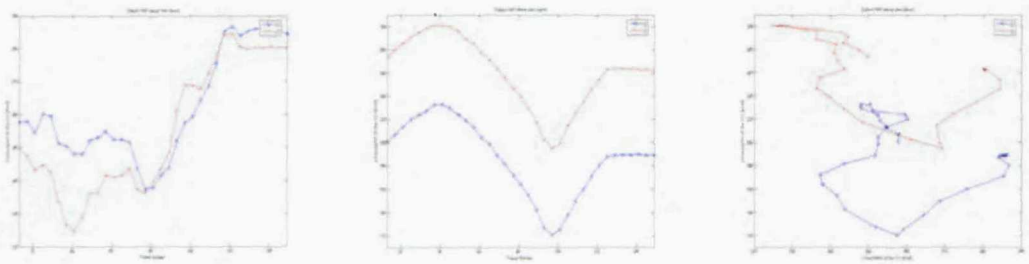

(a) (b) (c)

**Figure Appendix-46** The translation of the vertebrae L2 and L3 versus frame number of subject NW '*laton*'. (a) *x*-translation of the centre points of the vertebrae. (b) *y*-translation of the centre point of the vertebrae. (c) The translation of the centre points of the vertebrae in 2-D.

## J.2 Motion Tracking of the DVF Images from the Anterior/Posterior View

**Table Appendix-33** The measurement of rotation angles of subject NW.

| | | | | mean of the rotation (°) | std of the rotation (°) | Range of Motion (°) | mean of the error (°) | std of the error (°) | SE |
|---|---|---|---|---|---|---|---|---|---|
| Subject NW | patwo | L2 | *Kondracki* | 6.69 | 10.08 | 36 | -0.71 | 1.20 | 0.237 |
| | | | GHT | 5.97 | 9.07 | 31 | | | |
| | | L3 | *Kondracki* | 9.54 | 12.86 | 45 | -0.77 | 1.29 | 0.254 |
| | | | GHT | 8.77 | 11.89 | 42 | | | |
| | | L4 | *Kondracki* | 10.31 | 15.81 | 55 | -0.91 | 1.27 | 0.266 |
| | | | GHT | 9.40 | 14.86 | 52 | | | |

[+]*std is the standard deviation.*

[+]*SE is the standard error.*

**Table Appendix-34** The measurement of intervertebral angles of subject NW.

| | | | | mean of the IVA (°) | std of the IVA (°) | Range of Motion (°) | mean of the error (°) | std of the error (°) | SE |
|---|---|---|---|---|---|---|---|---|---|
| Subject NW | patwo | L2/3 | *Kondracki* | -2.86 | 3.36 | 11 | 0.06 | 1.03 | 0.174 |
| | | | GHT | -2.80 | 3.38 | 11 | | | |
| | | L3/4 | *Kondracki* | -0.77 | 3.58 | 12 | 0.14 | 1.09 | 0.186 |
| | | | GHT | -0.63 | 3.65 | 13 | | | |

[+] *IVA is the intervertebral angle.*

[+]*std is the standard deviation.*

[+]*SE is the standard error.*

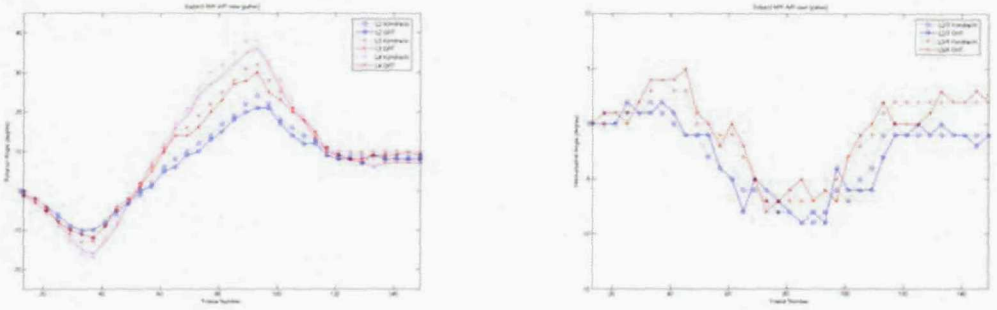

(a) (b)

**Figure Appendix-47** The rotation and intervertebral angles of the vertebrae L2,L3 and L4 versus frame number of subject NW '*patwo*'. (a) The rotation angles. (b) The intervertebral angles.

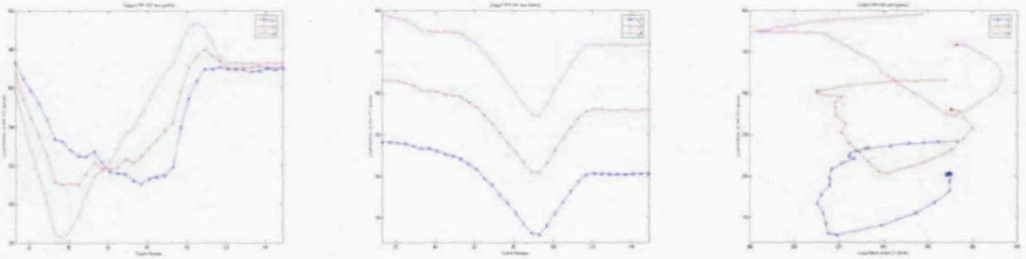

(a) (b) (c)

**Figure Appendix-48** The translation of the vertebrae L2, L3 and L4 versus frame number of subject NW '*patwo*'. (a) *x*-translation of the centre points of the vertebrae. (b) *y*-translation of the centre point of the vertebrae. (c) The translation of the centre points of the vertebrae in 2-D.

# Appendix K. Subject RM

## K.1 Motion Tracking of the DVF Images from the Anterior/Posterior View

**Table Appendix-35** The measurement of rotation angles of subject RM.

| | | | | mean of the rotation (°) | std of the rotation (°) | Range of Motion (°) | mean of the error (°) | std of the error (°) | SE |
|---|---|---|---|---|---|---|---|---|---|
| Subject RM | patwo | L2 | *Kondracki* | 3.69 | 7.40 | 28 | -0.40 | 1.12 | 0.200 |
| | | | GHT | 3.29 | 6.58 | 25 | | | |
| | | L3 | *Kondracki* | 4.69 | 10.38 | 36 | -0.43 | 1.40 | 0.248 |
| | | | GHT | 4.26 | 9.27 | 34 | | | |
| | | L4 | *Kondracki* | 5.63 | 12.98 | 47 | -0.60 | 1.48 | 0.270 |
| | | | GHT | 5.03 | 11.83 | 42 | | | |

[+]*std is the standard deviation.*

[+]*SE is the standard error.*

**Table Appendix-36** The measurement of intervertebral angles of subject RM.

| | | | | mean of the IVA (°) | std of the IVA (°) | Range of Motion (°) | mean of the error (°) | std of the error (°) | SE |
|---|---|---|---|---|---|---|---|---|---|
| Subject RM | patwo | L2/3 | *Kondracki* | -1.00 | 3.75 | 12 | 0.03 | 1.07 | 0.181 |
| | | | GHT | -0.97 | 3.33 | 10 | | | |
| | | L3/4 | *Kondracki* | -0.94 | 2.71 | 11 | 0.17 | 0.82 | 0.142 |
| | | | GHT | -0.77 | 2.78 | 12 | | | |

[+] *IVA is the intervertebral angle.*

[+]*std is the standard deviation.*

[+]*SE is the standard error.*

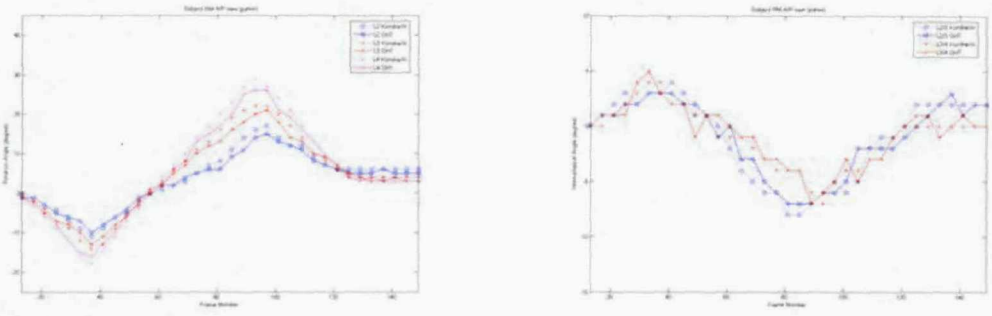

(a) (b)

**Figure Appendix-49** The rotation and intervertebral angles of the vertebrae L2,L3 and L4 versus frame number of subject NW '*patwo*'. (a) The rotation angles. (b) The intervertebral angles.

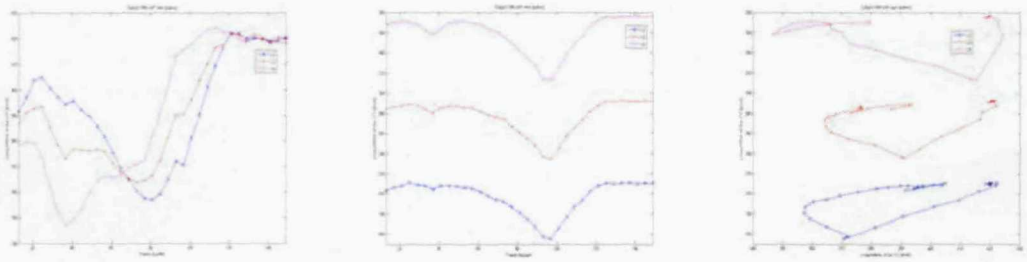

(a) (b) (c)

**Figure Appendix-50** The translation of the vertebrae L2, L3 and L4 versus frame number of subject RM '*patwo*'. (a) *x*-translation of the centre points of the vertebrae. (b) *y*-translation of the centre point of the vertebrae. (c) The translation of the centre points of the vertebrae in 2-D.